

Quality control of printed electronics using terahertz radiation

by

Mariia ZHULDYBINA

THESIS PRESENTED TO ÉCOLE DE TECHNOLOGIE SUPÉRIEURE
IN PARTIAL FULFILLMENT FOR THE DEGREE OF
DOCTOR OF PHILOSOPHY
Ph.D.

MONTREAL, JUNE 25, 2021

ÉCOLE DE TECHNOLOGIE SUPÉRIEURE
UNIVERSITÉ DU QUÉBEC



Mariia Zhuldybina, 2021



This Creative Commons license allows readers to download this work and share it with others as long as the author is credited. The content of this work cannot be modified in any way or used commercially.

BOARD OF EXAMINERS

**THIS THESIS HAS BEEN EVALUATED
BY THE FOLLOWING BOARD OF EXAMINERS**

M. François Blanchard, thesis supervisor
Department of Electrical Engineering, École de technologie supérieure

M. Ricardo Zednik, co-supervisor
Department of Mechanical Engineering, École de technologie supérieure

M. Vladimir Brailovski, president of the board of examiners
Department of Mechanical Engineering, École de technologie supérieure

M. Erik David, member of the jury
Department of Mechanical Engineering, École de technologie supérieure

M. Luca Razzari, external independent examiner
Institut national de la recherche scientifique - Centre Energie, Matériaux et Télécommunications

**THIS THESIS WAS PRESENTED AND DEFENDED
IN THE PRESENCE OF A BOARD OF EXAMINERS AND THE PUBLIC
ON APRIL 29, 2021
AT ÉCOLE DE TECHNOLOGIE SUPÉRIEURE**

FOREWORD

My PhD had a primary objective to develop the quality control solution for printed electronics using the terahertz time-domain spectroscopy. To the best of our knowledge, we have been the first ones who utilized the metamaterials' high sensitivity for quality control purposes. Our results demonstrate a new way of tracking the influence of printed conditions on the conductivity and geometry of printed devices fabricated in the industrial environment. The outcome of my PhD project is the start-up TRAQC, which is based on my PhD results with further development of the quality control of the printing process at the industrial environment.

ACKNOWLEDGEMENTS

My PhD path was long and not always straightforward. Ricardo, I would like to thank you for taking me as a PhD student and believing in my success.

François, I can't express how much I appreciate your help. Your passion about the research and consistent support are something that make me to be in love with my work. I could never think about doing an academic career and doing the research. I highly appreciate you for the opportunity to go to Japan for a fascinating working and life-changing experience. I truly believe that we will bring THz technology to the printed electronics industry and some others. Thank you for forcing me to take Dave's class in 2017. It was a game-changing term.

David Cooke, your course was the best one I have taken. The level of knowledge, the lectures, and the tricky homework assignments had a big influence on me. During this class, I finally could believe in myself. Thanks to the class, I met my friend and business partner – Ben, who has been giving and still giving a lot of support in work and life.

I would like to acknowledge my lab-mates from PuleTS and Tera-ETS for all these years being around. Xavier, you know how much you mean to me. I will never forget working in the lab on developing THz-TDS, writing articles together and discussing research, traveling for OTST 2019, and hiking Grand Canyon. Nice trips, and your support would never be forgotten. I would like to thank Leo for our lab-work together in Bordeaux. It was an amazing experience working in a new lab for me. Thanks to Louis-Phillipe for interesting questions about THz technology and good chats in the office during the pandemic.

I would like to thank professor K. Tanaka for giving me the opportunity to work with a near-field microscope. Also, I appreciate a lot the help from the lab-members of K. Tanaka group during my stay in Kyoto. Especially, Hiraoko-San, Kusaba-San, and Uchida-San, I appreciate your time for entertaining me. Thanks to Murate-San for showing the other way of working and nice trip in Nagoya.

VIII

While academic support has been discussed, this section would be incomplete if I left out the emotional support of my friends and family. Liza, thank you so much for all our phone calls for the last seven years non-stop. No one in the world knows me better and has gone with me through this path. Erika, you are my Montreal's sister. Our PhD journey together, difficulties with languages, and much more stay with me. Thank you for everything! Tanya, Oxana and Marina, thank you for always being there for me whenever I needed it. Dashka, you were the first in my life who was impressed with the optical table and mirrors. You made me feel like a scientist. Thank you for your help with the figures! Daria, you are my COVID-19's present. I would not survive without you during that time. Thank you for always being around and ready to give a supportive hug! Fred, I highly appreciate you for our scientific and philosophical discussion; your support means a lot to me. Salah, thank you so much for your help and everyday support. The family is a big part of my life. Spasibo mama, papa, Sasha, babushka, dedushka, Vera, Tanya, Andrey, Nadya and many more. Thank you for shaping me in who I am today. I would never be here without your tremendous support. I am sorry if I forgot someone. Thanks to everybody I met during these incredible years of PhD at ÉTS. You all made it special.

Finally, I gratefully acknowledge the participation of members of the jury in my Ph.D. defense professor Vladimir Brailovski, professor Eric David and professor Luca Razzari.

Contrôle de la qualité des produits électroniques imprimés utilisant le rayonnement térahertz

Mariia ZHULDYBINA

RÉSUMÉ

L'impression graphique et la production électronique sont deux technologies de fabrication à grand volume. Leur combinaison apporte une nouvelle technique de fabrication et une forme unique d'applications dans le domaine de l'électronique. L'électronique imprimable (EI) est une nouvelle technologie de fabrication avancée qui permet une fabrication à moindre coût pour la production en grand volume de dispositifs électroniques. L'EI est une façon alternative, prometteuse et respectueuse de l'environnement pour produire des produits électroniques, des affichages ou aider à produire de l'énergie verte à faible coût ainsi que de nouvelles solutions pour des dispositifs flexibles. L'un des principaux défis de cette nouvelle technologie est de l'implanter dans un environnement industriel. Pour réussir l'industrialisation de cette technologie, la fiabilité et la répétabilité de la qualité des dispositifs et des processus de fabrication doivent être vérifiés et assurés grâce à un contrôle de qualité efficace. Actuellement, le contrôle de la qualité est évalué manuellement ou à l'aide de techniques de laboratoire bien développées, qui ont les désavantages d'être destructeurs et longs. Pour appliquer ces méthodes dans une chaîne de production, il faut tenir compte des conditions spécifiques telles que : (i) un éclairage approprié, (ii) une direction particulière, (iii) une vitesse de production spécifique et (iv) un environnement contrôlé nécessitant une salle blanche. Ces conditions limitent fortement la nécessité de l'EI en tant que technique de fabrication industrielle. C'est pourquoi, il est primordial de développer la mise au point d'une technique de caractérisation en ligne efficace pour contrôler les propriétés des produits imprimés.

Ce travail s'est concentré sur l'étude, le développement et l'utilisation de la spectroscopie térahertz dans le domaine temporel (THz-TDS) comme outil de caractérisation pour le contrôle de la qualité des dispositifs d'EI. Au cours de la dernière décennie, la THz-TDS a été étudiée de façon intensive et il a été démontré que la THz-TDS peut être utilisée comme un outil de contrôle de qualité sans contact, non destructif, à haute résolution et non invasif. Dans les essais non destructifs des matériaux, le contrôle de la qualité est souvent basé sur l'échantillonnage de l'état d'une chaîne de production. Pour garantir l'interaction de la lumière THz avec les matériaux conducteurs imprimés, nous avons introduit une stratégie simple utilisant les métamatériaux THz comme barre de contrôle de la qualité d'impression (QCB).

Pour démontrer notre idée, nous avons imprimé des QCB en utilisant deux types de techniques d'impression. Cette technique pourrait être utilisée avec la technique de l'impression continue de rouleau à rouleau pour fabriquer des dispositifs imprimés fonctionnels de façon industrielle. Notre travail utilise les QCB de la même manière qu'il est indispensable d'utiliser une mire dans l'impression offset pour réaliser le contrôle de qualité. Dans l'impression offset, la surface imprimée de la structure de contrôle est d'environ 1 cm^2 . Ici, notre concept développé est assez similaire.

Dans le cadre de cette thèse, deux types de métamatériaux ont été conçus et étudiés pour le suivi de la qualité d'impression selon deux critères: la variation géométrique et la conductivité.

La mise en œuvre des métamatériaux comme structure de contrôle de la qualité est l'une des solutions possibles en tant que suivi de processus en ligne et in situ dans des environnements de production industrielle et une voie vers le contrôle de la qualité en boucle fermée.

Mots-clés: Électronique imprimée, contrôle de qualité, spectroscopie térahertz, tests non destructifs

Quality control of printed electronics using terahertz radiation

Mariia ZHULDYBINA

ABSTRACT

Graphic printing and electronics production are two high volume manufacturing technologies. Their combination brings a new fabrication technique and unique form of electronic applications. Printable electronics (PE) is a new advanced manufacturing technology that enables lower-cost fabrication for large-volume production of electronic devices. PE is a promising, environmentally friendly alternative route to produce display or energy products at a low cost and with new possibilities like flexible devices. One of the main challenges of this new technology is to scale it up to the industrial level. For the successful industrialization of this technology, reliability, and repeatability in both equipment and processes should be provided using efficient quality control. Currently, quality control is assessed manually or using well-developed laboratory techniques, which could be destructive or more time-consuming. To apply these methods in a production line, the specific conditions such as an appropriate illumination, a particular direction, a specific speed production, or even a cleanroom environment must be considered. These severely restrict the value of PE as an industrial manufacturing technique and requires developing an efficient in-line characterization technique to control the quality of fabrication process.

This work focuses on studying and developing terahertz time-domain spectroscopy (THz-TDS) as a characterization tool for the quality control of printed process. During the last decade, THz-TDS has received a lot of attention due to its contactless, non-destructive, high-resolution, non-invasive abilities for quality control. In non-destructive testing of materials, quality control is often based on sampling the condition of a production line. To ensure THz light interacts with the printed conductive materials, we introduced a simple strategy using THz metamaterials as a printing quality control bar (QCB).

To prove our idea, we printed QCBs using two types of printing techniques, which demonstrates the potential of using continuous roll to roll printing to manufacture functional printed devices. Our work employs QCBs in the same way that a test pattern is indispensable for quality control using offset color printing. In offset printing, the printed area of the control structure is around a 1 cm^2 . Our concept is quite similar.

In the framework of this thesis, two types of metamaterials have been designed and studied for the tracking of printing quality : geometrical variation and conductivity.

Implementation of metamaterials as a quality control structure is one of the possible solutions for an in-line and in-situ process monitoring in industrial production environments and a route to closed-loop control the quality.

Keywords: Printed electronics, quality control, terahertz spectroscopy, non-destructive testing

TABLE OF CONTENTS

| | Page |
|---|------|
| CHAPTER 1 INTRODUCTION | 1 |
| 1.1 Printed electronics | 1 |
| 1.2 Motivation of printed electronics | 3 |
| 1.2.1 Material choice | 4 |
| 1.2.1.1 Functional ink | 4 |
| 1.2.1.2 Substrates | 6 |
| 1.2.2 Existing printing methods | 6 |
| 1.2.2.1 Flexography printing | 7 |
| 1.2.2.2 Inkjet printing | 8 |
| 1.2.3 Post-processing: Sintering | 10 |
| 1.2.3.1 Thermal treatment | 11 |
| 1.2.3.2 Photonic sintering | 12 |
| 1.3 Current quality control | 13 |
| 1.3.1 Structural characterization | 17 |
| 1.3.1.1 Morphology | 17 |
| 1.3.1.2 Thickness | 23 |
| 1.3.1.3 Printing defects | 25 |
| 1.3.2 Electrical properties | 29 |
| 1.3.3 Milestones in quality control | 33 |
| 1.4 Terahertz sensing for quality control | 33 |
| 1.5 Thesis organization | 39 |
| CHAPTER 2 TERAHERTZ RADIATION AND APPLICATION | 41 |
| 2.1 Generation of terahertz | 41 |
| 2.1.1 Photoconductive antennas | 41 |
| 2.1.2 Optical rectification | 43 |
| 2.1.3 Pulse-front-tilt | 46 |
| 2.2 Detection of terahertz | 49 |
| 2.2.1 Photoconductive antennas | 50 |
| 2.2.2 Electro-optic detection | 51 |
| 2.3 Terahertz time-domain spectroscopy | 52 |
| 2.3.1 Principle of THz – TDS | 52 |
| 2.3.2 Frequency resolution of THz-TDS | 54 |
| 2.3.3 Normalized transmission | 55 |
| 2.3.4 Dual-wavelength spectroscopy | 55 |
| 2.4 Near-field terahertz imaging | 58 |
| CHAPTER 3 METAMATERIALS | 63 |
| 3.1 Metamaterials for THz applications | 63 |
| 3.1.1 Electromagnetic waves propagation in a medium | 67 |

| | | |
|--|--|-----|
| 3.1.2 | Transmission line approach | 70 |
| 3.1.3 | Effect of geometrical parameters | 73 |
| 3.1.3.1 | Babinet's principle | 78 |
| 3.1.4 | Effect of metal conductivity | 82 |
| 3.1.5 | Vortex phase plate | 86 |
| 3.2 | Toward a method of quality control assisted by metamaterials | 92 |
| CHAPTER 4 CHARACTERIZATION OF THE SPATIAL RESOLUTION | | 97 |
| 4.1 | Sample fabrication | 98 |
| 4.2 | Optical microscopy | 99 |
| 4.2.1 | Matlab algorithm for visual analysis | 101 |
| 4.3 | Terahertz time-domain spectroscopy | 103 |
| 4.3.1 | Normalized transmission | 105 |
| 4.3.2 | Dual-wavelength terahertz spectroscopy | 106 |
| 4.4 | Comparison of results | 109 |
| CHAPTER 5 CHARACTERIZATION OF ELECTRICAL PROPERTIES | | 119 |
| 5.1 | Samples fabrication | 120 |
| 5.2 | Analysis with conventional methods | 121 |
| 5.3 | Terahertz time-domain spectroscopy | 122 |
| 5.3.1 | Normalized transmission | 123 |
| 5.3.2 | Dual-wavelength terahertz spectroscopy | 123 |
| 5.3.3 | Simulations | 124 |
| 5.4 | Comparison of results | 126 |
| 5.5 | Near-Field microscopy | 130 |
| CONCLUSION AND RECOMMENDATIONS | | 137 |
| APPENDIX I FABRICATION OF LARGE APERTURE PHOTOCONDUCTIVE ANTENNAS | | 145 |
| APPENDIX II TWO-PROBE VS. FOUR-POINT PROBE ELECTRICAL MEASUREMENTS | | 147 |
| APPENDIX III GEOMETRIC CORRECTION FACTOR OF CONDUCTIVITY | | 149 |
| APPENDIX IV MATLAB CODE FOR VISUAL ANALYSIS | | 151 |
| BIBLIOGRAPHY | | 161 |

LIST OF TABLES

| | | Page |
|-----------|---|------|
| Table 1.1 | Comparison of traditional vs printable electronics | 5 |
| Table 1.2 | Functional materials for ink formulation..... | 6 |
| Table 1.3 | Comparison of flexography and inkjet printings..... | 7 |
| Table 1.4 | Techniques to characterize different parameters in PE | 32 |
| Table 5.1 | Comparison between terahertz results: THz-TDS & DWTS and conventional techniques: 4PP—four-point probe; MM—multimeter; 2MP—two microprobes; AFM - Atomic Force Microscopy | 129 |
| Table 5.2 | Summary of studied samples | 131 |

LIST OF FIGURES

| | Page |
|-------------|---|
| Figure 1.1 | Printed electronics target applications 2 |
| Figure 1.2 | Comparison between a) conventional lithography and b) printed electronics manufacturing process 4 |
| Figure 1.3 | A schematic diagram of flexography printing 8 |
| Figure 1.4 | Schematic diagram of : a) continuous and b) drop-on-demand inkjet printing methods 9 |
| Figure 1.5 | a) Metallic nanoparticles suspended in a liquid medium and encapsulated in organic additives prevent nanoparticles contact with each other; b) the solvent and organic additives and stabilising agents are evaporated; c) initial contact with neighboring metallic nanoparticles 12 |
| Figure 1.6 | Working principle of rotational viscometer 14 |
| Figure 1.7 | Viscosity curves for conductive inks 15 |
| Figure 1.8 | A liquid drop on a flat surface reaches its characteristic contact angle, θ , due to the three-phase surface tension balance. b) Representation of the various wetting states which can occur when a droplet is deposited onto a dry solid surface..... 16 |
| Figure 1.9 | Working principle of diffractometer for X-ray diffraction measurements. The inset is a diffracted pattern of printed Cu. b) Bragg's law is used to describe the interference pattern 18 |
| Figure 1.10 | a) A sketched principle of Raman scattering. b) A representation of a confocal Raman microscope..... 19 |
| Figure 1.11 | Working principle of a scanning electron microscope 20 |
| Figure 1.12 | A sketch of a working principle of atomic force microscope 21 |
| Figure 1.13 | The principle of the nanoindentation. The applied load P and the penetration depth h_c are measured to calculate the contact area A , the reduced elastic modulus E and the hardness H 22 |
| Figure 1.14 | Online noncontact thickness measurement of printed conductive silver patterns in Roll-to-Roll gravure printing 24 |

| | | |
|-------------|---|----|
| Figure 1.15 | Principle of an ellipsometer. Polarized light strikes the sample and the change in polarization is analyzed. Angle of incidence ϕ can be varied | 26 |
| Figure 1.16 | Optical subtraction of test sample: a) illustration of the reference image, the object image and the defect, b) the difference image showing materials missing from the conducting line, c) the difference image when no defect is present, d) binarised difference image showing the defect, e) binarised difference image when no defect is present | 27 |
| Figure 1.17 | The illustration of the tested layers and a principal setup with three different illumination modes. Photograph of the polymer solar cell modules: Active layer (left); PEDOT: PSS (center) and carbon black (right). The results obtained with different modules are presented below | 28 |
| Figure 1.18 | A typical resistance measurement tools using: a) a multimeter and b) four-point probe | 30 |
| Figure 1.19 | Schematic of experimental setup showing the sensor holder onto an XY stage next to the roller with the attached samples..... | 31 |
| Figure 1.20 | Electromagnetic spectrum | 34 |
| Figure 1.21 | The Gartner Hype Cycle, TRL evolution, and the current envisaged position of THz technologies..... | 37 |
| Figure 1.22 | Comparison of quality control in graphic printing and proposed solution for printed electronics | 38 |
| Figure 2.1 | A sketch of photo-conductive antenna for THz generation: a) the optical pulse ($\hbar\omega$) generates free electrons; b) Electrons are accelerated in the static field (\vec{E}_{DC}) and creates a photocurrent ($\vec{j}(t)$); c) THz pulse ($ \vec{E}_{THz}(t) $) is generated from transient photocurrent element | 42 |
| Figure 2.2 | A principle of THz generation using the optical rectification in a non-centrosymmetric crystal | 44 |
| Figure 2.3 | Two different schemes of THz excitation. For the usual Cherenkov geometry in a), the THz radiation is emitted as a cone characterized by the angle θ_c . Velocity matching is satisfied, but the exciting beam has to be very narrow. Velocity matching by pulse front tilting in b) | |

| | | |
|-------------|--|----|
| | creates a plane THz wave without any upper limit for the exciting beam cross-section..... | 47 |
| Figure 2.4 | A scheme of the tilted pulse front setup | 48 |
| Figure 2.5 | Reconstruction of temporal waveforms of THz pulses from repeated samplings..... | 49 |
| Figure 2.6 | Illustration of THz detection using photoconductive antenna a) an optical and THz pulses arrive to the antenna; b) a transient photocurrent induced between the electrodes, which is proportional to the THz field amplitude..... | 50 |
| Figure 2.7 | a) A sketch of electro-optical detection scheme using a non-centrosymmetric crystal; b) Change of the intensity of the probe light in the absence and presence of THz light before and after the polarization optics | 52 |
| Figure 2.8 | A sketch of a typical THz-TDS setup | 53 |
| Figure 2.9 | The principle of Fast Fourier Transform (FFT) to convert the time-domain signal to the frequency domain..... | 54 |
| Figure 2.10 | The sketch of the transmission measurement using THz-TDS, where $T(\omega)$ and $\Delta\phi(\omega)$ are the spectral information about a sample, i.e., normalized amplitude and phase difference, respectively..... | 56 |
| Figure 2.11 | a) One-shot and real-time spectroscopic system using multi-wavelength THz generation and detection. b) Results of real-time one-shot spectroscopy and reference spectra from the THz database (blue lines under each image). Maltose and Lactose were identified in real-time using five wavelength generation from the is-TPG | 57 |
| Figure 2.12 | THz near-field microscope: a) Pulse-front-tilt excitation of THz waves; b) Electro-optical sampling for the near-field detection of THz waves; the inset sketches the sensor made from a x -cut $LiNbO_3$ crystal deposited on top of the glass; c) Split images for balanced imaging | 60 |
| Figure 3.1 | a) A faced-centered cubic lattice of $NaCl$ with an inset of a unit cell; b) Designed intra-connected negative-index metamaterials made with an inset of a unit cell made from four-gap split-ring resonators, which are attached by diagonal connectors to outer square frames..... | 63 |

| | |
|------------|---|
| Figure 3.2 | a) Schematic of THz metasurface sensing of yeast. b) Normalized transmission amplitudes of the metasurface samples on the silicon wafer and the PI film. Comparisons of normalized transmission amplitudes of the metasurface: c) on the silicon wafer and d) on the PI film 65 |
| Figure 3.3 | The circuit model of a) a section of the transmission line with a series impedance and shunt admittance. b) A section of transmission line with a series inductance and shunt capacitance 70 |
| Figure 3.4 | a) Split-ring resonator (SRR); b) Equivalent circuit of SRR..... 72 |
| Figure 3.5 | a) Frequency selective surface made from metallic wires mesh with a period (lattice constant) d . \vec{k}_0 is the incident wave vector; \vec{k}_x is the transverse component of the incident wave vector and \vec{G} corresponds to the momentum needed to couple to the SPP mode. b) Lumped element model for a unit cell 74 |
| Figure 3.6 | a) Diffraction and typical transmission spectrum ($T(\lambda)$) of visible light through a subwavelength hole with a radii of r in an infinitely thin perfect metal film explained by Bethe theory. b) The triangular hole array was milled in a 225-nm-thick Au film on a glass substrate with an index-matching liquid on the air side (hole diameter 170 nm, period 520 nm). The transmission spectrum is measured at normal incidence using collimated white light. The inset shows the image of the actual array. I/I_0 is the absolute transmission of the array and η is the same transmission but normalized to the area occupied by the holes..... 75 |
| Figure 3.7 | Transmission spectra of THz waves through metal rectangular hole arrays versus frequency. The definitions of holes array are shown in the inset of a). a) The metal hole length and width (a_x and a_y) are both 80 μm , the lattice periods (d_x and d_y) are equaled each other and varied simultaneously. b) The lattice period of 200 μm and the hole length of 100 μm are constant. The metal hole widths are varied 77 |
| Figure 3.8 | Two scattering problems for Babinet's principle for a) SRR and b) its complementary screen illuminated by complementary incident field 78 |
| Figure 3.9 | Far-field transmission spectra were obtained from a 20×20 array of SRRs for two different incident beam polarizations relative to the sample indicated by the insets (top curves) and corresponding |

| | |
|-------------|---|
| | spectra of the complementary sample (bottom curves). Vertical dashed lines indicate characteristic resonances of the structures 81 |
| Figure 3.10 | An illustration of a) self-complementary metallic checkerboard (MCB); b) Inductive MCB (<i>i</i> -MCB) and c) Capacitive MCB (<i>c</i> -MCB) with corresponding lumped elements model 81 |
| Figure 3.11 | Drift of electrons in a conductor with an applied electric field 83 |
| Figure 3.12 | a) THz-TDS results and b) finite-element simulations of the LC-resonant transmission of metamaterials made from 300 nm thick <i>Pb</i> , <i>Al</i> , <i>Ag</i> , super <i>Ag</i> (<i>S.Ag</i>), and perfect electric conductor (<i>PEC</i>). The zoom image illustrates the simulated LC resonance 85 |
| Figure 3.13 | Diagram of different helical structures, phase-front, and intensity of the beams depending on the topological number. $l = 0$ corresponds to the Gaussian beam 87 |
| Figure 3.14 | a) Calculated phase and amplitude of scattered light from a straight rod antenna made from a perfect electric conductor. The vertical dashed line indicates the first-order dipolar resonance of the antenna. b) A V-shape antenna supports symmetric and antisymmetric modes, which are excited, respectively, by components of the incident field along the \hat{s} and \hat{a} axes. c) V-shape antennas corresponding to mirror images of those in b). The components of the scattered electric field perpendicular to the incident field in b) and c) have a π phase difference. d) and e) Analytically calculated amplitude and phase shift of the cross-polarized scattered light for V-shape antennas consisting of gold rods with a circular cross section and with various length h and angle between the rods Δ at $\lambda_0 = 8 \mu\text{m}$. The four circles in d) and e) indicate the values of h and Δ used in experiments 90 |
| Figure 3.15 | a) A complementary V-shaped antenna phase modulation unit. b) Eight kinds of complementary V-shaped antenna structures corresponding to phase shifts from $-3\pi/4$ to π with a $\pi/4$ interval. c) Photography of the central region of the designed VPP for $l = 1$ 91 |
| Figure 3.16 | a) THz transmission amplitudes, for transmission through a plain <i>Si</i> substrate, with (red solid line) and without (black dashed line) deposition of penicillia. (inset) A microscopic image of penicillia deposited on the <i>Si</i> substrate. b) THz transmission amplitudes measured before (black/blue line) and after (red solid line) the deposition. The inset is the microscope images of metamaterials patterns on <i>Si</i> substrate, with the deposition of penicillia 93 |

| | |
|-------------|---|
| Figure 3.17 | a) Measured transmission spectra of the THz metasensor device for different concentrations (4 <i>fmol</i> to 12 <i>fmol</i>) of SARS-CoV-2 spike protein. b) Variations of the toroidal mode frequency shift for different concentrations of injected spike proteins captured by relevant antibody ranging from 2 <i>fmol</i> to 20 <i>fmol</i> . The inset figure is an artistic rendering of the designed multipixel toroidal unit cell, including the dispersed functionalized gold NPs on top 94 |
| Figure 3.18 | a) Schematic diagram of the SRR pattern arrangement on the surface a 1 – μm -thick <i>LN</i> crystal for the experimental study; b) Normalized absolute amplitude of the experimental electric field of the SRR at LC resonance frequencies, i.e., 0.39 <i>THz</i> , 0.44 <i>THz</i> , 49 <i>THz</i> , and 54 <i>THz</i> . c), d) Respectively, experimental and simulated results of the absolute values of the electric field enhancement, E_y , in the gap of SRR 95 |
| Figure 4.1 | The industrial roll-to-roll printer consists of five printing units, where a blue rectangle indicates the location of the printing unit #3 used for the sample's fabrication. The red rectangle highlights the dryer module 99 |
| Figure 4.2 | The produced samples at the printing speed of 50 <i>m/min</i> 99 |
| Figure 4.3 | a) Designed samples, where black pixels correspond to ink and white is the substrate (voids): (i) <i>i</i> -MCB pattern with ink stretching of $\Delta d = +14 \mu\text{m}$; (ii) is the target MCB pattern for perfect transmission property; (iii) pattern with ink compression of $\Delta d = -14 \mu\text{m}$. One-quarter of the visible images of the printed patterns obtained with a speed of: b) 30 <i>m/min</i> and c) 50 <i>m/min</i> 101 |
| Figure 4.4 | a) Image of one of the <i>c</i> -MCB50 samples, which has the geometrical size of 10.24 <i>mm</i> and corresponds to 4096 pixels where 1 pixel corresponds to 2.5 μm . b) A zoomed view from the red square area shown in a). c) and d) correspond to the histograms of the size of the connections in the <i>X</i> - and <i>Y</i> - directions, respectively 102 |
| Figure 4.5 | Terahertz time-domain setup with photoconductive antennas for the generation and detection of THz signal in the transmission configuration. The blue arrow shows the polarization of THz light 103 |
| Figure 4.6 | a) Signals recorded in the time domain of an MCB (sample) and its reference (substrate); b) The THz transmitted amplitude spectra of an MCB and a substrate obtained by the Fast Fourier Transform of the time traces presented in a) 104 |

| | |
|-------------|---|
| Figure 4.7 | a) Principle of electromagnetic field interactions with the samples in X - and Y - directions: (i) i -MCB antisymmetric pattern for X - and Y - directions; (ii) i -MCB and c -MCB behavior for Y - and X - directions, respectively. Normalized transmission of printed i -MCB, MCB, and c -MCB samples with b) 30 m/min and c) 50 m/min105 |
| Figure 4.8 | a) Time-domain signal of humid (blue) and purged (red) air. The electric field is presented in arbitrary units (a.u.) due to the specification of the measurements; b) Frequency domain spectra of a) obtained by FFT. Green and violet areas represent signal and reference ranges for DWTS analysis, where the reference signal was varied through the entire spectrum. c) The standard deviation of DTWS analysis of humid and dry air. The inset shows the calculated integral values extracted from the spectra of b)..... 107 |
| Figure 4.9 | The principle of DWTS for i -MCB and c -MCB : I_1 contains the information about the resonance behavior conditioned by the connections between rhombuses, and I_2 is reference area outside of the water absorption lines.....108 |
| Figure 4.10 | a), b) Extracted values of lattices and laps/gaps from visible images for X - and Y - directions, respectively. The horizontal and vertical lines show the standard deviation obtained from measuring Δd and p of five replicas for each structure. The red downward triangle, circle and upward triangle show the design size of laps or gaps of i -MCB, MCB and c -MCB, respectively. The dashed lines correspond to the designed dimensions of patterns. c), d) Extracted values of lattices and laps/gaps from THz-TDS measurements for X - and Y - directions, respectively. The horizontal and vertical lines show the standard deviation obtained from measuring normalized transmission at 0.22 THz ($T\Delta d$) and the frequency minima (f_p) of five replicas for each structure. The dashed lines correspond to the expected transmission values of designed patterns110 |
| Figure 4.11 | The position of the resonance peak (black outline) and the Q-factor (grey outline) of resonance peak with different size of laps112 |
| Figure 4.12 | The normalized transmission from THz-TDS measurements as a function of the number of gaps measured by optical microscopy113 |
| Figure 4.13 | Comparison between OM and THz-TDS results, where normalized transmission from THz-TDS is plotted as a function of the metal occupancy. The red line shows the fit with the logistic function114 |

| | |
|-------------|--|
| Figure 4.14 | The results obtained with DWTS (integral value) and THz-TDS (normalized transmission)116 |
| Figure 4.15 | Illustration of the concept of spectral resolution for optical microscopy and 1-D THz-TDS117 |
| Figure 5.1 | The design of V-shape antennas. Dimensions of $p = 600 \mu m$, $w = 30 \mu m$, $\beta = 45^\circ$ were kept the same for all antennas. The length of the rod $h = 234, 246, 270, 450 \mu m$ and the angle between rods $\theta = 130^\circ, 120^\circ, 100^\circ, 60^\circ$ according to order of antennas. Taken from He, Wang, Hu, Ye, Feng, Kan & Zhang (2013)120 |
| Figure 5.2 | Sketch depicting the provided measurements: atomic force microscopy (AFM), four-point probe (4PP), multimeter, terahertz time-domain spectroscopy (THz-TDS). The left inset is the visible image of the center part of a printed vortex phase plate (VPP). The dark region is the substrate (PET) and the printed ink is shown with gray pixels. The right inset shows one representative V-shaped antenna unit with the geometrical parameters121 |
| Figure 5.3 | a) Time-domain spectra of a VPP with the highest conductivity and its reference and inset shows the spectra obtained with FFT. b) Normalized transmission spectra of the set of samples123 |
| Figure 5.4 | a) Transmitted amplitude THz spectra of a VPP with the highest conductivity and a substrate (PET), where the transmission dip from ω_1 to ω_2 shows the signal signature and no difference from ω_3 to ω_4 represents a reference signal. b) Standard deviation of DTWS analysis for different bandwidth of integrated areas124 |
| Figure 5.5 | Simulated transmission of a) SRR and b) VPP with different conductivities125 |
| Figure 5.6 | Simulated transmission amplitude at the central frequency of VPP ($0.26 THz$) vs. conductivity. The inset shows the blue dotted region126 |
| Figure 5.7 | Comparison of the conductivity values obtained by two microprobes (2MP) (violet), 4PP (red), normalized transmission from THz-TDS (blue) and DWTS (green) as a function of sintering time127 |
| Figure 5.8 | a) A designed vortex phase plate; b) A studied V-shape antenna131 |
| Figure 5.9 | Near-field THz microscope made from the four main parts: (1) THz wave generating unit; (2) Laser guiding unit; (3) THz wave detecting unit; (4) Scanning unit. The top zoom image is sketch of |

| | | |
|-------------|---|-----|
| | the new sensor made from $10\ \mu\text{m}$ x - and $1\ \text{mm}$ z - cut LN crystal. The bottom zoom image is a photo of the Olympus microscope | 132 |
| Figure 5.10 | a) THz pulses using $10\ \mu\text{m}$ - and $20\ \mu\text{m}$ -thick x -cut LN crystals mounted on $0.5\ \text{mm}$ -glass and $1\ \text{mm}$ z -cut LN crystal. b) Corresponding frequency spectra | 133 |
| Figure 5.11 | a) Visible image of sintered and non-sintered samples; on the right-hand side is the profile of the extraction red dashed line. THz near-field images in the frequency domain at $0.22\ \text{THz}$ of b) the amplitude and c) the phase, respectively, with the corresponding profile. The profile has been extracted for the area of $55\ \mu\text{m}$ | 134 |
| Figure 5.12 | a) The extracted profile of SS (line) and n -SS (dash-line) at $0.1474\ \text{THz}$, $0.1843\ \text{THz}$, $0.2211\ \text{THz}$, $0.2580\ \text{THz}$, and $0.2948\ \text{THz}$. The black lines show the position of the extraction of the normalized amplitude. b) and c) The maximum of normalized amplitude at $\sim 0.2\ \text{mm}$ and $0.67\ \text{mm}$ for the frequency range from $0.1\ \text{THz}$ to $0.9\ \text{THz}$ | 135 |

LIST OF ABBREVIATIONS

| | |
|----------|---|
| AFM | Atomic force microscope |
| CCD | Charge-coupled device |
| CIJ | Continuous inkjet printing |
| CMOS | Complementary metal–oxide–semiconductor |
| CW | Continuous wave |
| COVID-19 | Coronavirus disease 2019 |
| DMD | Digital micromirror device |
| DOD | Drop-on-demand inkjet printing |
| DSC | Differential scanning calorimetry |
| DWTS | Dual-wavelength terahertz spectroscopy |
| ECIS | Electro-chemical impedance spectroscopy |
| ETS | École de Technologie Supérieure |
| EM | Electro-magnetic |
| EO | Electro-optic |
| EOT | Extraordinary transmission |
| FFT | Fast-Fourier transform |
| 4PP | Four-point probe |
| FSS | Frequency selective surface |
| GATF | Graphic Arts Technical Foundation |

| | |
|-------|---------------------------------------|
| LG | Laguerre-Gaussian |
| LAPCA | Large aperture antennas |
| LED | Light-emitting diode |
| LT | Low-temperature |
| MIT | Massachusetts Institute of Technology |
| MO | Metal occupancy |
| MCB | Metallic checkerboard |
| MMs | Metamaterials |
| NIR | Near-infrared |
| NDT | Non-destructive testing |
| NP | Nanoparticle |
| OM | Optical microscopy |
| OR | Optical rectification |
| PCA | Photo-conductive antenna |
| PET | Polyethylene terephthalate |
| PEN | Polyethylene naphthalene |
| PI | Polyimide |
| PE | Printed electronics |
| QCB | Quality control bar |
| R&D | Research and Development |

| | |
|------------|---|
| R2R | Roll-to-roll |
| SARS-CoV-2 | Severe acute respiratory syndrome coronavirus 2 |
| SEM | Scanning electron microscope |
| SI | Semi-insulating |
| SRR | Split-ring resonator |
| SPP | Surface plasmon polariton |
| TRL | Technology readiness level |
| THz | Terahertz |
| THz-TDS | Terahertz time-domain spectroscopy |
| TGA | Thermogravimetric analysis |
| 2D | Two-dimensional |
| 2MP | Two microprobes |
| UPS | Ultraviolet photoemission spectroscopy |
| UV | Ultraviolet |
| VPP | Vortex phase plate |
| XRD | X-ray diffraction |

LIST OF SYMBOLS AND UNITS OF MEASUREMENTS

| | |
|-----------------|---|
| A | area |
| $a.u.$ | arbitrary units |
| a | lattice parameter |
| \vec{B}, B | magnetic field vector, magnetic field (T) |
| bcm | billion cubic microns per square inch |
| C | capacitance |
| c | speed of light ($3 \times 10^8 m/s$) |
| $c (subscript)$ | complementary, e.g. B_c = complementary magnetic field |
| \vec{D}, D | electric field displacement (C/m^2) |
| d | distance (m), second order nonlinear coefficient (pm/V) |
| \vec{E}, E | electric field vector, electric field (V/m) |
| e | electron charge ($1.6 \times 10^{-19} C$) |
| F | geometrical correlation factor |
| f | frequency (Hz) |
| \vec{G} | wave-vector of a lattice |
| g | distance (μm) |
| \vec{H}, H | magnetic field intensity, magnetizing field (A/m) |
| h | length (μm) |
| \hbar | Planck's constant divided by 2π ($\hbar = 1.0546 \times 10^{-34} Js$) |

| | |
|--------------------------|---|
| I | electric current (A), light intensity (W/m^2) |
| J | current density (A/m^2) |
| k | wave-vector (m^{-1}) |
| L | total orbital angular momentum, inductance |
| l | length (m), topological charge |
| m^* | effective mass (kg) |
| N | number of electrons, number of recorded points, number of turns |
| n | refractive index |
| P | polarization |
| p | periodicity (m), radial index |
| R | resistance (Ω) |
| r_{ij} | electro-optical tensor |
| r | reflection coefficient |
| s (<i>subscript</i>) | scatter, e.g. $\vec{E}^{(s)}$ scattered electric field |
| T | transmission |
| t | thickness (m), time (s), transmission coefficient |
| t (<i>subscript</i>) | transmission, e.g. $\vec{E}^{(t)}$ transmission field |
| V | voltage |
| v | velocity (m/s) |
| v_d | drift velocity [ms^{-1}] |

| | |
|--------------|--|
| w | width size (m), beam radius (m) |
| x | displacement |
| Z | impedance |
| z_R | Rayleigh range |
| α | absorption coefficient (m^{-1}) |
| β | angle |
| Δ | change, phase shift |
| ϵ | $\epsilon_0\epsilon_r$ permittivity of a medium (C/Vm) |
| ϵ_0 | permittivity of free-space ($8.85 \times 10^{-12} C/Vm$) |
| ϵ_r | relative permittivity or dielectric constant |
| η | impedance of free-space |
| λ | wavelength (m) |
| θ | angle |
| μ | $\mu_0\mu_r$ magnetic permeability (H/m) |
| μ_0 | permeability of free-space ($4\pi \times 10^{-7} H/m$) |
| μ_r | relative permeability |
| ρ | complex reflectance ratio, resistivity (Ωm) |
| r | reflectance |
| $\tan \Psi$ | amplitude ratio |
| Δ | phase shift |

| | |
|------------------|--|
| γ | surface tension (N/m), probability of collision (s^{-1}) |
| Ω/\square | sheet resistance (<i>Ohm per square</i>) |
| σ | electrical conductivity (S/m) |
| τ | time constant (s), mean electron scattering time [s] |
| Φ_G | Gouy phase |
| ϕ | angle |
| ρ | reflectance |
| χ | susceptibility |
| ω | angular frequency ($2\pi f$) |

CHAPTER 1

INTRODUCTION

Printed electronics (PE) combines the industries of printing and microelectronics. This fast-growing manufacturing technology enables the printing of a wide range of low-cost customized electronic devices. Having endless potential, PE still lacks an efficient way to control the quality. The main objective of this thesis is to develop the framework for a new contactless, non-destructive, and in-situ method to control the quality of PE devices.

This chapter provides a brief overview of PE with existing quality control techniques and includes the scope of this thesis.

1.1 Printed electronics

Printed electronics (PE) was originated from organic electronics, which story had started back in 1977 by Shirakawa, Louis, MacDiarmid, Chiang & Heeger (1977). They discovered that polymer could be conductive by doping certain molecules and it made them earned the Nobel Prize in Chemistry in 2000. Following this discovery, organic semiconductor (Ebisawa, Kurokawa & Nara (1983)) and organic photovoltaic materials (Tang (1986)) were developed in 1980s and organic electronics as a field of scientific interest had started. It foresaw an idea of printing electronic devices from organic polymers that could be naturally made into ink forms. In 1991, the first organic field-effect transistor was made on plastic substrate by Francis Garnier group, where electrodes were printed, and the organic semiconductors were deposited by vacuum evaporation (Garnier, Peng, Horowitz & Fichou (1991)). This work proved that transistors could be made on plastic substrates and opened the era of plastic electronics. In 1997, the fully printed transistors were made by a screen-printing technique onto polyester film by Dr. Zhenan Bao (Bao, Feng, Dodabalapur, Raju & Lovinger (1997)). The recent boom in the electronics was in 2011 when researchers from MIT created a flexible solar cell by inkjet printing on paper (Barr, Rowehl, Lunt, Xu, Wang, Boyce, Im, Bulović & Gleason (2011)). Further, the development of organic printed materials allows for printing organic solar cells with

a maximum of fifteen percent efficiency (Tsai, Asadpour, Blancon, Stoumpos, Durand, Strzalka, Chen, Verduzco, Ajayan, Tretiak et al. (2018)). The development of printing technology has been highly motivated by the rapidly growing PE market and its numerous applications. The total revenue of PE was 12B total in 2011 and expected to be 330B in 2027 (Keskinen (2012)).

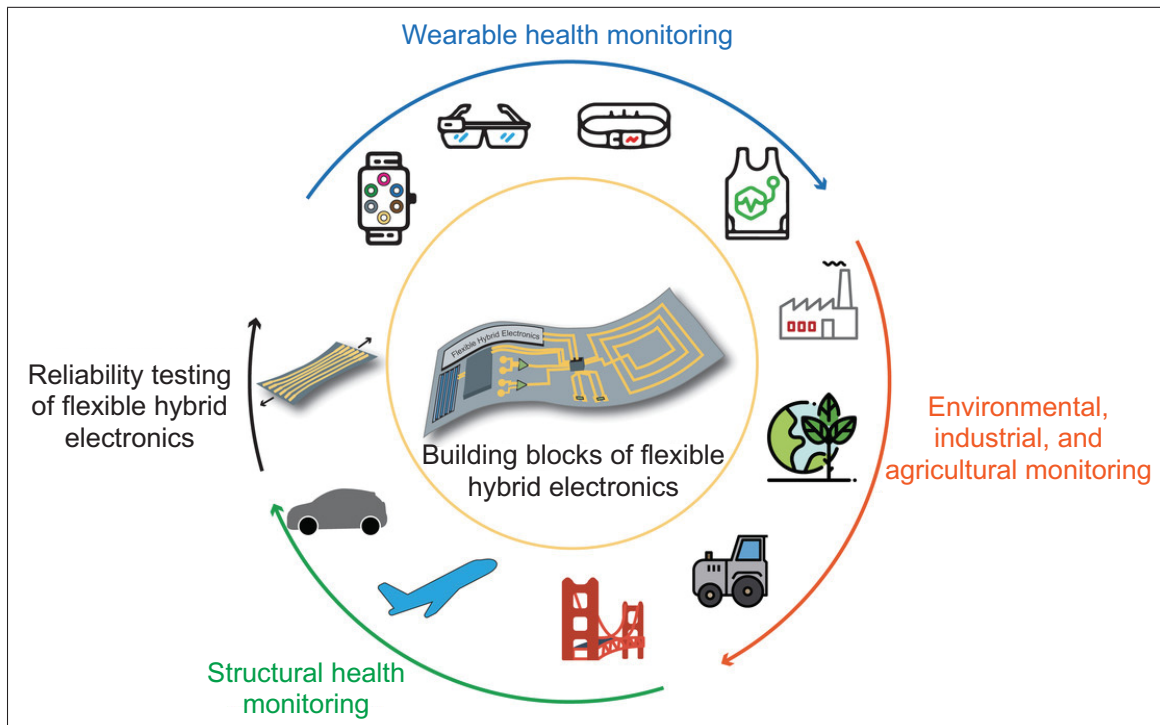


Figure 1.1 Printed electronics target applications
Taken from Khan *et al.* (2020)

With the development of PE, the form of electronics has changed from traditional rigid and rectangular shapes to more complex ones - soft and flexible. The brand new electronics have never existed before and realized bendable, rollable, wearable, or elastically stretchable devices (Khan, Lorenzelli & Dahiya (2014); Khan *et al.* (2020)). Non-traditional electronics became possible thanks to PE, which utilizes established industrial printing methods, but instead of printing text on a paper, one can print conductive, semiconductive or dielectric inks on any suitable substrates to create electrical structures (Fajardo, Garduño & Estrada (2020); Khan *et al.* (2014)). PE presents an exceptional combination of a large and continuous processing area to fabricate a variety of the low-cost customized electronics devices on flexible substrates using high-throughput

printing approaches. Printing is an eco-friendly process, which has received immense attention due to the additive nature of the manufacturing allowing for the reduction in materials loss (Abu-Khalaf, Saraireh, Eisa, Al-Halhouli et al. (2018); Altay, Bolduc & Cloutier (2020); Mitra, Mitra, Dzhagan, Pillai, Zahn & Baumann (2018a)). PE promises large markets to a large range of industries, from consumer goods, electronics, aerospace, automotive, pharmaceutical, biomedical, to textiles and fashion (Jenkins, Wang, Xie, Wu, Huang, Wang & Yang (2015); Liu, Pharr & Salvatore (2017); Singh, Haverinen, Dhagat & Jabbour (2010a); Wang & Liu (2016)). This technology provides an endless potential for fabrication for smart clothing, packaging, sensors and other devices which can be incorporated into the design of products and objects surrounding us, paving the way for the “Internet of Things” (Khan *et al.* (2020)). Figure 1.1 combines all of the target applications of flexible printed electronics.

1.2 Motivation of printed electronics

Photolithography is a conventional and the most widely used method for micro-structuring (Madou (2018)). Traditional electronic manufacturing requires multiple production steps, as shown in Figure 1.2a. For each layer of a device, it starts from a blanket material deposition onto a rigid substrate with following photolithography and etching to subtract non-needed materials (Khan *et al.* (2020)). Despite the high resolution of photolithography, which can be as large as the *nm* scale, many electronics applications do not require such high precision and dimension (Fukuda & Someya (2017)). Hence, the global market requires innovative fabrication techniques that are both faster and cheaper compared to traditional production methods. PE offers a very attractive alternative to photolithography for the production of electronic devices.

Compared to conventional lithography, PE manufacturing technique is capable of patterning electronic circuits with a typical resolution of tens of micrometers at a speed of several meters per minute (Fukuda & Someya (2017)). PE is an additive manufacturing process, as shown in Figure 1.2b. The production consists of the same three process steps as any other graphic arts industry: choosing the materials, press (printing), and post-press (sintering or drying) (Khan *et al.* (2014); Perelaer, Smith, Mager, Soltman, Volkman, Subramanian, Korvink & Schubert

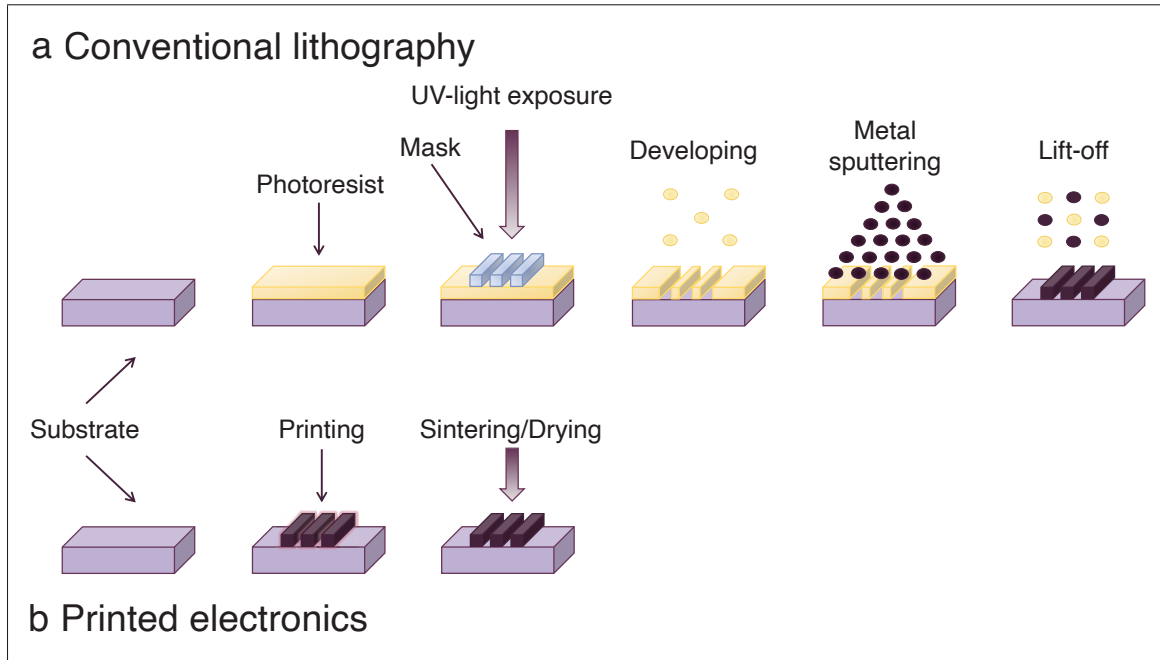


Figure 1.2 Comparison between a) conventional lithography and b) printed electronics manufacturing process

(2010)). PE shows tremendous advantages in terms of cost and throughput compared with lithographic fabrication processes for conventional inorganic semiconductor devices. However, PE components do not have the same high performance and reliability and will not be able to fully substitute the traditional silicon-based electronics in the near future. The comparison between conventional fabrication and printed electronics are summarized in Table 1.1 (Khan *et al.* (2020)).

1.2.1 Material choice

1.2.1.1 Functional ink

Particular PE components require specific functionalities of the ink. Nowadays, various kinds of conductive, semi-conductive, and dielectric inks are commercially available (Kamyshny & Magdassi (2014); Ko, Pan, Grigoropoulos, Luscombe, Fréchet & Poulidakos (2007); Matsuhisa, Kaltenbrunner, Yokota, Jinno, Kuribara, Sekitani & Someya (2015)). A typical ink is formulated

Table 1.1 Comparison of traditional vs printable electronics

| Traditional electronics | Printable electronics |
|--------------------------------------|-------------------------------------|
| High production cost | Low production cost |
| Subtractive manufacturing process | Additive process |
| Clean room conditions | Ambient conditions |
| Sophisticated fabrication (6+ steps) | Simple fabrication (3 steps) |
| Rigid substrates | Any kind of substrates |
| Small area | Large area |
| High integration density | Low integration density |
| Short switching times | Long switching times |
| High resolution | Low resolution |
| Constant repeatability | Low repeatability |
| Long product lifetime (~10 years) | Short product lifetime (~ 0.1 year) |
| Established fabrication method | Early-stage technology |

from functional material, vehicles, resins, and additives. Resins have the most considerable influence on ink properties and determine the binding formulation ingredients to each other and the adhesion with the substrate. The liquid portion of the formulation is a vehicle responsible for the transfer of the ink into the substrate and defining the drying speed. Additives enhance the properties of functional materials or provide additional properties. Different proportions of ink's constituents determine ink characteristics: rheology, viscosity, surface tension, oxidation, etc (Altay *et al.* (2020)). The development of ink is in high demand, especially with the transformation of the existing electronics toward eco-friendly, bio-sourced, and biodegradable PE to alleviate the environmental footprint of the electronics (Mirka, Fong, Rice, Melville, Adronov & Lessard (2019); Selivanova, Coady, Pignanelli, Ocheje, Schlingman, Malik, Prado & Rondeau-Gagné (2020); Tousignant, Rice, Peltekoff, Sundaresan, Miao, Hamad & Lessard (2020)). The most common example of functional materials is listed in Table 1.2.

Most electronic components start from the conductive layers or are fully made from conductors, further completed with additional layers of semiconductors or dielectric depending on the devices. Hence, in the current thesis framework, we only focused on metallic nanoparticles (NPs) conductive ink, which consists of suspensions of metallic nanoparticles in liquid. Every nanoparticle is encapsulated in a layer of insulating organic additives and stabilizing agents

Table 1.2 Functional materials for ink formulation

| Functionality | Materials |
|----------------|---|
| Conductors | Copper, silver, gold, aluminum, carbon, PEDOT:PSS, graphite, graphene (Khan <i>et al.</i> (2014)) |
| Semiconductors | Zinc oxide, zinc selenide Altay <i>et al.</i> (2020), π -conjugated polymers (Selivanova <i>et al.</i> (2020)), single-walled carbon nanotubes (Mirka <i>et al.</i> (2019)) |
| Dielectric | Cellulose nanocrystals, Poly (methyl methacrylate), poly(4-vinylphenol), and polystyrene (Tousignant <i>et al.</i> (2020)) |

to prevent the agglomeration of NPs as well as the current flow between particles. Organic additives and solvents are evaporated during a post-printing step (Tan, An, Chua & Tran (2019)).

1.2.1.2 Substrates

Some PE printing processes are able to fabricate using traditional rigid substrates such as silicon or glass (Fukuda & Someya (2017); Keskinen (2012)). However, one of the main goals of PE is towards flexible electronics. Compared to conventional methods, the low processing temperature of PE makes it compatible with most low-cost plastic films, which are usually not porous and can resist all fabrication steps, including pre- and post-printing processes (Trudeau, Bolduc, Beaupré, Topart, Alain & Cloutier (2017)). Mostly used substrates are foils made of polyimide (PI), polyethylene terephthalate (PET) or polyethylene naphthalene (PEN) (Keskinen (2012)).

1.2.2 Existing printing methods

The printing step includes the deposition of materials on the substrate with the required resolution, print definition, and dimension. PE industry has been established for over a decade and continues to advance with a wide range of printing techniques such as screen – printing, gravure (Ko *et al.* (2007)), and inkjet printing, etc (Hudd (2011); Khan *et al.* (2014); Nguyen, Lee, Kim, Shin & Lee (2013); Pan, Wang, Huang, Ling, Dai & Ke (2015)). These technologies, which are well-known for their roll-to-roll (R2R) print processing capabilities, offer different printing characteristics, e.g., high resolution, thicker layers, smoother layers, high edge sharpness, high scalability and

precision in print production, and even digital fabrication of the printed electronics products (Khan *et al.* (2014); Mitra, Kapadia, Hartwig, Sowade, Xu, Baumann & Zichner (2018b)).

Two of the most common printing techniques were used to fabricate the samples analyzed in this thesis and are reviewed in this section. The basic comparison of these two printing technologies is combined in Table 1.3.

Table 1.3 Comparison of flexography and inkjet printings

| Type of printing | Flexography | Inkjet |
|---------------------------------|-------------|---------------|
| Printing Form | Relief | Digital |
| Image Transfer | Direct | Non-contact |
| Resolution (<i>lines/cm</i>) | 60 | 60 to 250 |
| Line width (μm) | 20 to 50 | 1 to 20 |
| Ink viscosity ($Pa \cdot s$) | 0.05 to 0.5 | 0.001 to 0.03 |
| Film thickness (μm) | 1 to 2.5 | 0.5 to 15 |
| Printing speed (<i>m/min</i>) | 10 to 500 | 15 to 500 |

1.2.2.1 Flexography printing

Flexographic printing is a high speed, continuous R2R process, which is a well-known manufacturing technique commonly used by the packaging industry (Rossander, Zawacka, Dam, Krebs & Andreasen (2014a)). The minimum feature size is around $50 \mu m$, and its exceptionally high throughput of up to $35 m^2/s$ decreases the production cost drastically (Khan *et al.* (2014); Orrill & LeBlanc (2017); Rossander *et al.* (2014a)). Figure 1.3 shows the basic principle of flexography printing. At first, the ink is put in contact with a micro-engraved cylinder (anilox) and filling its cells, which is then scraped with a doctor blade to ensure that the cells are filled with a constant, controlled volume of ink (Kipphan (2001)). Aniloxes are defined by their theoretical volume.

In North America, this volume is expressed as $10^9 \mu m^3$ of ink contained in $1 in^2$ of cells or billion cubic microns per square inch, typically written as bcm/in^2 , $bcm/sq \cdot in$, or bcm . Secondly, the ink is transferred onto a cylindrical printing plate made of rubber or a photopolymer. The printing form defines the pattern information engraved as a positive relief in the printing plate

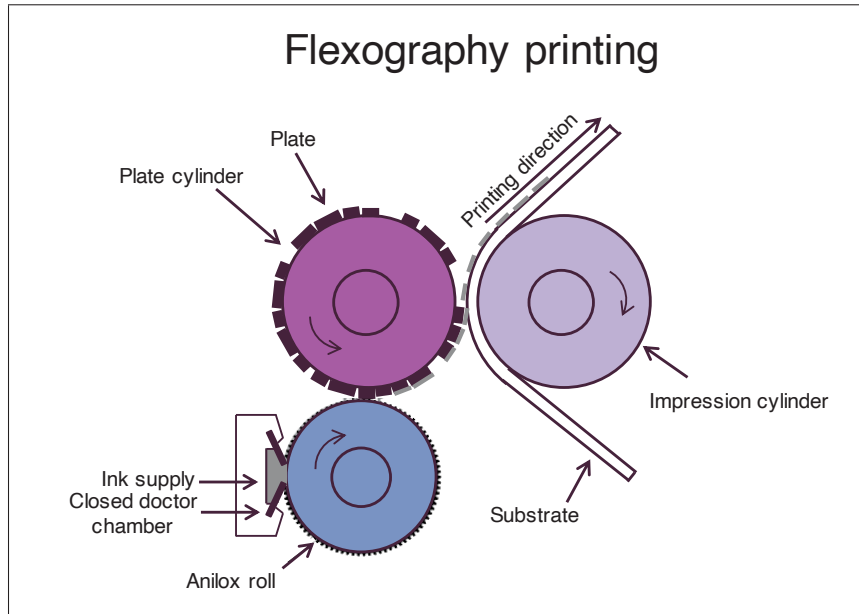


Figure 1.3 A schematic diagram of flexography printing

soft structure. Afterward, the inked pattern is pressed against the substrate in the nip zone between the printing form and an impression cylinder. The ink transfer onto the substrate is performed with the lowest possible pressure. This particularity has given the nickname "kiss printing" to the flexography. Due to the low pressure applied in the nip, the flexography is able to transfer ink onto a wide range of substrates, varying from fragile substrates such as corrugated board that could be flattened during printing, and self-adhesive labels that contain a layer made of adhesive, to smooth substrates such as plastics, foils or glass. The thickness of the printed film is defined by the anilox parameters and by the transfer rates from the printing plate cylinder to the printing substrate.

1.2.2.2 Inkjet printing

The benefits of inkjet printing include a low production cost, contactless deposition, compact equipment, and high resolution for printing fine features onto various substrates (Abu-Khalaf *et al.* (2018); Diaz, Ramon & Carrabina (2013); Kamyshny, Steinke & Magdassi (2011)). The low production cost of the inkjet printing is explained by the small use of the functional

materials and the relatively low price of the fabrication equipment ($\sim \$100,000$ for inkjet printing vs. $\sim \$1,000,000$ for flexography printing). The printer is controlled directly by an image processor in the digital format and can easily change and adjust the printing pattern. It opens the possibility for a new way to produce printed media, e.g. print-on-demand, personalized devices, and home printing (Khan *et al.* (2014)). The drastic disadvantage of the inkjet printing is the clogging of the printhead of the cartridge, which requires multistep development of printing protocol for different types of materials bringing to the enormous waste of materials (Kipphan (2001)).

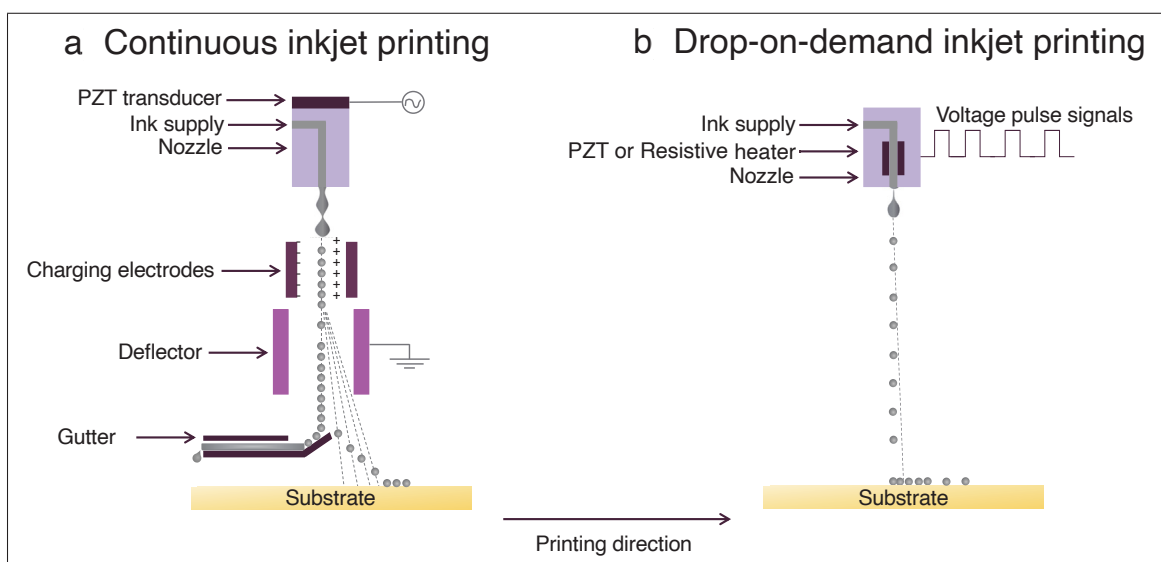


Figure 1.4 Schematic diagram of : a) continuous and b) drop-on-demand inkjet printing methods

All inkjet printing techniques are based on the digitally controlled ejection of drops of fluid from a print head. Figure 1.4 shows a schematic diagram of the two typical inkjet printing techniques: continuous (CIJ) and drop-on-demand (DOD) (Hudd (2011); Pan *et al.* (2015)).

CIJ printers are a non-contact form of high-speed printing that operates by channeling a continuous stream of ink through a nozzle. It uses plate electrodes to selectively charge individual droplets in a falling jet. The charged droplets are then directed to the proper location on the substrate by an electric field, while uncharged droplets are collected and returned for reuse.

Disadvantages include relatively large droplet size (usually), resulting in low print resolution. Additionally, there are limitations associated with the requirement that the printed fluid has to be electrically chargeable (Hudd (2011); Singh, Haverinen, Dhagat & Jabbour (2010b)). However, the majority of inkjet printers are based on DOD technology. It works either with thermal DOD and piezoelectric DOD. In contrast to continuous inkjet printing, the droplets are injected by a pressure pulse when required.

Thermal DOD inkjet is the technology most used in desktop printers. In this technology, the print cartridges consist of series of tiny chambers, each containing a heater. A pulse of current is passed through the heating element, causing the rapid formation of gas bubbles, which forces ink to leave the nozzle due to the increase in pressure. The ejected drop leaves a void in the chamber that is subsequently filled by a replacement fluid in preparation for creating the next drop (Hudd (2011)). Meanwhile, most commercial and industrial inkjet printers utilize mechanical deformation of piezoelectric material for the ejection of ink droplets. The voltage signal is applied to a piezoelectric transducer to control the ink droplet's volume, velocity, and frequency of ink. Drop formation in piezoelectric DOD printing systems highly depends on ink properties and input electric voltage waveforms for a given piezoelectric material and nozzle characteristics (Altay *et al.* (2020); Fajardo *et al.* (2020); Khan *et al.* (2020); Mitra *et al.* (2018a)). The main advantage of the technology is the compatibility of the DOD inkjet printing process with the R2R manufacturing process.

1.2.3 Post-processing: Sintering

Post-press processes also play a crucial role in the manufacturing of PE devices (Mitra *et al.* (2018a); Perelaer, Jani, Grouchko, Kamyshny, Magdassi & Schubert (2012)). The most commonly used sintering approaches are conventional thermal annealing (Halonen, Viiru, Ostman, Cabezas & Mantysalo (2012); Kamyshny & Magdassi (2014); Kamyshny *et al.* (2011)), microwave sintering (Eun, Chon, Yoo, Song & Choa (2015); Sowade, Polomoshnov & Baumann (2016)), and photonic sintering by either continuous-wave laser irradiation (Ko *et al.* (2007); Perelaer & Schubert (2013)) or high-power flashing lamps (Bolduc, Trudeau, Beaupré,

Cloutier & Galarneau (2018); Ermak, Zenou, Toker, Ankri, Shacham-Diamand & Kotler (2016)). Solid and uniform dielectric or metallic tracks from the printed pattern are obtained during this step. The electrical properties of printed patterns depend entirely on the sintering process. Thermal (Halonen *et al.* (2012); Kamyshny & Magdassi (2014); Kamyshny *et al.* (2011)) and photonics (Bolduc *et al.* (2018); Ermak *et al.* (2016); Ko *et al.* (2007); Perelaer & Schubert (2013)) sintering have been used for the fabrication of conductive samples for the sake of this thesis.

1.2.3.1 Thermal treatment

The standard method to convert printed non - conductive inks to conductive counterparts involves heating, either by drying in a chamber, a hot plate, or in a convection oven (Halonen *et al.* (2012); Kamyshny *et al.* (2011)). During the printing process, the substrate is slightly heated at a low temperature to initiate the adhesion of ink with the substrate. After printing, the conductivity of the pattern feature is very low since metallic nanoparticles are separated by a solvent and encapsulated in organic additives and stabilizing agents, as shown in Figure 1.5a. At the first step of sintering, the liquid is evaporated, and its volume equals the decrease in volume of the particle network (Khan *et al.* (2014); Perelaer *et al.* (2010)). Once all organic components are melted, nanoparticles are arranged tidily in a single layer film (Figure 1.5b). Necks begin to grow between contacting nanoparticles leading to the growth of grains (Keikhaie, Akbari, Movahhedi & Alemohammad (2014)). The film thickness decreases, and the density increases due to the particle being compacted. In the last step, the pores around the grains begin to collapse, and the film densification maximizes (Figure 1.5c). The increase of the sintering temperature leads to the growth of the grains, the boundaries recede, and the pores are completely collapsed. Since the sintered ink structures contain some defects (for example, an incomplete contact between particles and residual porosity), the resulting conductivity is lower than that of bulk material. A disadvantage of this technique is that it trades off the ink stability, which results in challenged printing repeatability and long-time storage (Kamyshny *et al.* (2011)).

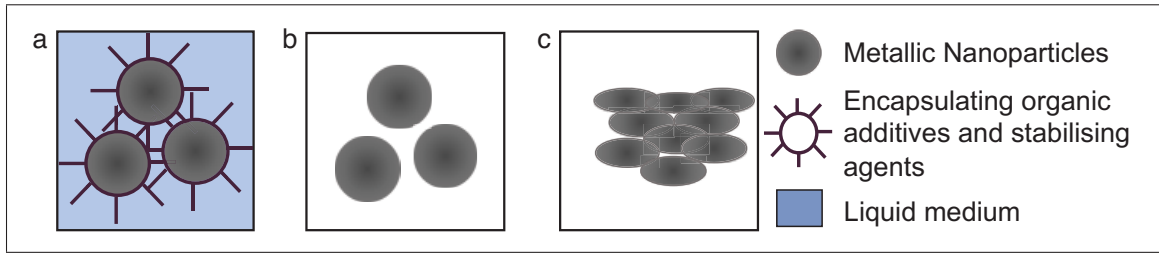


Figure 1.5 a) Metallic nanoparticles suspended in a liquid medium and encapsulated in organic additives prevent nanoparticles contact with each other;
 b) the solvent and organic additives and stabilising agents are evaporated;
 c) initial contact with neighboring metallic nanoparticles

1.2.3.2 Photonic sintering

Traditional thermal baking is the most used method for sintering or drying printed traces. However, to achieve a proper functionality of printed devices, it requires a long time of sintering, as well as this type of sintering is not compatible with the thermal stability of commonly used inexpensive polymer foils (e.g. PET or PEN) (Abbel, van Lammeren, Hendriks, Ploegmakers, Rubingh, Meinders & Groen (2012); Rahman, Shahzadeh, Rahman, Pisana & Grau (2020)).

Photonics sintering has advantages compared with traditional thermal baking. Photonic sintering uses intense pulsed light to sinter metal NP inks in a selective manner, reducing the heat-affected zone, and is especially relevant for plastic electronics application. The dark-colored printed NPs inks have higher absorbance of the radiant energy of the lamp than the polymer substrate, which results in a faster increase of the temperature in ink and causes rapid sintering of the metal nanoparticles without affecting the substrate (Bolduc *et al.* (2018); Jang, Joo, Chu, Uhm, Park, Ryu, Yu & Kim (2020)). These advantages increase manufacturing throughput, reducing the post-fabricating process to a few seconds. The photonic sintering mechanism of metal NPs is similar to that of thermal sintering. However, in this case, light absorbed by the printed metallic layer results in its heating followed by evaporation of liquid and sintering.

1.3 Current quality control

As shown in Figure 1.2b, the printing process can be split into three steps. Hence, each step requires proper quality control. The quality control during the production should be preferable with an inline response. Firstly, to initiate the printing process, the properties of printing materials must be determined, i.e., substrate's surface and the ink formulation. The preparation of the substrate's surface is critical since it influences the ink's behavior upon printing. Usually, PE requires a very clean initial surface and sometimes even added functional monolayers to improve electron mobility or surface adhesion (Fukuda & Someya (2017)). The presence or quality of these layers is usually controlled via optical methods, such as high-speed imaging (Hoath (2016)). Furthermore, the ink quality is inspected to ensure minimum spread and a higher print resolution. Each printing technique requires different ink viscosities, which quantify how the ink will flow (Altay *et al.* (2020)). For example, inkjet printing requires low viscosity ink to obtain high jetting velocity, while screen printing uses high-viscosity ink to produce thick conductive lines (Fukuda & Someya (2017)). To determine the viscosity of ink, a rotational rheometer is used. It allows for a complete analysis of the rheological behavior of the inks and an assessment of their suitability to a certain printing method. The working principle of the rheometer is shown in Figure 1.6. A motor drives a measuring bob inside of a measuring cylinder with the tested ink. The bob's rotation speed is pre-set and produces the motor torque, which has to overcome the viscous forces of the tested substance. The rotation speed and torque can be transformed into the rheological properties shear rate and shear stress (Urbas, Manojlović, Šumiga & Elesini (2017)). The dynamic viscosity of samples is defined by Newton's law, where the shear stress is divided by the shear rate. Figure 1.7 shows an example of a measured viscosity for two types of conductive inks. The nanoparticle silver ink has a lower viscosity, which is explained by smaller particle size and particle shape, than flake ink (Hrehorova, Rebros, Pekarovicova, Bazuin, Ranganathan, Garner, Merz, Tosch & Boudreau (2011)). The results show the possibility of using these inks for gravure or flexographic printing (Khan *et al.* (2014); Tone & Ganz (2016)). The thermal decomposition of the ink during the fabrication process is usually predicted by differential scanning calorimetry (DSC) and thermogravimetric analysis

(TGA). These techniques give information about the amount of energy absorbed or realized by the sample when heated or cooled, providing qualitative and quantitative information data on endothermic and exothermic processes (Halonen *et al.* (2012); Perelaer *et al.* (2012)). By predefining the ink's parameters, one may improve the print speed, quality, and resolution of printing patterns.

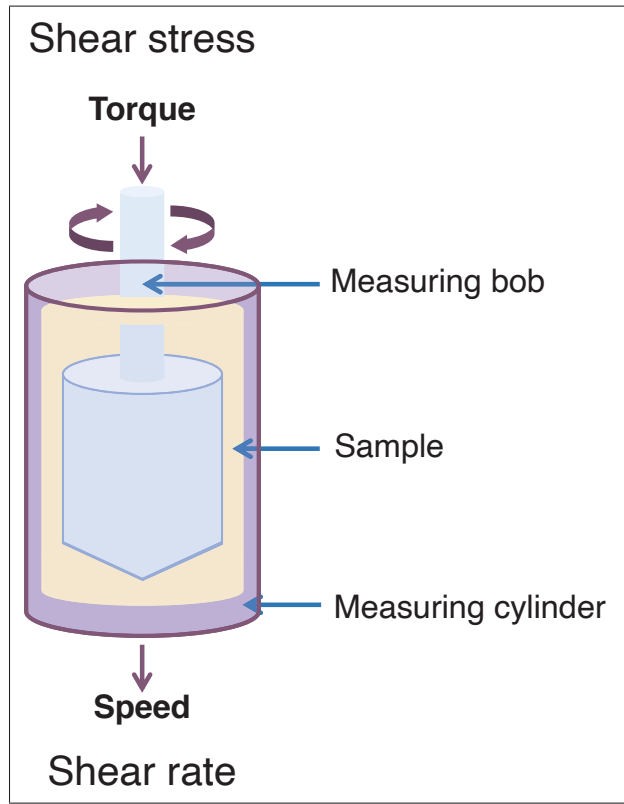


Figure 1.6 Working principle of rotational viscometer

Once a drop of an ink reaches a substrate's surface, the ink's spreading behavior is defined by the surface tension. It is the force acting tangentially to the interface. Figure 1.8a shows a drop with these three forces: substrate/air ($\gamma_{S/A}$), ink/air ($\gamma_{I/A}$), and substrate/ink ($\gamma_{S/I}$). The contact angle, θ , can be derived from the Young-Dupré equation (Beedasy & Smith (2020)):

$$\cos \theta = \frac{\gamma_{S/I} - \gamma_{S/A}}{\gamma_{I/A}} \quad (1.1)$$

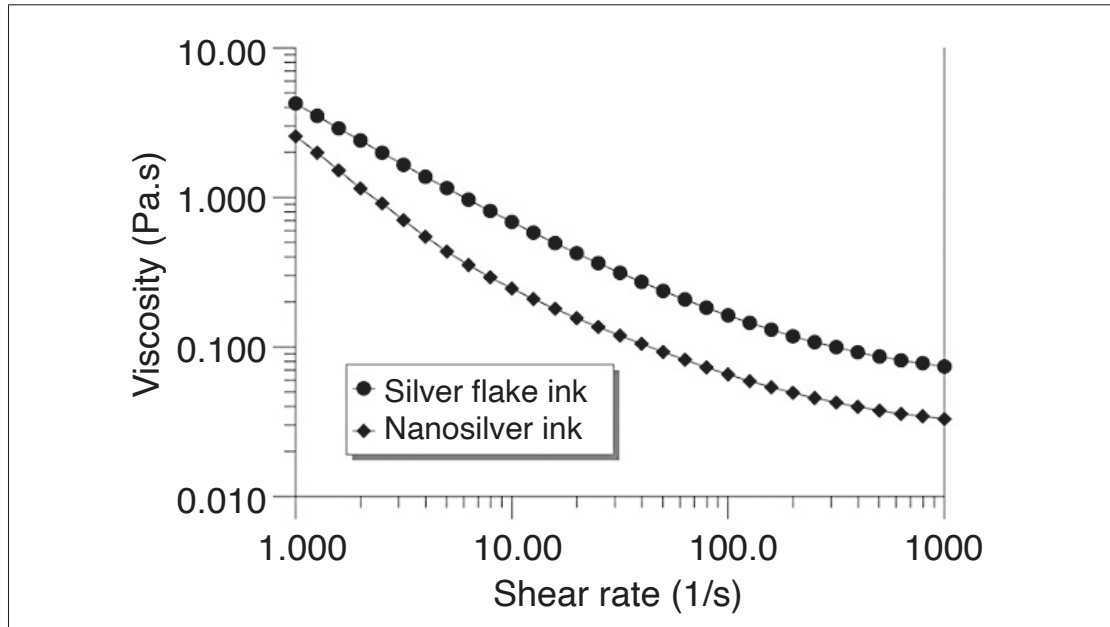


Figure 1.7 Viscosity curves for conductive inks
Taken from Hrehorova *et al.* (2011)

Figure 1.8b shows the various scenario of a drop behavior depending on the contact angle. According to the equation 1.1, if $\gamma_{S/A} < \gamma_{S/I} + \gamma_{I/A}$, a droplet will spread onto the surface towards to partial wetting. Conversely, if $\gamma_{S/A} > \gamma_{S/I} + \gamma_{I/A}$, a droplet will experience the non-wetting behavior, forming a spherical sphere resting on the surface. Basically, the minimization of overall surface energy causes the uniform distribution of the ink, leading to the contact angle of zero, where $\gamma_{S/A} = \gamma_{S/I} + \gamma_{I/A}$. The complete equilibrium (complete wetting state) is shown in the left-bottom side of 1.8b.

The contact angle is usually measured with shadowgraphy technique (Castrejón-García, Castrejón-Pita, Martin & Hutchings (2011)), where the object or media refract the light from the illumination source under study, and the obtained background arrives at the recording sensor. This method is often sufficient to ensure deposition control at consistent drop speeds, conditions, and control materials (Hoath (2016)).

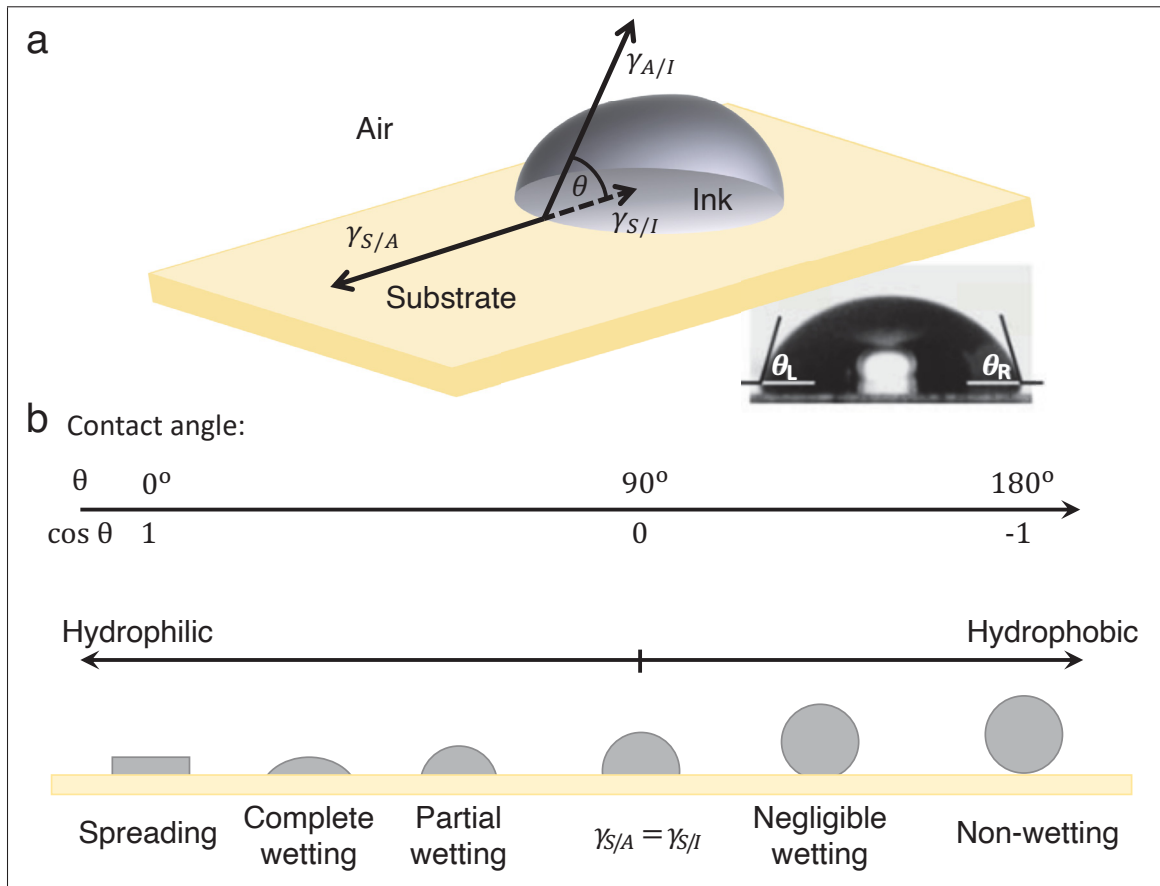


Figure 1.8 a) A liquid drop on a flat surface reaches its characteristic contact angle, θ , due to the three-phase surface tension balance.

b) Representation of the various wetting states which can occur when a droplet is deposited onto a dry solid surface

Adapted from Beedasy & Smith (2020); Hoath (2016)

The surface chemistry, thermal conductivity, as well as environmental conditions may cause changes in the ink behavior (Hoath (2016)). Understanding defect causes and analyzing properties of a substrate and an ink are essential for further optimization of the printing step.

The last step is the characterization of a functionalized printed surface. Current inspection methods for the quality of printed ink include well-known techniques, which are only established in a laboratory environment. They mainly control defects (Feng, Su, Happonen, Liu & Leach (2018); Kim & Sung (2015); Yang, Li, Xu, Cao, Zhang, Wang & Jiang (2018)), including electrical properties (Happonen, Kokko, Juntunen & Rönkä (2019); Lewis, Hunt, Thomas & Wickham

(2017); Sneek, Mäkelä & Alastalo (2018)), surface morphology (Hudd (2011); Nguyen *et al.* (2013); Pan *et al.* (2015)), or ink distribution, which induces dimensional distortions (Hsu & Lo (2019); Kim & Sung (2015); Sowade *et al.* (2016)).

1.3.1 Structural characterization

1.3.1.1 Morphology

The morphology of the active layer will influence charge transport and is therefore of paramount importance for a device's functionality. The arrangement of molecules in the layer defines the layer's morphology. The molecules may be located in partly crystalline domains or may have a preferred orientation, and the layer may be amorphous with an arbitrary molecular arrangement (Chen, Nikiforov & Darling (2012c); Tone & Ganz (2016)). Many spectroscopic techniques may be used to assess the quality of molecular arrangement in the deposited ink as well they can provide insight into the chemical composition. X-ray diffraction (XRD) is a non-destructive method that may monitor the layer developing process by recording the scattering measurements. Figure 1.9a sketches the working principle of diffractometer. X-ray measurements follow the crystal formation during the sintering step over the whole thickness (Eun *et al.* (2015); Rossander, Zawacka, Dam, Krebs & Andreasen (2014b)). To produce an X-ray diffractogram, the constructive interference of a monochromatic beam of X-rays is scattered at specific angles (θ) from each lattice plane in a sample, as shown in Figure 1.9b. The obtained fingerprint contains information about atomic positions within the lattice planes extracted from the position, shape, and intensity of the peak. An online search of a standard database for X-ray diffraction patterns enables quick identification of atoms combining the structures with preferred crystal orientations (texture) and other structural parameters, such as average grain size, strain, and crystal defects.

Raman spectroscopy also yields actual results in studying the surfaces and interfaces between constituent layers of low-dimensional structures (Nguyen *et al.* (2013)). The working principle is based on the Raman effect shown in Figure 1.10a. Incident light at wavelength 750–850

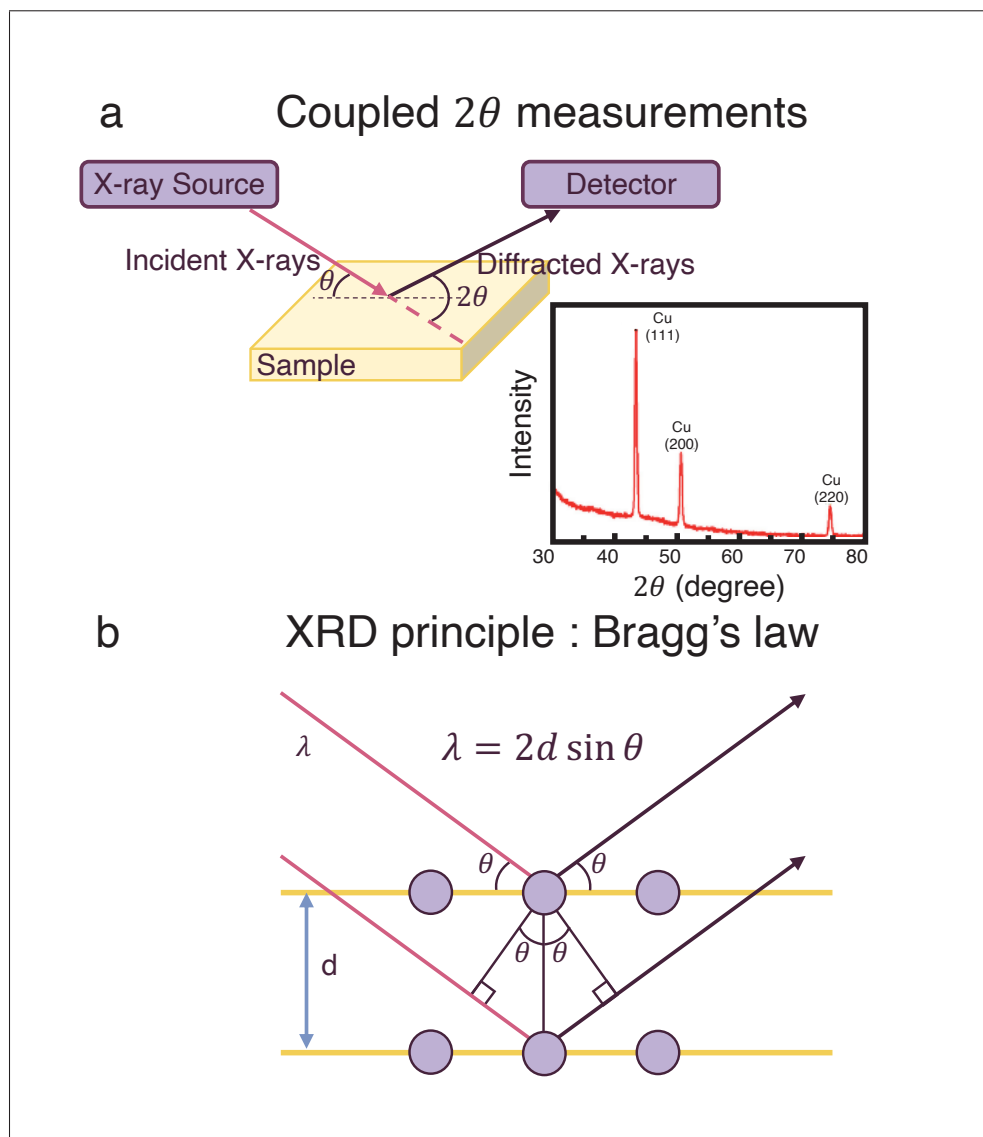


Figure 1.9 a) Working principle of diffractometer for X-ray diffraction measurements.
The inset is a diffracted pattern of printed Cu.
b) Bragg's law is used to describe the interference pattern
Adapted from Eun *et al.* (2015)

nm excites the molecule, reflecting the light in a different wavelength depending on chemical structure. However, Raman spectroscopy has a long acquisition time and yields no information regarding the vessel's geometry (Chen *et al.* (2012c); Nguyen *et al.* (2013)). Simple technique such a scatterometry is routinely used to characterize structured surfaces. The zeroth-order diffraction (reflected or transmitted beams) of light is monitored as a function of wavelength or

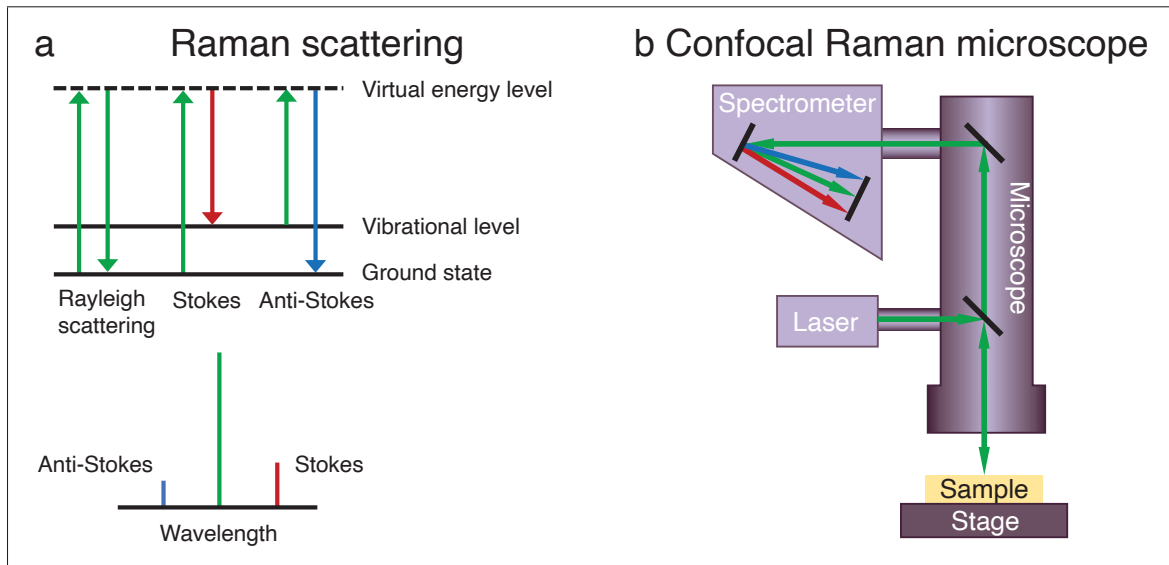


Figure 1.10 a) A sketched principle of Raman scattering.
b) A representation of a confocal Raman microscope

angle of incidence (Kreuzer, Whitworth, Francone, Gomis-Bresco, Kehagias & Sotomayor-Torres (2018)). To monitor all diffraction orders simultaneously, a diffractometry is applied. It is a subset of spatially coherent scatterometry and has a great potential to detect the deviations in nanostructures' critical dimensions. These are non-imaging techniques based on mathematical modeling to extract structural parameters of a surface.

The powerful imaging techniques such as scanning electron microscopy (SEM) and atomic force microscopy (AFM) (Perelaer *et al.* (2012); Saini, Saini & Sharma (2010)) are commonly used to investigate the printed surface morphology. The principle of SEM is shown in Figure 1.11. It is based on the interaction of the electrons with a few nanometers to several microns of the sample's surface. A beam of electrons is directed from a filament to the sample in a vacuum. After contact with the sample's surface, electrons are emitted primarily as either backscattered electrons or secondary electrons. The secondary electrons are produced as a result of interactions between electrons beam and weakly bound electrons in the sample's conduction band. They have low energy and escape within the first few nanometers of the sample surface as secondary electrons. The number of secondary electrons can be detected, and its intensity is

used to reconstruct the surface morphology. The SEM 2D-image formed results from the raster scan of the electron beam across the surface, recording the intensity value of emission from the sample at each (x, y) data point (Saini *et al.* (2010)).

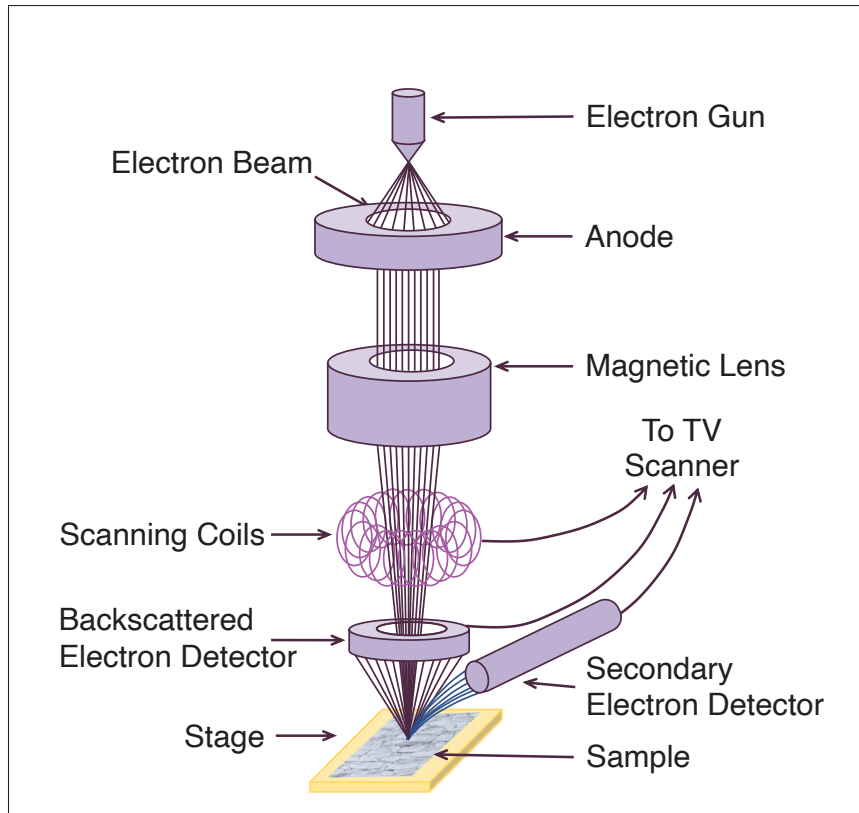


Figure 1.11 Working principle of a scanning electron microscope

Figure 1.12 shows the working principle of AFM, which maps out a 3D surface. AFM contains a flexible cantilever with a tip. A constant force is applied to the tip. The scanning motion is conducted by a piezoelectric tube scanner, which scans the tip in a raster pattern with respect to the sample. The tip's interaction with a sample is monitored by reflecting a laser off the back of the cantilever into a split photodiode detector. The difference in the photodetector output voltages detects changes in the cantilever deflection (Saini *et al.* (2010)).

SEM and AFM have the advantage of the high resolution of few nm are usually used to track the evolution of the porosity and the microstructure of printed patterns (Greer & Street (2007);

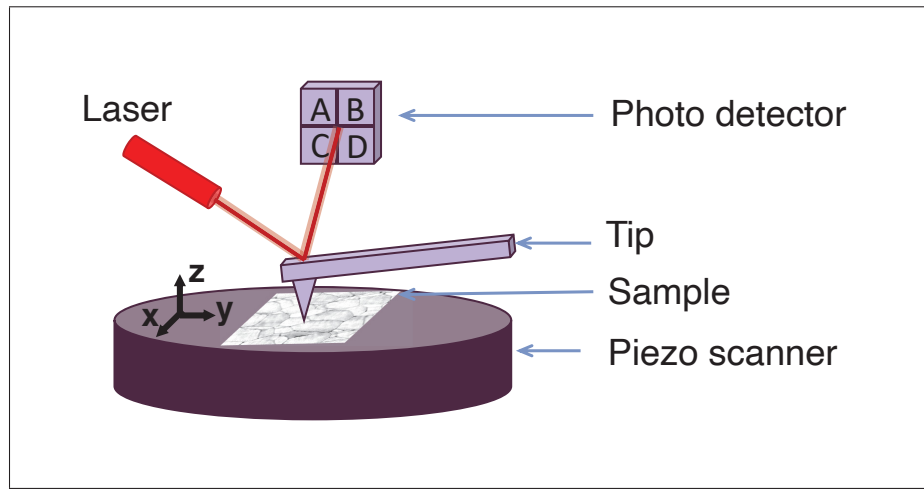


Figure 1.12 A sketch of a working principle of atomic force microscope

Kim & Sung (2015); Zhou, Xu, Cheng, Zhao & Chen (2015)). Unfortunately, they require special conditions, such as vacuum or helium environments, to avoid noise and damage (Chen, Nikiforov & Darling (2012b); Du, Hardt & Anthony (2019); Hedstrom, Henriksson, Wang, Andersson & Persson (2015); Logothetidis, Georgiou, Laskarakis, Koidis & Kalfagiannis (2013); Pastorelli, Accanto, Jørgensen, van Hulst & Krebs (2017); Rösch, Krebs, Tanenbaum & Hoppe (2012); Rossander *et al.* (2014b); Sneck *et al.* (2018)). Additionally, both of these methods are time-consuming, allow for a limited surface area observation ($\sim 100 \mu m^2$). These methods suit for the laboratory scale investigation of the surface morphology at the stage of a new ink formulation. For example, the surface made by NPs based conductive ink contains the grains with a minimum size of $\sim 30 nm$ (Mitra *et al.* (2018a,1)).

A most commonly used method for the surface evaluation of printed patterns is a conventional optical microscope. It may evaluate the surface morphology over a large area (few cm^2) than AFM or SEM with the imaging resolution above $120 nm$. Today, the machine vision based on the optical microscopy observation is in the developing stage to be applied for the in-situ measurements (Feng *et al.* (2018); Yang *et al.* (2018)).

All the discussed techniques are working using different light phenomena. The other way of defining the surface properties is nanoindentation, which is based on probing the mechanical

properties of thin films (Panin, Shugurov & Oskomov (2005)). Figure 1.13 presents a working principle of nanoindentation and the way to determine the mechanical properties. The surface of a sample is indented by a diamond probe with a tip of $\sim 100 \text{ nm}$ (Panin *et al.* (2005)). Usually,

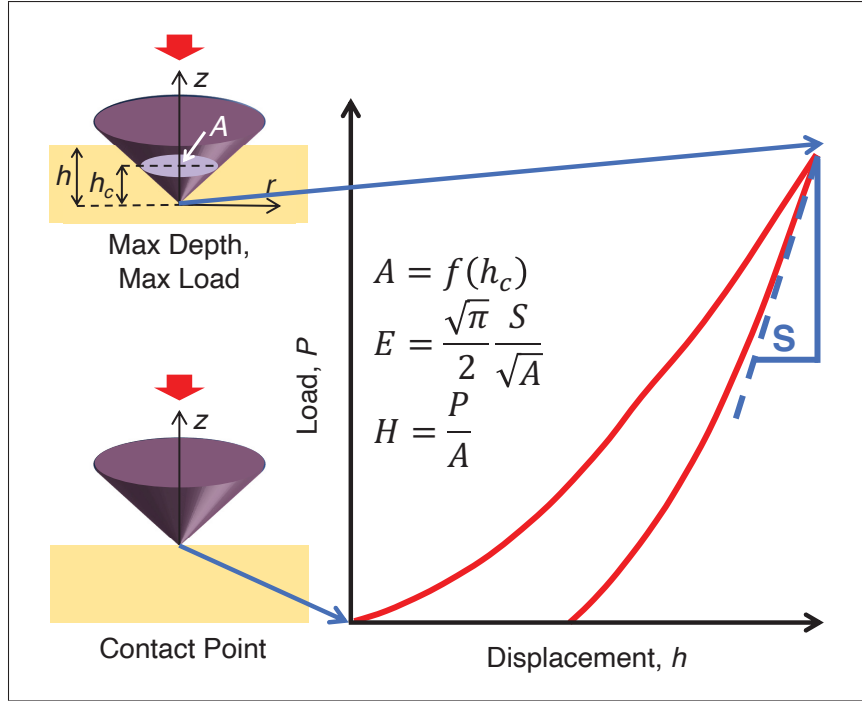


Figure 1.13 The principle of the nanoindentation. The applied load P and the penetration depth h_c are measured to calculate the contact area A , the reduced elastic modulus E and the hardness H

the applied load P and the depth of penetration of the tip h_c are simultaneously measured during the process. The unloading portion of the load-depth data contains the information on the stiffness S of the material being tested. The penetration depth and the geometry of the tip is used for the calculation of the contact area during the indentation. It is described by the indenter area function $A = f(h_c)$. Knowing the contact area and the stiffness, the reduced elastic modulus E and the hardness H of the material can be measured. The elastic modulus of printed film corresponds to the mean grain size of solidified ink (Hoath (2016); Panin *et al.* (2005)).

1.3.1.2 Thickness

The thickness of the printed layer strongly influences a printed device's performance. For example, the thickness of layers in organic photovoltaic cells must be determined precisely, since too thick layers hinder charge extraction, while thin ones are not able to efficiently absorb light (Tone & Ganz (2016)). Nowadays, it is impossible to predict a layer's thickness since it may vary during the fabrication process: when the ink is transferring and drying. Hence, the thickness of the printed layers must be controlled efficiently. Currently, probe-type measurements take the most significant niche as a thickness determination method, but they may damage the surface upon contact if the measurements are performed under unstable conditions. The most common tactile method is optical profilometry (Greer & Street (2007); Perelaer *et al.* (2012); Sowade *et al.* (2016); Tone & Ganz (2016)), where a probe connected to a cantilever drags over the sample's surface and measures its topography. In some systems (Tone & Ganz (2016)), the cantilever is connected to a ferromagnetic rod that extends into the center of a coil. The cantilever's tilt is inferred by measuring the coil's inductance, which is caused by the variation of the rod's position. Most of the systems use the deviation of a laser beam reflected by the cantilever giving the lateral resolution of a few angstroms (Greer & Street (2007); Perelaer *et al.* (2012); Sowade *et al.* (2016); Tone & Ganz (2016)). Unfortunately, there is a potential to crack soft (poorly sintered) samples and the measuring speed of such a system is relatively slow, since it requires to remove the samples from the production line.

Another probing technique is impedance spectroscopy (ECIS), which measures the impedance spectrum, whereby the capacitances of layers (C) can be characterized by the imaginary part of the impedance given by $Z_C = 1/i\omega C$ (Lewis *et al.* (2017); Tone & Ganz (2016)). Hereby, in this way, the thickness of smooth layers (t) may be extracted from the capacitance value: $C = \epsilon_0 \epsilon_r A/t$, where surface area (A) and permittivity (ϵ_r) should be known parameters of the layer (Zapka (2017)). The most precise method for the thickness determination of printed structures is AFM, which is another probe-based method (Fajardo *et al.* (2020); Kreuzer *et al.* (2018)).

The best-known imaging method for thickness determination is confocal laser microscopy (Merilampi, Björninen, Haukka, Ruuskanen, Ukkonen & Sydänheimo (2010)), which as well powerful as previously discussed methods. However, all of them have not been able to keep in line with these advances. All of them are time-consuming and require ex-situ measurements, and therefore cannot speed up the printing process (Kreuzer *et al.* (2018)). The current trends in the industrial printing market call for a fast, non-invasive method for performing dimension measurements, easily integrated into printers or presses.

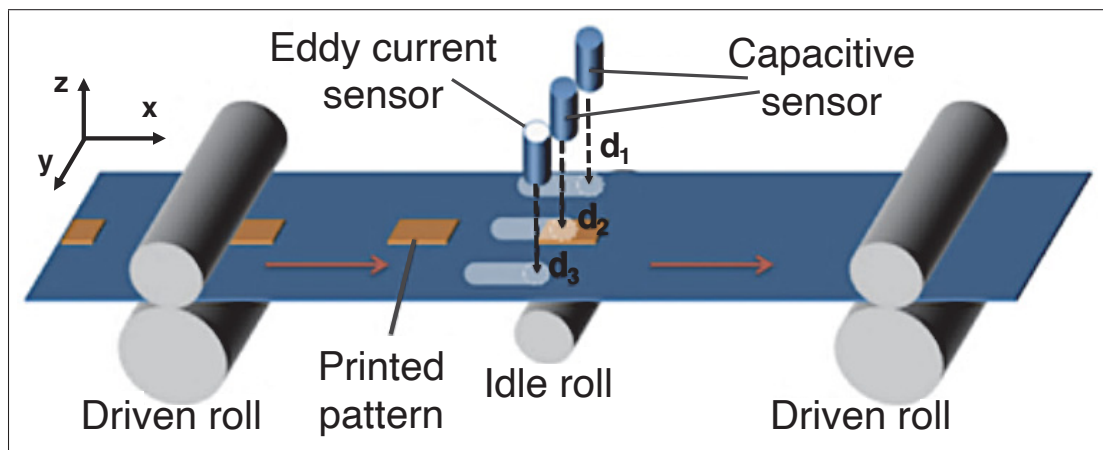


Figure 1.14 Online noncontact thickness measurement of printed conductive silver patterns in Roll-to-Roll gravure printing
Taken from Seong *et al.* (2015)

Seong *et al.* (2015) was the first group to propose the first online and non-contact thickness measurements of conductive ink adaptable for an industrial printing process such as R2R. Figure 1.14 shows the design module that contains two capacitive sensors, and one eddy current sensor enables in-situ measurements of the thickness. The design module is placed above the printing web, while an idle roller is placed under to minimize the fluctuation of the printing web. Capacitive sensors measure the distance from a sensor head to a substrate or a metallic printed line. The variation in the output signal from the capacitive sensors is utilized to calculate the thickness. The eddy current sensor is implemented to compensate for a low-frequency error from the web fluctuation and sensors' alignment errors (Seong *et al.* (2015)).

The other possibility is the implementation of spectroscopic techniques for rapid measurement in industrial printing presses, where reflection, absorption, or Raman spectroscopy are in high demand to determine film thicknesses at an even smaller scale (Hoath (2016); Kreuzer *et al.* (2018)). Scatterometry has great potential for detecting any changes in the height. In this technique, the diffraction efficiency of the devices depends on the input wavelength. It can be used to determine the height of an inspected structure by model-assisted, inverse problem-solving (Kreuzer *et al.* (2018)). The most established method for inline-thickness control is ellipsometry (Huemer, Jamalieh, Bammer & Hönig (2016)), which is based on measuring the change in the polarization of light reflected by a freshly printed layer (Huemer *et al.* (2016)). As schematically illustrated in Figure 1.15, the incident and the detected light can be decomposed into the s - and p - components. The recorded the s - and p - amplitudes are normalized to their initial values and denoted by r_s and r_p , which are used to calculate the complex reflectance ratio (ρ) given by:

$$\rho = r_p/r_s = \tan \Psi e^{i\Delta} \quad (1.2)$$

where $\tan \Psi$ is the amplitude ratio upon reflection, and Δ is the phase shift. The measured data are usually fitted to a suitable physical model and provide the optical properties and thickness of the sample. The ellipsometry is based on the self-normalized measurements. Hence, it provides quite accurate and reproducible the extracted values. In addition, this method is relatively insensitive to scatter and fluctuations and does not require a reference beam. Contrarily, the fitting may be quite complicated and inapplicable for non-uniform, multilayer structures (Hoath (2016)).

1.3.1.3 Printing defects

To increase electrical functionality of the printed devices, it is critical monitoring of the defects such as dimensional distortions, cracks, or voids (Seong *et al.* (2015)). It has been tested extensively (Feng *et al.* (2018); Kim & Sung (2015); Yang *et al.* (2018)). The widening effect of printed patterns can be predefined by matching conditions between the surface tension of used ink and the surface energy of a substrate or from printing parameters (Nguyen *et al.*

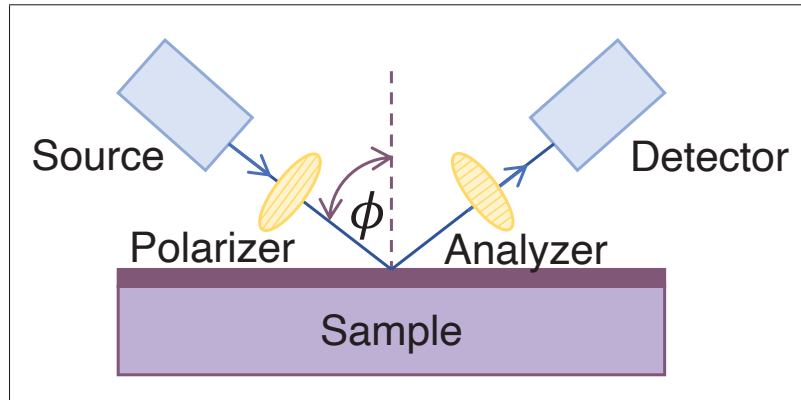


Figure 1.15 Principle of an ellipsometer. Polarized light strikes the sample and the change in polarization is analyzed. Angle of incidence ϕ can be varied

(2013)). However, nowadays, statistics from industrial environments do not contain specific information for all developed printing processes and used materials. The most established method for investigating dimensional defects such as enlargement or shrinkage of printed lines is optical microscopy associated with the imaging analysis to count the number of image pixels (Kim & Sung (2015); Sowade *et al.* (2016); Yang *et al.* (2018)). Nowadays, inspection techniques for detecting misalignment defects validation are based on two-dimensional optical imaging methods using machine vision cameras to capture images of the final product and compare them with the desired reference (Feng *et al.* (2018); Kim & Sung (2015); Yang *et al.* (2018)). Figure 1.16 shows an example of the extraction of the defects. An improved approach uses an all-optical difference engine sensor for the defects detection, which proposes a self-comparison strategy between the printed structures having the same designed dimensions (Feng *et al.* (2018)). However, these demonstrations include multistep image post-processing, generating large data sets that are hard to handle in real-time (Feng *et al.* (2018); Kim & Sung (2015); Yang *et al.* (2018)).

Another optical method is interferometry with a centimeter-scale measurement range and micrometer-scale resolution (Diaz *et al.* (2013); Nguyen *et al.* (2013); Yang *et al.* (2018)). The interferometry provides three-dimensional surface information, including geometrical defects detection. However, it requires several frames of camera data, which makes the systems

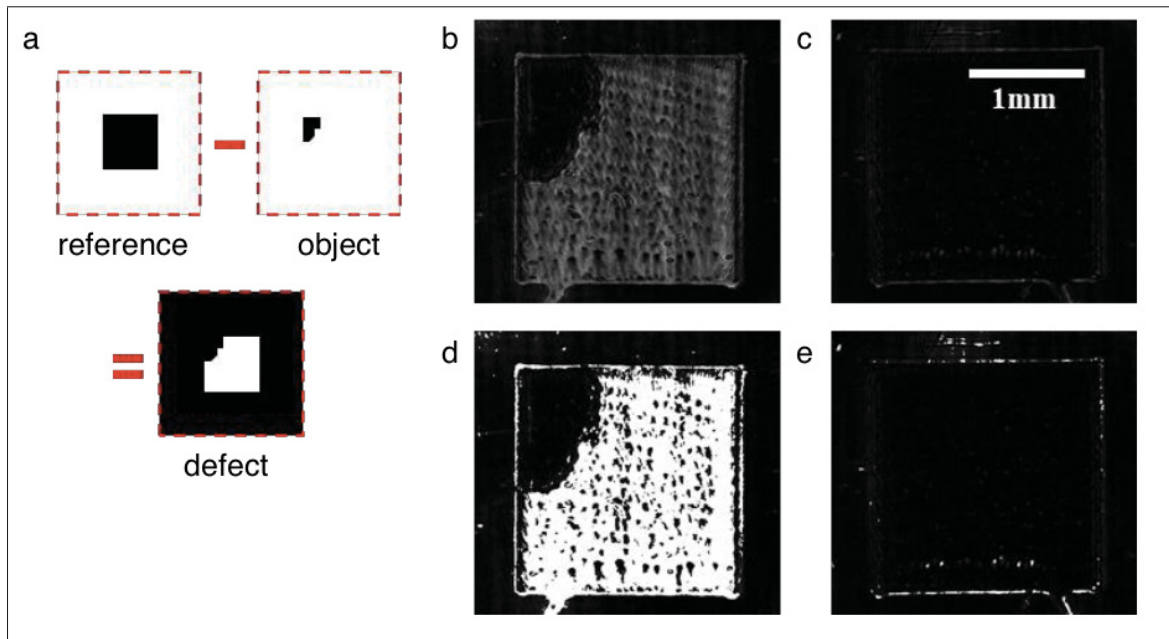


Figure 1.16 Optical subtraction of test sample: a) illustration of the reference image, the object image and the defect,
 b) the difference image showing materials missing from the conducting line,
 c) the difference image when no defect is present,
 d) binarised difference image showing the defect,
 e) binarised difference image when no defect is present
 Taken from Feng *et al.* (2018)

sensitive to vibration and unsuitable for in-line applications in the industrial environment (Kimbrough & Novak (2015)).

The coherent Fourier scatterometry has great potential for detecting a deviation in the critical dimensions, where all diffractive orders monitor simultaneously (Madsen & Hansen (2016)). However, it is based on comparing the relative intensities of the diffractive orders to the simulated data. The incident electric field is very sensitive to the optical alignment and aberrations in the system, where using a large numerical aperture microscope objective for scatterometry issues practical problems (Kreuzer *et al.* (2018)).

The combination of several imaging techniques gives the exact location of processing defects (Espinosa *et al.* (2013)). Figure 1.17 sketches the inline inspection system of different solar cell

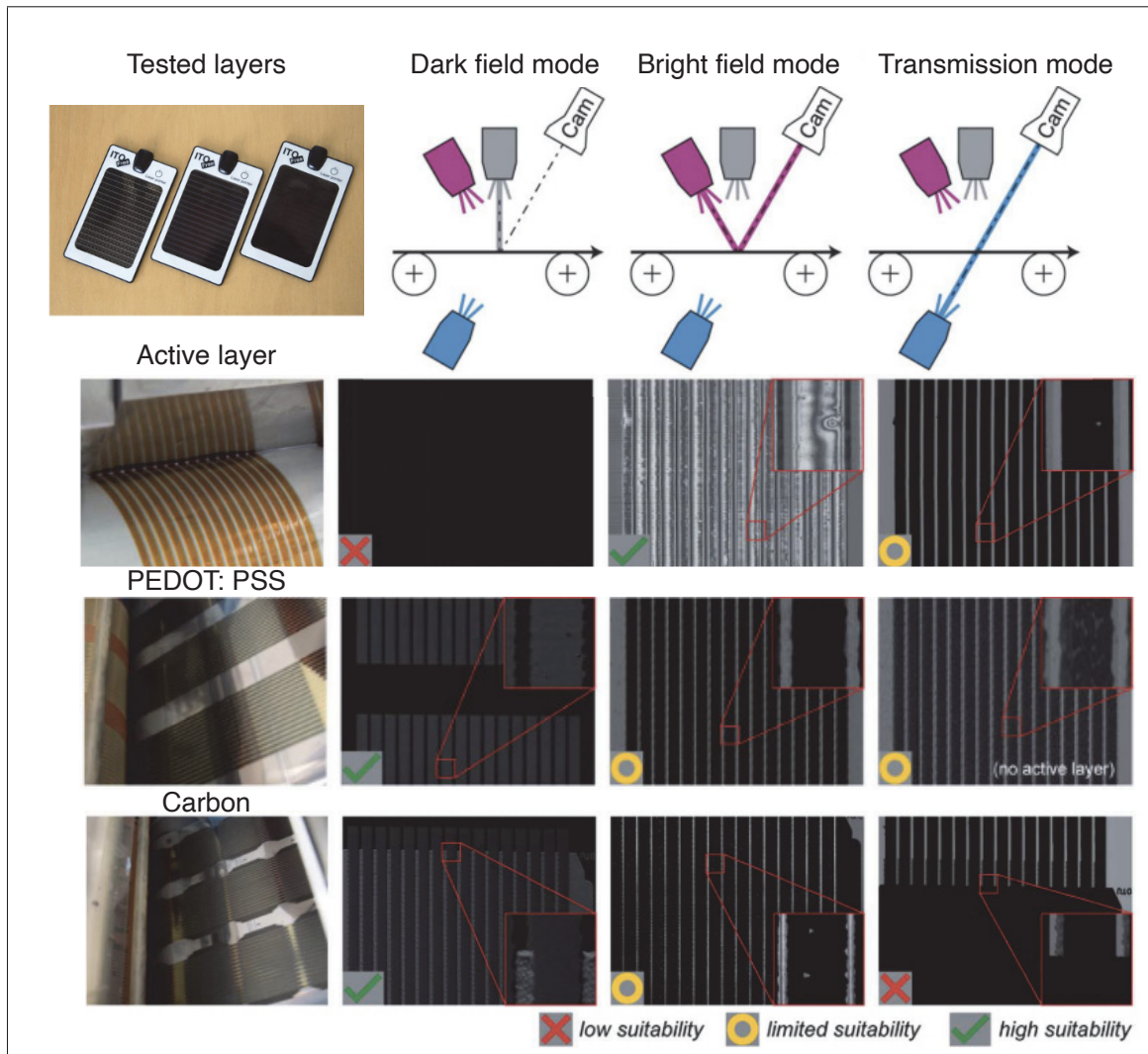


Figure 1.17 The illustration of the tested layers and a principal setup with three different illumination modes. Photograph of the polymer solar cell modules: Active layer (left); PEDOT: PSS (center) and carbon black (right). The results obtained with different modules are presented below

Taken from Espinosa *et al.* (2013)

layers based on three different illumination modes. The testing setup consists of LED-based light sources (white, red, blue) with two line-scan cameras, which have been used for the defect analysis of each printed layer (Espinosa *et al.* (2013)). Depending on the type of surface, e.g. transparent or opaque, thin or thick, one of the light sources was applied. The bright-field (red LED) and transmission modes (blue LED) are well suited for the thin and semi-transparent films, while

the dark mode (white LED) is used for the thick and rough surface. Electroluminescence and photoluminescence are complimentary used to distinguish between an electrode and photoactive layer with dark lock-in thermography. It is based on the heat evolution measurement provides the complex information of the origin of different defects leading to short cuts (Rösch *et al.* (2012)).

All of these methods are used to control printing defects and are applied under specific conditions, such as an appropriate illumination or in a particular direction, which might be inconvenient for the industrial environment. Therefore, a major challenge remains for the mass-production of PE devices to obtain on-line feedback on print quality to ensure consistent product quality (Cui (2019); Eun *et al.* (2015); Tan *et al.* (2019)).

1.3.2 Electrical properties

The electrical properties of the printed devices are the most critical parameters to control. The electrical functionality depends on: (i) substrate roughness, (ii) type of the printed ink, (iii) sintering method, (iv) sintering time, and (v) temperature in case of thermal sintering or the power/the speed of the laser in case of the photonic sintering (Sneck *et al.* (2018)).

To extract the fundamental information about printed electronics devices such as mobility and molecular interchain overlap, the nonlinear optical microscopy based on an ultrashort near-infrared laser pulse was utilized as a potential in-situ method (Pastorelli *et al.* (2017)). UV photoemission spectroscopy (UPS) is commonly used for the electrical characterization of a metallic layer to find the minimum energy (work function) needed to remove an electron from the metal surface to a vacuum outside the surface at 0 K. The work function is a crucial parameter for the application of printed metal layers as electron emitters or contact electrodes (Mitra *et al.* (2018a)).

The most tested parameters are DC conductivity or resistivity in the industrial environment. As shown in Figure 1.18, the electrical quality control of printed electronics is typically evaluated by a multimeter or four-point probe (4PP) (Greer & Street (2007); Hoath (2016); Merilampi *et al.* (2010); Perelaer *et al.* (2012); Sneck *et al.* (2018); Sowade *et al.* (2016)). The difference

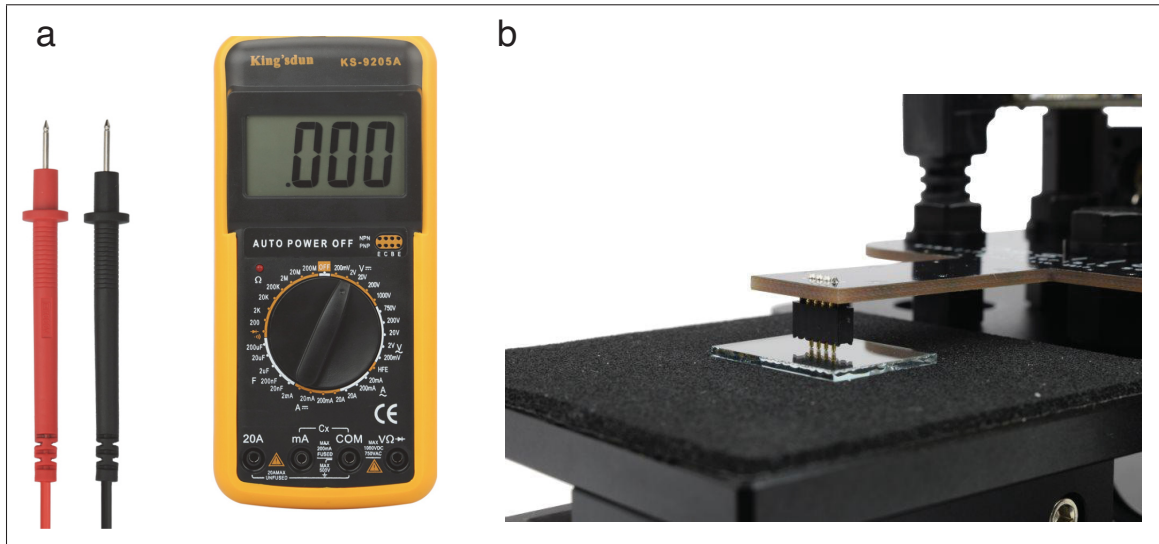


Figure 1.18 A typical resistance measurement tools using: a) a multimeter and
b) four-point probe

Taken from www.instructables.com & www.ossila.com

in the functionality between them is described in Appendix II. These techniques allow for the sheet resistance measurements. An advanced way of probe-based measurements is using a system made from multi pins, which are adopted for a particular printing design. The contact of pins with the printed area allows the detection of possible open and short circuits of printed devices (Happonen *et al.* (2019)). However, these tools require physical contact between the measurement probe and the device under test, which is impractical due to the high speed of manufacture. The contactless approach proposes to analyze the impedance of an inductive sensor, which is affected by the eddy currents induced in the printed samples (Lewis *et al.* (2017)). Figure 1.19 sketches the experimental setup used for measuring the impedance of six printed tracks by six sensors with different self-resonance frequency. To pick up the optimum operational frequency for each conductive trace, an impedance analyzer was used. However, the response of the system is limited to the high-conductive samples (Lewis *et al.* (2017); Nguyen *et al.* (2013)).

The described techniques are summarized in Table 1.4. However, many of the described techniques can be barely envisioned for high-volume R2R printing since off-site or in-line

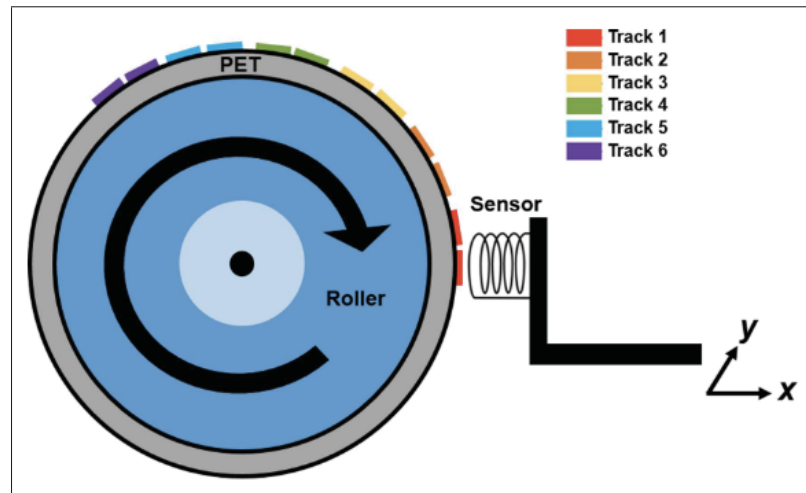


Figure 1.19 Schematic of experimental setup showing the sensor holder onto an XY stage next to the roller with the attached samples

Taken from Lewis *et al.* (2017)

contact methods are not compatible with continuous manufacturing tools. The others are not able to evaluate all the properties of printing structures simultaneously. One of the most important missing points for narrowing the gap between lab to fab is the non-contact, non-destructive, and in-line evaluation technique for quality control of PE devices. The ability to achieve this goal will lead to a decrease in the rate of a defect in the production process and the total cost of the device, as well as to new technological developments in advanced PE production. Thus, the improvement of the quality control inspection system is a significant economic incentive.

Table 1.4 Techniques to characterize different parameters in PE

| Method | Extracted information | | | | | |
|-----------------------------|-----------------------|--------------------|------------|-----------------------|---------------------|-----------------------|
| | Ink's properties | Surface morphology | Dimensions | Mechanical properties | Chemical properties | Electrical properties |
| Rotational rheometer | ✓ | | | | | |
| Shadowgraphy | ✓ | | | | | |
| DSC & TGA | ✓ | | | | | |
| XRD | | ✓ | | | | |
| Optical microscopy | | ✓ | ✓ | | | |
| AFM | | ✓ | ✓ | | | |
| SEM | ✓ | ✓ | ✓ | | ✓ | |
| Ellipsometry | | ✓ | ✓ | | ✓ | |
| Scatterometry | | ✓ | ✓ | | ✓ | |
| Raman spectroscopy | | | ✓ | | ✓ | |
| Nanoidentation | | | | ✓ | | |
| Profilometry | | | ✓ | | | |
| ECIS | | | ✓ | ✓ | | ✓ |
| Eddy current sensor | | | ✓ | | | ✓ |
| UPS | | | | | | ✓ |
| Four-point probe | | | | | | ✓ |
| Multimeter | | | | | | ✓ |

1.3.3 Milestones in quality control

Advanced fabrication technology has moved toward high-throughput and the large area of production. However, the methodologies required to produce on a large scale and to reduce barriers to entry into these high-performance technologies lag behind potential development. Achieving the feasibility of manufacturing these flexible devices has proven difficult and time-consuming, especially in the transition from small-scale R&D to high-volume production (Fajardo *et al.* (2020)).

The most prominent barrier to high-volume manufacturing development is the difficulty in implementing viable real-time and in-line process feedback. This is exceedingly important for industrial-scale production. Often, it is very costly for a manufacturer when a process goes out of control. This process shift is not detected until an entire roll of product is fabricated, and functional testing of the devices or materials on the substrate can be measured out of the production line. This troubling situation can result in large amounts of processed material, produced to a sub-standard grade, which needs to be scrapped at a potentially enormous loss. The large area processing will only be advantageous from a cost perspective if scrap rates can be kept low - necessitating the right non-destructive, in-line quality control for PE devices. Moreover, such a system could benefit not only mass production applications but also the new product or process development, as a higher throughput of metrology data during the research and development phases of new devices can significantly aid in lowering the overall development time required to bring a new printing process to maturity. A new method for non-destructive and in-line inspection of printed features is required to effectively pursue the fabrication techniques and flexible electronic devices of tomorrow.

1.4 Terahertz sensing for quality control

One of the most promising techniques for in-line and non-destructive testing (NDT) is the terahertz technology (THz). The goal of my thesis is to demonstrate the potential of THz waves for NDT quality control of PE devices and to prove that this concept is adaptable in an industrial

environment. During the last 30 years, the development of THz technology has opened a lot of possibilities for quality control in the industrial environmen (Chen & Pickwell-MacPherson (2019); Naftaly, Vieweg & Deninger (2019); Tao, Fitzgerald & Wallace (2020)). As shown in Figure 1.20, THz radiation corresponds to the frequency range of 0.1-10 THz, corresponding to 0.03-3 mm wavelength range, and photon energy of 1-10 meV.

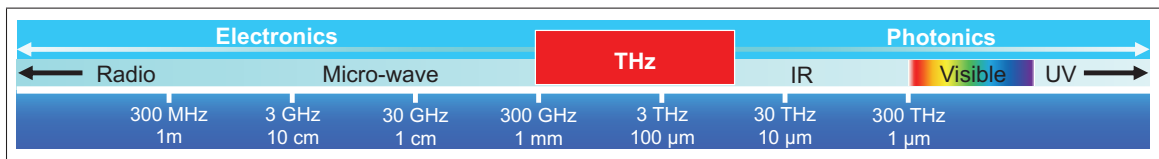


Figure 1.20 Electromagnetic spectrum

THz electromagnetic radiation lies between the microwaves and infrared light. The technical difficulty of producing efficient sources and detectors has blocked the industrial application of THz radiation with its potential and suitability for practical applications. However, with the development of ultrafast components in both photonics and electronics, the situation has improved drastically in the last two decades. This evolution has enabled the introduction of THz technology as a competitive method compared to systems based on (Zeitler & Shen (2012)):

- **X-ray:** THz waves are non-ionising radiation and present minimal known health risks due to low photon energy and can be deployed for a stringent safety inspection (Fan, Li, Zhou, Liu, Liu, Qi & Mu (2017))
- **Infrared:** Terahertz radiation penetrates dielectric materials and has relatively low Mie and Rayleigh scattering.
- **Microwave:** Terahertz technology can achieve significantly better spatial resolution because of the shorter wavelengths. Also, spectroscopic fingerprints are available in the terahertz range, for substance identification.
- **Ultrasonic:** Terahertz radiation enables non-contact inspection of materials (Fan *et al.* (2017)).

All of these advantages make THz technology attractive for the non-destructive and non-invasive testing and material characterization fields (Zeng, Edwards, Stevens, Bowen, Donnan & Yang (2017); Zhong (2019); Zhuldybina, Ropagnol, Trudeau, Bolduc, Zednik & Blanchard (2019b)).

The main application of THz radiation is spectroscopy. Even though, commercially available Fourier transform infrared (FTIR) spectrometers can operate in the spectral range down to 1.5 THz and are considered as a mature technology, their dynamic range is limited at low frequency range due to source and detector efficiency (Gowen, O'Sullivan & O'Donnell (2012)). In comparison with well-developed vibrational spectroscopic methods, e.g. near- and mid-infrared spectroscopy, THz spectroscopy provides specific fingerprints of many molecules such as water, drugs, explosive (Gowen *et al.* (2012)). Also, THz radiation is transparent through numerous optically opaque non-conductive or organic materials, e.g., polymers, plastic, paper, clothes, wood, and provides the opportunity to inspect the material composition (Jansen, Wietzke, Peters, Scheller, Vieweg, Salhi, Krumbholz, Jördens, Hochrein & Koch (2010); Naftaly *et al.* (2019); Zhong (2019)). Consequently, taking advantage of being transparent to clothes and being non-hazard radiation, THz technology can be applied for security operations such as passenger screening at airport terminals (Fan *et al.* (2017)).

THz radiation is highly absorbed by water since the hydrogen ($H - O$) bonds inside water molecules resonate strongly at THz frequencies. It makes THz spectroscopy very suitable for monitoring moisture content, which highly affects quality in food or construction industries (Afsah-Hejri, Hajeb, Ara & Ehsani (2019)). Many biological molecules have distinct THz signatures, which allows the precise determination of the residues in foods or sugar content in beverages (Gowen *et al.* (2012)). To enhance the interaction of THz radiation with the media under test and therefore improve the detected sensitivity, some of the innovative approaches use metamaterials (Berrier, Schaafsma, Nonglaton, Bergquist & Rivas (2012); Cai & Shalaev (2010); Chen, Li & Sun (2012a); Padilla, Aronsson, Highstrete, Lee, Taylor & Averitt (2007); Tao, Padilla, Zhang & Averitt (2010b)). Metamaterials are artificially engineered resonators, which enhance the light interaction with the medium. They have been extensively used for the detection of the biological cells and tissues (Dolai & Tabib-Azar (2020); Park, Hong, Choi, Kim,

Park, Han, Park, Lee, Kim & Ahn (2014); Yang, Yang, Luo & Fu (2016); Yu, Hao, Meiqiong, Jiaoqi, Wei, Jinying, Xueping, Weiling & Yang (2019)).

Another distinct feature of THz spectroscopy, in comparison with FTIR spectroscopy, is the possibility to measure the amplitude and the phase of the electric field, which gives direct access to many parameters of tested materials, e.g., conductivity, refractive index, and absorption coefficient (Gowen *et al.* (2012)).

Furthermore, the spatial resolution of THz waves is much higher than the microwave radiation due to its shorter wavelength. Consequently, THz imaging provides non-destructive, contactless, and nonionizing modality for the detection of defects with micrometers size in integrated circuits (Zeitler & Shen (2012)), cracks in cement-based materials (Fan *et al.* (2017)) or automotive painting (Tao *et al.* (2020)). In the food industry, it can be used to detect the precise location of potential contaminants, e.g., plastic or glass in chocolate (Gowen *et al.* (2012); Jansen *et al.* (2010); Mittleman, Gupta, Neelamani, Baraniuk, Rudd & Koch (1999); Qin, Ying & Xie (2013); Zeitler & Shen (2012)). In 2016, it was shown the ability to use THz imaging to distinguish the ink from the paper, which opens many doors in archaeology, for instance, reading of ancient books without opening them or non-destructive investigations of any cultural heritage including authenticating artifacts, or paintings, murals, etc (Cosentino (2016); Redo-Sanchez, Heshmat, Aghasi, Naqvi, Zhang, Romberg & Raskar (2016)).

Even though THz technology is relatively less explored than other parts of the electromagnetic spectrum, and the size of many THz devices are relatively bulky and have not been optimized yet for use on-site of the production line, THz spectroscopy for the industrial characterization scores high in technology readiness level 6 (Gowen *et al.* (2012); Naftaly *et al.* (2019)). Figure 1.21 shows the evolution and near-future forecast of THz technologies. With the development of some commercial THz system, for example TeraFlash system from TOPTICA (TOPTICA (2016)), THz radiation can be applied for in-line and non-destructive testing in the printed electronics, where the production speed (~ 10 s m/min). Running the industrial press at this

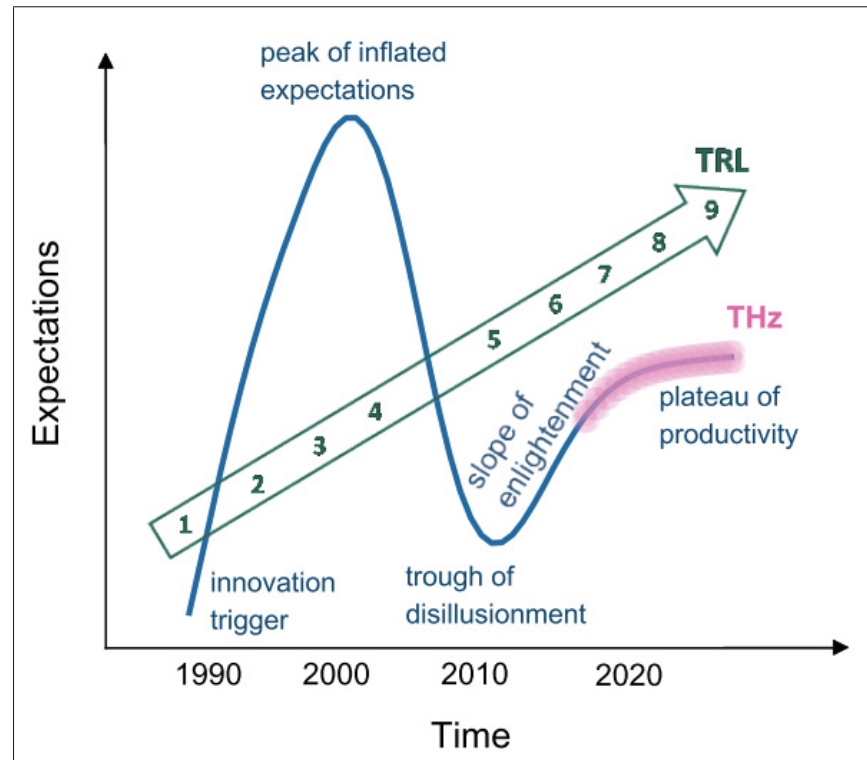


Figure 1.21 The Gartner Hype Cycle, TRL evolution, and the current envisaged position of THz technologies
Taken from Naftaly *et al.* (2019)

speed, the TeraFlash system (1600 scan per second) is able to track every millimeter of the production line.

In this study, we implemented the non-destructive nature of the THz waves for potential industrial process quality control of the printed electronics devices. Figure 1.22 shows a flashback to the traditional offset printing used in the manufacture of full-color magazines, posters, packaging, etc. The print quality is evaluated with a color control bar (GATF Standard Offset Color Bar) (Redo-Sanchez, Laman, Schulkin & Tongue (2013)). Using a densitometer or a spectrophotometer, these bars allow for accurate determination of ink density, dot gain, and screen angle accuracy. Generally, the color control bars are printed away from the immediate image area and are often cut off or hidden during final assembly.

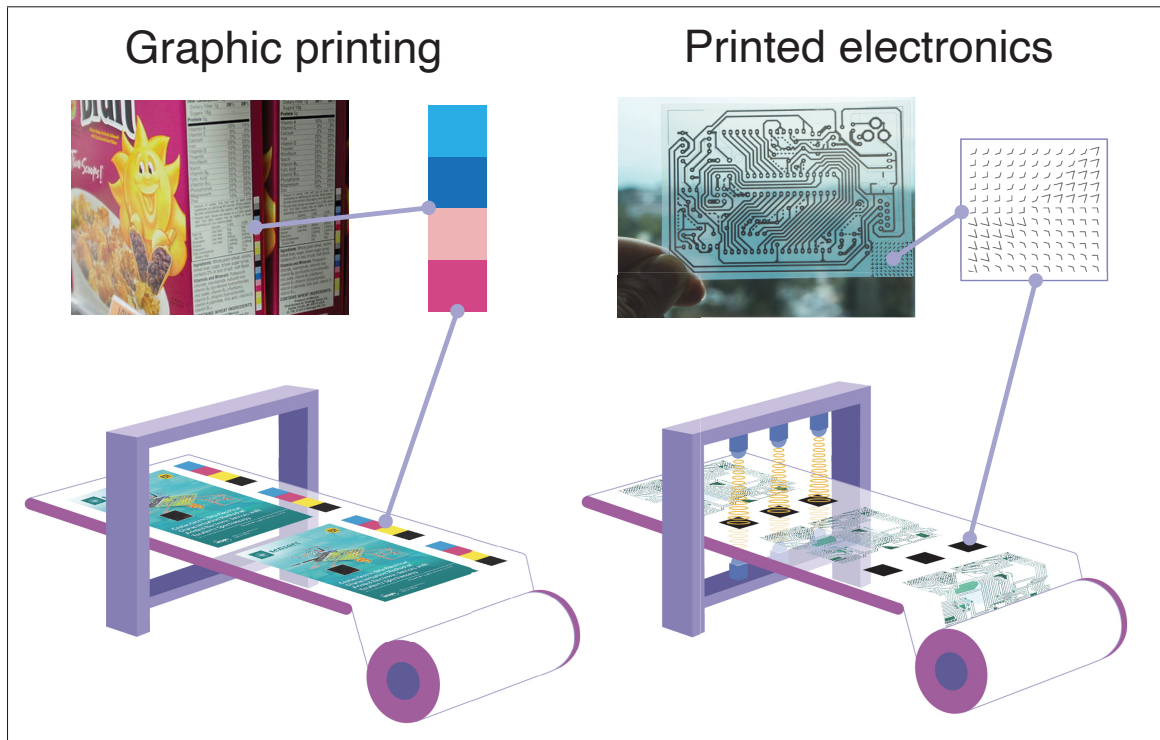


Figure 1.22 Comparison of quality control in graphic printing and proposed solution for printed electronics

Alternatively, we have introduced a simple strategy using a printed quality control bar (QCB). Printed devices are conductive materials and behave as mirrors for THz waves. To overcome this problem, we proposed to use THz metamaterials (MMs). Basically, MMs can exhibit a strong response in the THz frequency range in transmission- or reflection-type geometries with a high dependency on their designs which may be control by the variation of its unit cell, mesh and other geometric parameters or materials properties (Pipes (2005)). MMs act as QCB and are made at the same time with the same printing parameters as a printed device to probe the properties of printed ink in the production of PE devices. A key point of this strategy is the small printing area (e.g., 1 cm^2) required to retrieve the quality of ink during the printing process.

1.5 Thesis organization

This thesis focuses on developing a new quality control method to address the present gap for non-destructive and in-line inspection of PE devices at speeds and costs compatible with high-throughput PE processes. To accomplish this, two types of quality control patterns in the shape of THz metamaterials are studied to validate this inspection framework experimentally, and two functions of the proof-of-concept are detailed and tested.

Chapter 2 describes the THz spectroscopy background starting from the generation and detection techniques for THz time-domain spectroscopy (THz-TDS). Then, two normalized transmission and dual-wavelength THz spectroscopy (DWTS) for data analysis of experimental results are discussed. DWTS has been developed in the framework of this thesis. Finally, the near-field real-time terahertz microscopy is presented.

Chapter 3 discusses the motivation behind studies on the application of THz metamaterials for quality control. Two main approaches are covered in terms of testing the geometrical specification and electrical properties.

Chapter 4 focuses on analyzing ink distribution during the printing process using optical microscopy and THz-TDS.

Chapter 5 is addressed to the quality control of the electrical properties of PE devices. The conventional methods are compared with THz-TDS. The last section includes the data analysis of conductivity using near-field real-time THz microscopy.

The last part contains the conclusion summarizes the obtained results with a discussion of further possible research directions.

CHAPTER 2

TERAHERTZ RADIATION AND APPLICATION

Terahertz systems are typically one of two types: broadband and narrowband systems (Tao *et al.* (2020)). The latter is usually represented by the continuous waves (CW), which are used for single frequency THz generation. CW THz waves could be generated by photo-mixing in low-temperature-grown gallium arsenide (Zhong (2019)) or electronically (Tao *et al.* (2020)). CW systems are applied for intensity measurements (Cai & Shalaev (2010); Padilla *et al.* (2007); Singh, Azad, O'Hara, Taylor & Zhang (2008)), which can be well suited for quality control in an industrial environment. Unlike a CW system, broadband emission can be achieved by a pulsed system, where the time-domain profile of THz waves can be recorded. A variety of techniques for broadband generation of THz radiation by accelerating carriers excited from ultrafast pulses or nonlinear conversion methods in optical crystals have been developed since its first demonstration in 1982s by D. Auston *et al.* (Fattinger & Grischkowsky (1989); Jepsen, Cooke & Koch (2011)).

In this thesis, photoconductive antennas (PCA) were mainly used as a source and detector of THz radiation. The pulse-front-tilt technique in $LiNbO_3$ crystal has been used as an intense THz source for the near-field imaging of printed samples during the campaign of experiment in Kyoto, Japan. These generation techniques are presented in detail in the Chapter 2.1. The detection of THz fields is also done with either a photoconductive antenna or nonlinear crystal (see Chapter 2.2).

2.1 Generation of terahertz

2.1.1 Photoconductive antennas

The photoconductive antenna (PCA) is made from a semiconductor crystal with a pair of metallic electrodes separated by a gap (Burford & El-Shenawee (2017)). The concept of the PCA for THz generation is sketched in Figure 2.1. A femtosecond optical pulse with the photon energy of $\hbar\omega$

is incident on the antenna gap. Absorbed photons generate free electrons ($N(t)$) in the conduction band (Figure 2.1a). To excite electrons to the conduction band, the photon energy of the optical beam must overcome the semiconductor bandgap energy (E_{gap}). As shown in Figure 2.1b, an applied bias field (E_{DC}) accelerates free electrons leading to a photocurrent $j(t)$. The variation in photocurrent density emits a THz electromagnetic wave with a time-domain amplitude $E(t) \propto dj/dt$ (Figure 2.1c). The rise of the transient photocurrent is mainly determined by the temporal duration of the laser pulse, and the THz electric field is linearly proportional to the bias field.

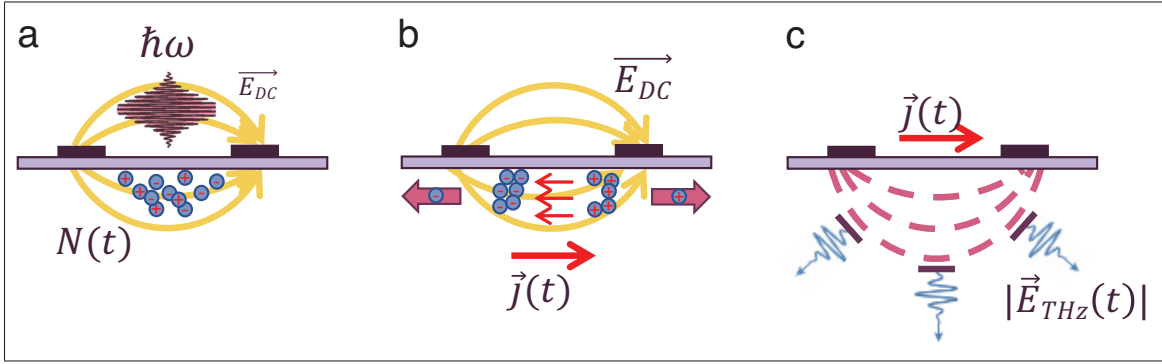


Figure 2.1 A sketch of photo-conductive antenna for THz generation: a) the optical pulse ($\hbar\omega$) generates free electrons; b) Electrons are accelerated in the static field (\vec{E}_{DC}) and creates a photocurrent ($\vec{j}(t)$); c) THz pulse ($|\vec{E}_{THz}(t)|$) is generated from transient photocurrent element

The most commonly used semiconductor for the substrates of PCAs is semi-insulating *GaAs* (*SI – GaAs*) and low-temperature *GaAs* (*LT – GaAs*). The main characteristics of these substrates for THz radiation with PCA are: (i) a large dielectric strength, (ii) high carrier mobility. The bandgap energy of *GaAs* is $\sim 1.42 \text{ eV}$, which is slightly less than the photon energy of a 800 nm laser beam. The other factor determining the antenna's functionality is the shape and the length of the electrodes. Many designs have been proposed and tested, such as strip-line type, bow-tie type, and dipole type Jepsen *et al.* (2011). PCAs are usually equipped with a high-resistivity hemispherical silicon lens to collect the THz radiation into a collimated beam as well as to minimize total reflections at the air-substrate boundary to improve the output coupling. High-resistivity silicon has a refractive index of ~ 3.42 , which is very similar to *LT – GaAs* all

over THz frequencies (Burford & El-Shenawee (2017)). In comparison with other THz sources, the main advantage of using PCA is that they can get very high efficiency even with few nJ laser pulses energy, which makes them perfectly suited to be pumped by oscillator laser. Indeed, most THz energy is provided by the bias source rather than by optical energy. Many factors influence the characteristics of the THz pulses, such as:

- Antenna's shape;
- Applied biased voltage;
- Semiconductor substrate.

For the generation of intense THz pulses, PCA with a large aperture (LAPCA) is required (Ropagnol, Kovács, Gilicze, Zhuldybina, Blanchard, Garcia-Rosas, Szatmári, Földes & Ozaki (2019)). During my PhD, I made the microfabrication of interdigitated LAPCAs using a conventional negative lithography method for international collaboration with the department of experimental physics at Szeged University (see Appendix I). The silver interdigitated antennas have been patterned on top of the wide-band semiconductor. Using a Kr:F UV laser, an intense THz pulses with the highest record of energy per pulse up to $11 \mu J$, have been generated using these interdigitated LAPCAs. Appendix I includes the details of this work.

2.1.2 Optical rectification

Optical rectification (OR) is a nonlinear optical technique for the generation of THz radiation in a non-centrosymmetric crystal that contains a second-order nonlinear optical susceptibility. The principle of OR is sketched onto Figure 2.2. When a fs laser pulse passes through a non-centrosymmetric nonlinear media, an induced polarization ($P(t)$) results from the charge displacement (Lee (2009)). Hence, the nonlinear polarization of the material created by the incident electric field $E(t)$ can be described by expanding of $\chi(E)$ in powers of the field E :

$$P(t) = (\chi^{(1)} + \chi^{(2)}E(t) + \chi^{(3)}E(t)^2 + \dots)E(t), \quad (2.1)$$

where we will be focused only on the second order polarization for describing OR. Considering

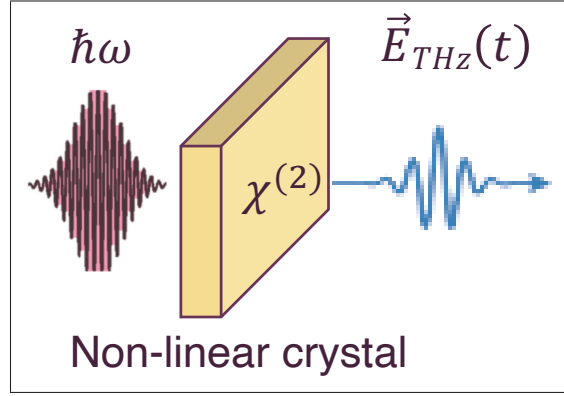


Figure 2.2 A principle of THz generation using the optical rectification in a non-centrosymmetric crystal

two frequency components, the electromagnetic field can be expressed as:

$$E(t) = E_1 e^{-i\omega_1 t} + E_2 e^{-i\omega_2 t} + c.c. \quad (2.2)$$

Hence, the second-order polarization can be rewritten as:

$$P_2(t) = \chi^{(2)} E(t)^2 \propto \dots + 2\chi^{(2)} [E_1 E_1^* + E_2 E_2^*], \quad (2.3)$$

This term is the frequency-independent polarization term and is proportional to the square of the electromagnetic wave amplitude, i.e., directly proportional to the intensity (Dexheimer (2017); Lee (2009)). According to Maxwell's equations, the time-varying polarization acts as a source term and gives rise to electromagnetic radiation expressed by (Guerboukha, Nallappan & Skorobogatiy (2018)):

$$\vec{E}_{THz} \propto \frac{\partial^2 P}{\partial t^2} \propto \chi^{(2)} \frac{\partial^2 I}{\partial t^2}, \quad (2.4)$$

where I is the intensity of the laser pulse.

Efficient THz generation can be achieved when the group velocity of the laser pulse and the phase velocity of the generated THz pulses are the same in the crystal. These conditions are fulfilled when the group refractive index of the crystal at the optical (n_{opt}^{gr}) is equal to the refractive index of the crystal at the THz frequencies (n_{THz}):

$$n_{opt}^{gr}(\omega_{opt}) = n_{THz}(\omega_{THz}), \quad (2.5)$$

where ω_{opt} is the laser excitation frequency and ω_{THz} is the THz frequency. Generally, the refractive indices are not exactly identical, resulting in a drop of efficiency for the OR process (Dexheimer (2017)). To ensure the greatest possible constructive overlap of interacting electromagnetic waves in a sample, it is extremely important to optimizing nonlinear effects, and involves matching the wave vectors \vec{k} , which is given by $\vec{k} = \frac{n\omega}{c}$. The phase-matching conditions and coherence length plays a critical role in efficient OR and given by:

$$\Delta k = k(\omega_{opt} + \omega_{THz}) - k(\omega_{opt}) - k(\omega_{THz}) = 0, \quad (2.6)$$

$$l_c(\omega_{THz}) = \frac{\pi c}{\omega_{THz} |n_{opt}^{gr}(\omega_{opt}) - n_{THz}(\omega_{THz})|}$$

For example, *ZnTe* is a well phased matched crystal for THz generation allowing a colinear configuration (Jepsen *et al.* (2011)). Even for *ZnTe*, the refractive indices are quite different $n_{THz}(1\ THz) = 3.25$ and $n_{opt}^{gr}(800\ nm) = 2.85$. This mismatching affects the coherence length ($0.55\ mm$) and does not allow for a significant THz signal produced from an optical pulse. Additionally, the strong phonon absorption limits the broadband response up to $5.3\ THz$. To overcome this limitation, a nonlinear crystal such as *GaP* should be chosen, providing the broadband response to $7 - 8\ THz$, which can be achieved only with a thin crystal (Jepsen *et al.* (2011)). The main factors that influenced on the efficiency of THz radiation using OR is:

- The 2d order nonlinear coefficient of a nonlinear crystal;
- The absorption of the crystal at THz frequency;

- The velocity phase-matching conditions between the THz and optical pulse:

$$v_{opt}^{gr} = v_{THz}^{ph} \quad (2.7)$$

2.1.3 Pulse-front-tilt

Compared to widely used *ZnTe* and *GaP*, some of the crystals have extremely high second-order nonlinear coefficients, which are generally related to the nonlinear susceptibility through the relationship $d_{ijk} = 1/2\chi_{ijk}^{(2)}$. For example, *LiNbO₃* (*LN*) has $d_{LN} \approx 198 \text{ pm/V}$ versus $d_{ZnTe} \approx 67 \text{ pm/V}$ (Ofori-Okai, Sivarajah, Huang & Nelson (2016)). However, OR cannot be efficient over long interaction length in *LN* crystal in a collinear configuration since there is a large difference in the group and refractive indexes at optical and THz waves. The electro-optic Cherenkov effect can generate THz radiation propagating along a cone, as shown in Figure 2.3a (Hebling, Yeh, Hoffmann, Bartal & Nelson (2008a)). The Cherenkov angle is determined by:

$$\theta_c = \cos^{-1} \frac{v_{THz}^{ph}}{v_{opt}^{gr}} \quad (2.8)$$

However, this way of propagation makes it very difficult to collect the THz radiation (Dexheimer (2017); Hebling *et al.* (2008a)).

Hebling *et al.* (2008a) proposed tilting the pulse front of the optical wave, which is done by creating an angle between the direction of propagation of the optical pump versus the direction of propagation of the THz pulse. Figure 2.3b sketches the velocity matching by pulse-front tilting. The tilt angle creates a projection of the pump pulse velocity, which is used for the generation of THz radiation along this tilted-pulse-front direction. Consequently, by choosing a proper tilting angle γ , the group velocity v_{opt}^{gr} of the pump pulse can match with the phase velocity v_{THz}^{ph} of THz radiation in materials with a large dielectric constant (Hebling, Almasi, Kozma & Kuhl (2002)):

$$v_{THz}^{ph} = v_{opt}^{gr} \cos \gamma \quad (2.9)$$

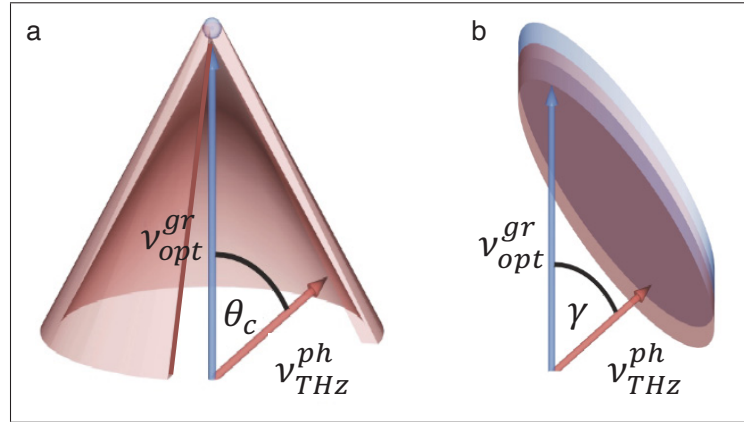


Figure 2.3 Two different schemes of THz excitation. For the usual Cherenkov geometry in a), the THz radiation is emitted as a cone characterized by the angle θ_c . Velocity matching is satisfied, but the exciting beam has to be very narrow. Velocity matching by pulse front tilting in b) creates a plane THz wave without any upper limit for the exciting beam cross-section

Taken from Hebling *et al.* (2008a)

The pulse-front-tilt enables the phase matching by tilting the angle (γ) inside of $LiNbO_3$ crystal to 63° . Otherwise, $LiNbO_3$ has an index of refraction at $1\ THz$ ($n_{LN,THz}^{ph} \approx 4.96$) twice as large as at optical wavelength of $800\ nm$ ($n_{LN,opt}^{gr} \approx 2.25$) (Hebling *et al.* (2008a); Hebling, Yeh, Hoffmann, Bartal & Nelson (2008b)). Due to the dispersion of light in the crystal, the tilt angle of the front of the pump pulse decreases, and it requires external tilt of the pump at $\gamma_0 = 78^\circ$ according to (Lee (2009)):

$$\tan \gamma = \frac{1}{n_{opt}^{gr}} \tan \gamma_0 \quad (2.10)$$

Figure 2.4 shows a setup for generation of THz radiation in LN using diffraction grating (Blanchard, Doi, Tanaka & Tanaka (2013)).

To tilt the front of the optical pump pulse, gratings or echelon mirrors combined with imaging systems have been extensively studied (Blanchard *et al.* (2013); Hebling *et al.* (2002)). However, diffraction gratings are dispersive and introduce pulse duration degradation everywhere except

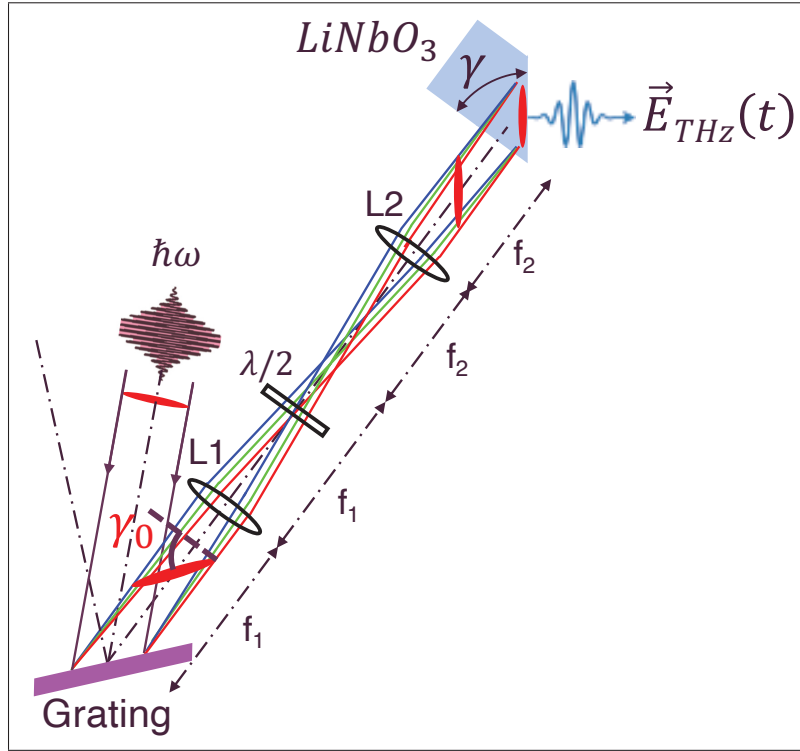


Figure 2.4 A scheme of the tilted pulse front setup
Taken from Blanchard *et al.* (2013)

on the image plane and imperfect imaging, limiting the efficiency of THz generation in *LN*. In opposition, the echelon mirror allows avoiding the pulse dispersion at the crystal position but has only one fixed configuration (Blanchard *et al.* (2013); Guerboukha *et al.* (2018)). Recently, an alternative scheme for tilting the optical pulse was shown using a digital micromirror device (DMD). The latter behaves like an echelon mirror but can modulate the incoming beam for introducing beam patterns (Murate, Roshtkhari, Ropagnol & Blanchard (2018)). This opens new possibilities for spatial modulation of THz beam directly by the pump pulse, which can be eventually used for near field single-pixel imaging and compressive sensing imaging (Stantchev, Sun, Hornett, Hobson, Gibson, Padgett & Hendry (2016); Zhao, Yiwen, Williams, Zhang & Boyd (2019)). The tilted-pulse-front excitation geometry in *LN* source is the most used and the most efficient technique for THz generation with kHz amplified system laser with the highest conversion efficiency to be $\sim 3.8\%$ until now (Huang, Granados, Huang, Hong, Zapata & Kärtner (2013)).

2.2 Detection of terahertz

To detect THz waves, two methods can be distinguished. One is used on energy detectors of THz waves, i.e., a pyroelectric detector, which estimates total energy through the entire THz spectrum. The other method is based on sampling, which enables the recording of the time-domain profile of the THz pulse electric field. Further, the spectrum is obtained by Fast Fourier Transform (FFT). This technique requires a pump-probe assembly. Figure 2.5 illustrates the principle of sampling. The probe, which is the ultra-short laser pulse (~ 10 fs), will "probe" the THz pulse (about 1 ps) by measuring at each instant the value of the THz electric field. To reconstruct the time-domain profile of the THz pulse, a motorized delay stage is used to provide a changing-time-delay between the two paths and map out the temporal waveforms of the THz pulses by the repeated samplings of the electric fields (Lee (2009); Withayachumnankul & Naftaly (2014)).

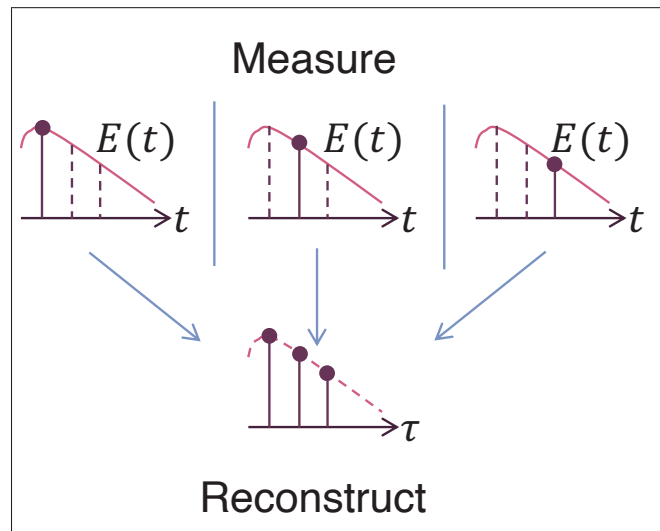


Figure 2.5 Reconstruction of temporal waveforms of THz pulses from repeated samplings

Usually, the detection of THz waves through sampling is achieved by photoconductive antennas or electro-optical sampling.

2.2.1 Photoconductive antennas

Figure 2.6a shows the THz detection principle using PCA, which can be performed with similar devices as used for THz generation. The main difference is that electrodes of a PCA are not biased with an external voltage source. Instead, the electrical field of THz radiation replaces the transient bias electric field. The femtosecond optical pulse is focused onto the semiconductor gap producing an impulse of carriers, as shown in Figure 2.6b.

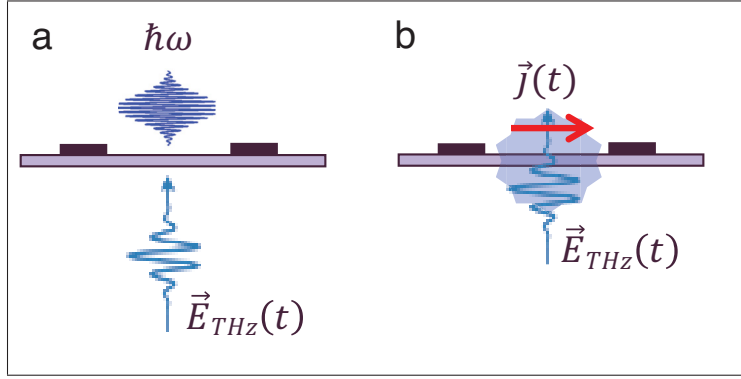


Figure 2.6 Illustration of THz detection using photoconductive antenna a) an optical and THz pulses arrive to the antenna; b) a transient photocurrent induced between the electrodes, which is proportional to the THz field amplitude

When the optical pulse is matched on time with a THz pulse simultaneously arrive onto the PCA, a transient photocurrent is induced between the electrodes. The density of the photocurrent is linearly proportional to the THz field amplitude focused on the gap (Kim (2009)). Indeed, the photocurrent is a convolution of the THz electric field, and the photoconductivity of the semiconductor crystal induced by the optical pulse:

$$J(\tau) \propto \int_{-\infty}^{+\infty} g(t - \tau) E_{THz}(t) dt, \quad (2.11)$$

where τ is the time delay between the THz and the optical pulses, $J(t)$ is the transient photocurrent and $g(t)$ is the probe pulse (Jepsen *et al.* (2011)). It must be noted that the surface conductivity limits the detectable bandwidth of the antennas and depends on the trapping and recombination

of the free carriers in the semiconductor and the shape of electrodes (Burford & El-Shenawee (2017)).

2.2.2 Electro-optic detection

The linear electro-optic (EO) effect is based on the Pockels effect, which describes the birefringence in EO crystal in response to an applied electric field (Jepsen *et al.* (2011); Lee (2009)). The THz pulse can be approximated as a pseudo-static field (~ 1 ps) compares with the optical pulse (~ 100 fs). When a THz and an optical pulses are incident on a medium with a second-order nonlinearity $\chi^{(2)}$, a polarization at optical frequency is generated:

$$P_i(\omega) = 2\epsilon_0 \sum_{jk} \chi_{ijk}^{(2)}(\omega = \omega + 0) E_j(\omega) E_k(0) \quad (2.12)$$

The induced polarization changes the refractive index of the detection crystal along a particular axis n_i according to the material's electro-optical tensor r_{ij} . When the optical pulse is overlapped in space and time with the THz field, the polarization-induced birefringence applies a slight retardance to the optical pulse components along the affected axis, creating ellipticity in the optical pulse polarization.

To resolve this polarization's change of the probe beam, it can be detected, as shown in Figure 2.7a. In the absence of THz field, the nonlinear material does not induce any change in the polarization of the optical pulse. Consequently, a linear polarized electric field of a probe beam is becoming circular after passing through a quarter-wave plate. A Wollaston prism then splits the beam into two with s - and p - polarizations and sends them into a differential detector, which records the intensity difference. As shown in the upper part of Figure 2.7b, the s - and p - components of the intensity are the same, since the light is circularly polarized, and the intensity difference is zero ($I_{total} = I_p - I_s = 0$) (Dexheimer (2017)). The appearance of the THz field induces a phase change that transforms the linear polarization of the probe beam into the elliptical polarization. The probe beam experiences the phase retardation $\Delta\phi$ due to the Pockels effect over a propagation distance (L) in the zincblende crystals and it is given by (Jepsen *et al.*

(2011)):

$$\Delta\phi = \frac{\omega L}{c} n_{opt}^3 r_{eff} E_{THz}, \quad (2.13)$$

where r_{eff} is the effective electro-optic coefficient. Hence, after passing a Wollaston prism, the difference between s - and p - polarizations at a differential detector is:

$$I_{total} = I_p - I_s = I\Delta\phi = I \frac{\omega L}{c} n_{opt}^3 r_{eff} E_{THz} \propto E_{THz} \quad (2.14)$$

Thus, the balanced photodetector measures the THz field amplitude.

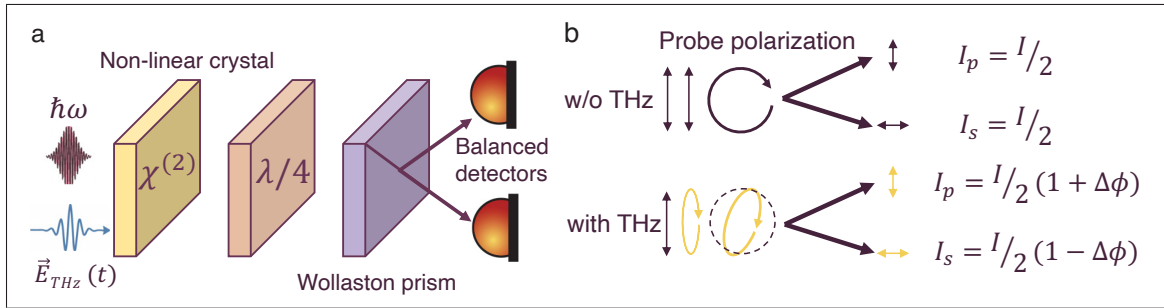


Figure 2.7 a) A sketch of electro-optical detection scheme using a non-centrosymmetric crystal;

b) Change of the intensity of the probe light in the absence and presence of THz light before and after the polarization optics

2.3 Terahertz time-domain spectroscopy

2.3.1 Principle of THz – TDS

The basis of THz spectroscopy measurements is the ability to probe a sample with a THz pulse and then extract full complex response functions from changes in the transmitted or reflected radiation and compare them to a reference. The most case of this technique is THz Time-Domain Spectroscopy (THz-TDS), which is based on direct time-domain sampling. Measurement characteristics, including the dynamic range, bandwidth, signal-to-noise ratio, and frequency resolution, are tied up into pulse shape (Withayachumnankul & Naftaly (2014)). A typical

THz-TDS setup is shown in Figure 2.8a. It starts from a femtosecond laser pulse train, which is usually split into two parts. One part is used for a THz generation (some methods have been discussed in Chapter 2.1). The other part goes through a delay stage to act as the sampling pulse (Lee (2009); Withayachumnankul & Naftaly (2014)). After being generated, the THz beam passes through a sample or a reference and is focused onto a detector. Some of the detection methods have been described in Chapter 2.2 (Lee (2009); Withayachumnankul & Naftaly (2014)).

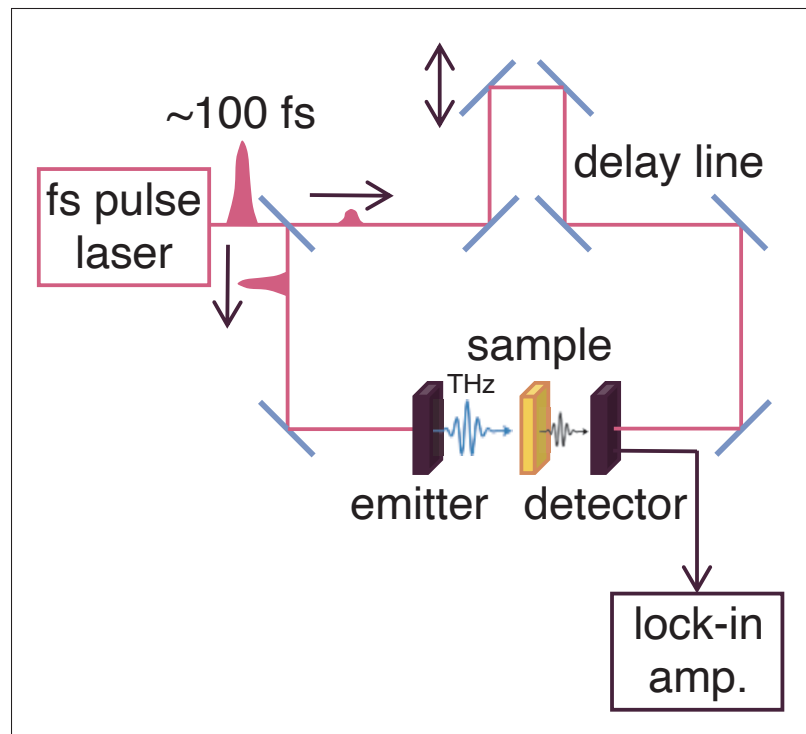


Figure 2.8 A sketch of a typical THz-TDS setup

Mechanical chopping is used on the THz beam in conjunction with a lock-in amplifier to optimize the detection sensitivity by using a lock in detection. The noisy incoming signal is multiplied by a sine wave at the reference frequency. After, it sends through a low-pass filter to extract the DC components. This component is the amplified signal of interest (Neu & Schmittenmaer (2018)). It allows measuring a small change of the THz field amplitude in the presence of considerable noise coming from air currents, environment changes, and laser power fluctuations.

2.3.2 Frequency resolution of THz-TDS

THz-TDS directly measures temporal waveforms of THz electric fields. To obtain frequency-domain information, a fast Fourier transform is applied (Blanchard & Tanaka (2016)). Figure 2.9 sketches the principle of FFT, including the main definition of the temporal and spectral parameters. The resolution of THz-TDS in frequency-domain is defined by the time window of the time-domain signal (t). From the definition of a discrete FFT, the frequency resolution is given by: $\Delta f = 1/t = 1/N\Delta t$, where N is the number of recorded points and Δt is step-size of the time-delay line. To improve the frequency resolution, the duration of the scan must be increased by recording more points. The maximum cut-off frequency is defined by the step-size: $f_{max} = 1/2\Delta t$.

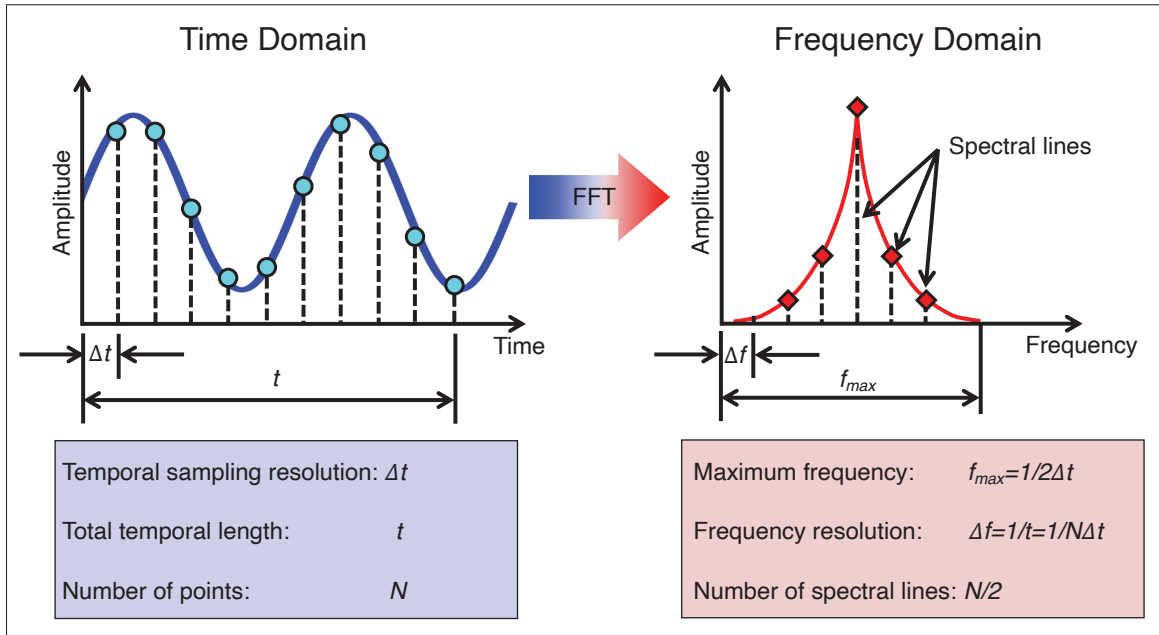


Figure 2.9 The principle of Fast Fourier Transform (FFT) to convert the time-domain signal to the frequency domain

2.3.3 Normalized transmission

To characterize transmission properties of materials, the time-domain trace of the transmitted waveforms through a sample material and a reference are recorded: $E_{sam}(t)$ and $E_{ref}(t)$ (Gueboukha *et al.* (2018)). Figure 2.10 sketches the time-domain traces of reference and sample signals, recorded after passing through a reference medium (blue) and a sample (red), respectively. Applying the FFT to THz pulses' temporal profile, we can extract the spectral amplitude and phase, which are illustrated in Figure 2.10. The ratio of the spectral amplitude gives a complex transmission coefficient and phase difference (Walther, Fischer, Ortner, Bitzer, Thoman & Helm (2010)):

$$\frac{E_{sam}(\omega)}{E_{ref}(\omega)} = T(\omega)e^{i\Delta\phi(\omega)}, \quad (2.15)$$

where $E_{sam}(\omega)$ and $E_{ref}(\omega)$ are Fourier-transforms of $E_{sam}(t)$ and $E_{ref}(t)$, respectively.

The major advantage of THz-TDS is the simultaneous measurement of the phase and the spectral amplitude, which allows the calculation of some complex-valued physical quantities of materials such as the absorption, the refractive index, and conductivity. For example, the frequency-dependend absorption and refractive index of free-standing samples with the thickness of d can be extracted without resorting to using the Kramers-Kronig relationship (Jepsen *et al.* (2011); Walther *et al.* (2010)):

$$\alpha(\omega) = -\frac{2}{d} \ln \left[T(\omega) \frac{(n(\omega) + 1)^2}{4n(\omega)} \right], \quad (2.16)$$

$$n(\omega) = 1 + \frac{c}{\omega d} \Delta\phi(\omega)$$

However, the scattering effect for inhomogeneous samples must be considered.

2.3.4 Dual-wavelength spectroscopy

THz-TDS requires two measurements of the reference and a sample. Unfortunately, these measurements are sensitive to environmental conditions, which could induce some unwanted variations between each subsequent measurement. For spectroscopic methods in the visible and

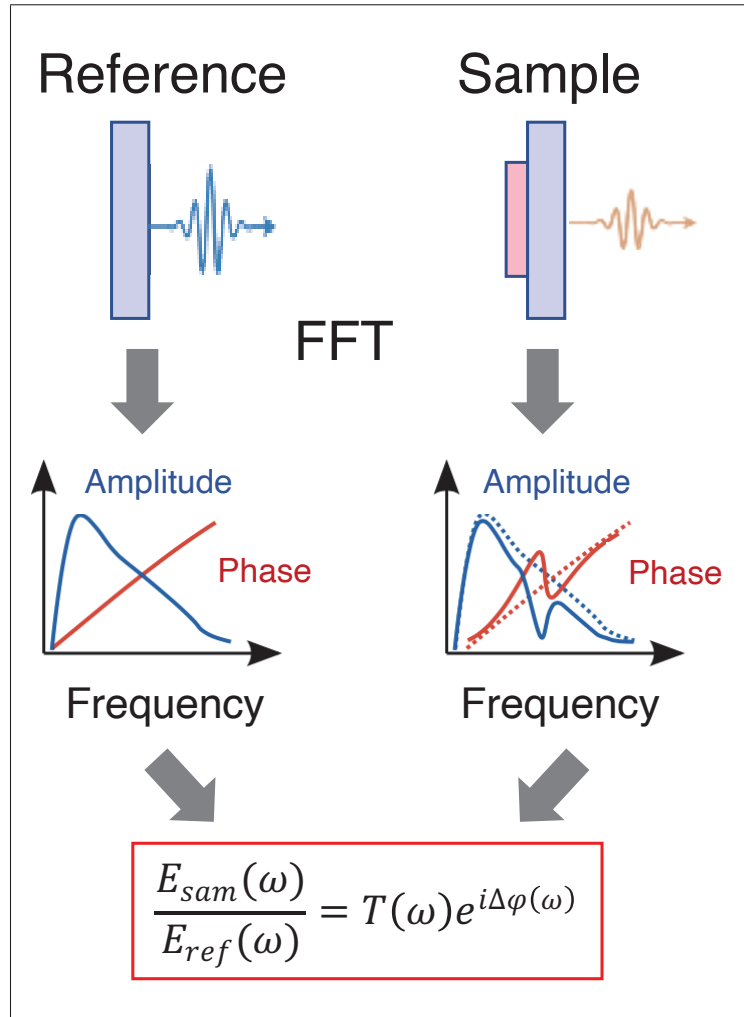


Figure 2.10 The sketch of the transmission measurement using THz-TDS, where $T(\omega)$ and $\Delta\phi(\omega)$ are the spectral information about a sample, i.e., normalized amplitude and phase difference, respectively

ultraviolet range, such unwanted fluctuations are often avoided by a dual-wavelength measurement approach (Walther *et al.* (2010)). The principle is simple: simultaneously measuring at two wavelengths (reference and signal) and recording the difference of values at these particular wavelengths. This technique is also called a balanced measurement. For example, this method is very well-known in the medical field for measurements of the concentration of drugs in tablets using UV radiation (Abdelwahab, El-Zeiny & Tohamy (2012); El Haddad, Canioni & Bousquet (2014); Owen (1996)). The idea of this method is to find an intensity dependence ratio between

the active element (signal) and the matrix (reference). After proper calibration, this value is directly proportional to the concentration of an element of interest.

In THz range, Murate & Kawase (2018) have introduced a real-time spectroscopic system using multiwavelength THz wave generation from injection-seeded THz parametric generator (is-TPG) shown in Figure 2.11a. The generation angle of detection beams are changed with each wavelength under phase matching condition. Consequently, it makes possible to detect each wavelength separately and to measure the sample in real-time. As an example, the experiment was carried on using saccharides. It has been shown that attenuation of the THz-waves matched the absorption spectra of the corresponding reagent. Figure 2.11b shows the achieved qualitative identification of the saccharides in real-time. This spectroscopic measurements can be implemented for non-destructive testing using extraction of the amplitude values at particular wavelengths. It can be adopted for the dual-wavelength spectroscopy as it was described above for UV range. However, this technique requires the high-power source and quite bulky set-up to be implemented at the industrial scale.

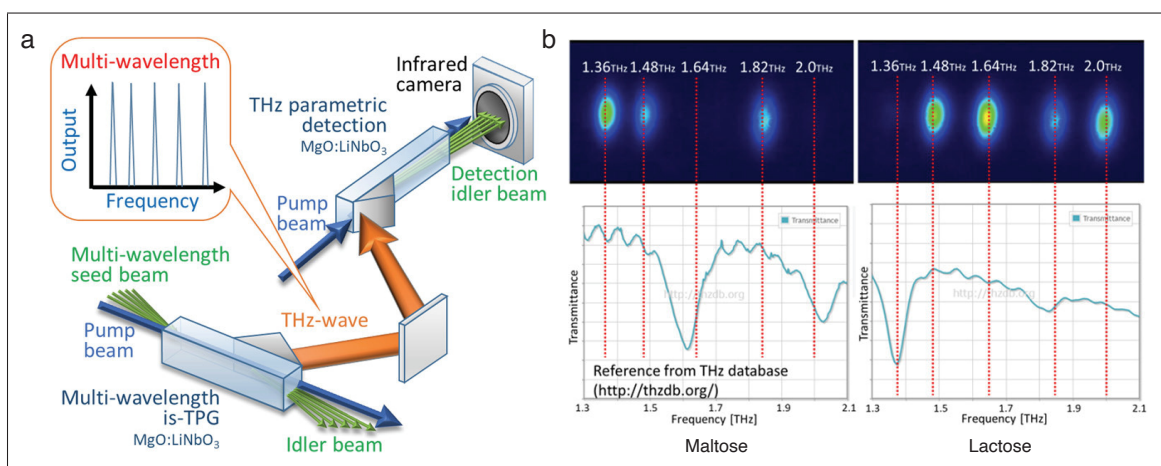


Figure 2.11 a) One-shot and real-time spectroscopic system using multi-wavelength THz generation and detection.

b) Results of real-time one-shot spectroscopy and reference spectra from the THz database (blue lines under each image). Maltose and Lactose were identified in real-time using five wavelength generation from the is-TPG

Taken from Murate & Kawase (2018)

Meanwhile, conventional photoconductive THz antennas emit THz radiation that covers a broad range of frequencies, e.g., typically from 100 GHz to 10 THz . Therefore, differentiating between two distinct signal frequencies, within the same pulse spectrum, is a straightforward manipulation. In the current thesis framework, we will introduce a self-normalized dual-wavelength THz spectroscopy (DWTS) analysis, which is optimized for rapid scan measurements since it only requires a single THz measurement to characterize the transmission properties of materials (Abdelwahab *et al.* (2012)).

2.4 Near-field terahertz imaging

Rayleigh's resolution limit claims that an electromagnetic wave cannot be confined to a space region with a width smaller than $\approx \lambda/2n$. Consequently, if a THz wave with a frequency of 1 THz is propagating away from a sample through space in the far-field, it cannot carry the information about spatial scales smaller than $\sim 150\mu\text{m}$, limiting the imaging resolution of a THz system (Lee (2009)). The relationship for the wave-vector is given by:

$$k^2 = k_x^2 + k_y^2 + k_z^2 = n^2 \left[\frac{\omega}{c} \right]^2 = \frac{4\pi^2 n^2}{\lambda^2} \quad (2.17)$$

It is clear mathematically that the resolution limit can be beaten if one of the components of k is imaginary since its square gives a negative value. It allows the other components to increase arbitrarily and provide subwavelength information. In this case, the waves no longer propagate in the direction of the imaginary component of k , for example, in the z - dimension. Hence, the electric field is described as:

$$E(z, t) = E_0 e^{-|k|z} e^{-i\omega t}, \quad (2.18)$$

where $k^2 = k_z^2 < 0$. This is the case of the evanescent waves, which exist only at a very short distance from the object and can provide near-field optical information due to overcoming the diffraction limit. During the last decade, many near-field THz techniques have been exploited to enable THz imaging at the subwavelength regime (Murate *et al.* (2018); Stantchev *et al.* (2016); Zhao *et al.* (2019)). Mostly, these imaging techniques are based on the mechanical scanning

of subwavelength-size apertures or tips. These require long measurement times and are not compatible with the real-time visualization of samples that move or involve dynamic interactions. Hence, it demands real-time imaging techniques. This work is focused on a real-time near-field imaging microscope, which has been developed by F. Blanchard *et al.* (Blanchard, Doi, Tanaka, Hirori, Tanaka, Kadoya & Tanaka (2011); Blanchard, Ooi, Tanaka, Doi & Tanaka (2012); Blanchard & Tanaka (2016); Blanchard *et al.* (2013); Blanchard, Chai, Tanaka, Arikawa, Ozaki, Morandotti & Tanaka (2018); Doi, Blanchard, Hirori & Tanaka (2010); Doi, Blanchard, Tanaka & Tanaka (2011); Guerboukha *et al.* (2018)). I used the near-field microscopy for three months-internship in Japan (Guiramand, Zhuldybina, Arikawa, Tanaka & Blanchard (2020)).

The near-field two-dimensional (2D) imaging microscope is a direct contact method, where a sample is placed at the surface of an electro-optical (EO) sensor. It allows capturing of the evanescent waves before diffraction occurs to map out the ultrafast two-dimensional amplitude and phase distributions of the electric field with high spatial resolution (Blanchard *et al.* (2013,1)). Figure 2.12 sketches the scheme of the near-field THz microscope. As shown in Figure 2.12a, the pulse-front tilt technique (described in Chapter 2.1.3) is applied using diffraction grating for the generation of high-power THz pulses. Ti: Sapphire laser with a wavelength of 780 nm with a pulse duration of 85 fs at 1 kHz repetition rate delivers 4 mJ pulses. As shown in Chapter 2.1.3, the cut angle of the *LN* is equal to 63° to match the velocity matching conditions inside the crystal. Further, to maximize the THz field's peak at the sample position, a system of off-axis mirrors expands, collimates, and focuses the THz beam.

Figure 2.12b and the inset zoom image on its left depicts the EO sensor used to perform 2D imaging using THz waves. It is made from a $20\text{ }\mu\text{m}$ *LiNbO₃* *x*-cut deposited on top of 0.5 mm thick glass. The sensor is covered with a high reflection and an antireflection coating for 780 nm on the top and bottom, respectively. The detection of THz pulses is based on free-space EOS, where the sample is placed on top of an *LN* crystal to access the near-field region. The THz waveform is reconstructed using an optical delay line. Figure 2.12b shows the path of the optical beam at 780 nm to probe THz waves. The probe beam creates an image of a mask on the top of the EO crystal surface (sample side) after passing through an achromatic lens (*L3*) with a

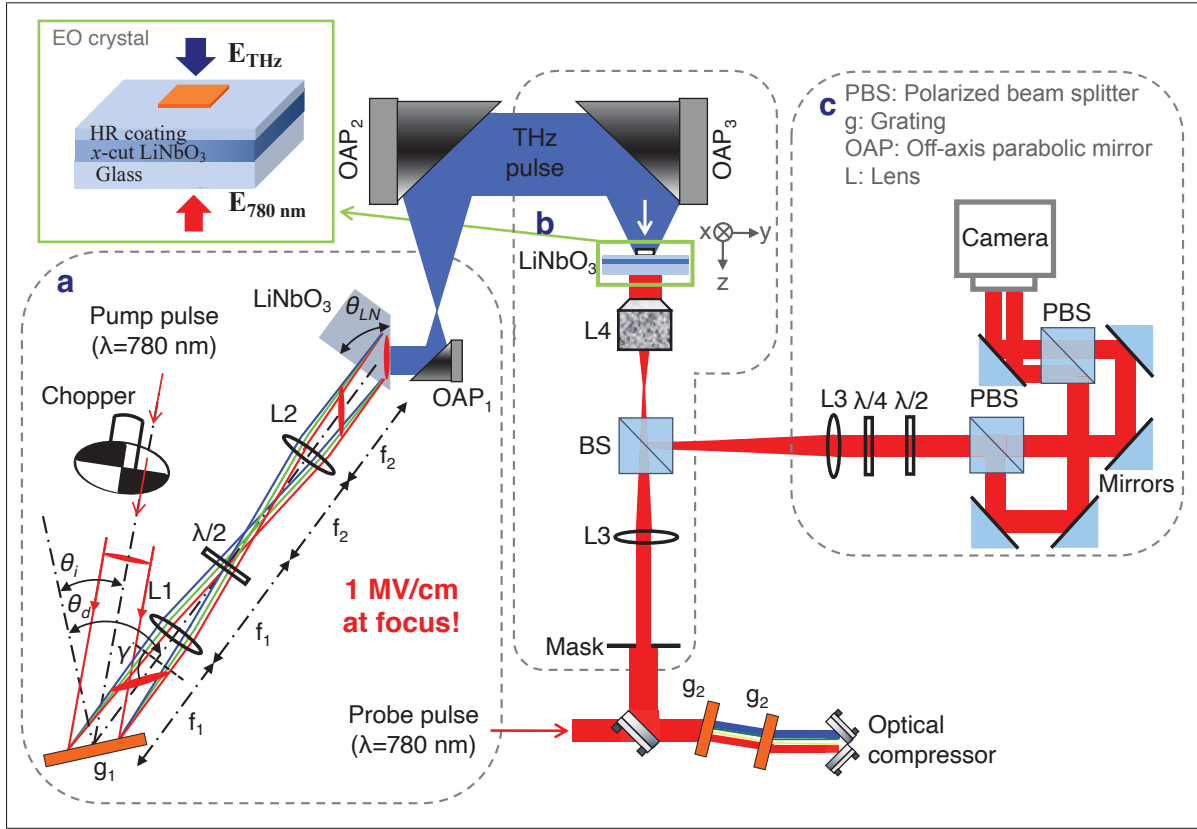


Figure 2.12 THz near-field microscope: a) Pulse-front-tilt excitation of THz waves;
b) Electro-optical sampling for the near-field detection of THz waves; the inset sketches the sensor made from a x -cut LiNbO_3 crystal deposited on top of the glass;
c) Split images for balanced imaging
Taken from Blanchard *et al.* (2011)

200 – mm focal length and a 10x objective lens ($L4$) with an 18 – mm focal length. The reflected images of the mask are returned to the lens $L4$ and passed through the second achromatic lens $L3$ with a 200 – mm focal length. A CCD camera with a non-polarizing beam splitter cube is placed 200 – mm after $L3$ to fulfill the imaging condition and records the reflected images. Figure 2.12c sketches the balanced detection technique used to improve the SNR and acquisition time. It includes the spatial separation of the two polarized images (s – and p –polarized) and a simultaneously captured image by a CMOS camera, model PCO Edge 5.0 with 1200×1200 pixels, yielding a maximum of 32 background-free images per second, with a size of 256×512

pixels and a resolution depth of 16 bits (limited by the camera specifications) (Blanchard *et al.* (2018)).

Blanchard *et al.* (2013) used the EO crystal made from x -cut LN crystal of $10\ \mu m$ mounted on a $0.5\text{ -- }mm$ -thick glass. Reducing the thickness of x -cut LN crystal to $1\ \mu m$ improves the spatial resolution up to $\lambda/150$ at $0.8\ THz$ (Blanchard *et al.* (2011,1,1); Doi *et al.* (2010,1)). Later, it was shown a SNR improvement via spectral filtering of the probe beam (Blanchard & Tanaka (2016)). Basically, installing short pass and long pass filters before and after the EO crystal, respectively, in the probe beam allows for photons selection. One part of them contributes to the EO signal, and the rest of the photons are blocked, reducing the input noise. By using spectral filtering and reducing the crystal thickness down to $1\ \mu m$, the SNR has been improved, and the detected bandwidth was extended. Hence, the spatial resolution up to $\lambda/600$ at $0.1\ THz$ has been demonstrated (Blanchard & Tanaka (2016)).

CHAPTER 3

METAMATERIALS

3.1 Metamaterials for THz applications

The properties of bulk materials are typically determined by the chemical elements and bonds inside them. Metamaterials (MMs) are artificial materials with physical properties that do not depend on their chemical composition intrinsic properties but instead on their specific internal structure. MMs are typically made from periodic arrays of resonator elements with subwavelength dimensions embedded in an insulating or dielectric medium (Cai & Shalaev (2010)). These artificial structures function act as atoms and molecules in traditional materials

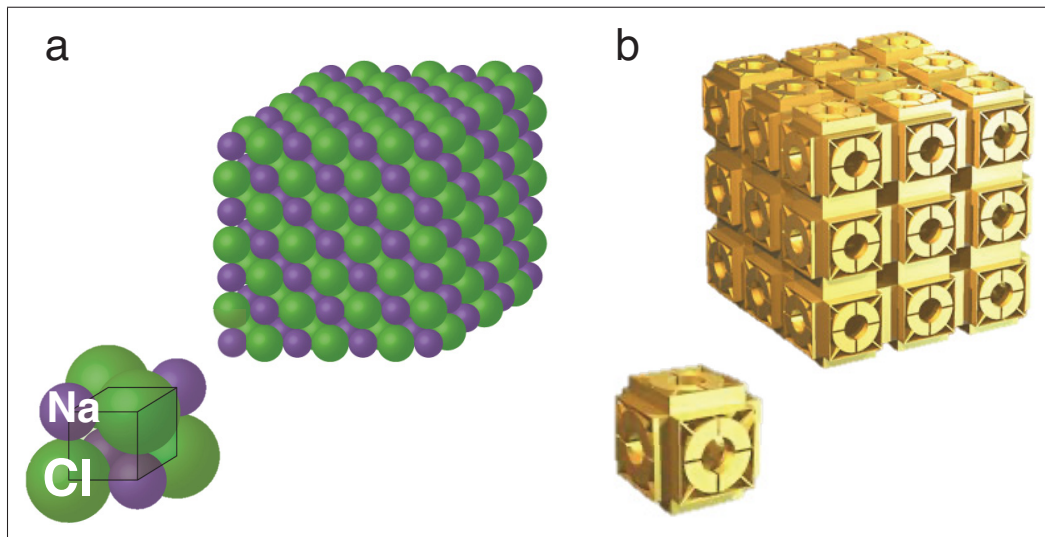


Figure 3.1 a) A faced-centered cubic lattice of $NaCl$ with an inset of a unit cell; b) Designed intra-connected negative-index metamaterials made with an inset of a unit cell made from four-gap split-ring resonators, which are attached by diagonal connectors to outer square frames

Adapted from Güney *et al.* (2010)

(Yue, Wen, Zhang, Gerardot, Wang, Zhang & Chen (2017)). Figure 3.1a illustrates a typical face-centered cubic lattice of sodium chloride ($NaCl$) with a unit cell made from two ions: Na^+ and Cl^- . Figure 3.1b shows a 3D intra-connected negative index metamaterial, where a unit

cell consists of six four-gap split-ring-resonators (SRR) connected diagonally to an outer square frame (Soukoulis & Wegener (2011)).

For many years the term 'metamaterials' used to refer to double-negative artificial materials. The theoretical prediction of simultaneous negative permittivity and permeability was introduced by Veselago (1968). Only thirty years later, D. Smith *et al.* have experimentally demonstrated Veselago's prediction using a combination of SRR to achieve negative permeability (Pendry, Holden, Robbins & Stewart (1999)) and straight wires to exhibit negative permittivity (Smith, Padilla, Vier, Nemat-Nasser & Schultz (2000)). It was the first experimental demonstration of the negative refractive index. Following with this publication, left-handed metamaterials have received tremendous attention in the last years due to their intriguing electromagnetic phenomena, which are not found in nature and are not observed in traditional materials, such as negative refractive index, artificial magnetism, and super focusing (Chen, Taylor & Yu (2016); Güney *et al.* (2010); İbili, Karaosmanoğlu & Ergül (2018)). Currently, the term metamaterials is broadly used to refer to any engineered discrete media for manipulating electromagnetic properties. However, the difficult micro- and nano-fabrication of the required three-dimensional structures is one the big challenge in MMs research Soukoulis & Wegener (2011). Meanwhile, planar metamaterials are easily fabricated using existing technologies such as lithography and nanoprinting methods. It made many metamaterial researchers to focus on single-layer or multi-layer stacks of planar structures. They are considered as the two-dimensional (2D) equivalent of bulk metamaterials and called metasurfaces Chen *et al.* (2016). The main advantage of metasurfaces is that the unit cell can be created to resonate at various frequencies, leading to unique electromagnetic responses (Chen *et al.* (2016)). This is different from the electromagnetic responses of natural material, where properties are limited since they are obtained from simple atoms and molecules in a unit cell. By adjusting the dimensions, metasurfaces applications' spectral area can be extended over a broad range of the electromagnetic spectrum such as the THz, infrared and optical spectra (Singh *et al.* (2008)).

Metasurfaces in the terahertz regime provide a unique opportunity to develop next-generation terahertz components to realize applications ranging from spectroscopic identification of haz-

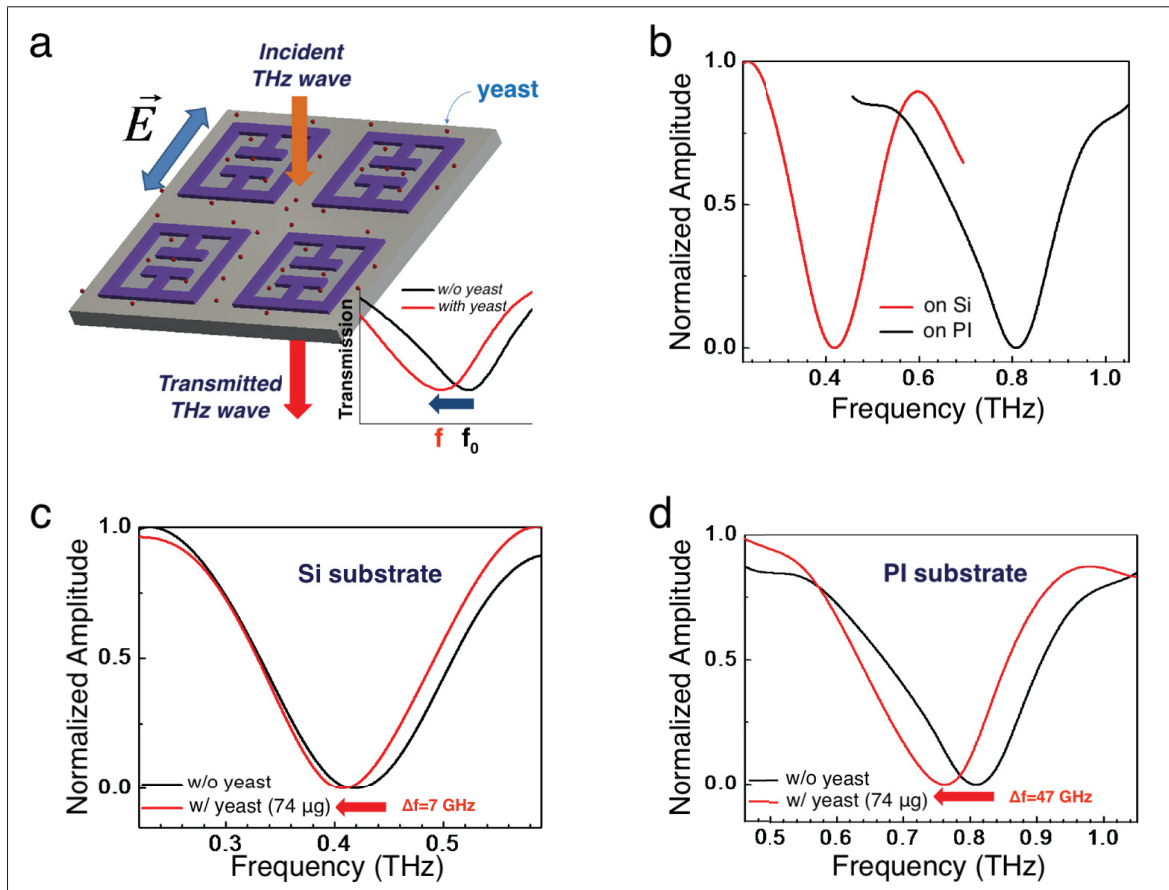


Figure 3.2 a) Schematic of THz metasurface sensing of yeast.
b) Normalized transmission amplitudes of the metasurface samples on the silicon wafer and the PI film.

Comparisons of normalized transmission amplitudes of the metasurface:

c) on the silicon wafer and d) on the PI film

Taken from Tenggara *et al.* (2017)

ardous materials to non-invasive imaging (Chen *et al.* (2016); İbili *et al.* (2018); Singh *et al.* (2008); Tao, Bingham, Pilon, Fan, Strikwerda, Shrekenhamer, Padilla, Zhang & Averitt (2010a); Yue *et al.* (2017)). Hence, MMs are a promising approach to manipulate terahertz waves (Chen, O'Hara, Azad & Taylor (2011); Tao *et al.* (2010a)). THz metasurfaces have been traditionally fabricated by standard conventional techniques such as electron-beam lithography, interference lithography, and others (Cai & Shalaev (2010); Nasr, Richard, Skirlo, Heimbeck, Joannopoulos, Soljacic, Everitt & Domash (2017); Soukoulis & Wegener (2011)). The traditional fabrication methods consist of multiple steps, producing huge waste of materials, and requiring cleanroom

facilities. However, THz waves have submillimeter/millimeter wavelength, consequently THz metasurfaces have relatively large dimensions, often hundreds of microns. During the last decade, the development of printed electronics (which includes direct-write processes) allowed for rapid fabrication of THz metasurfaces devices using inkjet (Lee, Sung & Lim (2016); Lee, Gee, Kang & Kee (2010); Sushko, Pigeon, Donnan, Kreouzis, Parini & Dubrovka (2017); Walther, Ortner, Meier, Löffelmann, Smith & Korvink (2009)), digital aerosol jet (Jahn, Eckstein, Schneider, Born, Hernandez-Sosa, Balzer, Al-Naib, Lemmer & Koch (2018); Oakley & Chahal (2018)), laser printing (Kim, Melinger, Khachatryan, Charipar, Auyeung & Piqué (2010)), or electro-hydrodynamic jet (Paulsen & Nahata (2015); Tenggara *et al.* (2017); Yudistira, Tenggara, Nguyen, Kim, Prasetyo, Choi, Choi & Byun (2013)). The printing of metasurfaces is advantageous in terms of both productivity and large-area output (Hokari, Kurihara, Takada & Hiroshima (2018)). It opens the door for rapid and easy fabrication of functional THz devices such as frequency selective surface filters (Jahn *et al.* (2018); Lee *et al.* (2010); Paulsen & Nahata (2015); Sushko *et al.* (2017)), polarizers (Kaltenecker, Fischer, Bollgruen, Korvink & Walther (2012); Lee *et al.* (2010); Oakley & Chahal (2018)) or split-ring resonator absorbers consisting of array of square rings (Lee *et al.* (2016); Skirlo, Richard, Nasr, Heimbeck, Joannopoulos, Soljacic, Everitt & Domash (2016)) or plasmonic structures for THz waves (Gupta, Pandey, Guruswamy & Nahata (2014)). Such devices are manufacturable in large amounts for applications in security or structural monitoring (Chanana, Paulsen, Guruswamy & Nahata (2016); Nasr *et al.* (2017); Skirlo *et al.* (2016)). In another field, THz molecular metasurface-based sensors are known to be highly sensitive devices due to their distinctive characteristics and molecular signature in this frequency range (Chen *et al.* (2012a); Taleb, Al-Naib & Koch (2020)). Their sensitivity can be improved by using substrates with a lower refractive index such as polyimide (PI) or polyethylene terephthalate (PET) films instead of rigid semiconductors (Nasr *et al.* (2017); Tenggara *et al.* (2017)). As described in Chapter 1, PE can use a wide choice of flexible substrates (Walther *et al.* (2009)), which are thin and have effective dielectric constant close to the dielectric constant of air (Hokari *et al.* (2018); Nasr *et al.* (2017); Tenggara *et al.* (2017)). For example, Tenggara *et al.* (2017) have printed MMs on PI and silicon substrates for accurate detection of microorganisms. Figure 3.2a shows a sketch of the designed experiment.

The resonance frequency of metasurfaces depends on the dielectric constant of the substrate. As shown in Figure 3.2b, the higher refractive index of *Si* gives a resonance at lower frequency ($\sim 0.4THz$) compared with *PI* substrate ($\sim 0.8THz$). At the presence of the micro-organism, it is clear that the plastic substrate has provided six times higher sensitivity than the one printed on the silicon wafer (Figure 3.2c vs. Figure 3.2d).

The electromagnetic (EM) response of 2D-MMs remarkably depends on the material properties, the lattice shape and the unit cell's dimensions comprising it (Chen *et al.* (2016)). Generally, changing the geometrical specifications or intrinsic properties presents a way to tune and determine whether the EM wave is transmitted, reflected, or absorbed. 2D-metamaterials can also control the phase and amplitude of the light beam and modulate the incoming radiation spatially. This chapter provides information on how the EM response of 2D-MMs is affected by varying geometrical parameters and conductivity, using particular examples of structures utilized in this thesis's framework.

3.1.1 Electromagnetic waves propagation in a medium

All electromagnetic phenomena can be described classically using Maxwell's equations. These fundamental equations describe electromagnetic fields and how they evolve over time. In a region of space with no free charges or currents, these equations take the following form:

$$\begin{aligned}
 \nabla \cdot \vec{D} &= 0 \\
 \nabla \cdot \vec{B} &= 0 \\
 \nabla \times \vec{E} &= -\frac{\partial}{\partial t} \vec{B} \\
 \nabla \times \vec{H} &= \frac{\partial}{\partial t} \vec{D},
 \end{aligned} \tag{3.1}$$

where \vec{E} [V/m] and \vec{H} [A/m] are the electric and the magnetic field intensities, respectively. In materials, the two other related parameters, \vec{D} [C/m²] and \vec{B} [T], are the electric flux density

and the magnetic flux density, respectively, where

$$\begin{aligned}\vec{D} &= \epsilon \vec{E}, \quad \epsilon = \epsilon_r \epsilon_0 \\ \vec{B} &= \mu \vec{H}, \quad \mu = \mu_r \mu_0\end{aligned}\tag{3.2}$$

The fundamental constants $\epsilon_0 = 8.854 \times 10^{-12} [F/m]$ and $\mu_0 = 4\pi \times 10^{-7} [H/m]$ are the electric permittivity of free space and free's space magnetic permeability, respectively. It is convenient to define ϵ_r , the relative electrical permittivity or dielectric constant, and the material's relative magnetic permeability, μ_r . Since the research presented within this dissertation concerns non-magnetic materials, we will only consider cases where $\mu_r = 1$ and $\vec{B} = \mu_0 \vec{H}$. Under an applied electric field \vec{E} , the electrons within a material will respond according to the equation, inducing an electric polarization density $\vec{P} [C/m^2]$. For a linear material:

$$\vec{D} = \epsilon_r \epsilon_0 \vec{E} = \epsilon_0 (1 + \chi_e) \vec{E} = \epsilon_0 \vec{E} + \vec{P}\tag{3.3}$$

where χ_e is the electric susceptibility of the material. Hence, the polarization density is given by:

$$\vec{P} = \epsilon_0 \chi_e \vec{E}\tag{3.4}$$

These quantities describe the classical electromagnetic behavior of any given linear material. Assuming a source-free, linear, isotropic, and homogeneous medium, Maxwell's curl equations for time varied electric and magnetic field can be written as:

$$\begin{aligned}\nabla \times \vec{E} &= -i\omega \mu \vec{H} \\ \nabla \times \vec{H} &= i\omega \epsilon \vec{E},\end{aligned}\tag{3.5}$$

where ω is the angular frequency. One can decouple the electric and magnetic field by taking the curl of equations 3.5:

$$\begin{aligned}\nabla^2 \vec{E} + \omega^2 \mu \epsilon \vec{E} &= 0 \\ \nabla^2 \vec{H} + \omega^2 \mu \epsilon \vec{H} &= 0\end{aligned}\tag{3.6}$$

which yield the wave equations for a wave propagating along $+z$ direction with only $x(y)$ component of electric (magnetic) field:

$$\begin{aligned}\frac{d^2 E_x}{dz^2} + k^2 E_x &= 0, \\ \frac{d^2 H_y}{dz^2} + k^2 H_y &= 0\end{aligned}\tag{3.7}$$

where $k = \omega\sqrt{\mu\epsilon} [m^{-1}]$ is the wave vector, which indicates the direction of propagation in the medium (k_0 is the wave vector in the free space, which expresses as : $k_0 = \omega\sqrt{\mu_0\epsilon_0} [m^{-1}]$). Note that k may be complex, where real and imaginary parts can be denoted:

$$k = \beta - i\alpha\tag{3.8}$$

Hence, the solution of the wave equation for the defined propagation is given by:

$$E_x = E_0 e^{-ikz} = E_0 e^{-i\beta z} e^{-\alpha z}\tag{3.9}$$

i.e., the amplitude declines exponentially in the direction of propagation. The solution for the magnetic field can be written as:

$$H_y = \frac{E_0}{\eta} e^{-ikz}\tag{3.10}$$

where $\eta = \sqrt{\mu/\epsilon} [\Omega]$ is defined as the intrinsic impedance of the medium. The free-space impedance is equal to $\eta_0 = \sqrt{\mu_0\epsilon_0} = 120\pi [\Omega]$. Hence, the impedance of the medium can be given as: $\eta = \eta_0 \sqrt{\mu_r/\epsilon_r}$. Let us define the index of refraction as

$$n = \sqrt{\mu_r \epsilon_r},\tag{3.11}$$

which parametrizes the optical density of the medium. It shows that the denser the medium is, the lower the velocity of propagation (speed of light in the material) becomes.

3.1.2 Transmission line approach

Transmission lines are widely employed to guide signals in the radiofrequency regime when the wavelength is comparable with the circuit's size. The wave properties of the electric field have to be considered. A transmission line has impedance ($Z' [\Omega]$) and admittance ($Y' [S]$) per unit length and can be modeled as lumped-element circuits with distributed elements, shown in Figure 3.3a.

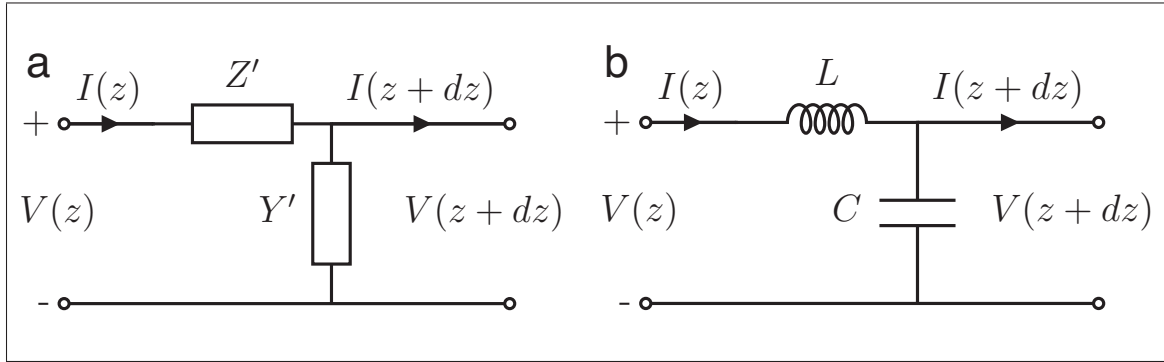


Figure 3.3 The circuit model of a) a section of the transmission line with a series impedance and shunt admittance.

b) A section of transmission line with a series inductance and shunt capacitance

By applying Kirchhoff's voltage ($V [V]$) and current ($I [A]$) law to the outer loop and the central node, respectively, we obtain (Solymar & Shamoni (2009)):

$$\begin{aligned} V(z + dz) - V(z) &= -Z' I(z) dz, \\ I(z + dz) - I(z) &= -Y' V(z + dz) dz \end{aligned} \quad (3.12)$$

Hence, the relationship between the line voltage and current can be derived as:

$$\begin{aligned} \frac{dV(z)}{dz} &= -Z' I(z), \\ \frac{dI(z)}{dz} &= -Y' V(z) \end{aligned} \quad (3.13)$$

Differentiating either of the above differential equations and rearranging them yields:

$$\begin{aligned}\frac{d^2 V(z)}{dz^2} - Y' Z' V(z) &= 0, \\ \frac{d^2 I(z)}{dz^2} - Y' Z' I(z) &= 0\end{aligned}\tag{3.14}$$

Comparing the above equations with the wave equations 3.7, we find the following analogies:

$$E_x \longleftrightarrow V, H_y \longleftrightarrow I, ik \longleftrightarrow \sqrt{Y' Z'}, \eta \longleftrightarrow \sqrt{Z' / Y'},$$

Consequently, the transmission line model results can be directly applied to solve electromagnetic wave propagation problems. The equivalent impedance and admittance per unit length for the effective permeability and permittivity can be expressed such as:

$$\begin{aligned}Z' &= i\omega\mu_r, \\ Y' &= i\omega\epsilon_r\end{aligned}\tag{3.15}$$

Now, let us consider the circuit shown in Figure 3.3b with a series of inductance ($L [H]$) and a shunt capacitance ($C [F]$). We have

$$\begin{aligned}i\omega L' &= i\omega\mu_r \rightarrow L' = \mu_r, \\ i\omega C' &= i\omega\epsilon_r \rightarrow C' = \epsilon_r\end{aligned}\tag{3.16}$$

We came up with the analogy between the material parameters of a medium and the circuit elements of a transmission line, explaining the plane wave's characteristics in terms of capacitance and inductance.

The simplest case of an LC-circuit is a split-ring resonator (SRR), which is the pioneer of metamaterials research and has been used to achieve a strong magnetic response. Figure 3.4 sketches an SRR and its equivalent circuit. Generally, the self-inductance is given by: $L = N\mu A/t_m$, where N is the number of turns, $A [m^2]$ is a cross-section area, and $t_m [m]$ is a thickness. To describe the self-inductance of an SRR, let us the first order of approximation for

the SRR as a closed square with the length l [m], the number of turns equal to 1 ($N = 1$) and the permeability of the surrounded material is μ . Hence, the inductance is expressed as:

$$L \approx \frac{\mu l^2}{t_m} \quad (3.17)$$

The general definition for the capacitance is $C = \epsilon A/g$, where A is the area of the plates, g [m] and ϵ is the distance and permittivity of the material in between them, respectively. Extending the same analogy onto SRR, the capacitance can be described as:

$$C = \frac{\epsilon w t_m}{g} \quad (3.18)$$

where w is the width and t_m is the thickness of the SRR.

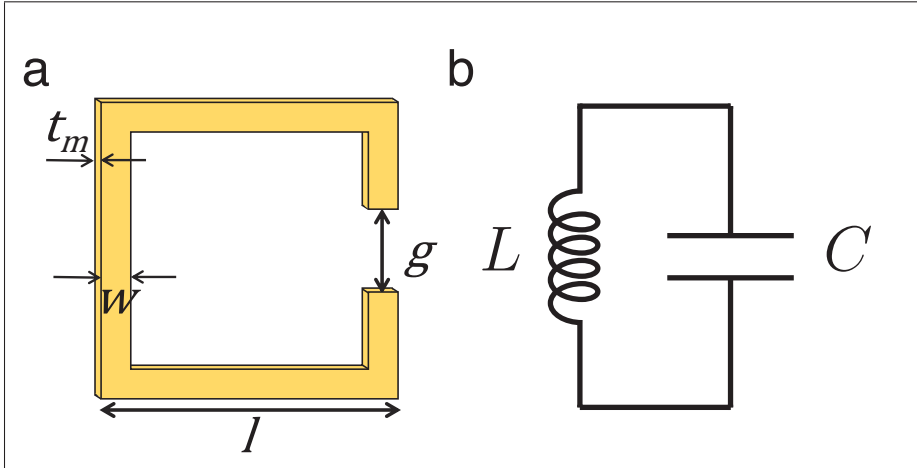


Figure 3.4 a) Split-ring resonator (SRR);
b) Equivalent circuit of SRR

Hence, the single SRR is essentially an LC resonator with the resonance frequency ω_0 expressed by L (Eq. 3.17) and C (Eq. 3.18):

$$\omega_0 \approx \frac{1}{\sqrt{LC}} = \sqrt{\frac{g}{\epsilon \mu w l^2}} = \frac{1}{n} \sqrt{\frac{g}{w l^2}}, \quad (3.19)$$

where n is defined from the equation 3.11. This approximation considers the $\lambda/10$ size condition for the 2D-MMs to avoid diffraction and interference effects Cai & Shalaev (2010).

Let us denote the size of unit cell (also known as the lattice constant) of the single SRR as a [m], which is served as a scaling factor. All of the geometrical parameters of SRR are varied proportionally to a . Consequently, the resonance frequency is given by:

$$\omega_0 \propto \frac{1}{a} \quad (3.20)$$

This simple approximation expresses the scaling capability of SRR, where the resonance frequency is inversely proportional to the size of SRR. The LC model can be improved by upgrading to an RLC model or including mutual inductance for the periodic structures. The LC mode occurs at the lowest frequency and, as a result, is the most deeply subwavelength where effective medium approaches are the most valid.

3.1.3 Effect of geometrical parameters

Frequency selective surfaces (FSS) in the shape of metallic wire meshes have been studied since the middle of the last century due to their bandpass behavior (Bravo-Abad, Martín-Moreno, García-Vidal, Hendry & Rivas (2007)). Figure 3.5 sketches an FSS with a corresponding equivalent circuit. Applying the LC-model proposed above, the transmission behavior can be explained as a parallel connection of an inductor and a capacitor and is described by the admittance:

$$Y = \frac{1}{i\omega L} + i\omega C = \frac{1 - \omega^2 LC}{i\omega L} \quad (3.21)$$

which approaches 0 at the resonance frequency $\omega_0 \approx \frac{1}{\sqrt{LC}}$. It produces an open circuit, and all of the energy is transmitted. Considering the mesh dimensions, the maximum transmission appears at a frequency near the period of the array.

Hence, the period of the FSS determines its interaction with the incident light. FSSs attracted tremendous attention after discovering the effect of extraordinary transmission (EOT) of optical

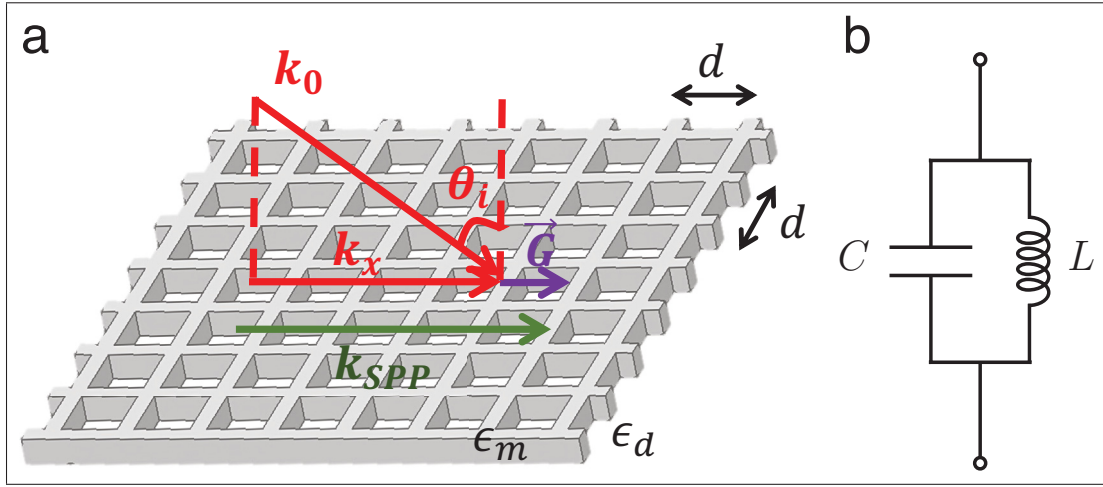


Figure 3.5 a) Frequency selective surface made from metallic wires mesh with a period (lattice constant) d . \vec{k}_0 is the incident wave vector; \vec{k}_x is the transverse component of the incident wave vector and \vec{G} corresponds to the momentum needed to couple to the SPP mode.

b) Lumped element model for a unit cell

light through optically thick metallic hole arrays with subwavelength diameters in 1998 by (Genet & Ebbesen (2007)). The maximum transmission occurs at wavelengths just to the red-shift of the array period. The amount of transmitted light is remarkably different from that predicted by classical Bethe aperture theory (Degiron, Lezec, Yamamoto & Ebbesen (2004)), which states that the transmission through a single aperture in an infinitely thin and perfectly conducting metal screen decays as $(r/\lambda)^4$, where $r \ll \lambda$ is the radius of the hole, as shown in Figure 3.6a. This phenomena is explained by a surface plasmon polaritons (SPP), which are electromagnetic waves confined at a metallic-dielectric surface interface due to an EM field interaction with the free electron oscillations in the metal. When the field illuminates the metallic holes array, it excites localized surface plasmons at single isolated metallic nano-holes. These plasmons travel to other holes and can interfere constructively with other plasmons and with the illuminated field directly transmitted through the holes. This resonance phenomenon enhances the field at each of the holes, where it is converted back into a propagating light wave. This combination of the surface waves and the sub-wavelength apertures provides the enhanced

transmission phenomenon. Figure 3.6b shows an example of the EOT in the triangular hole array in the visible range (Bethe (1944)).

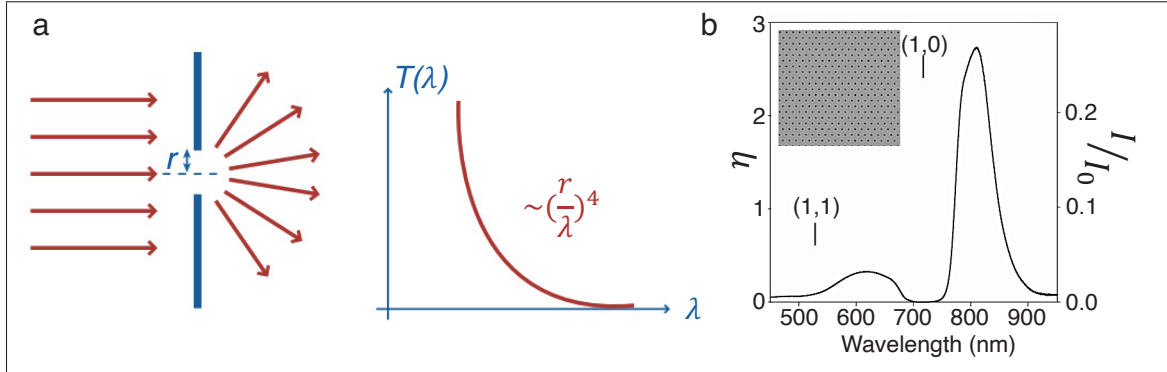


Figure 3.6 a) Diffraction and typical transmission spectrum ($T(\lambda)$) of visible light through a subwavelength hole with a radii of r in an infinitely thin perfect metal film explained by Bethe theory

Taken from Bethe (1944)

b) The triangular hole array was milled in a 225 – nm-thick *Au* film on a glass substrate with an index-matching liquid on the air side (hole diameter 170 nm, period 520 nm). The transmission spectrum is measured at normal incidence using collimated white light. The inset shows the image of the actual array. I/I_0 is the absolute transmission of the array and η is the same transmission but normalized to the area occupied by the holes

Taken from Genet & Ebbesen (2007)

To describe the nature of SPP, let us consider a metal-dielectric interface. We denote the frequency-dependent dielectric function of the dielectric and the metal by $\epsilon_d(\omega)$ and $\epsilon_m(\omega) = \epsilon_{mr} + i\epsilon_{mi}$, correspondingly, where ϵ_{mr} and ϵ_{mi} are the real and imaginary parts of the metal-dielectric function. The wave-vector of the SPP is defined as $k_{SPP}(\omega) = (\omega/c)\sqrt{\frac{\epsilon_d(\omega)\epsilon_m(\omega)}{\epsilon_d(\omega)+\epsilon_m(\omega)}}$. The wavenumber $k_{SPP}(\omega)$ is always larger than the freely propagating light of the same frequency. The mismatch in wave vector between the component of the wave vector of the incident light parallel to the surface momentum $k(\omega) = (\omega/c)\sin\theta_i$ (where θ_i is an incident angle relative to the normal) and k_{SPP} is usually overcome by patterning the metal surface with prisms or gratings of grooves or holes (as shown in Figure 3.5) with the lattice constant d . Considering the periodic hole arrays, the wave-vector of a square lattice, $G = |G_x| = |G_y| = 2\pi/d$, leads to momentum conservation of: $k_{SPP}(\omega) = (\omega/c)\sqrt{\epsilon_d(\omega)}\sin\theta_i \pm mG_x \pm nG_y$, where m and n are integer numbers. Under normal incidence, the resonant frequency for a squared patterned array

of metallic subwavelength holes is given by:

$$\lambda_{sp} = \frac{d}{\sqrt{m^2 + n^2}} \sqrt{\frac{\epsilon_d(\omega)\epsilon_m(\omega)}{\epsilon_d(\omega) + \epsilon_m(\omega)}}. \quad (3.22)$$

The scalability of MMs allows bringing this effect to the THz region. However, the ratio between the real and imaginary part of the dielectric constant $\epsilon_{mr}/\epsilon_{mi} \ll 1$ for metal is small, and the metal behaves as a perfect conductor. Hence, SPPs are not presented at the metal-dielectric interface, and it requires plasmonic metamaterials, which are called ‘spoof SPP structures’. Periodic corrugated metallic surfaces with 2D holes or grooves have been used to change the effective dielectric constant for mimicking SPPs-like generation (Genet & Ebbesen (2007)).

The metallic hole arrays have attracted much attention as FSS. To excite SPPs, an incident wavelength must be approximately equal to one of the main dimensions of the unit cell and the lattice of the structure (He *et al.* (2009)). Figure 3.7a that the array’s periodicity determines the position of the resonance frequency of the transmitted EM wave. The metal hole length and width (a_x and a_y) are constant at $80 \mu m$, the lattice periods (d_x and d_y) are $140 \mu m$, $180 \mu m$, $200 \mu m$, $220 \mu m$, $240 \mu m$ and $280 \mu m$. For example, the resonance position (transmission minimum) shifts from $2.2 THz$ for $140 \mu m$ up to $1.1 THz$ for $280 \mu m$. The geometry of a subwavelength hole plays a vital role in determining the strength and the corresponding resonance shape (De Abajo, Gómez-Medina & Sáenz (2005)). The interaction of the incident EM wave with a metallic hole arrays reveals a Fano-type resonant transmission, explained by the existence of the resonant and non-resonant transmission channels (Azad, O’Hara, Singh, Chen & Taylor (2012)). The non-resonant contribution is coming from each hole as if they were in an array with no EM interaction between them. It is represented by the transmission maximum in the Fano picture, followed by a transmission minimum. The last contribution is the resonance input, which appears from the EM coupling between holes in a 2D array. The interference between the resonant and the non-resonant channels gives the Fano-type interaction (Bravo-Abad *et al.* (2007); De Abajo (2007); Edmunds, Hibbins, Sambles & Youngs (2010)). Figure 3.7b shows the results for a constant lattice period of $200 \mu m$ and the hole length of

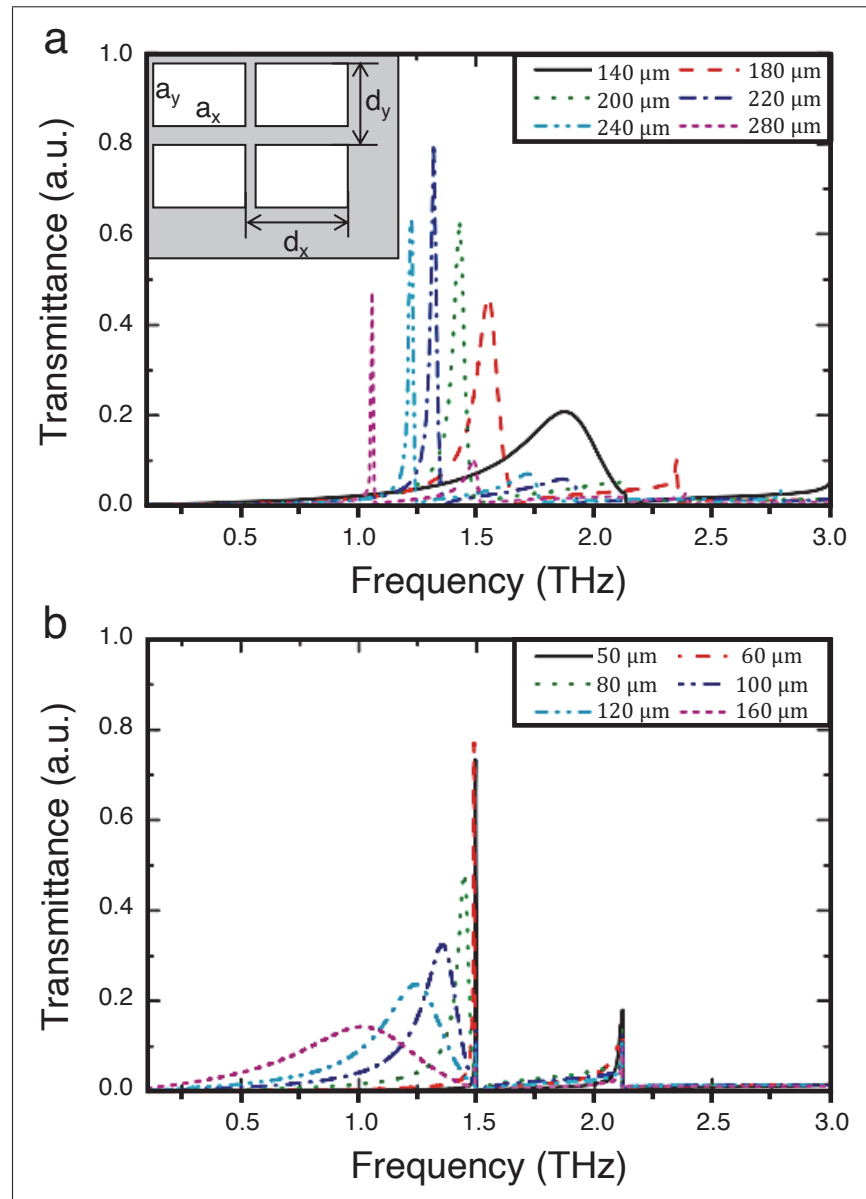


Figure 3.7 Transmission spectra of THz waves through metal rectangular hole arrays versus frequency. The definitions of holes array are shown in the inset of a).
a) The metal hole length and width (a_x and a_y) are both 80 μm , the lattice periods (d_x and d_y) are equaled each other and varied simultaneously.
b) The lattice period of 200 μm and the hole length of 100 μm are constant. The metal hole widths are varied
Taken from He *et al.* (2009)

100 μm , while the metal hole widths are varied 50 μm , 60 μm , 80 μm , 100 μm , 120 μm , 160 μm . In this case, the diffraction due to scattering from small holes induces narrow resonances close to the diffraction edge. In contrast, the diffraction from larger holes induces a broadening of the resonance and a shift to lower frequencies. The resonant transmission characteristics in the THz region have been explored in a range of element geometries for metal holes, including circular, square, or rectangular (He *et al.* (2009)). The rectangular holes exhibit strong effects on light polarization due to the different aspect ratio of the rectangle's sides. To obtain the polarization-independent effect, any shape with fourfold symmetry can be applied (He *et al.* (2009)).

3.1.3.1 Babinet's principle

The complementary structures of the metallic holes array exhibit complementary transmission properties. This effect is called Babinet's principle and has been extensively studied for different frequencies, ranging from visible light to microwave radiations (Bitzer, Ortner, Merbold, Feurer & Walther (2011)).

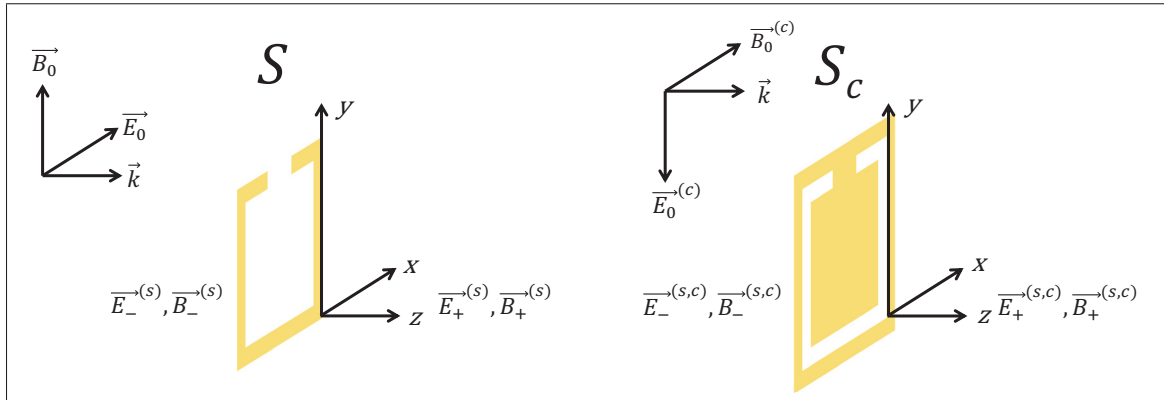


Figure 3.8 Two scattering problems for Babinet's principle for a) SRR and b) its complementary screen illuminated by complementary incident field
Adapted from Miyamaru *et al.* (2006)

Let us discuss the concept of Babinet's principle in terms of the two scattering problems shown in Figure 3.8. Here S denotes an original SRR and its complementary structure is S_c . We assume

an incident EM field onto the original surface \vec{E}_0, \vec{B}_0 and the scattered fields produced by S are given by $\vec{E}_\pm^{(s)}, \vec{B}_\pm^{(s)}$. The incident EM field for the complementary surface is described as $\vec{E}_0^{(c)}, \vec{B}_0^{(c)}$ and the scattered field is given by $\vec{E}_\pm^{(s,c)}, \vec{B}_\pm^{(s,c)}$. Note, we solve the scattering problem behind the structure ($z > 0$) for $\vec{E}_+^{(s)}, \vec{B}_+^{(s)}$. The scattering fields on the left-side have the opposite sign to match boundary conditions for the perfect conducting surface, where both the total magnetic polarization perpendicular to the screen and the total electric polarization parallel to the screen vanish.

Babinet's principle concerns the fields scattered by two complementary plane structures provided that both are illuminated by complementary waves (Azad *et al.* (2012); Bravo-Abad *et al.* (2007); De Abajo (2007); De Abajo *et al.* (2005); Edmunds *et al.* (2010); Miyamaru *et al.* (2006); Stevens, Edmunds, Hibbins & Sambles (2011); Takano, Miyamaru, Akiyama, Miyazaki, Takeda, Abe, Tokuda, Ito & Hangyo (2014); Tremain, Durrant, Carter, Hibbins & Sambles (2015)). As shown in Figure 3.8 complementary waves correspond to a $\pi/2$ rotation around the propagation axis. Hence, the incident and scattered EM field of the complementary structures can be related to the original ones as

$$\begin{aligned}\vec{E}_0^{(c)} &= c\vec{B}_0 \text{ and } \vec{B}_0^{(c)} = -\vec{E}_0/c, \\ \vec{E}^{(s,c)} &= -c\vec{B}^{(s)} \text{ and } \vec{B}^{(c)} = \vec{E}^{(s)}/c.\end{aligned}\tag{3.23}$$

Let us solve the problem 3.23 for plane waves. The incident EM for the original (\vec{E}_0) and complementary ($\vec{E}_0^{(c)}$) surfaces is given by

$$\begin{aligned}\vec{E}_0 &= E_0 \vec{e}_1 e^{(i\vec{k} \cdot \vec{r})} \\ \vec{E}_0^{(c)} &= c\vec{B}_0 = cE_0(\vec{k}/|\vec{k}| \times \vec{e}_1) e^{(i\vec{k} \cdot \vec{r})}\end{aligned}\tag{3.24}$$

And the scattered field ($\vec{E}^{(s)}$) from the original surface is defined as:

$$\vec{E}^{(s)} = \vec{E}^{(t)} - \vec{E}_0,\tag{3.25}$$

where $\vec{E}^{(t)}$ is transmitted field through the original surface. Assuming the same direction of propagation for the transmitted ($\vec{E}^{(t)}$) and the incident ($\vec{E}^{(0)}$) field in the original structure and

applying Babinet's principle, the transmission field in the complementary problem can be found:

$$\vec{E}^{(t,c)} = \vec{E}^{(s,c)} = -c\vec{B}^{(s)} = -\vec{k} \times \vec{E}^{(s)} = -\vec{k} \times (\vec{E}^{(t)} - \vec{E}_0) = -(E^{(t)} - E_0)(\vec{k}/|\vec{k}| \times \vec{e}_1)e^{(i\vec{k} \cdot \vec{r})} \quad (3.26)$$

Thus, we obtain the component of the transmitted field for the complementary surface:

$$E^{(t,c)} = E_0 - E^{(t)} \quad (3.27)$$

By dividing each term in equation 3.27 by E_0 and using the definition of the Fresnel's coefficient, we get:

$$\frac{E^{(t)}}{E_0} + \frac{E^{(t,c)}}{E_0} = t + t^{(c)} = 1 \quad (3.28)$$

Considering the normal incidence and using the relation between the transmission and reflection coefficients, the transmission coefficient of the complementary structure is related to the reflection coefficient as:

$$\begin{aligned} t &= 1 + r, \\ t^{(c)} &= -r \end{aligned} \quad (3.29)$$

If scattering into other propagating diffracted modes and polarization conversion are negligible, then the corresponding power transmittances satisfy the following equation for normal incidence:

$$|t|^2 + |r|^2 = |t|^2 + |t^{(c)}|^2 = 1 \quad (3.30)$$

The equation 3.30 shows that the complementary problem's power transmission spectrum is opposite that of the original one. Figure 3.9 shows the transmission spectra obtained from SRR and its complementary structure, confirming the obtained relationship above. In the self-complementary structure, half of the power is transmitted, and the other half is reflected. It highlights the frequency-independent response of the fully self-complementary structures. Basically, an ideal self-complementary structure could behave as a 50/50 beam splitter. Due to this theoretical phenomenon, there have been many studies exploring the response of self-complementary structures for different frequencies, ranging from visible light to microwave radiation (Bitzer *et al.* (2011)).

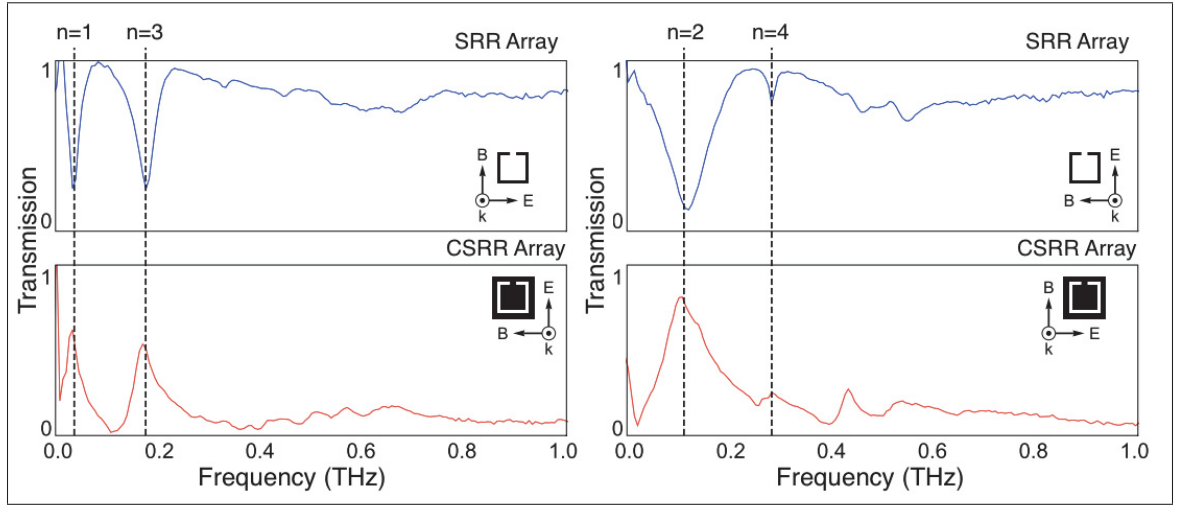


Figure 3.9 Far-field transmission spectra were obtained from a 20×20 array of SRRs for two different incident beam polarizations relative to the sample indicated by the insets (top curves) and corresponding spectra of the complementary sample (bottom curves). Vertical dashed lines indicate characteristic resonances of the structures

Taken from Bitzer *et al.* (2011)

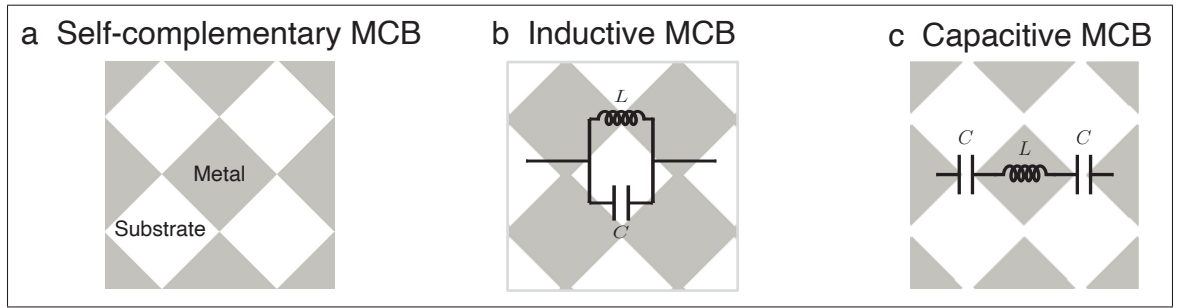


Figure 3.10 An illustration of a) self-complementary metallic checkerboard (MCB); b) Inductive MCB (*i*-MCB) and c) Capacitive MCB (*c*-MCB) with corresponding lumped elements model

One such structure is the metallic checkerboard (MCB) (Takano *et al.* (2014)). Figure 3.10 shows an MCB made from the square patches with the side length a rotated by 45° . The periodicity of the arrays is $p = \lambda_g [m]$ and corners of squares meet at $a = \lambda_g / \sqrt{2} [m]$. In principle, it is impossible to realize an ideal point of contact between patches. Hence, the instantaneous change of the response of the MCBs depends on the connection or separation between the neighboring metallic patches and makes impossible a frequency-independent response. This critical behavior

has been explained by percolation theory, identifying the ideal MCB as a structure representing the percolation threshold between connected and disconnected patches (Kempa (2010)). The connected patches present a metallic hole array with diamond-shaped holes, usually called inductive MCBs (*i*-MCBs) and shown in Figure 3.10b. The complementary structure of the *i*-MCB is the capacitive MCB (*c*-MCB), with separated metallic patches (Figure 3.10c). In this case, the *c*-MCB behaves as a low-pass FSS since the long-wavelength cannot drive current around the system. The EM interaction with *c*-MCBs shows an inverse Fano-resonance (Edmunds *et al.* (2010); Takano *et al.* (2014)). In the this thesis framework, we used MCBs for the quality control of printed electronics devices. Chapter describes our findings in detail.

3.1.4 Effect of metal conductivity

One of the most important characteristics of electronic devices is electrical conductivity. This is the ability of conducting electricity, which is determined in metals by the movement of electrons. The presence of valence electrons represents the properties of the atoms of metal elements. The valence electrons are located in the external shell of an atom and can move around freely. Hence, they can move via the lattice of the metal and conduct an electric current (Kasap (2006)). The electric current density \vec{j} is defined as the net amount of charge (Δq) flowing across an unit area (A) per unit of time (Δt):

$$\vec{j} = \frac{\Delta q}{A\Delta t} \quad (3.31)$$

When an electrical voltage is applied to a conductor, electrons are accelerated under the force $e\vec{E}$, where e is the charge of an electron. Thus electrons move randomly, but with a net drift in the inverse direction to the electric field (Fig. 3.11).

The drift velocity of the electrons is denoted by \vec{v}_d . Suppose that N is the concentration of electrons in the conductor. During time Δt , electrons move a distance of $\vec{v}_d\Delta t$. Hence, the total charge Δq crossing the area A is $\Delta q = eNA\vec{v}_d\Delta t$. It follows that the current density is defined as:

$$\vec{j} = \frac{eNA\vec{v}_d\Delta t}{A\Delta t} = eN\vec{v}_d \quad (3.32)$$

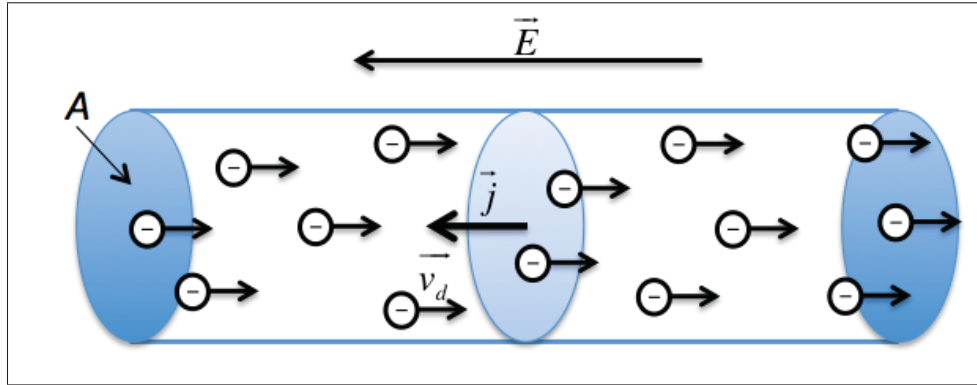


Figure 3.11 Drift of electrons in a conductor with an applied electric field
Adapted from Kasap (2006)

To calculate the drift velocity v_d of the electrons due to the applied field E , τ is denoted as the mean time among electrons' collisions and m^* is effective mass of electron. Since $e\vec{E}/m^*$ is the acceleration of the electrons, the drift velocity is then given by

$$\vec{v}_d = \frac{e\tau}{m^*} \vec{E} \quad (3.33)$$

Equation (3.33) shows that the applied electric field and the drift velocity are linearly proportional. The constant of proportionality $e\tau/m^*$ is called drift mobility μ_d (Kasap (2006)). The mobility shows how fast electrons will drift due to the application of an electric field. Then, the current density could be expressed as:

$$\vec{j} = en\mu_d \vec{E} = \sigma \vec{E} \quad (3.34)$$

where the conductivity σ is the coefficient of proportionality, which shows that the increasing of an applied field is proportional to a current density. Conductivity in metals depends on the mobility as well as on the concentration of conduction electrons and can be determined as:

$$\sigma_{DC} = \frac{Ne^2\tau}{m^*} \quad (3.35)$$

The classical model of a metal is a gas of free charges. To describe the transport properties of electrons, the Drude model plays a significant role in determining matter properties. This model has the following assumptions:

- The collisions between electrons are instantaneous uncorrelated events;
- The electrons travel in straight lines between scattering events;
- The probability of collision per unit time is $\gamma = 1/\tau [s^{-1}]$.

Hence, under the influence of an applied electric field:

$$\vec{E} = E_0 e^{-i\omega t} \quad (3.36)$$

The Newton's 2d law can describe the displacement $x [m]$ of a carrier from its equilibrium position:

$$m^* \ddot{x} + m^* \tau^{-1} \dot{x} = e \vec{E} \quad (3.37)$$

where the first term describes the acceleration force, and the second is the electron collisions in the presence of the external EM field. The displacement of an electron can be described by a harmonic function similar to the EM field in 3.36:

$$\vec{x} = x_0 e^{-i\omega t} \quad (3.38)$$

Substitution of the equation 3.38 into the equation 3.37 readily yields \dot{x} :

$$m^* [-i\omega \dot{x} + \tau^{-1} \dot{x}] = -e E_0 e^{-i\omega t} \quad (3.39)$$

$$\dot{x} = \frac{-e E_0 e^{-i\omega t}}{m^* (\tau^{-1} - i\omega)} = v_d \quad (3.40)$$

Hence, the substitution of 3.40 into 3.32, 3.34 and 3.35 gives the frequency-dependent conductivity:

$$\sigma(\omega) = \frac{\vec{j}}{\vec{E}} = \frac{e N v_d}{\vec{E}} = \frac{\sigma_{DC}}{1 - i\omega\tau} \quad (3.41)$$

The conductivity of metals at THz frequencies is proportional to dc conductivity since the probability of collisions in the order of 10^{15} s ($\gamma_{Ag} = 0.032 \times 10^{15} \text{ s}^{-1}$ Cai & Shalaev (2010)).:

$$\sigma_{THz} \propto \sigma_{DC} \quad (3.42)$$

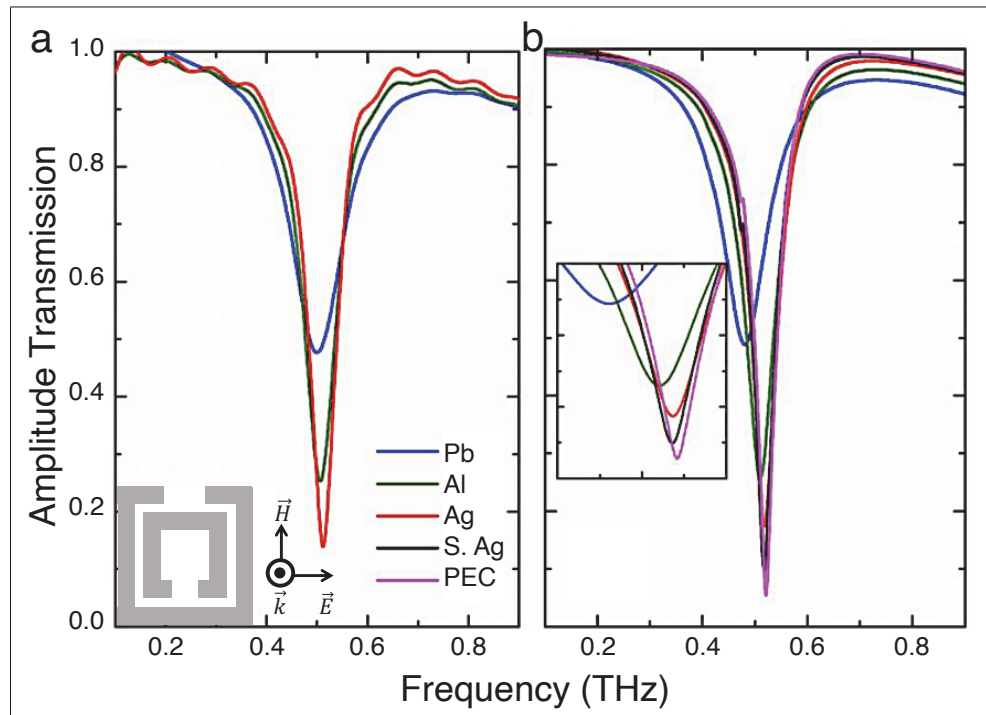


Figure 3.12 a) THz-TDS results and
b) finite-element simulations of the LC-resonant transmission of
metamaterials made from 300 nm thick *Pb*, *Al*, *Ag*, super *Ag* (*S.Ag*), and
perfect electric conductor (*PEC*). The zoom image illustrates the simulated
LC resonance

Taken from Azad *et al.* (2012); Singh *et al.* (2008)

The influence of conductivity on MMs' resonance response fabricated using conventional photolithography has been studied for different metals in the THz range (Azad *et al.* (2012); Singh *et al.* (2008); Wen, Ma, Bailey, Matmon, Aeppli & Yu (2014)). Singh *et al.* (2008) have studied the LC response of SRRs made from *Pb*, *Al*, and *Ag*, as a function of the Drude permittivity. In the THz range, the Drude conductivity is proportional to the static conductivity of metals as it was proved in the equation 3.42. As shown in Figure 3.12, Variation of the

transmission amplitude and the shape, as well as a slight shift of the LC resonance to lower frequency, were observed for metal when decreasing the DC conductivity ($\sigma_{Pb} < \sigma_{Al} < \sigma_{Ag}$, consequently, $f_{Pb} < f_{Al} < f_{Ag}$). The decreasing of the transmission amplitude at the resonance frequency correlates with the ratio of the real and imaginary parts of conductivity: $-\sigma_r/\sigma_i$, which are usually higher for the better conductivity in the visible range. Following the Drude conductivity function 3.41 in the THz range, this ratio is inversely proportional to the damping rate (τ). These results are consistent with observations in the visible range. The same dependencies between conductivity and transmission behavior have been found for hole arrays structures and for absorption modulators made from different bulk metals (Azad *et al.* (2012); Wen *et al.* (2014)). These results clarify that the underlying material properties change the resonance response of metamaterials.

3.1.5 Vortex phase plate

An optical vortex beam can be described as the light which is twisted like a corkscrew around its propagation axis. This beam's intensity profile on a flat surface has a doughnut shape with zero intensity in the center. It is explained by a phase singularity that is located in the space, where the phase is undefined. The intensity profile of a vortex beam usually is described by Laguerre-Gaussian (LG) modes (Azad *et al.* (2012); Wen *et al.* (2014)):

$$E_p^l(r, \phi, z) \propto \left[\frac{\sqrt{r}}{w(z)} \right] L_p^{|l|} \left(\frac{2r^2}{w(z)^2} \right) \exp[i l \phi] \exp \left[-\frac{r^2}{w(z)^2} - i \frac{k z r^2}{2(z_R^2 + z^2)} + i \Phi_G(z) \right], \quad (3.43)$$

where k is the wavenumber in a vacuum, $L_p^{|l|}$ is the generalized Laguerre polynomial of order l and p . p is the radial index, which is 0 for a linear polarized LG mode, $w(z)$ [m] is the beam radius at a distance z [m]:

$$w(z) = w_0 \sqrt{1 + z^2/z_R^2}, \quad (3.44)$$

where w_0 is the radius of the beam waist and $z_R = k w_0^2/2$ is the Rayleigh range. $\Phi_G(z) = (2p + |l| + 1) \arctan(z/z_R)$ is the Gouy phase shift, which is an additional phase shift for a beam passing through the focal region (He *et al.* (2013)).

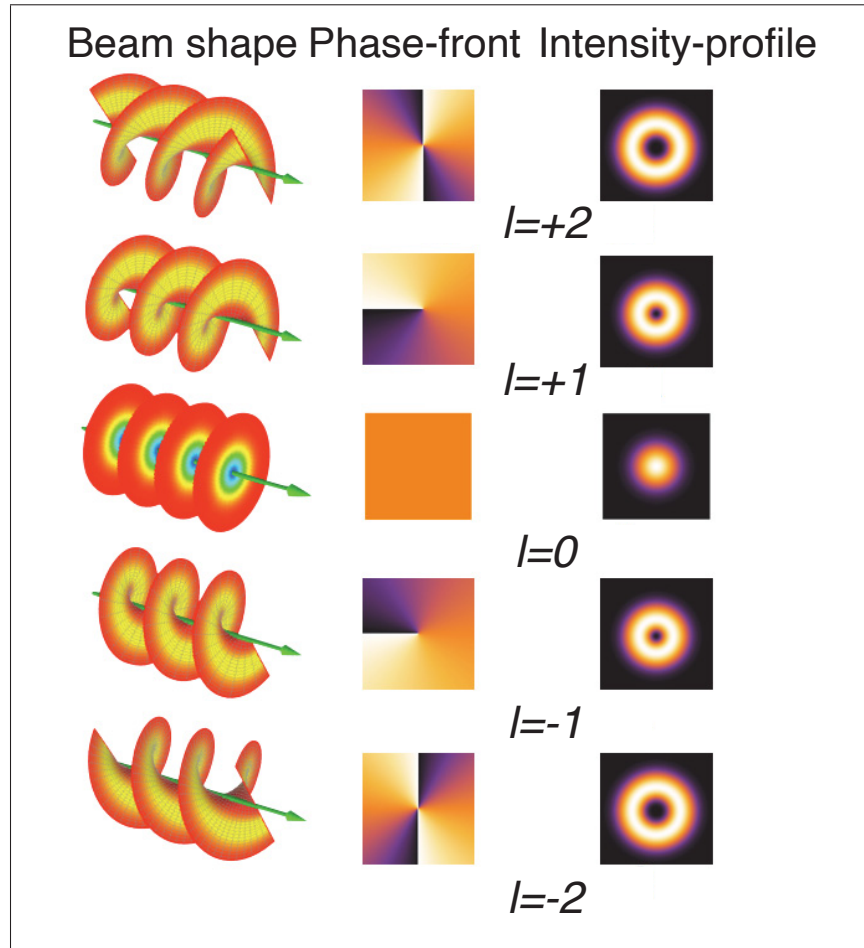


Figure 3.13 Diagram of different helical structures, phase-front, and intensity of the beams depending on the topological number.

$l = 0$ corresponds to the Gaussian beam.

Taken from Wikipedia (2007)

For $p = 0$, the LG mode is linearly polarized. As shown in Figure 3.13, for $l = 0$, $p = 0$ this expression reduces to that of an ordinary Gaussian beam, taking into account that $L_0^0(z) = 1$. For $l \neq 0$, the amplitude of the field vanishes at the center, and the phase changes by $2\pi l$ as one circles the origin in a counter-clockwise sense at constant z , exhibited by the term $\exp(il\phi)$ (Gbur (2007)). The number of twists (l) is called the topological charge of the vortex beam and is related to the orbital angular momentum (L) of photons shaped in this beam by the relation $L = \hbar l$. As shown in Figure 3.13, the topological charge indicates the direction of rotation and the vortex's strength at the beam center (He *et al.* (2013)). The topological charge's opposite

value corresponds to the same strength of vortex beam with a mirrored phase-profile and beam direction. Optical beams with helical phase profiles can carry additional information and provide many opportunities in many fields, including stimulated emission depletion microscopy, optical tweezers for particle trapping and manipulation, and optical communication systems (Hu, Wang, Feng, Ye, Sun, Kan, Klar & Zhang (2013)).

Recent research in the THz regime proposes many techniques for generating THz pulses with a phase singularity. THz vortex beams are conventionally generated in existing THz Gaussian beams by imposing phase modulation using spiral phase plates (Miyamoto, Kang, Kim, Sasaki, Niinomi, Suizu, Rotermund & Omatsu (2016); Wang, Shi, Sun, Feng, Han, Ye & Zhang (2016)). Computer-generated holograms (Knyazev, Choporova, Mitkov, Pavelyev & Volodkin (2015)), photopatterned birefringence liquid crystals (Ge, Chen, Shen, Sun, Wang, Hu, Zhang & Lu (2017)), and segmented half-wave plates with specially designed optical axes (Minasyan, Trovato, Degert, Freysz, Brasselet & Abraham (2017)) have also been reported. Recent approaches propose methods based on a direct generation of THz vortices (Al Dhaybi, Degert, Brasselet, Abraham & Freysz (2019); Ivanov, Thiele, Bergé, Skupin, Buožius & Vaičaitis (2019); Lin, Zheng, Song, Zeng, Cai, Li, Chen, Zha, Pan & Xu (2019)). Ivanov, M. *et al.* (Al Dhaybi *et al.* (2019); Ivanov *et al.* (2019); Lin *et al.* (2019)) demonstrated the generation of a broadband vortex beam in air-plasma induced by a coupling between a Gaussian fundamental harmonic and a second harmonic, which was carrying an optical vortex. This gives the spatial variation of a relative phase difference between two harmonics leading to the THz beam's intensity modulation along the azimuthal angle (Ivanov *et al.* (2019)). Recently, Lin *et al.* (2019) directly generated THz vortices from the NIR pulses. The optical difference-frequency mechanism between a pair of NIR chirped pulses with a relative time delay and different topological charges were used to obtain stable THz vortex pulses with topological charges of ± 2 (Lin *et al.* (2019)). The LOMA group reported converting an infrared vector beam with an azimuthal order of l into a terahertz vortex beam. The generation mechanism is based on optical rectification of femtosecond radially polarized IR pulses in a ZnTe (Al Dhaybi *et al.* (2019)). These methods avoid any manipulation in the THz beam itself.

In 2012, the first solutions for vortex beam generation using a metasurface were employed in the IR regime (Genevet, Yu, Aieta, Lin, Kats, Blanchard, Scully, Gaburro & Capasso (2012)). P. Genevet *et al.* build a vortex phase plate from V-shaped antennas. Previously, Yu, Genevet, Kats, Aieta, Tetienne, Capasso & Gaburro (2011) designed a metasurface from a V-shaped antennas structure to achieve phase modulation for cross-polarized scattered fields in the infrared. V-shape antenna is made from two rectangular rods with equal length of h attached at one end at a specific angle Δ . Figure 3.14a shows the resonance behavior of a single rectangular rod. The rod antennas can cover a shift from 0 to 2π ; however, the scattering amplitude is significantly smaller due to only a single resonance mode (Chen *et al.* (2016)). Hence, double-resonance properties of V-shape antennae have been used. V-shape antenna supports two types of current excitation symmetry according to the orientation of the incident electric field, as shown in Figure 3.14b and c. Simultaneous excitation of symmetric (\hat{s}) and antisymmetric (\hat{a}) modes is achieved by making the angle between the V-antenna symmetry and the incident polarization 45° . The schematic current distribution is represented by colors on the antenna (blue for symmetric and red for antisymmetric mode), with brighter color representing larger currents. The direction of current flow is indicated by gradient arrows. The choice of an appropriate combination between h and Δ provides a large range of phases and amplitudes for a given wavelength (Yu *et al.* (2011)).

Figure 3.14d and e show four V-shaped antennas with the same scattering amplitude, which provide a constant phase difference of $\pi/4$. The rod geometry enables analytical calculations of the phase and amplitude of the scattered light, without requiring the extensive numerical simulations to compute the same quantities for "flat" antennas with a rectangular cross-section, as used in the experiments. The optical properties of a rod and "flat" antenna of the same length are quantitatively very similar, when the rod antenna diameter and the "flat" antenna width and thickness are much smaller than the length. To achieve an additional π phase change, mirror structures of these antennas are used. It allows one to construct a vortex phase plate (VPP), which enables a full phase change from 0 to $2\pi n$ by segmenting the interface in $8n$ equiangular sectors (Genevet *et al.* (2012); Yu *et al.* (2011)).

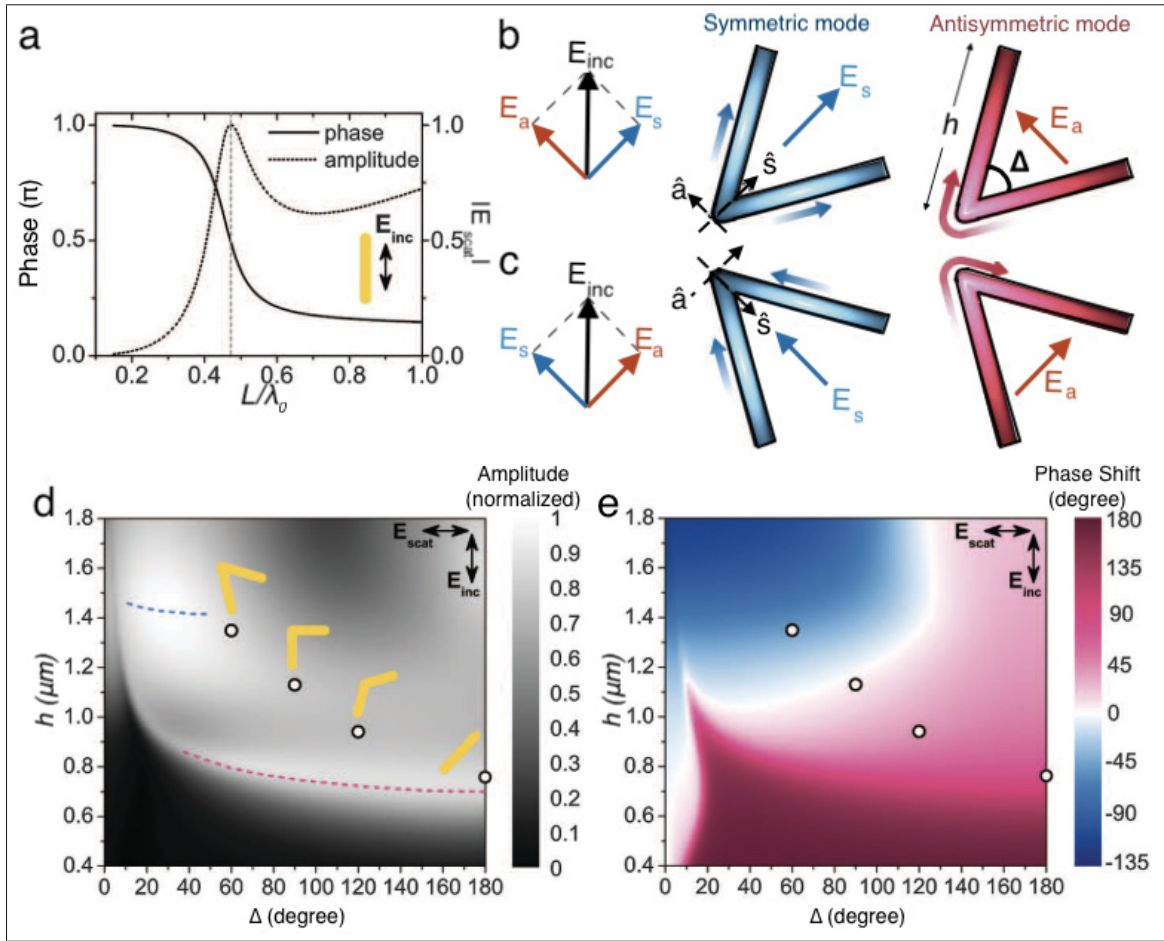


Figure 3.14 a) Calculated phase and amplitude of scattered light from a straight rod antenna made from a perfect electric conductor. The vertical dashed line indicates the first-order dipolar resonance of the antenna.

- b) A V-shape antenna supports symmetric and antisymmetric modes, which are excited, respectively, by components of the incident field along the \hat{s} and \hat{a} axes.
- c) V-shape antennas corresponding to mirror images of those in b). The components of the scattered electric field perpendicular to the incident field in b) and c) have a π phase difference.
- d) and e) Analytically calculated amplitude and phase shift of the cross-polarized scattered light for V-shape antennas consisting of gold rods with a circular cross section and with various length h and angle between the rods Δ at $\lambda_0 = 8 \mu m$. The four circles in d) and e) indicate the values of h and Δ used in experiments

Taken from Genevet *et al.* (2012)

In 2013, He *et al.* (2013) extended the structure into the THz range and showed the vortex beam generation using a complementary VPP. The VPP is designed for one specific topological charge

of $l = 1$ and applies to a narrow bandwidth for THz waves. The designed VPP is made from eight sections, with each of them containing identical antennas separated by a $200\ \mu\text{m}$ distance, which is smaller than the wavelength of the incident light. The sectors are arranged into an azimuthal pattern with a phase shift of $\pi/4$ and supply a discretized spiral phase distribution from 0 to 2π to the incident light wavefront. Figure 3.15 illustrates the design of antennas with the notation of the geometrical parameters.

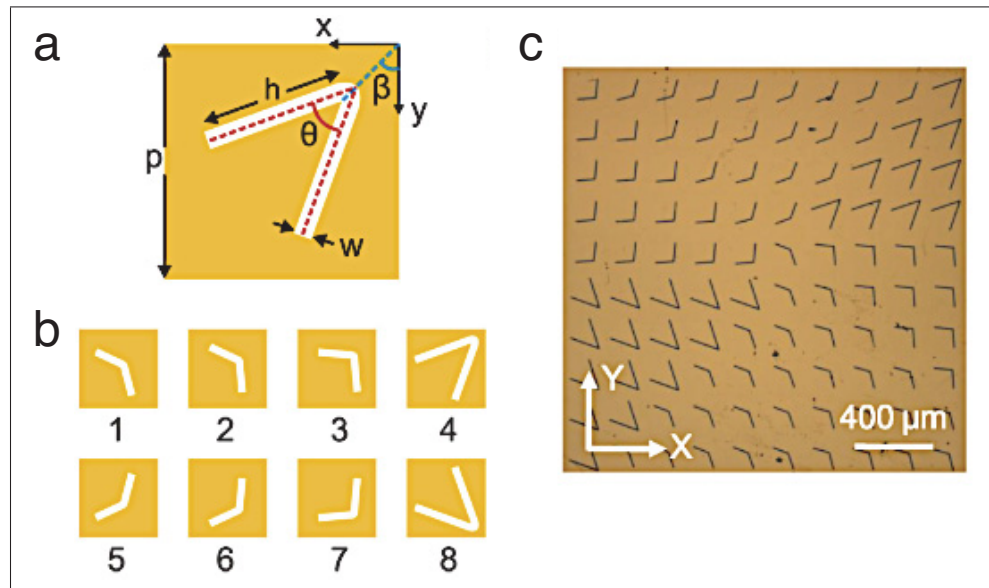


Figure 3.15 a) A complementary V-shaped antenna phase modulation unit.
b) Eight kinds of complementary V-shaped antenna structures corresponding to phase shifts from $-3\pi/4$ to π with a $\pi/4$ interval.

c) Photography of the central region of the designed VPP for $l = 1$

Taken from He *et al.* (2013)

Importantly, the VPP functions appropriately, creating the vortex beam at the targeted frequency of 0.75 THz , which corresponds to a wavelength of $400\ \mu\text{m}$. This was the most important property for choosing this structure as a pattern for quality control of the printed electronics devices.

3.2 Toward a method of quality control assisted by metamaterials

2D-metamaterials are of particular interest in the THz regime, where most natural materials exhibit only weak electric and magnetic responses and hence cannot be utilized for controlling radiation. THz metasurfaces can drastically advance THz research and development (Withayachumnankul & Abbott (2009)). Two decades ago, 2D-MMs were mainly implemented for controlling or confining light on the subwavelength scale (Azad *et al.* (2012); Cai & Shalaev (2010); Chen *et al.* (2011); Genet & Ebbesen (2007); Tao *et al.* (2010b)). In recent years, 2D-MMs have found many applications in sensing, and thus open the door for quality control (Miyamaru *et al.* (2006); Tenggara *et al.* (2017); Zhuldybina *et al.* (2019b); Zhuldybina, Ropagnol, Bois, Zednik & Blanchard (2020)).

THz spectroscopy has proven to be a powerful method for label-free, non-contact, and non-destructive detection of chemical and biological substances (Tenggara *et al.* (2017)). However, tiny micro-organisms have a small scattering cross-section, and they mostly behave as a transparent medium for THz waves. To overcome the low-scattering problem, THz 2D-MMs have to be applied. As shown in Chapter 3.1, any change in MM's parameters influences the resonance behavior. When sensing micro-organisms, the MM's surrounding medium is changing; hence, the resonance frequency depends on the dielectric function of 2D-MMs (Tenggara *et al.* (2017)). Figure 3.16 shows an example of using metasurfaces to identify the density number of micro-organisms (Park *et al.* (2014)). As shown in Figure 3.16a, the presence of penicillia is not detectable on a pure *Si* substrate. Whenever the substrate is patterned with 2D-MMs structures as shown in the inset of Figure 3.16b, the LC-resonance shift indicates the appearance of a micro-organism, and its position highly depends on the effective dielectric constant. This approach can be used for food security and safety to discriminate different harmful additives, such as pesticides or antibiotics (Xie, Gao, Shu, Ying & Kono (2015); Xu, Xie, Zhu, Wang, Ye, Ma, Tsai, Chen & Ying (2017)). Xie *et al.* (2015) have used FSSs made from square holes and showed that the detection limit of antibiotics concentration is 100 pg/L , which is a $\sim 10^{10}$ times enhancement compared to the case where only pure silicon is used ($\sim 1 \text{ g/L}$).

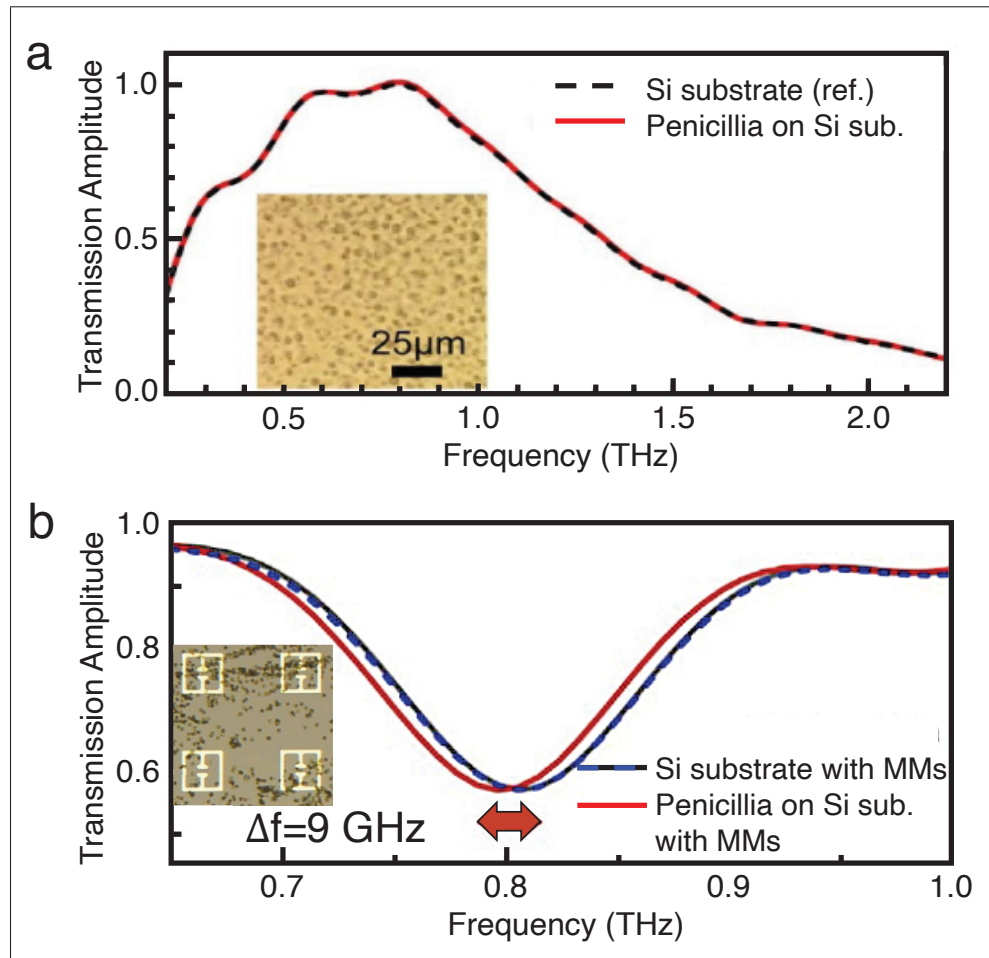


Figure 3.16 a) THz transmission amplitudes, for transmission through a plain *Si* substrate, with (red solid line) and without (black dashed line) deposition of penicillia. (inset) A microscopic image of penicillia deposited on the *Si* substrate.
 b) THz transmission amplitudes measured before (black/blue line) and after (red solid line) the deposition. The inset is the microscope images of metamaterials patterns on *Si* substrate, with the deposition of penicillia
 Taken from Park *et al.* (2014)

Another vital application of 2D-metamaterials is virus detection, e.g., HIV, Zika, and Ebola, which have been extensively studied during the last decade (Ahmadvand, Gerislioglu, Ramezani, Kaushik, Manickam & Ghoreishi (2020); Cheng, He, Huang, Zhang, Liu, Shu, Fang, Wang & Luo (2018); Park, Cha, Shin & Ahn (2017)). To date, one of the most significant worldwide problems is COVID-19 diagnostics, which requires a short sample-to-result duration. Ahmadvand

et al. (2020) detected SARS-CoV-2 spike proteins using THz plasmonic metasurfaces made from THz toroidal MMs with functionalized colloidal gold NPs. The presence of gold NPs improves the binding properties of the biomolecules with the metasurface. Figure 3.17 shows the measured transmission spectra of the metasensor (added in the inset). The growth of the SARS-CoV-2 concentration leads to a bigger red-shift of the LC-resonance. The main advantage of this approach is the short diagnostic time, which takes $\sim 80 \text{ min}$ and can help for early-stage COVID-19 infection diagnosis even in the presence of fmol biomolecule densities.

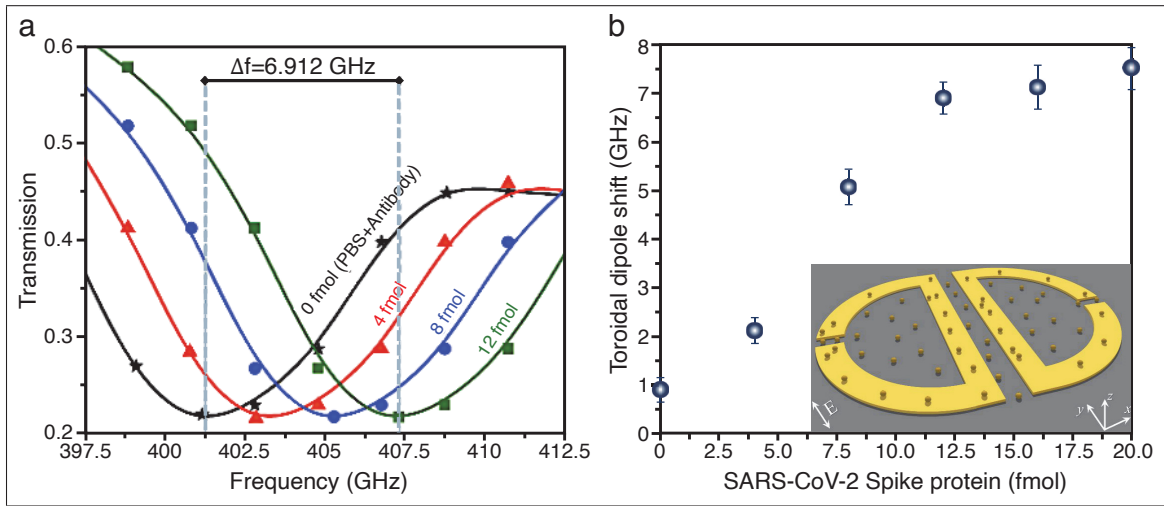


Figure 3.17 a) Measured transmission spectra of the THz metasensor device for different concentrations (4 fmol to 12 fmol) of SARS-CoV-2 spike protein.

b) Variations of the toroidal mode frequency shift for different concentrations of injected spike proteins captured by relevant antibody ranging from 2 fmol to 20 fmol. The inset figure is an artistic rendering of the designed multipixel toroidal unit cell, including the dispersed functionalized gold NPs on top

Taken from Ahmadiwand *et al.* (2020)

To be able to detect liquid samples, reflection-based THz-TDS is used since water molecules strongly absorb THz waves. To increase the sensitivity, complementary 2D-MMs are usually applied due to their higher sensitivity in reflection mode. High sensitivity detection of the different concentrations of sugar molecules was demonstrated, which can be helpful for early-stage recognition of kidney disease or diabetes mellitus (Miyamaru, Hattori, Shiraga, Kawashima, Suga, Nishida, Takeda & Ogawa (2014); Taleb *et al.* (2020)).

Amirkhan, Sakata, Takiguchi, Arikawa, Ozaki, Tanaka & Blanchard (2019) have applied SRRs to characterize thin-film EO materials in the near-field region. Figure 3.18a depicts a schematic image of a sensor made from $1\text{ }\mu\text{m}$ -thick x -cut LN crystal, which was covered with five different orientations of SRRs. The proposed method allows retrieving the EO components of unknown materials with only one measurement, which is impossible for the standard measurements. This way of patterning with SRRs gives the ability to extract THz field polarizations simultaneously within the same viewing area, as shown in Figure 3.18b and c.

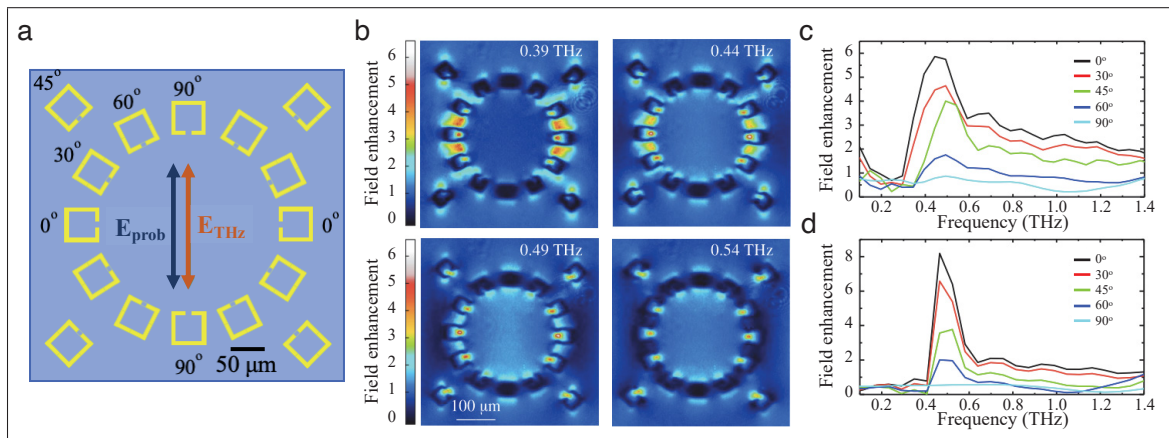


Figure 3.18 a) Schematic diagram of the SRR pattern arrangement on the surface a $1\text{ }\mu\text{m}$ -thick LN crystal for the experimental study;
 b) Normalized absolute amplitude of the experimental electric field of the SRR at LC resonance frequencies, i.e., 0.39 THz , 0.44 THz , 0.49 THz , and 0.54 THz .
 c), d) Respectively, experimental and simulated results of the absolute values of the electric field enhancement, E_y , in the gap of SRR
 Taken from Amirkhan *et al.* (2019)

The application of 2D-metamaterials is largely focused on sensitive measurement and a broad range of optical effects, which show extreme sensitivity to any variation of the MMs' parameters. However, to the best of our knowledge, the application of metamaterials for quality control has not been exploited. The main idea of this PhD project is to implement THz 2D-metamaterials for the quality control of printed electronics. As it was shown in this chapter, the physical and functional properties of 2D-metamaterials exhibit a strong influence on the resonance response,

and this was successfully adopted to complete geometrical verification (see Chapter 4) as well as conductivity measurement (see Chapter 5) of PE devices (Zhuldybina *et al.* (2019b,2)).

CHAPTER 4

CHARACTERIZATION OF THE SPATIAL RESOLUTION

This chapter is based on the work "Printing accuracy tracking with 2D optical microscopy and super-resolution metamaterial-assisted 1D terahertz spectroscopy" (Zhuldybina *et al.* (2020)). It was demonstrated the significant dependence of the printing speed on the quality of the printed result, including the quantity and distribution of the printed ink.

Looking from the industrial perspective, non-destructive testing for quality control in the industrial environment is often based on sampling the condition of a production line. For this work, the samples have been printed with different speeds using an industry-standard commercial flexography process, demonstrating the potential of using continuous roll to roll (R2R) for manufacturing functional printing devices. R2R continuous printing process exhibits defects and deformation, similar to any other industrial tool. There is variability in the production conditions, such as the ratio of supply liquids to substrate velocity, anilox specification, the cohesion of the liquid, shear stress changes of the liquid, tension applied on the web inducing thermal deformation of the substrate in the drying sections, etc. In an offset printing press for production of newspapers or food packaging, a mechanical dot-gain structure is indispensable to the production line's quality control Kipphan (2001). The printed area of the control structure to characterize the dot gain is around a few cm^2 . This work proposes a quite similar concept. It employs MCB (see Chapter 3.1.3.1) which is not only representative on its own (i.e., in the small area of $\sim 1 cm^2$), but it gives a direct insight into the printing behavior at a given time. It is also easy to place several of these tags on the production sheet and repeat them every few minutes or seconds during production, depending on the degree of control required.

The main goal was to show the ability of THz spectroscopy to track the printing accuracy and ink distribution of an industrial roll-to-roll press with a flexography printing unit. As presented in Chapter 3.1.3, the geometric properties of 2D-metamaterials strongly affect the transmission of an electromagnetic wave through changes in its cell-unit, lattice size, and other geometric parameters (Zhuldybina *et al.* (2019b,2)), which is perfectly suited for this purpose. For this

demonstration, two printing speeds and three geometric variations of the same pattern are used as feeding parameters. Our method uses the unique electromagnetic transmission properties of the MCB pattern. It yields simultaneous information about the lattice and unit cell variations and allows investigating the influence of the printing speed on the resulting distribution accuracy of deposited ink. A small modification of its unit cells near self-complementarity produces a unique resonant signature, highly suitable for tracking variations in printouts. Finally, to evaluate the ability of THz spectroscopy to follow the input printing parameters, we compared our results with those from standard visible optical microscopy (OM) using Matlab software for visual analysis.

4.1 Sample fabrication

Samples were printed by an industrial roll-to-roll, shown in Figure 4.1. R2R press contains five units, which can be used for flexography or screen- printing. For the fabrication of our sample, the press was assisted with a flexography printing unit (OMET Varyflex V2). The principle of the flexography is shown in Figure 1.3. The ink is put in contact with a micro-engraved cylinder (anilox) at a rate of 12 billion cubic microns per square inch (*bcm*), and ink is then transferred onto a printing form, which defines the pattern information. The inked pattern is then pressed against the polyethylene terephthalate (PET) substrate in the nip zone between the printing form and an impression cylinder.

Only unit #3 was used for the printing designs during the current fabrication, highlighted with blue rectangular on Figure 4.1. It was filled out with a silver water-based ink from SunChemical (Sun AFT6700) with adjusted viscosity and drying retardant. Further, the drying unit was adjusted at 100 °C. The drying module is circled with red rectangular in Figure 4.1. The linear resistance of printed samples was $2.0 \Omega/cm$. The printing speed was varied between 30 *m/min* and 50 *m/min*. As shown in Figure 4.2, it has been printed around ~ 1 km of printed devices with the quality control structure in the shape of MBCs.



Figure 4.1 The industrial roll-to-roll printer consists of five printing units, where a blue rectangle indicates the location of the printing unit #3 used for the sample's fabrication. The red rectangle highlights the dryer module

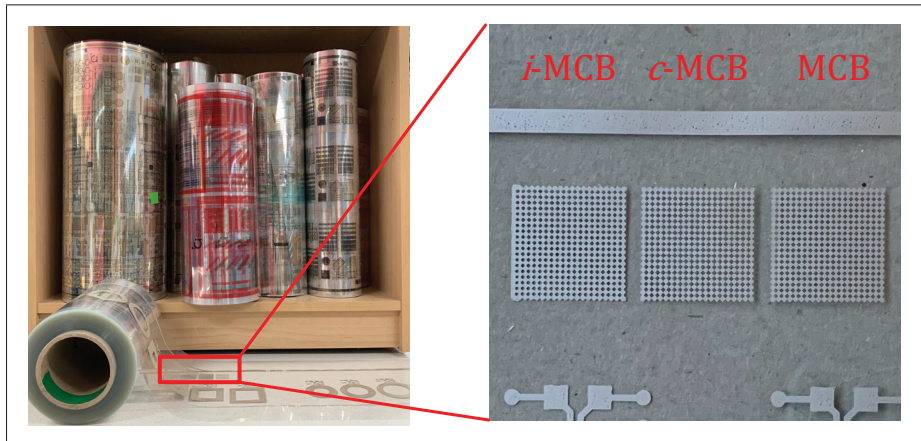


Figure 4.2 The produced samples at the printing speed of 50 m/min

4.2 Optical microscopy

Figure 4.3 illustrates the set of designed samples, which contains three structures: (i) an inductive MCB (i -MCB), (ii) a perfect MCB, and (iii) a capacitive MCB (c -MCB). The MCB is a self-complementary structure when c -MCB and i -MCB are complementary to each other. The designed structure was chosen to suit the spatial resolution characteristics of the printer. The predetermined period was the same in both directions $p = p_x = p_y = 1 \text{ mm}$ and for all structures. The size of the ink's laps (+) or gaps (-) were varied between samples as follow:

$\Delta d_{c-MCB} = -14 \mu m$, $\Delta d_{MCB} = 0 \mu m$, $\Delta d_{i-MCB} = +14 \mu m$, was however, kept constant in the X - and Y - directions ($\Delta d_x = \Delta d_y$). The production line was moving along the indicated y -direction in Figure 4.3. One-quarter of the visible images of the two printed sets are shown in Figure 4.3b and c, respectively, where the black color represents the printed metallic ink (metallic patches) and the whitish color represents the substrate (voids). In b and c, visible images of size $10.24 \times 10.24 \text{ mm}^2$ and containing 4096×4096 pixels were obtained with a visible laser confocal microscope (model LEXT OLS4000), where 1 pixel corresponds to $2.5 \mu m$. The images were taken in stitching mode, with a $5\times$ objective lens with a 2 Megapixel charged coupled device (CCD) camera.

From a simple visual observation of Figure 4.3, it is clear that none of the printed structures in b or c correspond perfectly to the designed ones in a, where all metallic patches are much bigger and voids smaller. The visual analysis also clearly reveals the changes in pattern shapes for the two printing speed conditions. At a slower printing speed, far away from the optimized press run rate, printing quality/printability is sub-optimal, and printing conditions might be irregular. In the configuration press/ink/substrate, it appears that the ink tends to spread more, thus creating larger laps between each pattern. Meanwhile, increasing the print speed to approach optimal printing conditions gives better printability control and therefore produced patterns with sharper edges (Bravo-Abad *et al.* (2007); De Abajo (2007); De Abajo *et al.* (2005); Edmunds *et al.* (2010); Stevens *et al.* (2011); Takano *et al.* (2014)). Especially for c -MCB printed at 50 m/min (c -MCB50), it can be seen that the lap sizes are smaller, with some gaps appearing between patches. Besides, we cannot identify variations in the lattice between all printed samples. Geometrical variation information provides an important insight into the printing performance and is crucial for enabling the desired final printed pattern tuning. Theoretically, an accurate repetitive shape can be reached by seeking out the correct printing parameters. In the framework of this thesis, our goal was to follow the printing variations precisely.

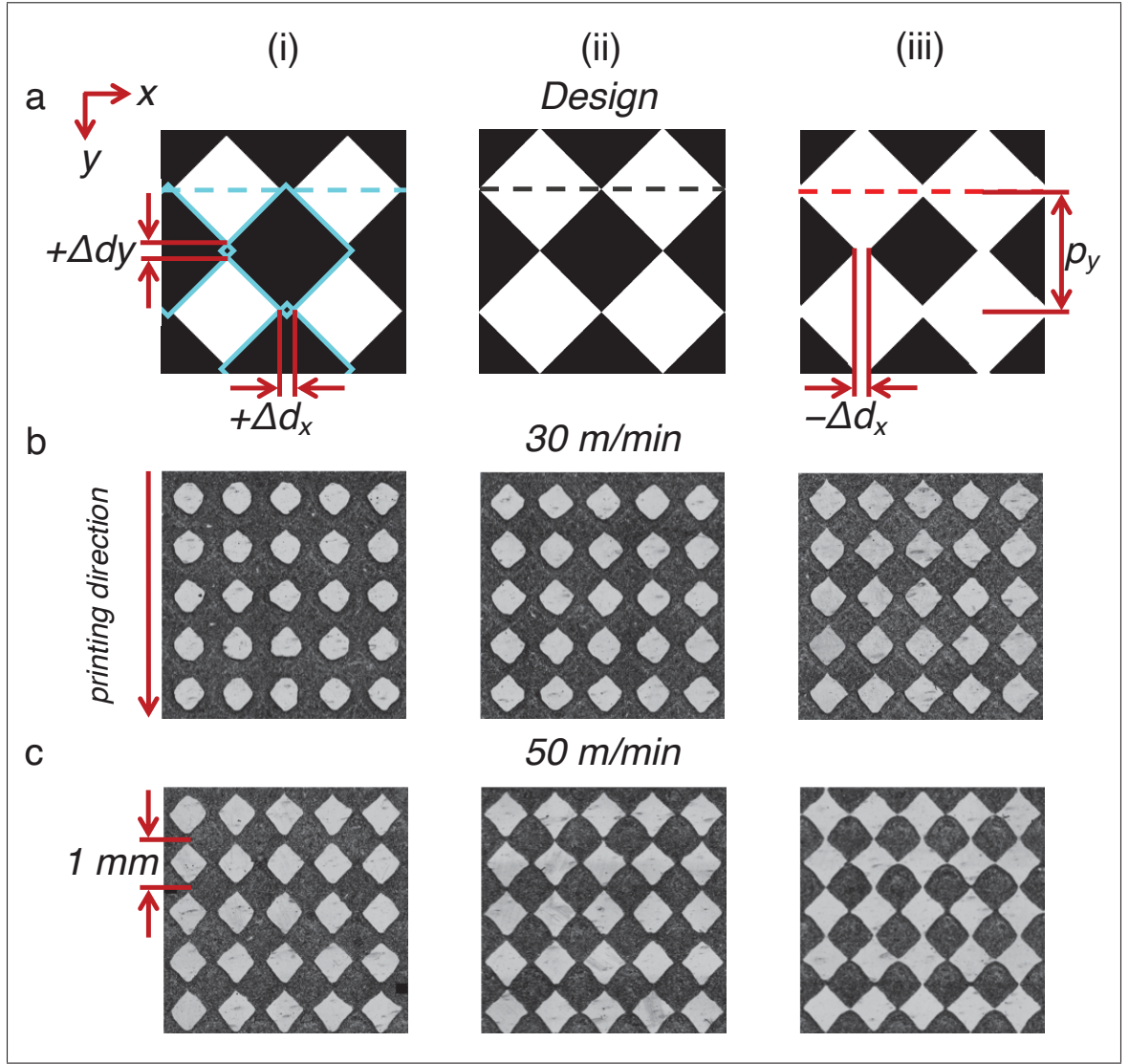


Figure 4.3 a) Designed samples, where black pixels correspond to ink and white is the substrate (voids): (i) *i*-MCB pattern with ink stretching of $\Delta d = +14 \mu\text{m}$; (ii) is the target MCB pattern for perfect transmission property; (iii) pattern with ink compression of $\Delta d = -14 \mu\text{m}$.

One-quarter of the visible images of the printed patterns obtained with a speed of:

b) 30 m/min and c) 50 m/min

4.2.1 Matlab algorithm for visual analysis

For a more pragmatic assessment of the geometrical specifications of structures, we used Matlab software (see Appendix IV). We counted the number of black or white pixels to extract the

sizes of the lattice (p_x , p_y) and laps/gaps (Δd_x , Δd_y) for the X - and Y - directions. An example of a complete 4096×4096 pixel image for a sample of c -MCB50 is shown in Figure 4.4a with the zoomed in image in Figure 4.4b. The blue and red shaded rectangular areas identify the extraction areas for tracking connection or disconnection sizes in the X - and Y - directions, respectively. To identify the lap size ($+\Delta d$), the algorithm looks for the least narrow area between the metal parts and extracts the number of black pixels, which have been converted into the geometrical size of a lap. If there is a separation between patches, the white pixels neighboring patches are used to calculate the size of a gap ($-\Delta d$).

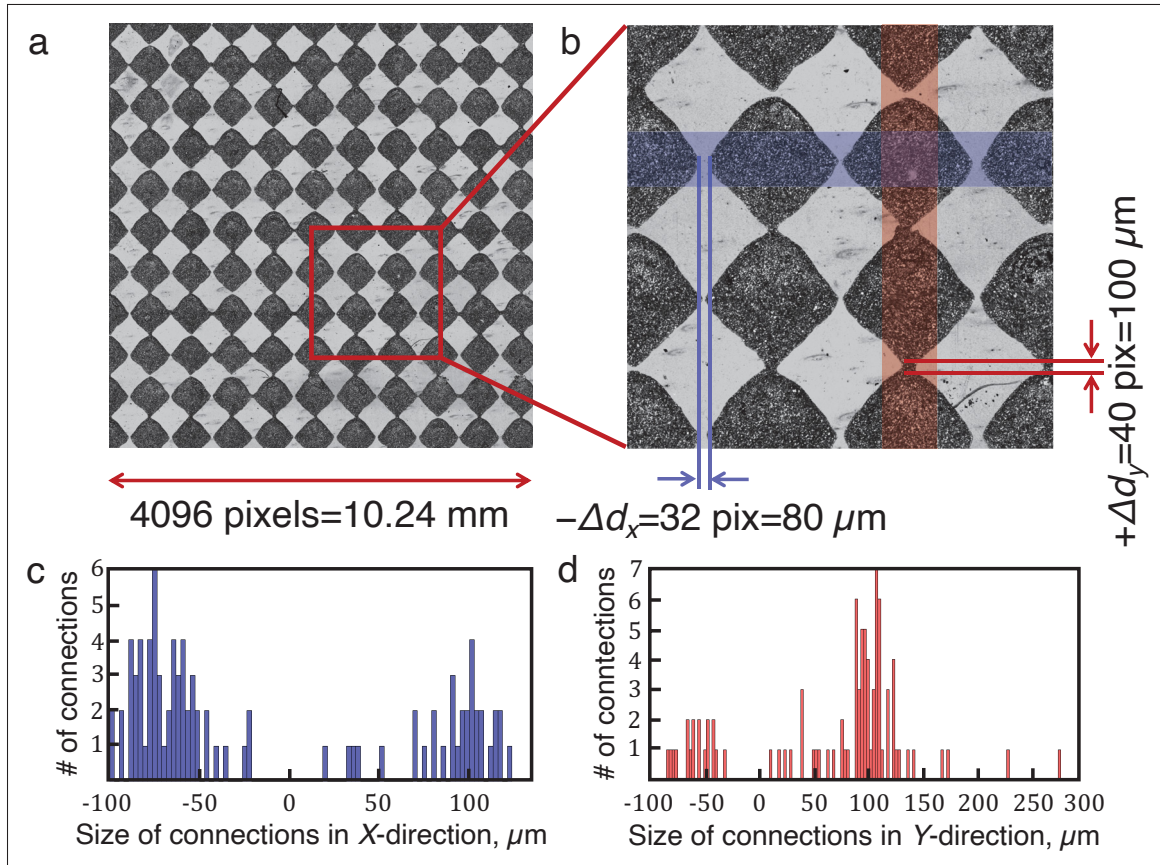


Figure 4.4 a) Image of one of the c -MCB50 samples, which has the geometrical size of 10.24 mm and corresponds to 4096 pixels where 1 pixel corresponds to $2.5 \mu\text{m}$.

b) A zoomed view from the red square area shown in a).

c) and d) correspond to the histograms of the size of the connections in the X - and Y - directions, respectively

Figure 4.4c and d show the histograms summarize the different types of connections: gaps and laps for both directions. The Y -direction contains mostly laps and described the size distribution by the Gaussian function. The function of the X -direction connections has a double Gaussian shape. It can be explained by the tensile stress that appeared between neighboring metallic patches, which tend either connect or separate.

In addition, these shaded areas were used to calculate metal occupancy as a function of direction. The purpose of evaluating metal occupancy as a function of direction is to identify the printing behavior for the X - and Y -directions separately. The procedure consists of counting the total number of black pixels framed in this rectangular area, which was then compared to the expected number of "ink" pixels. The metal occupancy was calculated for the further comparison with THz-TDS results shown in Chapter 4.4

4.3 Terahertz time-domain spectroscopy

Terahertz time-domain set up is shown in Figure 4.5. An ultrafast Ti: Sapphire oscillator laser with a center wavelength of 805 nm producing pulses with a duration of $\sim 20\text{ fs}$ and a repetition rate of 80 MHz was used in combination with two LT-GaAs photoconductive antennas from Teravil (Vilnius, Lithuania). A beam splitter 80:20 splits the laser beam into an optical pump and a probe beam for THz generation and detection, respectively. The emitter and the detector were placed in front of each other, separated by a distance of around 40 cm . An optical chopper at 330 Hz was placed just after the emitter, allowing for lock-in detection.

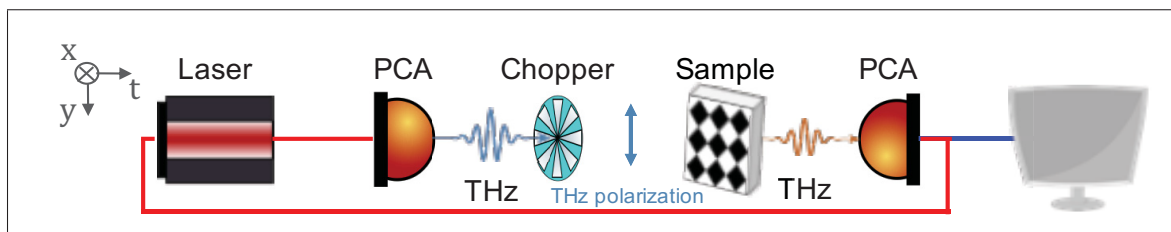


Figure 4.5 Terahertz time-domain setup with photoconductive antennas for the generation and detection of THz signal in the transmission configuration. The blue arrow shows the polarization of THz light

The samples were placed between the emitter and the detector for transmission spectroscopy in the air at room temperature and pressure at the normal incidence of THz pulses with a peak frequency of 0.2 THz with vertical polarization. In our measurements, the scan duration of 204.8 ps with 100 fs step size and signal-to-noise ratio in amplitude of 10^3 was limited by the echo coming from the silicon lens in PCA. Figure 4.6a shows typical time traces for THz-TDS measurements, where Figure 4.6b presents the spectra obtained by the Fourier transform.

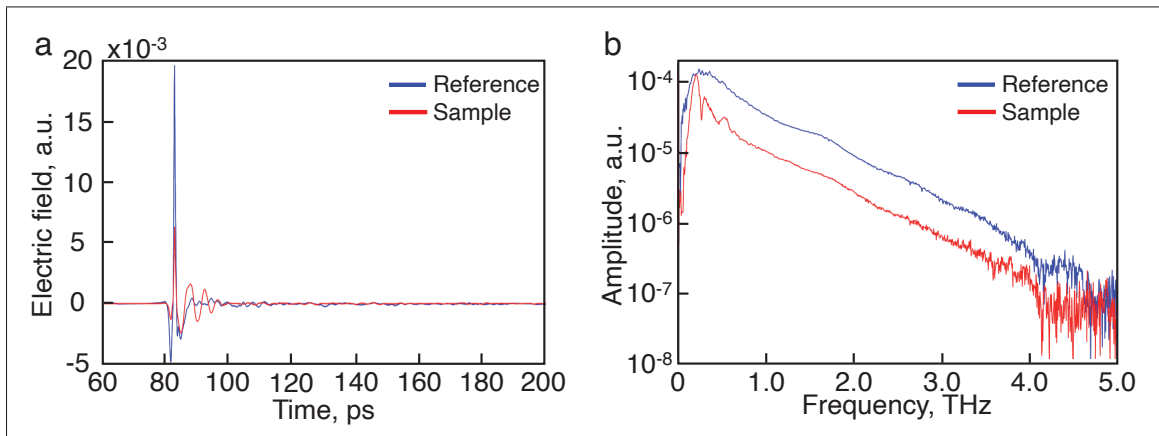


Figure 4.6 a) Signals recorded in the time domain of an MCB (sample) and its reference (substrate);
b) The THz transmitted amplitude spectra of an MCB and a substrate obtained by the Fast Fourier Transform of the time traces presented in a)

To measure transmissions of two different directions (X - and Y -), samples were rotated 90° according to the initial placing. Figure 4.7a shows the way of interactions of the light with different polarizations. Basically, the left picture in Figure 4.7a depicts the case of samples printed with low speed, where all of the patches are connected according to the observation in Figure 4.3b. The right picture in Figure 4.7a shows the interaction of the light with samples printed with higher speed, where disconnections between patches appear for the X - direction as shown in Figure 4.3c-III.

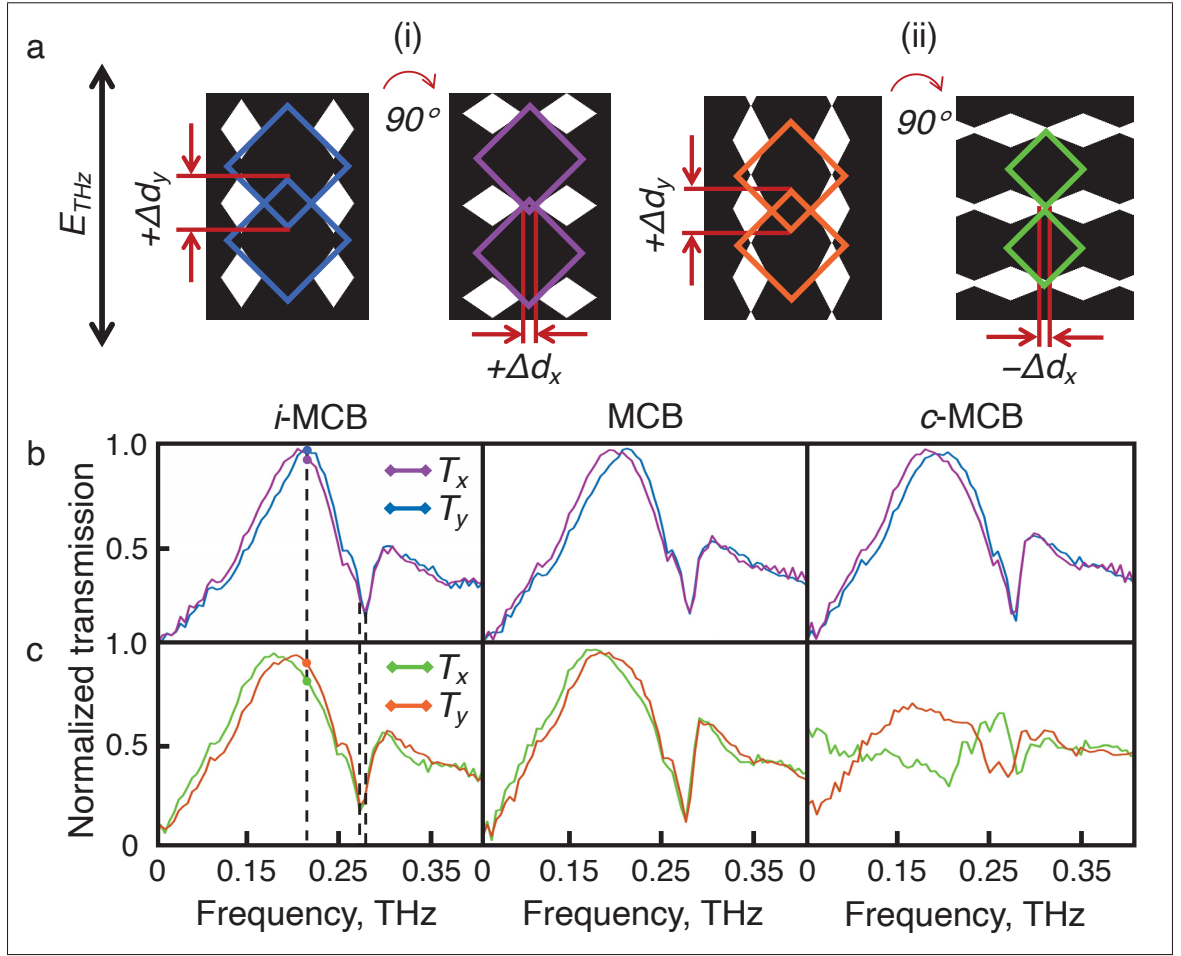


Figure 4.7 a) Principle of electromagnetic field interactions with the samples in X- and Y- directions: (i) *i*-MCB antisymmetric pattern for X- and Y- directions; (ii) *i*-MCB and *c*-MCB behavior for Y- and X- directions, respectively. Normalized transmission of printed *i*-MCB, MCB, and *c*-MCB samples with
b) 30 m/min and c) 50 m/min

4.3.1 Normalized transmission

To ascertain the EM properties of the printed MCB, we measured the normalized transmission responses using the THz-TDS system. A commonly used normalized transmission can be inferred from a measurement of two transmitted THz pulses propagating through a substrate ($E_{ref}(t)$) and through a sample ($E_{sam}(t)$) in the time domain (Sowade *et al.* (2016)). A ratio between Fourier transform of the time-domain reference ($E_{ref}(\omega)$) and sample ($E_{sam}(\omega)$) waveforms

gives the sample's normalized transmission:

$$T = \frac{E_{sam}(\omega)}{E_{ref}(\omega)} \quad (4.1)$$

Figure 4.7b and c present examples of the normalized THz spectra from the samples presented in Figure 4.3b and c, respectively. To analyze the THz-TDS results, we evaluated the resonance behavior at the designed resonance frequency, which was $0.22\ THz$. In Figure 4.7b and c, a clear difference in THz transmission at $0.22\ THz$ is found between the X - and Y -inspected directions, which agreed with the OM observations in Figure 4.3. For example, at a low printing speed for i -MCB (Figure 4.7b), we can observe a small drop in transmission at $0.22\ THz$, from the Y - to X -direction, indicating a reduction in the lap sizes. However, by printing at higher speeds, we can see a clear drop in transmission, which is even more pronounced for the X - versus the Y -directions. By comparing Figure 4.7b with Figure 4.7c, we observe a clear change of the transmission properties between the different printing speeds. Nevertheless, from these transmission spectra, the most interesting case is certainly Figure 4.7c (c -MCB), where laps and gaps coexist. In this case, the peak of normalized transmission has decreased drastically from 0.95 to 0.65, which is closer to the perfect transmission case condition of 0.5.

4.3.2 Dual-wavelength terahertz spectroscopy

The principle of DWTS for printed electronics characterization consists of selecting two frequency ranges from the spectrum. One of the areas represents the signal, where a clear fingerprint of the sample appears. The reference part of a spectrum should avoid the appearance of the water lines because they are absorbed by THz waves and influence on the DWTS results. To evaluate the performance of DWTS, we measured the time-domain signal of humid and purged (dry) air using a conventional THz-TDS system (Figure 4.8a) based on PCA. The obtained frequency domain spectra from FFT are shown in Figure 4.8b.

To investigate of the humidity influence on the results, the transmission spectrum between $0.195 - 0.205\ THz$ was chosen as the signal range. The reference range had the same bandwidth

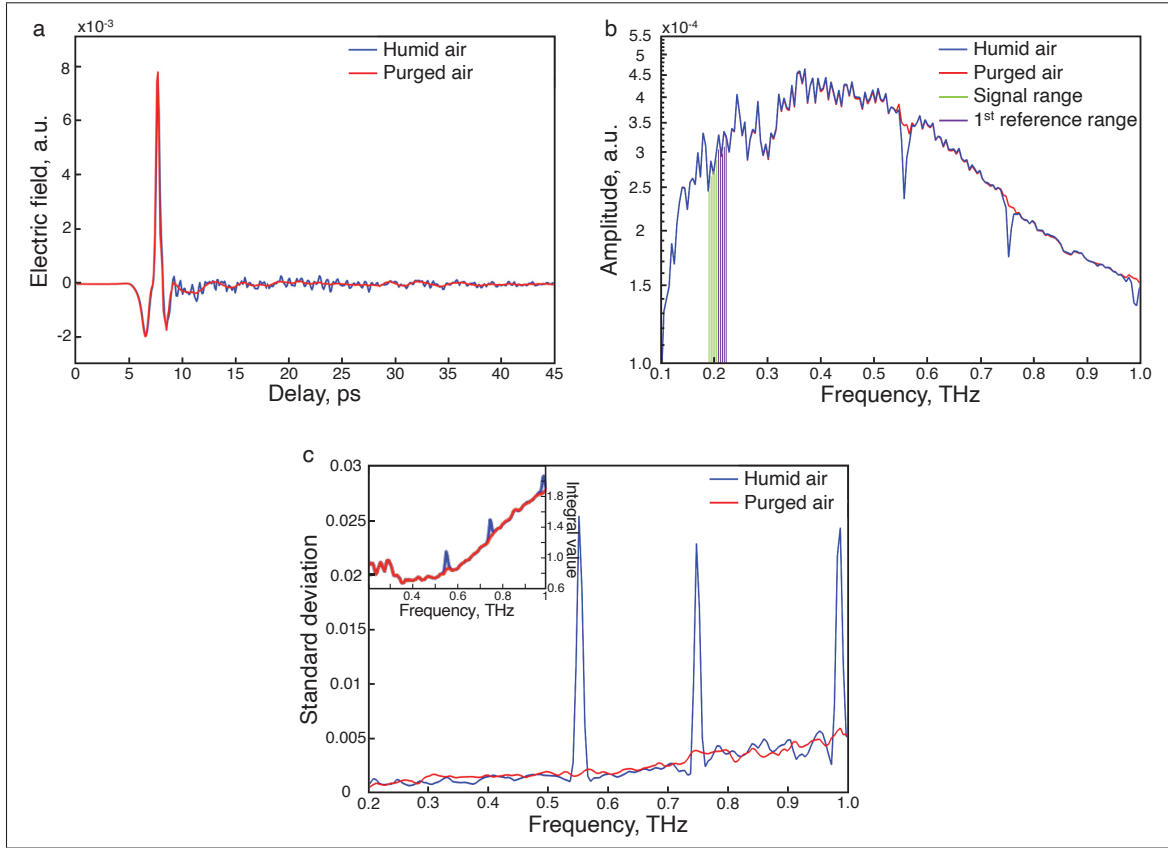


Figure 4.8 a) Time-domain signal of humid (blue) and purged (red) air. The electric field is presented in arbitrary units (a.u.) due to the specification of the measurements; b) Frequency domain spectra of a) obtained by FFT. Green and violet areas represent signal and reference ranges for DWTS analysis, where the reference signal was varied through the entire spectrum. c) The standard deviation of DTWS analysis of humid and dry air. The inset shows the calculated integral values extracted from the spectra of b).

of 10 GHz as the signal and was varied through the spectrum, starting from 0.205 THz to 1 THz .

$$I = \frac{I_{\text{signal}}}{I_{\text{reference}}} = \frac{\int_{0.195}^{0.205} |E(\omega)d\omega|}{\int_{\omega}^{\omega+0.01} |E(\omega)d\omega|} \quad (4.2)$$

Figure 4.8b shows the obtained THz spectra used for DWTS. We can see a strong absorption from water lines, as expected for an ambient condition with humid air (e.g., at 0.55 THz , 0.75 THz , and 0.98 THz). Applying the DWTS through the whole spectrum, Figure 4.8c shows that the standard deviation for five repeated measurements increases with increasing frequency. The

average behavior of both spectra (i.e., dry air and humid air) are comparable, except for the water absorption frequency position. The inset of Figure 4.8c plots the calculated integral values, which fully overlap for dry and humid air, except the water absorption lines as well. It confirms that DWTS can be applied in ambient environmental conditions with varied humidity.

Using DWTS, the reference and signal ranges are taken simultaneously, the ambient condition's noise is suppressed in the normalization process. DWTS will provide similar performance as a dry air laboratory condition by selecting an appropriate frequency window for the reference signal that does not show any perturbative signatures. Hence, it opens the door for the industrial characterization of the quality control based on DWTS, where the single measurement approach eliminates the influence of experimental conditions and reduces the measurements time.

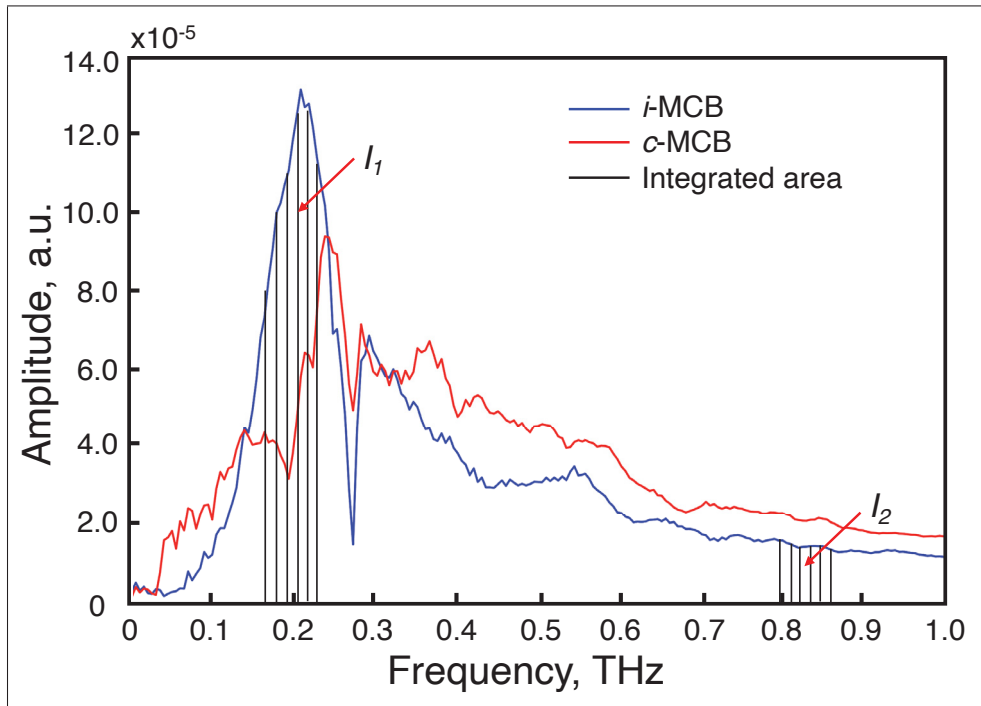


Figure 4.9 The principle of DWTS for *i*-MCB and *c*-MCB : I_1 contains the information about the resonance behavior conditioned by the connections between rhombuses, and I_2 is reference area outside of the water absorption lines.

In the case of MCBs, two areas have been chosen as shown in Figure 4.9. The signal area (I_1) is located around 0.22 THz , while the reference has been selected around 0.8 THz . The choice of the reference signal corresponds to the region outside of the water absorption lines. The resonance behavior highlights the type of dominant connections between rhombuses. The integral value is varied with the variation of the ink amount.

4.4 Comparison of results

Matlab algorithm has been applied to recover the variation in printing accuracy, where the standard deviation extracted from five replicas printed for each structure. Figure 4.10a and b summarize the printing accuracy of the different structures and printing speeds, where the x -axis shows the size of laps/gaps and the lattice size is plotted on the y -axis. The dashed lines correspond to the expected dimensions of the designed MCBs, and the grid represents twice the spatial resolution limit of $5\text{ }\mu\text{m}$. It confirms our simple visible observations, where slowly printed samples have large bridges between patches, as compared to fast printing. These systematic assessments help identify the fact that printed patterns are not symmetric, barely observed with OM. There is always more ink in the Y - direction (Δd_y), which means that the patch's size is bigger on the Y - versus X -axis. Importantly, in Figure 4.10a and b, we can see a small difference induced in the lattice for the different patterns and printing speeds. As is shown in the figures Figure 4.10a and b, the lattice size is always bigger in the Y - direction than in the X - direction. The extension of the lattice and patch sizes in the Y - direction relative to the X - direction is in good agreement with the placement of the print sheet relative to production line's direction. In general, compared to printing in the X - direction, the Y - direction is stretched during production (Cho, Jeong, Kim, Kwon, Lee, Kim, Kang & Lee (2017)).

To summarize, a visual analysis with an OM shows that the printing behavior can be controlled and observed from tiny changes induced in the feeding parameters, i.e., between the 3 cases shown in Figure 4.3a-i, ii, and iii. However, considering the large spatial variation of structures within a sample of about $\pm 50\text{ }\mu\text{m}$ obtained from the standard deviation, optical microscopy allows differentiation of a change in printing on the order of $100\text{ }\mu\text{m}$. For example, c -MCB's

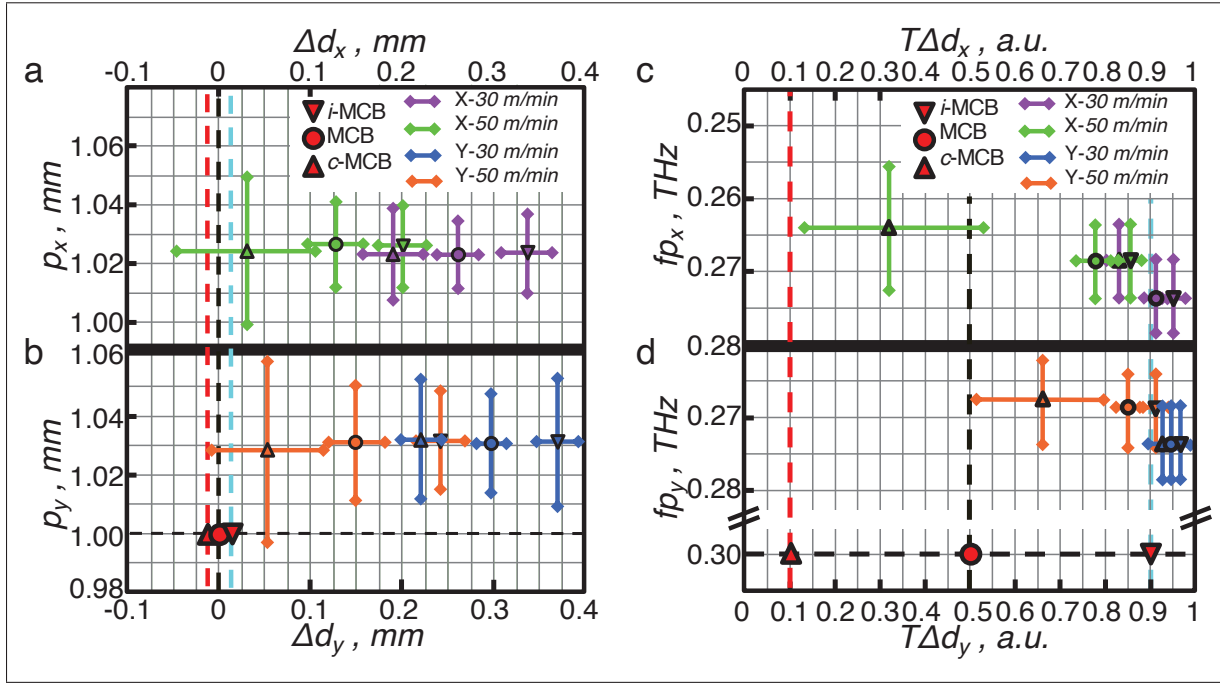


Figure 4.10 a), b) Extracted values of lattices and laps/gaps from visible images for X- and Y- directions, respectively. The horizontal and vertical lines show the standard deviation obtained from measuring Δd and p of five replicas for each structure. The red downward triangle, circle and upward triangle show the design size of laps or gaps of *i*-MCB, MCB and *c*-MCB, respectively. The dashed lines correspond to the designed dimensions of patterns. c), d) Extracted values of lattices and laps/gaps from THz-TDS measurements for X- and Y- directions, respectively. The horizontal and vertical lines show the standard deviation obtained from measuring normalized transmission at 0.22 THz ($T\Delta d$) and the frequency minima (f_p) of five replicas for each structure. The dashed lines correspond to the expected transmission values of designed patterns

Δd_x is $30 \pm 70 \mu\text{m}$ while MCB's is $125 \pm 30 \mu\text{m}$. The second important conclusion that can be drawn is that the shape of printed patterns highly depends on the printing speed. For example, printing the patterns at a higher speed (50 m/min) produces shapes that are closer to the designed cases, but at the expense of a greater lattice and lap/gap size variability as compared to low printing speeds. Figure 4.3c (iii) shows that the *c*-MCB50 contains laps and gaps and is the closest printed pattern to the perfect MCB shape, represented by the vertical black dotted line. As shown above, using microscopy analysis, ink distribution information can be extracted by testing a small print area. However, OM can be challenging to implement for quality control in

an industrial environment as it is subject to special conditions for correct observation, such as a stabilized imager.

The THz transmission measurements' accuracy was investigated onto the same five replicas used for the OM investigation and summarize the THz results for the X - and Y - directions in Figure 4.10c and d, respectively. The transmission values has been extracted at 0.22 THz ($T\Delta d_{x,y}$), and in the frequency, minima located close to 0.27 THz ($f_{p_{x,y}}$), which provide information on the laps/gaps and lattice signatures, respectively. The transmissions for laps/gaps are shown on the x -axis, while the y -axis represents the frequency response from the lattice size. To allow a direct comparison with OM results, the y -axis is depicted in decreasing frequency order. A larger lattice size exhibits a lower resonant frequency response, whereas a smaller size resonates in the higher frequency range. From Figure 4.10c and d, we can see that the lattice of the printed sample has a signature at a lower frequency than the design sample (depicted by the horizontal dashed line), which highlights the enlargement of the lattice, as was observed with OM. As with any other industrial tool, the printed electronic process is subject to great variations that continuously affect print quality. Here, the standard deviation of the THz results illustrates this existing condition as a function of the printing speed. Despite these large variations, THz transmission, just like the OM results, allows clear discrimination of the print quality according to the initial geometry of the print pattern. For example, in Figure 4.10c, the largest standard deviation observed for Δd_x is of the order of 20% over the normalized transmission value. Still, the THz data allows greater discrimination between the c -MCB and MCB samples than obtained by OM, i.e., transmission of 0.32 ± 0.2 for the c -MCB and 0.75 ± 0.1 for the MCB. By calibrating these results with those obtained by OM: Δd_x for c -MCB becomes $30 \pm 40\text{ }\mu\text{m}$ while Δd_x for MCB is $125 \pm 20\text{ }\mu\text{m}$. Given the 0.22 THz ($\lambda = 1.36\text{ mm}$) electromagnetic wavelength used to probe this variation, this spatial resolution performance far exceeds the diffraction limit imposed by the Rayleigh criterion (Blanchard *et al.* (2013)), confirming our method's remarkable ability to achieve super-resolution detection in a far-field regime.

Intuitively, a large variation between similar samples should also mean a greater influence between the printed conditions and the THz transmission. To validate this hypothesis, we

investigated the THz transmission behavior of samples at the designed resonance frequency (0.22 THz) and compared our results with OM observation. Figure 4.11 shows the position of the resonance peak and Q factor of the resonance peak as functions of the size of the laps for different samples printed in the shape of inductive MCBs. The resonance peak Q factor was defined as the ratio between the resonance center frequency to its full width of half maximum (FWHM). As the size of the laps increases, the peak position shifts to the higher frequency, and Q factor increases, resulting in the narrowing of the resonance peak. It explains by decreasing the resonant transmission through smaller holes due to the growth of laps size. Figure 4.11 shows 11 sets of points corresponding to X - and Y - polarizations of printed samples excluding c -MCB50, since it contains gaps and produces different types of response. These results are in accord with the work of (He *et al.* (2009)).

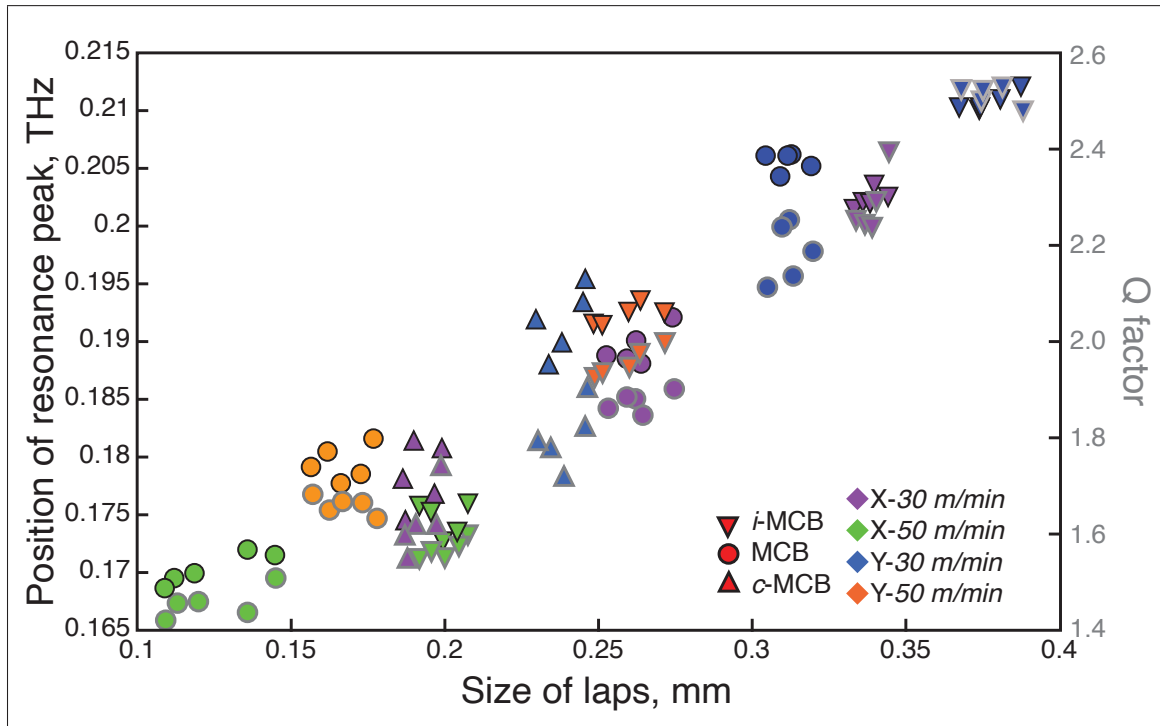


Figure 4.11 The position of the resonance peak (black outline) and the Q -factor (grey outline) of resonance peak with different size of laps

As shown Figure 4.12, it is evaluated the effect of the presence of gaps on THz transmission. The nonlinear behavior of the THz transmission (T) as a function of the number of gaps (G) can

be observed and described by the following function:

$$T(G) = 0.92e^{-0.023G} \quad (4.3)$$

From our fitting parameter, we have an exponential behavior as long as the number of gaps is relatively small (lower than 5). Notably, whenever there are no more gaps in the MCB structure, the sensitivity of the THz transmission remains high enough to measure the variation in the size of the diamond due to variations in the size of the lap. Of note, the presence of gaps has a higher impact on the THz transmission.

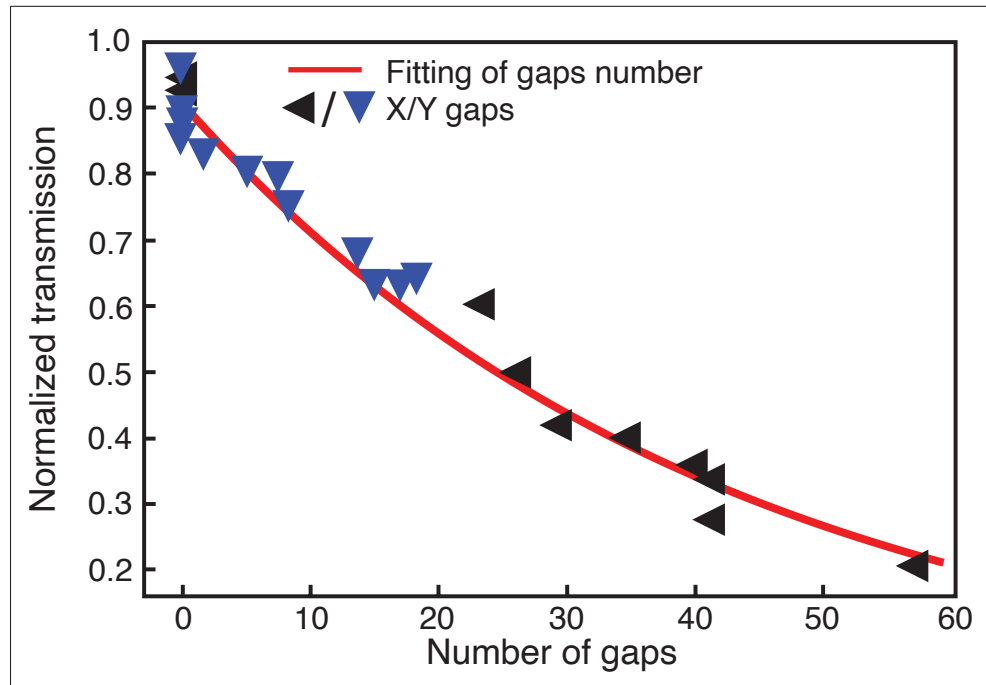


Figure 4.12 The normalized transmission from THz-TDS measurements as a function of the number of gaps measured by optical microscopy

Further, we evaluate the THz transmission for the X - and Y -directions of 14 samples, for a total of 28 measurements, with the same c -MCB print pattern as a function of the percentage of metal occupancy revealed by OM observations shown in Figure 4.13. In this group of samples, five were printed at 30 m/min (the blue dots) and the rest at 50 m/min (the black dots). These results are plotted as a function of their metal occupancy rate measurements obtained by the OM

method. Note that the metal occupancy (MO) depends on the amount of ink and its distribution, which for the MCB pattern defines the number and sizes of gaps/laps. In this Figure 4.13, the first striking observation is the growth of 10% to 90% in THz transmission, where the metal occupancy only changes from 55% to 61.5%.

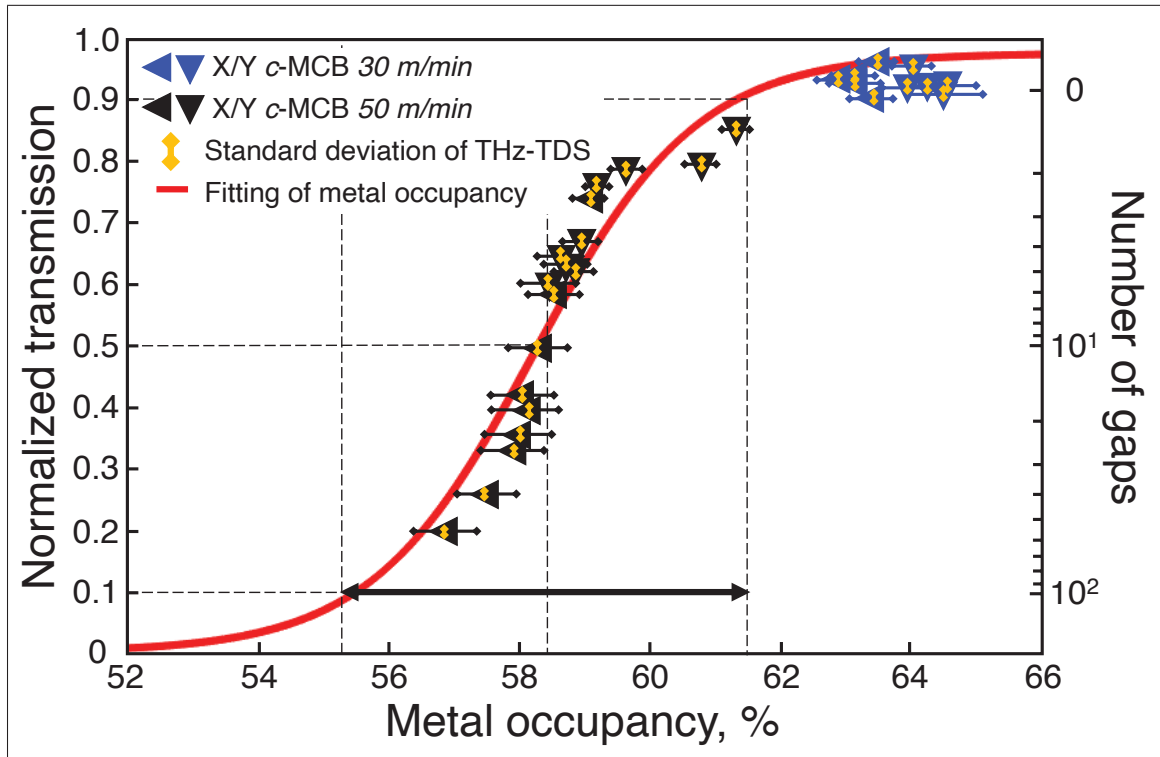


Figure 4.13 Comparison between OM and THz-TDS results, where normalized transmission from THz-TDS is plotted as a function of the metal occupancy. The red line shows the fit with the logistic function

Besides, as it can be seen by the areas identified in dotted lines in Figure 4.13, a difference between the printing behaviors for the X - and Y - directions is easily discernible by the THz transmission measurement. This extreme sensitivity in THz response corresponds to the conversion of 60 gaps into laps, where the self-complementary transmission flipped from capacitive to inductive. As shown on the y -axis on the right side, a sample is composed of 100 gaps and perfectly follows a log scaling to match the observed transmission comportment.

In Figure 4.13, the initial stage of growth is approximately exponential, and then the growth slows to linear and finally stops. This tendency of the THz transmission $T(MO)$ can be described by the so-called logistic function (S-curve) defined by:

$$T(MO) = \frac{L}{1 + e^{-k(MO-MO_0)}} \quad (4.4)$$

where L shows the maximum transmission value ($L = 0.97$), MO_0 is the S-curve midpoint, and k is the steepness of the curve ($k = 0.81$). Here, the midpoint of the curve is 58.24%, which corresponds to 0.5 in THz transmission. For the specific design of the MCB studied here, the midpoint at 58.24% defines a sensitivity range of 8% in the variation of metal occupancy, i.e., from 52% to 64%, as highlighted with the black arrow in Figure 4.13. Note that the sensitivity range and the midpoint can be modified by changing the lattice and gap dimensions' parameters. Significantly, while the metal occupancy changes only for 8%, the terahertz transmission is varied through the entire range of sensitivity.

As can be observed in Figure 4.13, the transmission of 0.5 corresponds to 58.24% in metal occupancy, which is supposed to be for a perfect MCB case. However, this pattern contains 10 gaps out of 100 possible connections, and the rest are laps with sizes up to $100 \mu m$. A balanced transmission/reflection condition occurs when the transmission of the overlapped patches compensates those with gaps. In other words, gaps have a more significant influence on THz transmission than a lap.

Additionally, DWTS has been investigated to simplify the measurement and compared with THz-TDS results. Figure 4.14 shows a comparison between the two methods. The DWTS follows the behavior the normalized results from THz-TDS, where the integral varies from 3 to 9 and the normalized transmission from 0.2 to 1. Interestingly, the variation of the normalized transmission from 0.9 to 1, corresponds to change in the integral from 7 to 9, which is 33% of the entire spectrum. It highlights the high sensitivity of DWTS results and proves that this approach reduces the measurements time and can be adapted for industrial measurements with two compact CW sources.

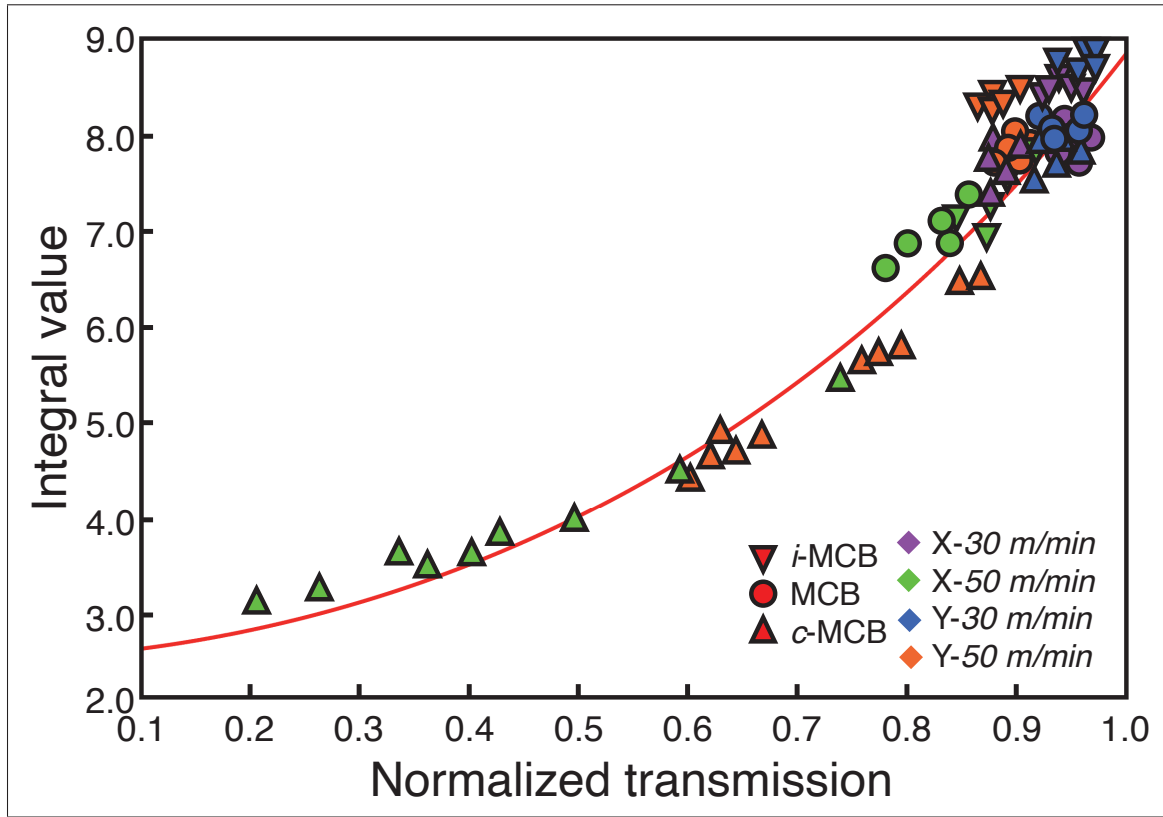


Figure 4.14 The results obtained with DWTS (integral value) and THz-TDS (normalized transmission)

The relationship between space and time resolution in our demonstration is quite appealing for quality control of printing conditions. It is well known that OM is designed to identify small elements. However, a larger field of view is required to achieve greater accuracy in order to resolve small changes in a structure that is periodic across positions in space, as illustrated in Figure 4.15. In our measurements, the size of the image is limited to $10.24 \times 10.24 \text{ mm}^2$, which means that the spatial frequency resolution is inherently set to $\sim 0.1 \text{ cycle/mm}$. For THz-TDS measurements, a scan duration of 204.8 ps long provides a spectral resolution of 4.8 GHz . As we demonstrate in our work, when combined with metamaterials and especially for self-complementary structures, a THz-TDS system's spectral resolution is converted into spatial resolution capability (as shown in Figure 4.15). Basically, any improvement in spatial resolution is solely a function of the duration of the temporal scan (i.e., no additional space

is required). Remarkably, under certain conditions, THz spectroscopy of metamaterials can operate as a super-resolution far-field THz microscope.

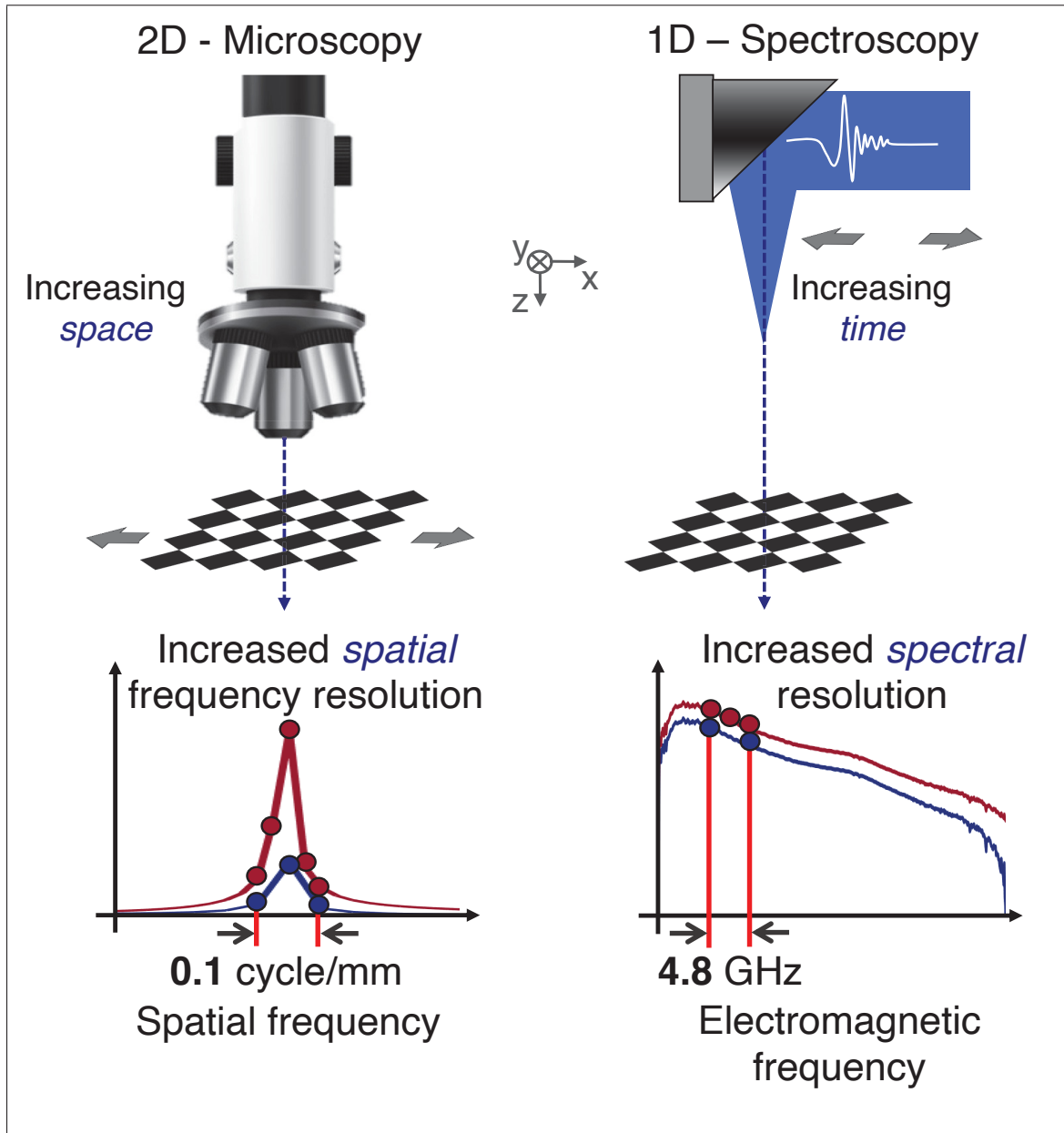


Figure 4.15 Illustration of the concept of spectral resolution for optical microscopy and 1-D THz-TDS

Strikingly for a small sample evaluation, the THz response shows a more precise quantification of the geometrical printed parameters than a high-resolution visible microscope capability.

Our demonstration confirmed the uses of THz radiation as a characterization tool to remotely measure the quantity and distribution of the printed ink.

The main goal of this work was to present to the printable electronics community an innovative way to control the printing quality and, at the same time showing amazing physical properties of metamaterials to exhibit super-resolution capability at THz wavelength. We strongly anticipate that our solution will be well adapted for PE printing production in the near future, similar to a dot gain tracking in an offset printing press. Even though the system used in this demonstration will not be used for application in the PE industry. There are systems available with 1000 scans per second (e.g., TeraScan from TOPTICA). Such a speed is high enough to follow the printing condition with only a few scans. A more straightforward solution may involve THz CW sources and detectors, as no scanning is required. Note that for our demonstration, only an average of three measurements were required. Assuming a speed of 50 m/min , and a TOPTICA TDS system of 1600 scans per second, two consecutive measurements would be still reading the same patch sample with a shift of only $500\text{ }\mu\text{m}$ between these two scans. Such small shift does not cause any changes in the average resonance of the pattern sample, which can still reveal the printing condition.

CHAPTER 5

CHARACTERIZATION OF ELECTRICAL PROPERTIES

This chapter is based on the work "Contactless in situ electrical characterization method of printed electronic devices with terahertz spectroscopy" (Zhuldybina *et al.* (2019b)). In this manuscript, terahertz time domain spectroscopy (THz-TDS) was employed to introduce a new contactless quality control method for industrial production of printed electronics devices.

To investigate the electrical properties, particularly conductivity, we have used the quality control structure in the shape of the metamaterials. Metamaterials was made from the V-shape antennas and aligned as a vortex phase plate (VPP). The VPP with the topological number $l = 1$ was designed according to the work of He *et al.* (2013). It is made of eight sectors, which supply a phase changing from 0 to 2π with a step size of $\pi/4$. Each sector was formed from one type of V-shaped antenna, as depicted in Figure 5.1, and made from two rectangular rods attached at one end at a specific angle (θ). We kept all geometrical aspect values of angles θ and β , whereas β was the angle between the bisector line of a V-shaped antenna and the x -axis. Due to the resolution of our printer, and according to the frequency spectrum of our THz source, the dimensions of the unit cell (p) and the length of the rod (h) were increased three-fold. A feature width (w) of $30\ \mu m$ was set and chosen according to the minimum dimension of printed silver ink traces, only limited by the printer spatial resolution. Figure 5.1 illustrates eight types of antennas with the notation of geometrical parameters. The full sample area consisted of 30×30 V-shaped antennas, with its central frequency expected to be around $0.25\ THz$.

Their properties were studying with THz-TDS and two microprobe station. Further, to validate the viability of characterizing PE with THz-TDS, we studied a prototype of a printed device in the rectangular shape was characterized with conventional characterization methods as AFM, 4-point probe, and two microprobes station. Figure 5.2 summarizes our investigation methods.

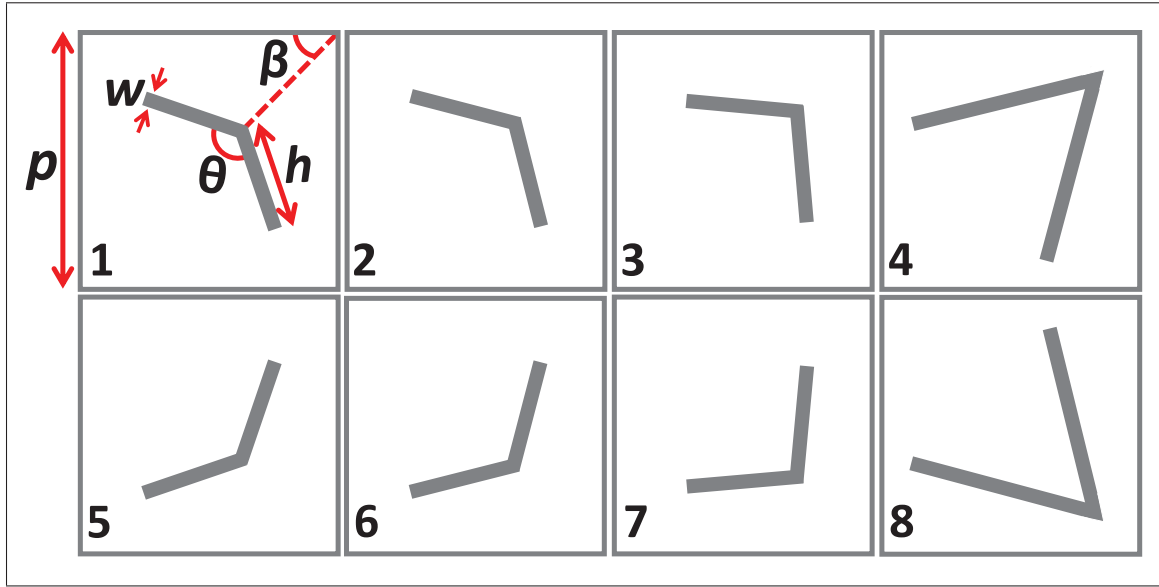


Figure 5.1 The design of V-shape antennas. Dimensions of $p = 600 \mu m$, $w = 30 \mu m$, $\beta = 45^\circ$ were kept the same for all antennas. The length of the rod $h = 234, 246, 270, 450 \mu m$ and the angle between rods $\theta = 130^\circ, 120^\circ, 100^\circ, 60^\circ$ according to order of antennas.

Taken from He *et al.* (2013)

5.1 Samples fabrication

Samples were printed using a Ceradrop F-Serie Inkjet Printer (Limoges, France) with 1 *pl* Dimatix cartridge (FUJIFILM Dimatix, Santa Clara, CA, USA). The drops were dispensed with a center-to-center distance between ejected drops of $20 \mu m$. Only one nozzle was used to perform the printing. The jetting frequency was set at 500 Hz . We used a commercially available conductive silver ink DGP 40TE-20C (ANP, Pleasanton, CA, USA) that contains silver nanoparticles (Ag NPs) of sizes around 50 nm with $30 - 35 \text{ wt.}\%$ in triethylene glycol monomethyl ether solvent (He *et al.* (2013)). The substrate used for printing was a heat-stabilized polyethylene terephthalate (PET) polyester film (Melinex ST505, New Berlin, WI, USA). The chuck was maintained at a constant temperature of 60°C during the printing process (Bolduc *et al.* (2018)). The sintering step was performed with an in situ Adphos Near Infrared (NIR) Dryer Module CER-42-250 (Bruckmühl, Germany). The displacement time of the lamp was varied from 0.03 s/mm to 0.2 s/mm to obtain a set of samples with different conductivities. A confocal laser microscope (Olympus LEXT OLS4000, Center Valley, PA, USA) was used to

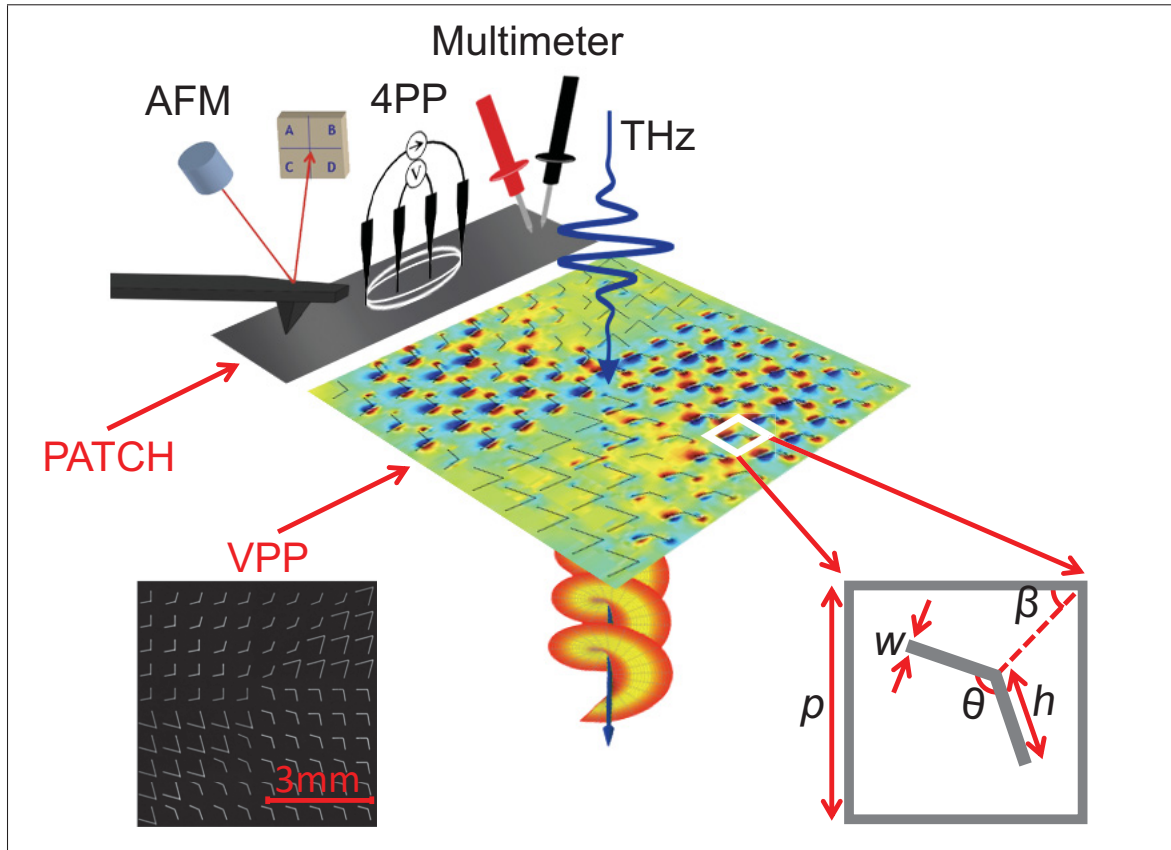


Figure 5.2 Sketch depicting the provided measurements: atomic force microscopy (AFM), four-point probe (4PP), multimeter, terahertz time-domain spectroscopy (THz-TDS). The left inset is the visible image of the center part of a printed vortex phase plate (VPP). The dark region is the substrate (PET) and the printed ink is shown with gray pixels. The right inset shows one representative V-shaped antenna unit with the geometrical parameters

determine the thickness of the printed structure, which was found to be around 400 nm . The precise definition of the V-shaped antennas observed in the left inset of Figure 5.2 confirms the ability of the inkjet printer to achieve the proper design.

5.2 Analysis with conventional methods

The conventional conductivity measurements were performed with a multimeter with two probes and the state-of-the-art four-point probe methods. Using a conventional multimeter instrument (MM) and two microprobes (S-shaped tungsten micro-probe tips), the electrical conductivity of

a print pattern was extracted using the following equation (Bolduc *et al.* (2018)):

$$\sigma = \frac{L}{RA_c}, \quad (5.1)$$

where σ is the electrical conductivity, R is measured resistance, L and A_c are the length and the cross-section area of a tested printed structure, respectively.

As it was described in the Chapter 1, the four-point probe method (4PP) enables higher precision measurements of the electrical conductivity. To ensure a perfect match between our sample size (semi-infinite surface) and the 4PP tips, the measurement set-up has four in-line array probes with the spacing of $100 \mu m$ (MCW-28-7188, GGB industries, Naples, FL, USA). The measurement with 4PP provides a sheet resistance in which the conductivity value is extracted using the following equation (Kang, Kim, Ryu, Hahn, Jang & Joung (2010)):

$$\sigma = \frac{\ln(2)}{\pi t R}, \quad (5.2)$$

where the geometric factor $\frac{\ln(2)}{\pi}$ describes the current rings emanating from the outer probe tips, t is the thickness of the patch and R is the measured sheet resistance. The evaluation of the geometrical correction factor is described in Appendix III.

To confirm the good agreement between the conductivity of the printed control bar and the conductivity value of the patch, we also measured the resistance of a V-shaped antenna with two microprobes (2MP) and extracted its conductivity. Finally, to ensure that the sintering speed was responsible for the changes in conductivity, the surface morphologies of the printed samples were characterized using the AFM (EnviroScope, Santa Barbara, CA, USA) system in tapping mode.

5.3 Terahertz time-domain spectroscopy

We have utilized the same setup as described in Chapter 4, except we did not use the purged box and all experiments were conducted in the ambient conditions.

5.3.1 Normalized transmission

Figure 5.3a shows the recorded time-domain traces of the reference and sample signals, where PET substrate was used as a reference. Using FFT and the normalization procedure, the normalized transmission was extracted. Figure 5.3b illustrates the normalized transmission amplitude of the different VPP samples obtained from equation 2.15. A dip in the transmission is observed due to the generation of a vortex beam at 0.22 THz , as expected. As mentioned previously, a higher resonance response (i.e., which translates to a lower transmission at 0.22 THz) indicates a sample with higher electrical conductivity.

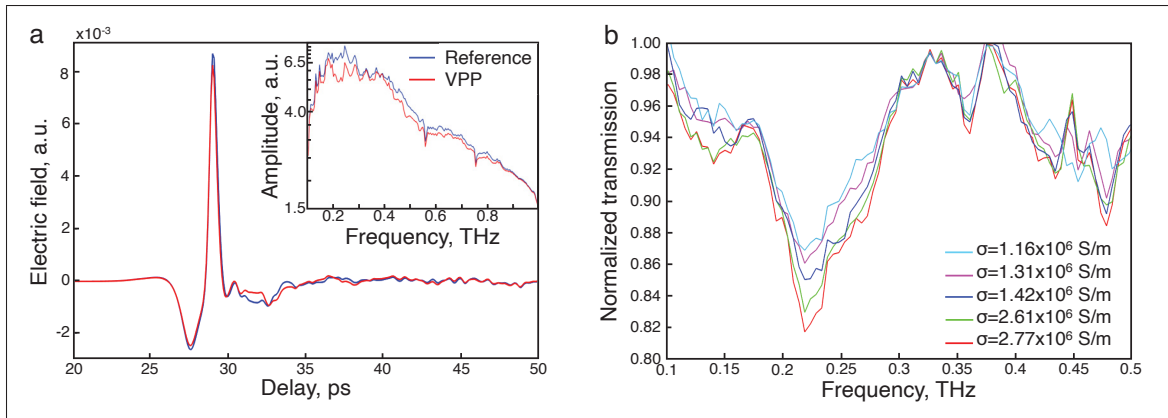


Figure 5.3 a) Time-domain spectra of a VPP with the highest conductivity and its reference and inset shows the spectra obtained with FFT.
b) Normalized transmission spectra of the set of samples

5.3.2 Dual-wavelength terahertz spectroscopy

Figure 5.4a shows the selected areas for the calculation of the integral. The signal region ($\omega_1 - \omega_2$) was chosen around the central frequency of VPP at 0.22 THz . We have studied the influence of the selection of the bandwidth of the integrated areas: 9.8 GHz ($0.2197 - 0.2295\text{ THz}$); 29.3 GHz ($0.21 - 0.2393\text{ THz}$) and 49 GHz ($0.195 - 0.244\text{ THz}$). To evaluate the precision of the chosen areas, the standard deviation has been calculated from three measurements of signal. Figure 5.4b shows the variation of the standard deviation as a function of different bandwidth

and different reference areas, as explained in Chapter 2.3.4. Basically, the spikes appear at the water absorption lines, which are more sensitive for smaller bandwidth of the integrated areas. This fact opens the door for CW sources characterization, where the bandwidth is in the range of a few MHz. For the calculation of integral in this experiment, the reference area was chosen at $0.195 - 0.244 THz$. The reference signal corresponds to the area around $0.615 - 0.664 THz$ based on the finding in Chapter 4.3.2 to avoid the water absorption lines that can occur due to ambient humidity.

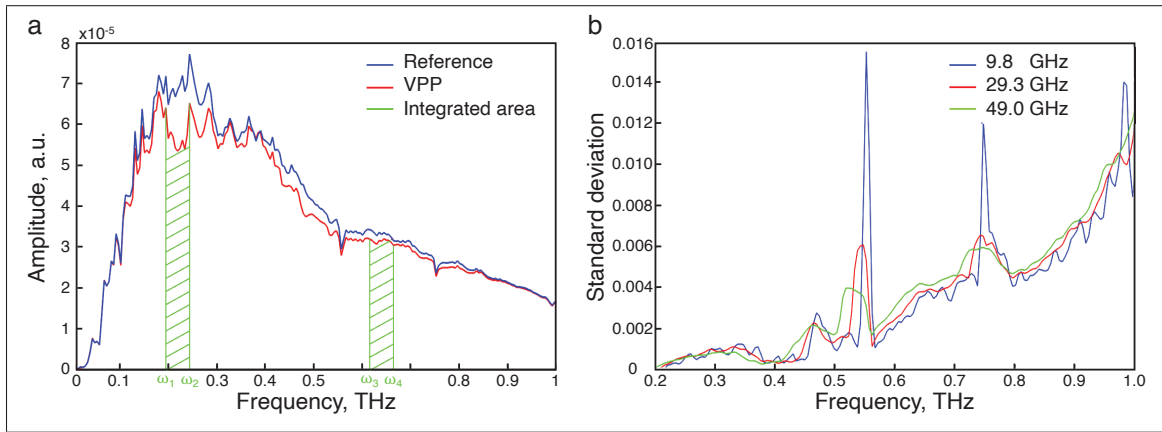


Figure 5.4 a) Transmitted amplitude THz spectra of a VPP with the highest conductivity and a substrate (PET), where the transmission dip from ω_1 to ω_2 shows the signal signature and no difference from ω_3 to ω_4 represents a reference signal.
b) Standard deviation of DTWS analysis for different bandwidth of integrated areas

5.3.3 Simulations

To validate the accuracy of THz sensing of vortex plates as a function of material conductivity, we performed 3D finite difference time domain (FDTD) simulations using the Lumerical software. A THz Gaussian beam with a central frequency at $0.26 THz$ has interacted with a VPP placed in the air to avoid Fabry-Perot effect coming from a plastic substrate. The central frequency of the pulse was chosen in order to use most of the energy for the interaction with VPP designed for $250 GHz$. The duration of the pulse was $709 ps$ to get better the low-frequency resolution. To access the far-field information, a 2D monitor was set $60 mm$ under the structure. In simulation only E_y component of electromagnetic field was extracted. VPP had a defined and uniform

conductivities of a hypothetical printed metal. The reference information was taken by sending the beam in an empty space. To confirm our simulation adjustment, an SRR structure was placed in the same conditions and compared with the reference. Figure 5.5 shows the overlap with reference results, as it was discussed in the Chapter 3.1.4. This simulation result shows the very high sensitivity at 0.26 THz for conductivity variation and opens the possibility of using SRR structure as a quality control structure for conductivity characterization of printed electronics.

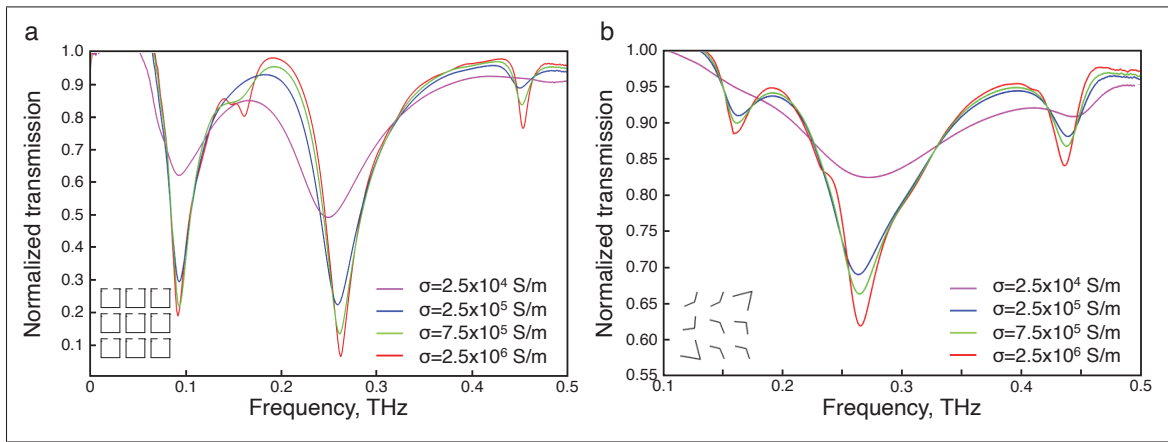


Figure 5.5 Simulated transmission of a) SRR and b) VPP with different conductivities

Figure 5.5b shows the simulated transmission spectra of VPPs, which have been designed for our experiment. The central frequency of the designed VPP is located at 0.260 THz , and the transmission dips from the left and right correspond to the resonance frequencies of the individual V-shape antennas. It is clearly observed that the transmission decreases as a metal conductivity function. Additionally, the position of the transmission dip is slightly move to the right for a higher conductive samples as it was shown in Chapter 3.1.4. The experimental (Figure 5.3b) and simulation differ in the degree of transmission difference as a function of metal conductivity. We attribute this difference to the perfect reading of the central vortex information in the simulated case. Practically, the photoconductive antenna reads a spatially integrated range of information containing the central intensity part of a donut-shaped beam, together with a large

contribution from its wings. Nevertheless, the numerical simulations are in good agreement with experimental findings.

The correlation between metal conductivity and simulated transmission values is shown in Figure 5.6. It is important to note that this function clearly reveals the extremely high sensitivity of THz wave sensing for low conductivity samples (e.g., below $1 \times 10^7 \text{ S/m}$, the blue dotted region in inset). Above this conductivity value, the dip in transmission exhibits less sensitivity, with an almost saturated behavior (i.e., closer to a perfect metal resonance).

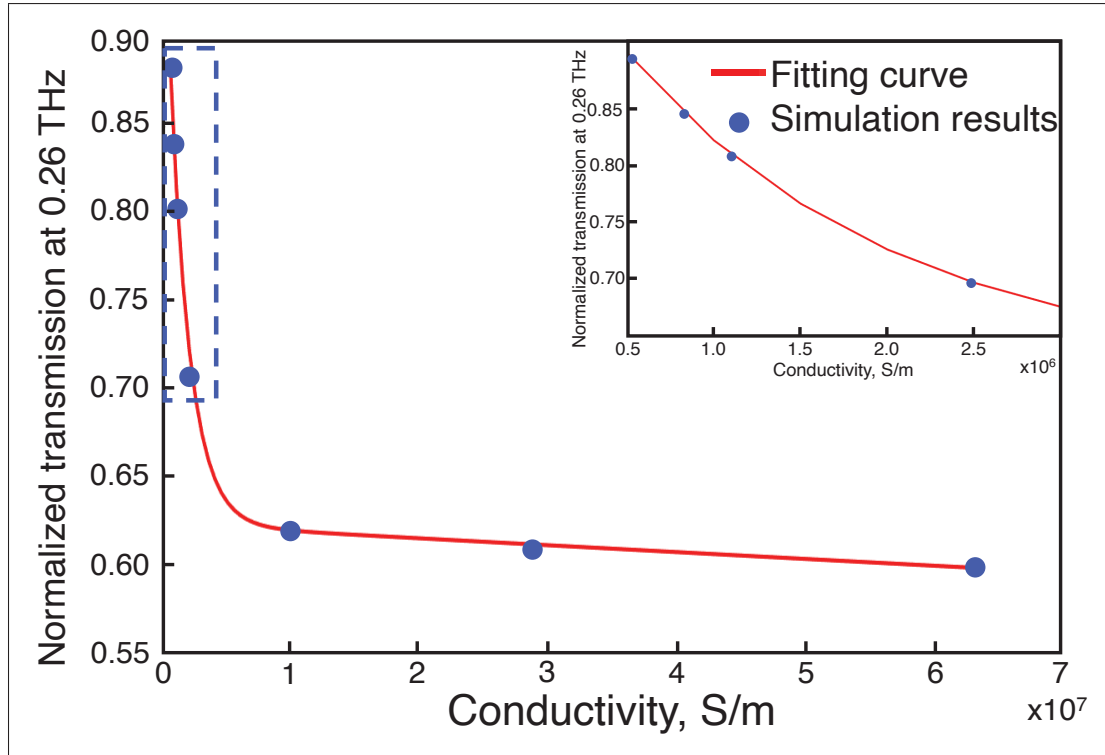


Figure 5.6 Simulated transmission amplitude at the central frequency of VPP (0.26 THz) vs. conductivity. The inset shows the blue dotted region

5.4 Comparison of results

Figure 5.7 gives the measured conductivity of five samples using four different methods: 2MP, 4PP, THz-TDS and DWTS as a function of sintering speed. The error bar corresponds to the standard deviation obtained from ten measurements for each method. The 4PP method was

performed on the patch samples, while 2MP, THz-TDS, and DWTS measurements provide the corresponding conductivity results from the VPP samples. To compare the performance of THz-TDS and 4PP, the THz transmission amplitudes at 0.22 THz were calibrated to the expected conductivity values obtained from 4PP. Since the 4PP measurements cover a limited range of conductivity, from $1 \times 10^6\text{ S/m}$ to $3 \times 10^6\text{ S/m}$, a simple calibration using a linear fit was chosen (in agreement with inset of Figure 5.6). We assumed that the non-sintered sample would always have the same conductivity and choose it as the starting point. Its transmission value of 0.88 was related to $1.15 \times 10^6\text{ S/m}$ obtained from 4PP analysis.

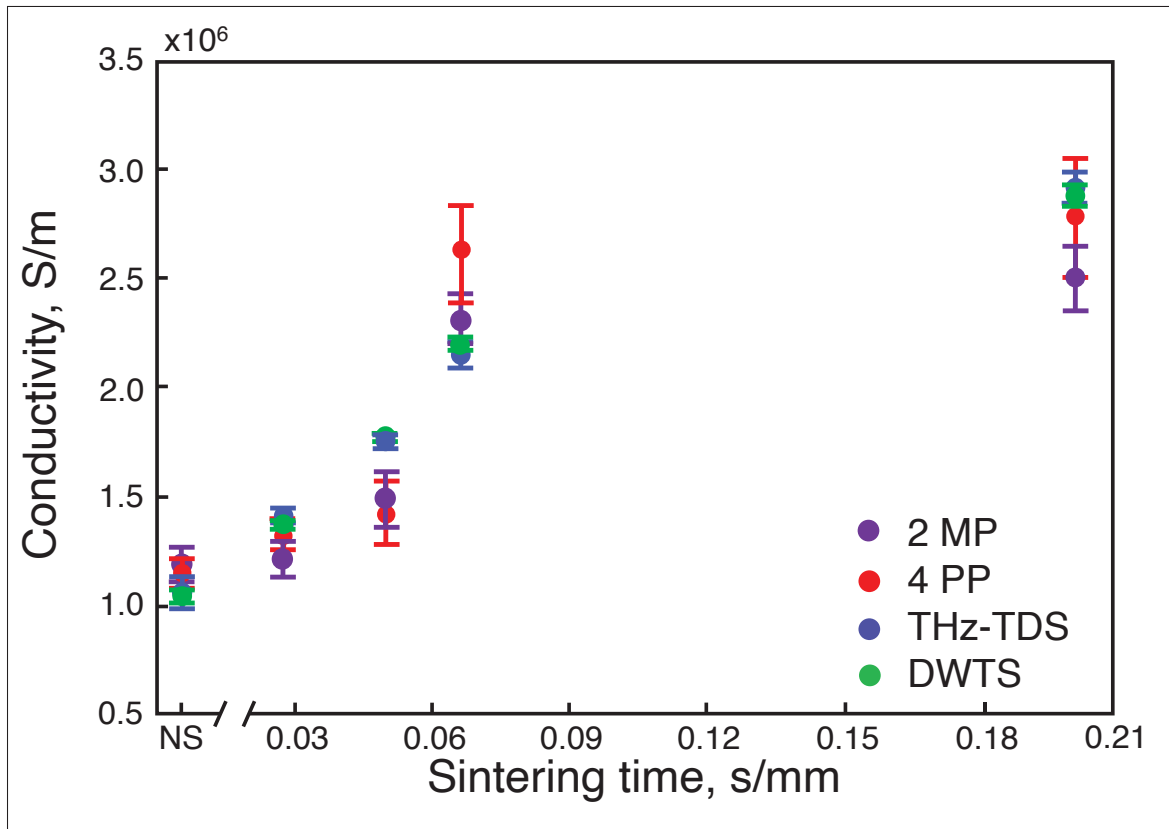


Figure 5.7 Comparison of the conductivity values obtained by two microprobes (2MP) (violet), 4PP (red), normalized transmission from THz-TDS (blue) and DWTS (green) as a function of sintering time

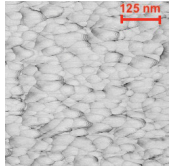
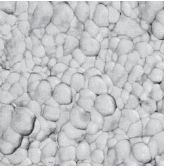
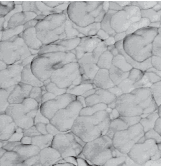
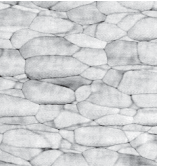
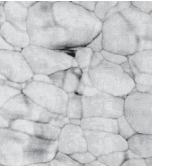
Figure 5.7 shows similar increases in conductivity behavior as a function of sintering exposure time for the measurements taken by THz-TDS and 4PP. More importantly, all sintering conditions

are well discriminated by THz measurements, whereas 4PP failed in differentiating the three lowest conductivity conditions (i.e., $< 1.5 \times 10^6 \text{ S/m}$), and the two highest conductivity conditions (i.e., $> 2.5 \times 10^6 \text{ S/m}$). Besides, we repeated the measurements ten times for each method and calculated the standard deviation. Interestingly, THz-TDS exhibits better repeatability than the conventional 4PP method. We attribute this difference to the contactless nature of the THz method: 4PP can locally damage the ink surface and may render repeated measurement less accurate. Similarly to THz-TDS, the integral values from DWTS were normalized and calibrated with respect to the retrieved conductivity using the 4PP method.

In the final step, we review the patch versus VPP samples' analysis using the various methods described previously. Table 5.1 summarizes the obtained results. To establish a comparative measurement performance, we carried out several resistance measurements at the different patch and V-shaped antennas and presented their relative standard deviation (RSD). As mentioned previously, the 4PP and multimeter retrieved the resistance on the patch. To clearly validate that VPP conductivity is linked to patch conductivities, 2MP was also used to evaluate the VPP resistance directly. It has to be mentioned that, due to the extremely small effective volume of VPP unit cell, the 2MP method can easily over- or underestimate the conductivity (e.g., conductivity dependency on sample volume, as shown in (5.2)). However, the 2MP measurements confirmed the good agreement between the sintering exposure time for the patch and VPP samples together.

In order to confirm the provided conductivity measurements, the evolution of the sintering of Ag ink was studied using AFM analysis at five different sintering stages. The last row of Table 5.1 depicts the printed ink surfaces after sintering. The non-NIR-sintered sample (NS) showed poor contact between Ag NPs, resulting in the lowest conductivity ($1.15 \times 10^6 \text{ S/m}$). The next stage of sintering for the sample with the shortest annealing time (0.03 s/mm) shows necks began to grow between NPs prompted by surface energy minimization. With a longer annealing time of 0.05 s/mm , the NPs get more compact and the printed structure densifies.

Table 5.1 Comparison between terahertz results: THz-TDS & DWTS and conventional techniques: 4PP—four-point probe; MM—multimeter; 2MP—two microprobes; AFM - Atomic Force Microscopy

| Sintering time | | Not Sintered | 0.03 s/mm | 0.05 s/mm | 0.07 s/mm | 0.2 s/mm |
|---|---------|---|---|---|---|---|
| Conductivity, $\times 10^6 \text{S/m}$ Obtained by | 4 PP | $1.15 \pm 4.70\%$ | $1.31 \pm 4.47\%$ | $1.42 \pm 10.3\%$ | $2.61 \pm 8.67\%$ | $2.77 \pm 9.82\%$ |
| | MM | $1.10 \pm 21.1\%$ | $1.19 \pm 12.1\%$ | $1.48 \pm 17.9\%$ | $2.15 \pm 22.2\%$ | $3.01 \pm 36.7\%$ |
| | 2MP | $1.23 \pm 6.59\%$ | $1.28 \pm 8.44\%$ | $1.49 \pm 8.73\%$ | $2.29 \pm 6.83\%$ | $2.51 \pm 7.58\%$ |
| | THz-TDS | $1.08 \pm 6.14\%$ | $1.38 \pm 3.06\%$ | $1.75 \pm 1.55\%$ | $2.14 \pm 2.52\%$ | $2.91 \pm 2.77\%$ |
| | DWTS | $1.06 \pm 3.44\%$ | $1.37 \pm 1.28\%$ | $1.78 \pm 1.21\%$ | $2.18 \pm 1.44\%$ | $2.89 \pm 1.80\%$ |
| | AFM |  |  |  |  |  |

It shows that a slight increase of annealing time to 0.07 s/mm led to a further increase in conductivity. The longest annealing time (0.2 s/mm) led to the highest density and the highest conductivity ($2.77 \times 10^6\text{ S/m}$). According to AFM observations of the surface morphology of the samples, the obtained samples were consistent with the sintering parameters and measurements of the conductivity with different techniques.

As shown Table 5.1, as expected, the measurements provided by a conventional multimeter were the least precise since the probes of the multimeter easily break the patch's surface after contact. Meanwhile, the micro-probe provides a safer way to avoid destroying the sample surface. The average conductivities measured with the different techniques are in the same range and have similar behavior as a function of the sintering time. It should be emphasized that the trend in electrical static conductivity measurements on the printed patch and the VPP using the different techniques are all in good agreement. This confirms the feasibility of characterizing the variability in ink conductivity during mass production of PE devices simply by reading a test structure. Finally, the best RSD for repeatability was obtained for DWTS and THz-TDS.

The main reason to choose VPP for the quality control of conductivity was its self-normalization inside one measurement. As it was observed in the transmission spectra, the deep of the vortex is varied as a function of the conductivity. Theoretically, by measuring the vortex's strength in the center and on the wings, the conductivity variation can be extracted within one single measurement.

5.5 Near-Field microscopy

In the previous section, the printed vortex phase plate has been studied as a function of conductivity using terahertz time-domain spectroscopy (Zhuldybina *et al.* (2019b)). Our idea was that the intensity of the generated vortex beam is directly related to the conductivity of the printed ink. To evaluate the influence of the printed ink onto the generation of the vortex beam, the one type of V-shape antennas has been studied using near-field THz microscopy described in the Chapter 2.4.

To achieve vortex beam generation around $\sim 300\text{ GHz}$, the dimensions of the V-shape antennas have been changed accordingly compared with Figure 5.1. For near field analysis, Figure 5.8a shows the designed vortex phase plate, where the longest V-shape antenna has been taken for the investigation shown in Figure 5.8b.

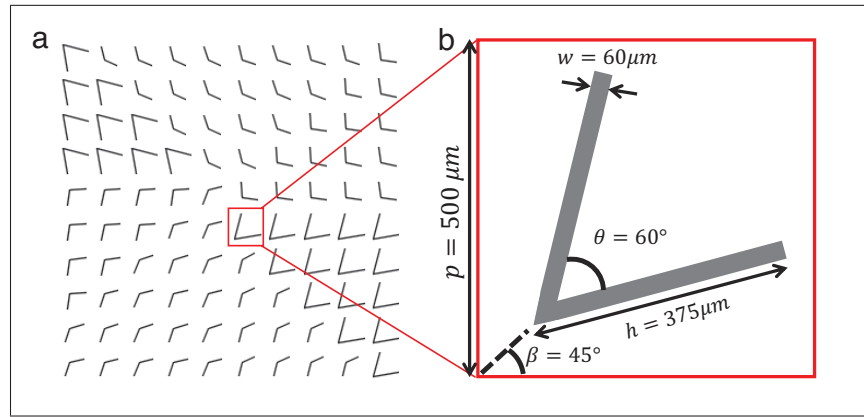


Figure 5.8 a) A designed vortex phase plate;
b) A studied V-shape antenna

The set of samples was printed in the same manner as it was described in the Chapter 5.1. However, the sintering step has been changed from photonic to thermal treatment as described in Chapter 1.2.3 to achieve higher conductivity. We have investigated two samples, where one of them was sintered at the temperature of 180°C and the other was slightly heated ($\sim 60^\circ\text{C}$) during the printed process. The resistivity has been measured with a conventional 4PP. The thickness of sample was evaluated using an [optical profilometer](#). The conductivity was obtained using the equation (5.2). The main characteristics of samples are summarized in the Table 5.2.

Table 5.2 Summary of studied samples

| Sample | Sintered sample (SS) | Non-sintered sample (<i>n</i> -SS) |
|------------------------------------|----------------------|-------------------------------------|
| Thickness, <i>nm</i> | 500 | 500 |
| Sheet Resistance, Ω/\square | 0.13 | 7.11 |
| Conductivity, <i>S/m</i> | 2.7×10^6 | 4.9×10^4 |

The visual image of the studied samples has been taken with the Olympus microscope. The near field experiment was carried out using the experimental set-up shown in Figure 5.9. The

main difference between Figure 2.12 (Blanchard *et al.* (2011,1); Doi *et al.* (2011)) and the used set-up is a new type of sensor used in this investigation (Guiramand *et al.* (2020)). Previously, an x -cut LiNbO_3 (LN) crystal with a thickness of $20\ \mu\text{m}$ was used, mounted on a 0.5--mm thick glass. This sensor produced a first echo of its back reflection after only 7.5 ps , limiting the total scanning time and therefore the spectral resolution.

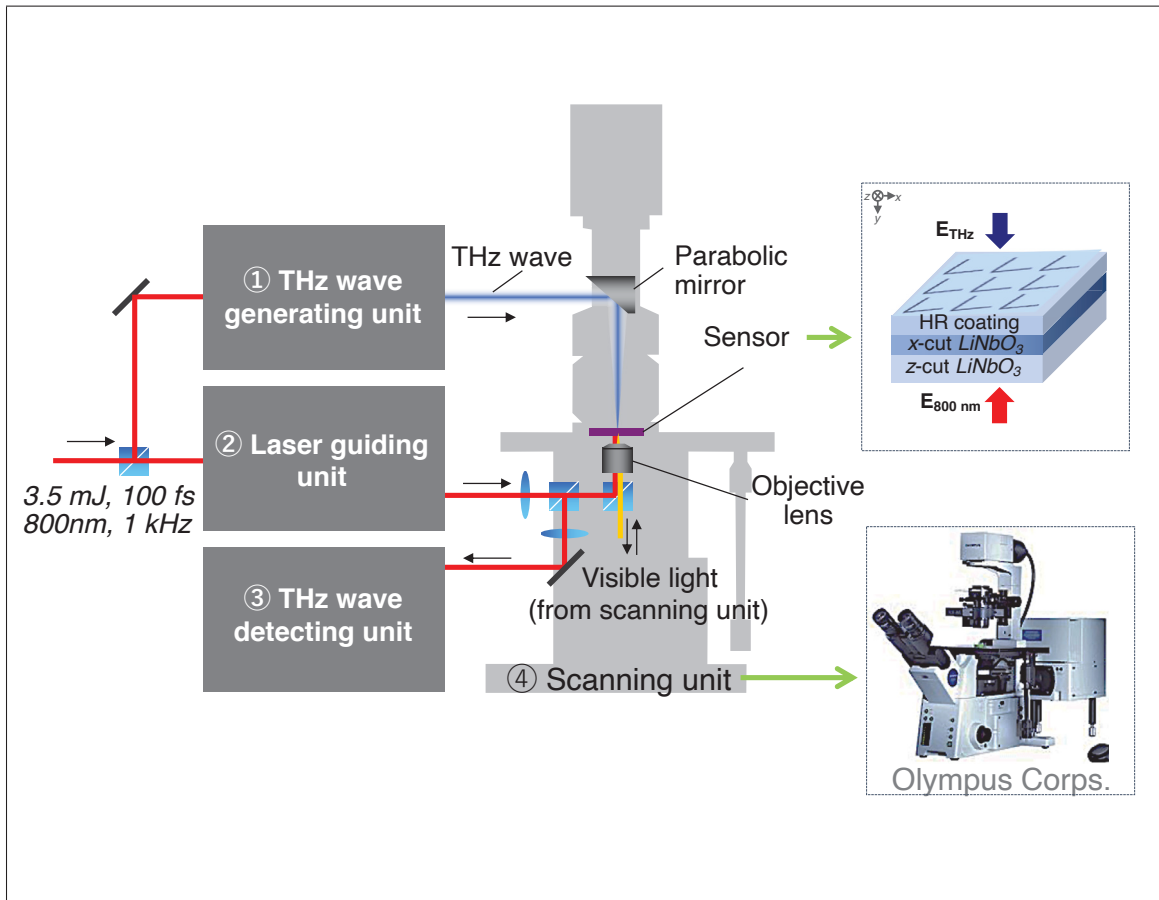


Figure 5.9 Near-field THz microscope made from the four main parts: (1) THz wave generating unit; (2) Laser guiding unit; (3) THz wave detecting unit; (4) Scanning unit. The top zoom image is sketch of the new sensor made from $10\ \mu\text{m}$ x - and 1 mm z - cut LN crystal. The bottom zoom image is a photo of the Olympus microscope

Our new sensor is composed of an x -cut LN crystal with a thickness of $20\ \mu\text{m}$ mounted on a 1.0--mm thick z -cut LN crystal. The use of a thick passive z -cut LN crystal as substrate allows to delay the echo signal of the main signal of by ~ 8 times compared to previous EO sensors.

Figure 5.10a shows that the temporal scan duration was 24 ps with the spectral resolution of 37 GHz versus 7.5 ps time-duration and $\sim 133\text{ GHz}$. Figure 5.10b shows the frequency domain results with improved spectral resolution. As it can be seen, it allows for the improvement of the low-frequency response and spectral resolution (Guiramand *et al.* (2020)).

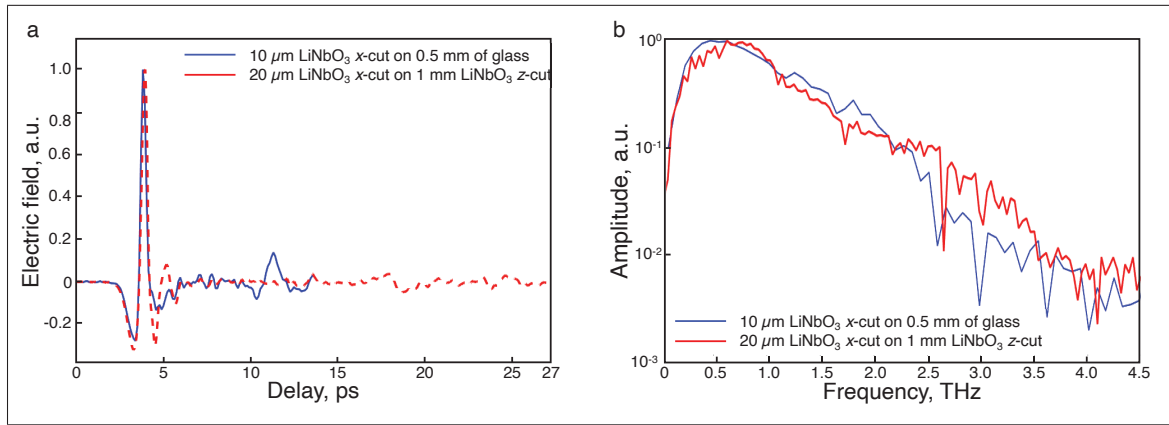


Figure 5.10 a) THz pulses using $10\text{ }\mu\text{m}$ - and $20\text{ }\mu\text{m}$ -thick x -cut LN crystals mounted on 0.5 mm -glass and 1 mm z -cut LN crystal.
b) Corresponding frequency spectra

To see the THz electric field evolution in the near-field region of a SS and n -SS, we performed time-domain two-dimensional near-field THz imaging. A movie obtained without a sample served as a reference. Both movies (sample and reference) are 300 frames long with a 53 fs time step. The full duration of the movie was 27 ps . All frames with the size of $1080 \times 960\text{ pixels}$ were obtained from 100 averaged images taken at a 35 Hz repetition rate and repeated 2 times. The images area was $2.5 \times 2.5\text{ mm}^2$. The reference signal has been taken through a PET substrate. We normalized the sample movie to the reference movie to clarify the resonance behavior of V-shape antennas.

Figure 5.11 shows the visible, normalized amplitude and phase images of a printed V-shape printed antennas with two conductivity values. The extracted profile is plotted in the last column. From the initial observation of the visual image, the extracted profile of SS and n -SS shows almost no difference in the x -direction. The amplitude and phase images were obtained after applying of 2D FFT to the movies. The THz-near-field images are shown at the resonance

frequency of the V-shape antenna 0.22 THz , which corresponds to the spatial length of $750\text{ }\mu\text{m}$ of the printed silver. From the normalized amplitude images, it can be clearly seen the appearance of the charges on top of the antennas with the higher conductivity in the direction of the THz propagation.

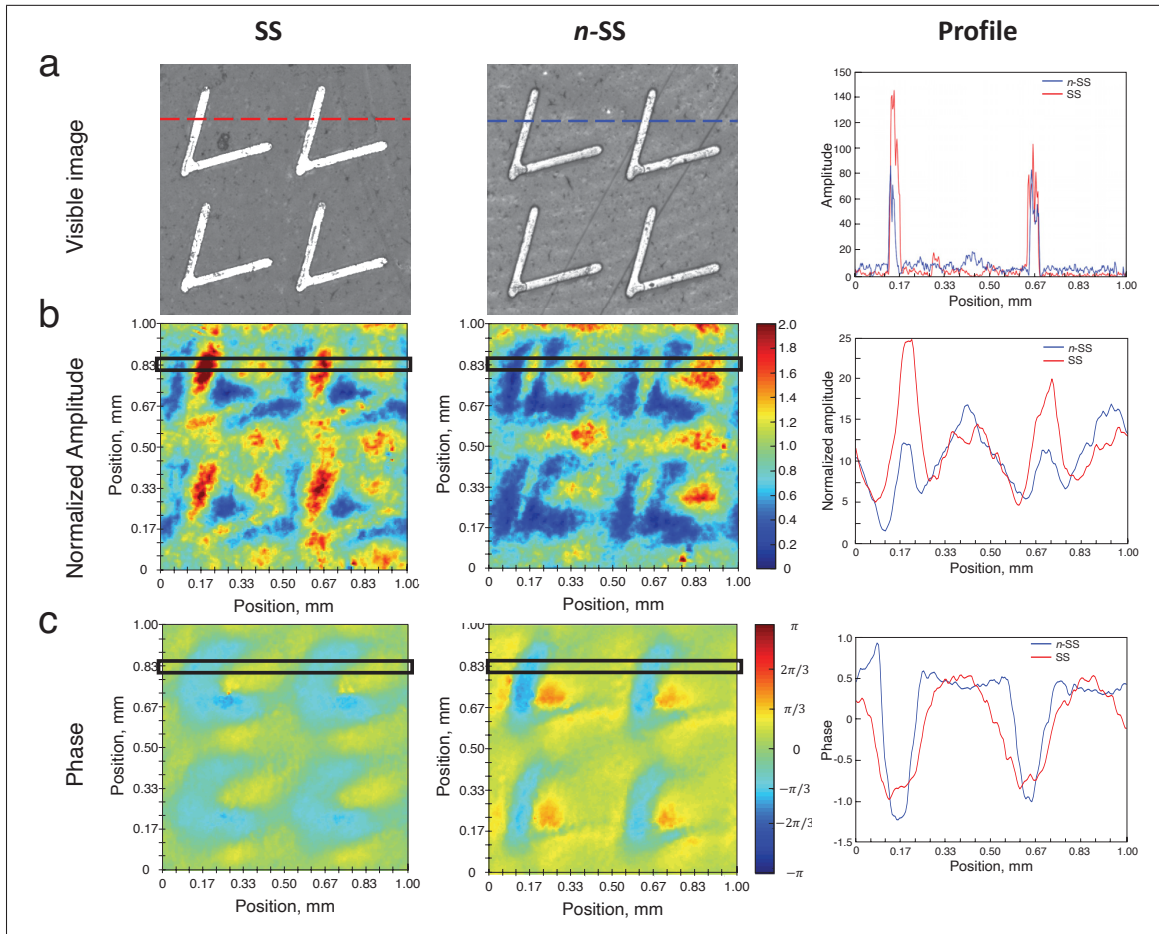


Figure 5.11 a) Visible image of sintered and non-sintered samples; on the right-hand side is the profile of the extraction red dashed line.

THz near-field images in the frequency domain at 0.22 THz of

b) the amplitude and c) the phase, respectively, with the corresponding profile. The profile has been extracted for the area of $55\text{ }\mu\text{m}$

The profile of the images was extracted for an area of 10 pixels thick which corresponds to the dimension of $\sim 55\text{ }\mu\text{m}$. From the extracted profile at the resonance frequency, it is clear the appearance of the enhancement for the SS. The transmission of SS is twice bigger than n-SS.

Further, the profile has been taken for range of frequencies. Figure 5.12 shows the extracted profile of SS (line) and n -SS (dash-line) for five frequencies: 0.1474 THz , 0.1843 THz , 0.2211 THz , 0.2580 THz , and 0.2948 THz . The positions of the transmission maximums correspond to the position of the antenna's arms parallel to the polarization of the THz field. Looking at the variation of the amplitude, it is clear that the resonance frequency of the V-shape antenna is 0.22 THz . Afterwards, the maximum of the transmission has been extracted for two positions: $\sim 0.2\text{ mm}$ and 0.67 mm . This two profiles clearly show the decreasing of the enhancement after the resonance frequency, where the normalized transmission decreases with the factor of 1.11 for both samples. By investigation of the set of samples with different conductivities, it will be possible to find out the correlation between the normalized transmission amplitude and the conductivity values.

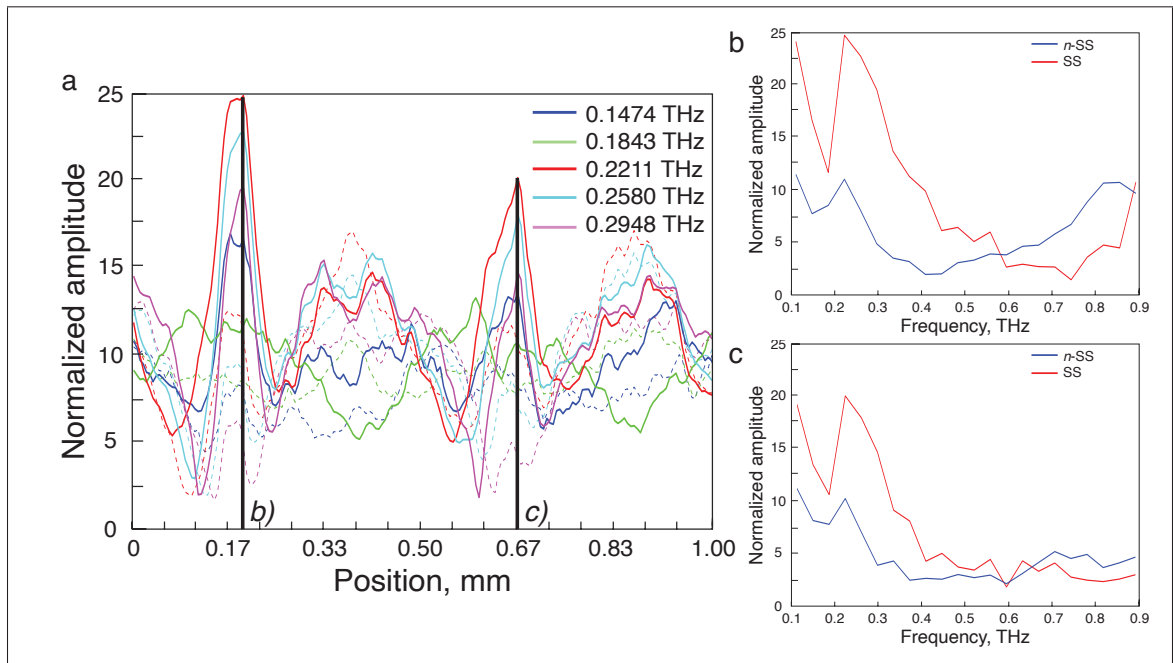


Figure 5.12 a) The extracted profile of SS (line) and n -SS (dash-line) at 0.1474 THz , 0.1843 THz , 0.2211 THz , 0.2580 THz , and 0.2948 THz . The black lines show the position of the extraction of the normalized amplitude.

b) and c) The maximum of normalized amplitude at $\sim 0.2\text{ mm}$ and 0.67 mm for the frequency range from 0.1 THz to 0.9 THz

We evaluated the spatial resolution of the microscope by taking the time-resolved spatial distribution of the electric field of an edge varying from 10% to 90% in amplitude. We found a spatial resolution of $36\ \mu\text{m}$ with a $20\text{ -- }\mu\text{m}$ -thick LN x -cut crystal optically contact onto 1 -- mm -thick LN z -cut.

For the first time, to the best of our knowledge, we have demonstrated the near-field observation for the inkjet printed metamaterials.

CONCLUSION AND RECOMMENDATIONS

In conclusion, we developed a novel technique based on metamaterials working in the terahertz (THz) range for quality control of industrial printing process of printed electronics (PE) devices. The advantage of using metamaterials is its ability to be scalable to any terahertz resonance frequency.

In the framework of this thesis, two types of metamaterials have been designed and studied for the inspection of printing quality.

Metamaterials in the shape of a metallic checkerboard pattern (MCB) rotated at 45° were implemented for tracking the amount of deposited ink and the expected dimensional accuracy during the printing process. MCB exhibits Babinet's principle transmission at 0.20 THz and reveals its transmission signature's direct influence with the printed quality. MCBs have complementary transmission properties, which are drastically varied due to the connection or separation between neighboring rhombuses. The samples have been printed in industrial conditions using a variable speed flexography printing press. Using the single point THz spectroscopy method, we have revealed that the resonance behavior of MCBs is very sensitive to the variation of the printing speed. The THz information can track the geometrical accuracy and amount of printed ink with a similar precision level as an optical microscope for visible light. 2D optical microscopy and 1D THz time-domain spectroscopy (THz-TDS) methods are in excellent agreement with each other.

For quality control of electrical conductivity, we designed a vortex phase plate (VPP). The VPP was formed from V-shaped antennas with a central frequency at 0.22 THz and was studied for the range of conductivities. THz-TDS was employed to analyze the transmission properties of printed VPP. Our results showed that the THz transmission response of a resonant sample enables us to follow the changes in the sintering condition of the printed ink. We validated our results with a simulation study and introduced dual-wavelength THz spectroscopy (DWTS) as a

fast and straightforward method to quickly determine the transmission response of VPP. Our analysis also confirms the similar conductivity behavior between adjacent printed structures and the VPP sample as a function of sintering exposure time. This important observation enables to track the changes in the sintering process of PE devices during the manufacturing process using a simple control bar. Finally, using the conventional four-point-probe method as a reference, we confirmed that a calibrated quality control bar in the shape of the VPP could be used to determine the static electrical properties of non-resonant printed devices that are printed simultaneously with the VPP samples.

THz-TDS could be conveniently adopted for routine quality control of PE in the industry, which should allow PE to maintain a required printing accuracy. Our results pave the way for a remote characterization tool to probe the dimensional accuracy and could ultimately be used as feedback parameters for improving the overall printing performances in real-time. Being a non-contact and non-destructive testing technique, it is highly suitable for in-line characterization of high-speed roll-to-roll printing repeatability of PE devices.

We have shown that our single measurement approach reduces the measurement time and avoids measuring the reference information. With the development of THz technology, we believe that our strategy could be adapted for industrial measurements with two compact CW sources with signal and reference signals.

The new THz sources based on CMOS or RDT technologies are in the development/lab stage. These technologies will reach out to the higher technology level in the near future and be applied to our strategy for quality control

The outcome of my project opens the door for in-line quality control of PE devices and strongly helps the development of PE at the industrial scale. Nowadays, I found a company: TRAQC, which is working on bringing my PhD project to the PE industry.

Thus, my PhD goal directly correlates to the main moto of ÉTS: "Engineering for industry".

RESEARCH CONTRIBUTIONS

This work has been published in the peer-reviewed journals.

- M. Zhuldybina, X. Ropagnol, C. Bois, R. J. Zedik and F. Blanchard, "Printing accuracy tracking with 2D optical microscopy and super-resolution metamaterial-assisted 1D terahertz spectroscopy", *npj Flexible Electronics* 4 (1), 1-7 (2020)
- M. Zhuldybina, X. Ropagnol, C. Trudeau, M. Bolduc, R. J. Zedik and F. Blanchard, "Contactless In Situ Electrical Characterization Method of Printed Electronic Devices with Terahertz Spectroscopy", *Sensors* 2019, 19(3), 444 (Editor choice, Cover page)

The result of the work has been patented.

- F. Blanchard; M. Zhuldybina, inventors; Method of assessing ink deposition accuracy in an electronic device printing process; PCT/CA2020/051590
- F. Blanchard; M. Zhuldybina, inventors; 05.12.2019; Electronic device testing system, electronic device production system including same and method of testing an electronic device; WO/2019/227220; PCT/CA2019/050743

As well as, it has been presented at local and international conferences in the form of oral and poster presentations.

- M. Zhuldybina, X. Ropagnol, C. Bois, R. J. Zedik and F. Blanchard, "Quality Control of Conductive ink distribution using terahertz spectroscopy", *IRMMW - THz, Virtual conference* (November 9-13, 2020)
- M. Zhuldybina, X. Ropagnol, C. Bois, R. J. Zedik and F. Blanchard, "Perspectives of Using Two Terahertz Frequencies for Industrial Quality Control of Printable Electronics", *OSA Advanced Photonics Congress, Virtual conference* (July 13-16, 2020)
- L. Guiramand, M. Zhuldybina, T. Arikawa, K. Tanaka, F. Blanchard, "Near-field THz imaging of a printed metallic checkerboard pattern", *OSA Advanced Photonics Congress, Virtual conference* (July 13-16, 2020)
- M. Zhuldybina, X. Ropagnol, C. Bois, R. J. Zedik and F. Blanchard, "Babinet's principle for quality control of printed electronics", *22d Photonics North, Virtual conference* (May 26-28, 2020)
- M. Zhuldybina, X. Ropagnol, C. Trudeau, M. Bolduc, R. J. Zedik and F. Blanchard, "Contactless characterization of the conductivity of printed devices", *The third Montreal photonics networking event*, Montréal, Canada (December 5, 2019)
- M. Zhuldybina, X. Ropagnol, C. Trudeau, M. Bolduc, R. J. Zedik and F. Blanchard, "Quality control of printed electronics with terahertz waves", *CAÉC ÉTS*, Montréal, Canada (November 20, 2019)

- M. Zhuldybina, X. Ropagnol, C. Trudeau, M. Bolduc, R. J. Zedik and F. Blanchard, "Quality control of printed electronic devices", *Women in Physics = Femmes en Physique*, Montréal, Canada, (June 25-28, 2019)
- M. Zhuldybina, X. Ropagnol, C. Trudeau, M. Bolduc, R. J. Zedik and F. Blanchard, "Caractérisation d'électronique imprimable", *87e Congrès de l'Association francophone pour le savoir(ACFAS)*, Gatineau, Canada, (28-30 mai, 2019)
- M. Zhuldybina, X. Ropagnol, C. Bois, R. Zednik, F. Blanchard, "Dual-wavelength terahertz spectroscopy", *21st Photonics North Conference*, Québec, QC, Canada, (May 21-23, 2019)
- M. Zhuldybina, X. Ropagnol, C. Trudeau, M. Bolduc, R. J. Zedik and F. Blanchard, "Contactless characterization of printed electronic devices with a printed terahertz vortex phase plate", *OTST-2019*, Santa Fe, New Mexico, USA (2019)
- X. Ropagnol, Zs. Kovács, B. Gilicze, M. Zhuldybina, F. Blanchard, S. Szatmári, I.B. Földes and T. Ozaki, "Intense Sub-terahertz radiation from wide bandgap photoconductive antennas excited by UV laser beam", *OTST-2019*, Santa Fe, New Mexico, USA (2019)
- M. Zhuldybina, X. Ropagnol, C. Trudeau, M. Bolduc, R. J. Zedik and F. Blanchard, "Terahertz quality control pattern for printed electronic devices", *LaCIME*, Montréal, Canada (2019)
- B. Bastola, M. Zhuldybina, X. Ropagnol, H.Cusson-Bouthillier and F. Blanchard, "Identification of the optimum THz emitter to perform compressive sensing THz microscopy capability", *LaCIME*, Montréal, Canada (2019)
- X. Ropagnol, Zs. Kovács, B. Gilicze, M. Zhuldybina, F. Blanchard, S. Szatmári, I.B. Földes and T. Ozaki, "Sub-terahertz radiation from large aperture photo-conductive antennas excited by UV laser beam", *EuroLab meeting*, Paris, France (2018)
- M. Zhuldybina, X. Ropagnol, C. Trudeau, M. Bolduc, R. J. Zedik and F. Blanchard, "Terahertz-characterization of a printed vortex phase plate", *iCamp-2018*, poster, Montréal, Canada (2018)
- M. Zhuldybina, X. Ropagnol, C. Trudeau, M. Bolduc, R. J. Zedik and F. Blanchard, "Terahertz vortex phase plate from a printed electronic device", *20th Photonics North*, Montréal, Canada(2018)

I had a chance to participate in the international collaborations.

- 2019 International collaboration, Solid State Spectroscopy Group, Kyoto University, Kyoto, Japan.
Near-field THz microscopy of v-shape antennas with different conductivities; vortex phase plates
- 2019 International collaboration, Laser & Photonics in Aquitaine, University of Bordeaux, Bordeaux, France.
Far-field THz imaging of vortex phase plate

I have been actively participating in different student competitions and applied for various scholarships.

- 2021 The 2d place in "LACIME congrès" – LACIME, ÉTS (Montréal, Canada)
- 2021 The 3d place in "GreEN network competitions" – ICI, GreEN (Montréal, Canada)
- 2020 The 1st place in "3MT" competitions – ÉTS (Montréal, Canada)
- 2020 3eme prix Génie en affaires – ACFAS (Montréal, Canada)
- 2020 The 2d place in Dobson Cup – McGill (Montréal, Canada)
- 2019 Best poster awards – 3d Montréal Networking Event (Montréal, Canada)
- 2019 MITACS Globalink – \$6,000 (Montréal, Canada)
- 2019 Best poster awards – OTST 2019 (Santa Fe, USA)
- 2019 Bourse de Substance – ÉTS (Montréal, Canada)
- 2019 Best poster awards – LACIME (Montréal, Canada)
- 2019 Bourse de mobilité pour doctorants – 1,000 Euro (LAPHIA, France)
- 2019 Le rayonnement de la recherche – \$1,000 (ÉTS, Montréal, Canada)
- 2017 Bourse Hydro-Québec – \$ 12,000 (Québec, Canada)

APPENDIX I

FABRICATION OF LARGE APERTURE PHOTOCONDUCTIVE ANTENNAS

Photolithography is a complex, time-consuming manufacturing process. Figure I-1 shows the fabrication steps.

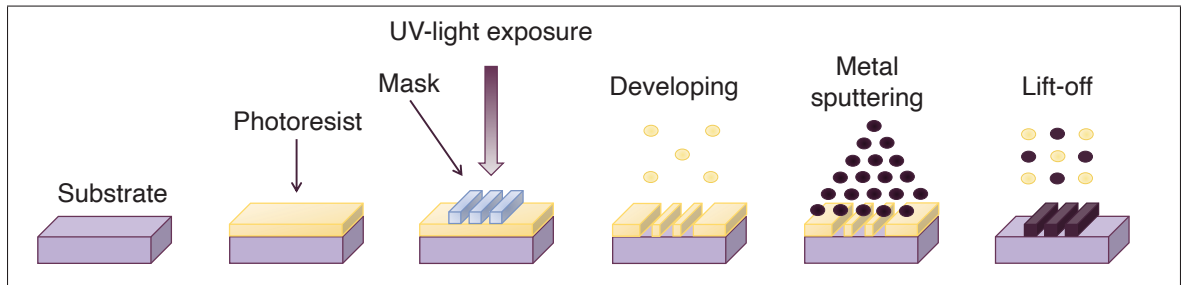


Figure-A I-1 Conventional photolithography

Firstly, a layer of negative photosensitive resin (photoresist) was deposited on a flat rigid wafer surface, followed by the baking process. To fabricate the interdigitated large aperture photoconductive antennas (ILAPSA), the different wide-bandgap semiconductor crystals ($ZnSe$, GaN , $6H-SiC$, $4H-SiC$ and $\beta-Ga_2O_3$) was used as the substrate (Altay *et al.* (2020)). Secondly, photolithographic patterning is applied using ultraviolet (UV) light using mask-less technique. After exposure, the wafer is rinsed in a developing solution, which removes the photoresist's unexposed areas and leaves a pattern. The pattern's size was $40 \times 60 \text{ mm}$ with a 1 mm gap. Afterward, the metal was deposited by sputtering on the wafer with the photoresist's pattern. To achieve higher adhesion between silver (Ag) and wafer, the layer of chrome (Cr) was deposited (Altay *et al.* (2020)). As the last step, the chemical bath immersion process is utilized to remove the remaining photoresist and unwanted metal that is not covered by it. The subtractive process wastes significant quantities of expensive toxic materials, including both functional materials and photoresist, which inherently increases manufacturing cost. The fabricated samples are shown in Figure I-2.

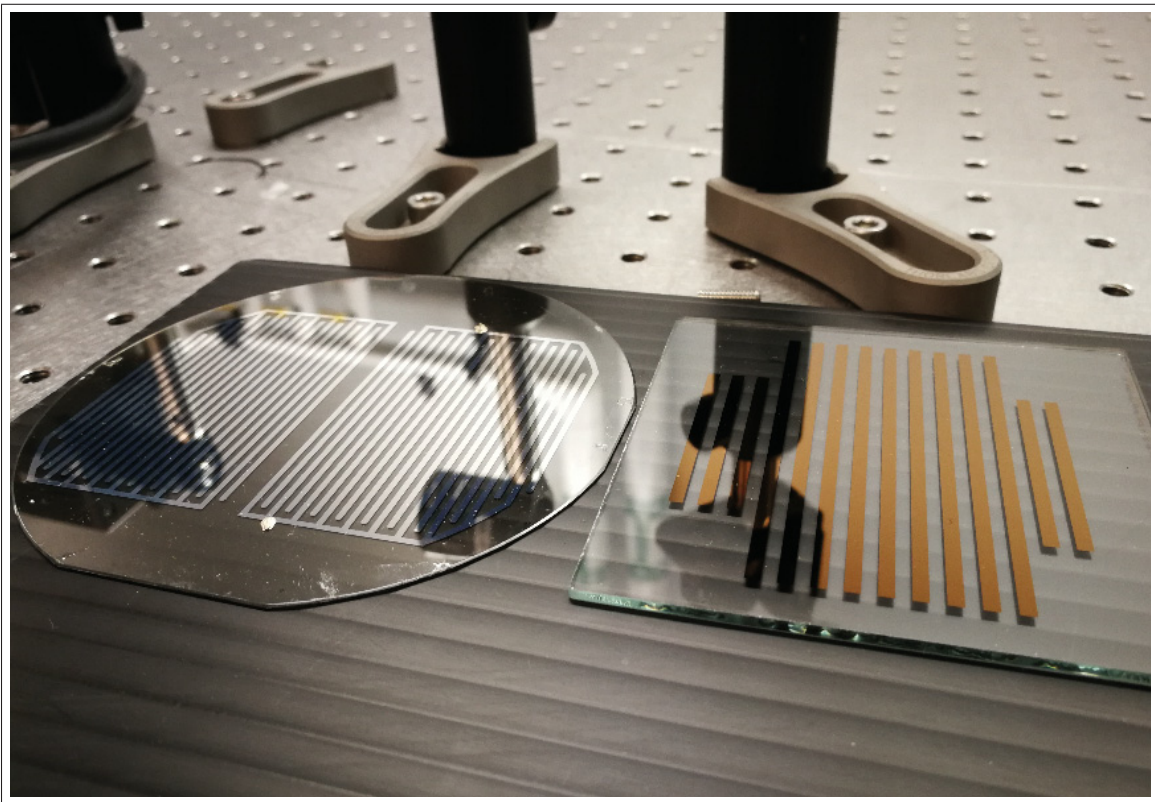


Figure-A I-2 Photo of the structure of two ILAPCAs on a 4 *inch* diameter 6H – SiC wafer and the shadow mask on the right

APPENDIX II

TWO-PROBE VS. FOUR-POINT PROBE ELECTRICAL MEASUREMENTS

Figure II-1 shows two typical methods for evaluating the electrical properties of printed electronics: multimeter (two-probe) and four-point probe (4PP) (Greer & Street (2007); Hoath (2016); Merilampi *et al.* (2010); Perelaer *et al.* (2012); Sneek *et al.* (2018); Sowade *et al.* (2016)). The multimeter uses only two probe contact resistance measurements, which is easier to manipulate. However, the interpretation of results is more complicated (Janesch (2013)). Figure II-1a sketches the estimation of the measured resistance. A considerable error comes from the lead resistance, which is added to measurements since a small current causes a small but significant voltage drop across the lead resistances. The measured voltage does not show the same as the voltage directly across the test resistance. In the four-point probe system, as illustrated on Figure II-1b, two probes are used for sourcing current while another two probes are employed to measure the voltage. The probes are placed so that they are equally spaced. Then, they are brought into contact with the material of unknown resistance. Measurement errors resulting from the probe resistance, the resistance due to the contact between each metal probe and the material, and the distribution of the resistance under each probe, become negligible when four probes are used. A geometric correction factor is usually required to convert the voltage/current ratio measured by the 4-point probe into sheet resistance. This correction factor accounts for the sample size, shape, and probe spacing (Greer & Street (2007)).

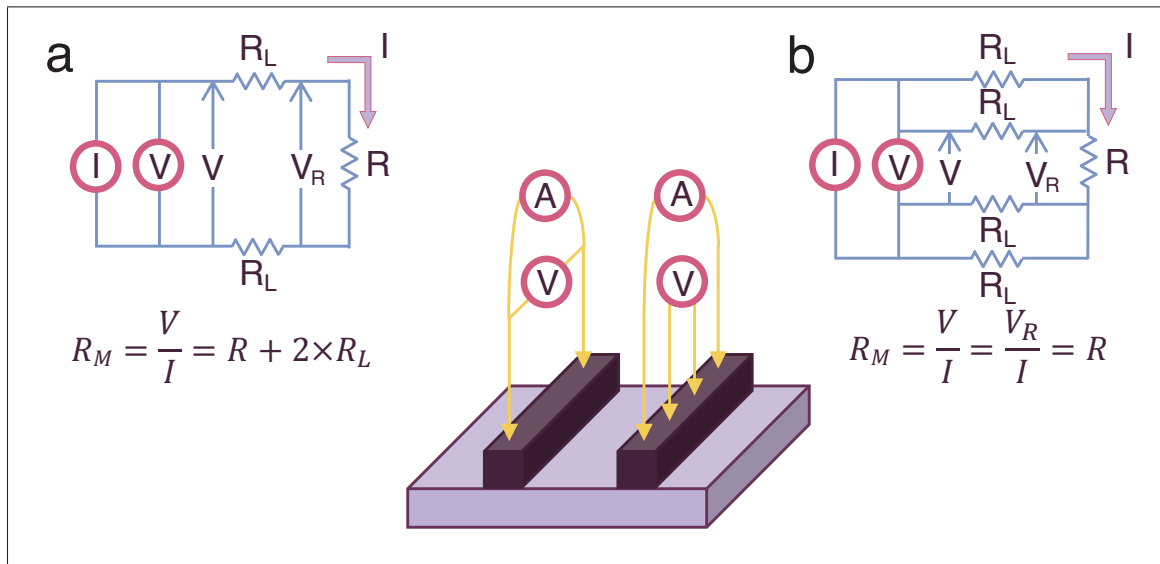


Figure-A II-1 A schematic principle of a) two point and b) four-point probe setup to measure resistivity.

I is the test current; V is the measured voltage; V_R is the voltage across the test resistance R .

R_L is the lead resistance

Adapted from Janesch (2013)

APPENDIX III

GEOMETRIC CORRECTION FACTOR OF CONDUCTIVITY

The example of measuring conductivity using four-point probe is shown in Figure III-1a (Yilmaz (2015)).

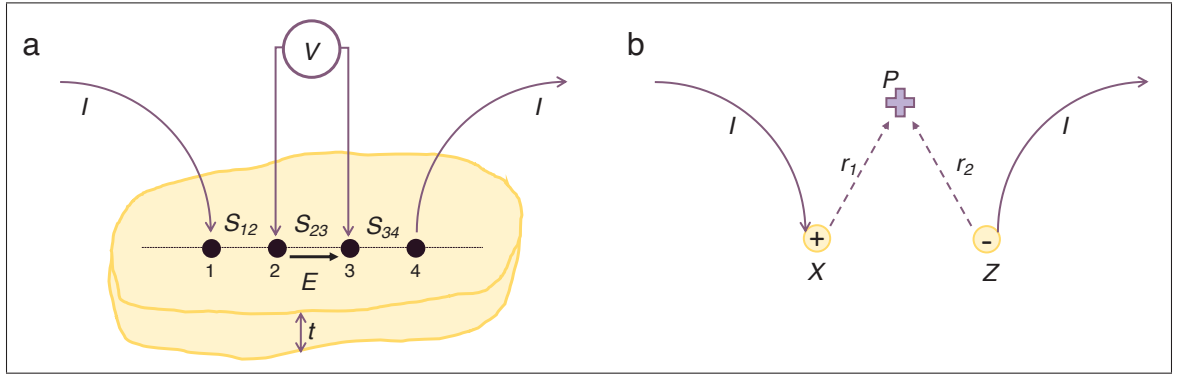


Figure-A III-1 a) A schematic principle of four-point probe measurements of resistivity.
b) The charges are carried to P point from X and Z points. r_1 and r_2 are the distance to P from X and Z , respectively
Adapted from Yilmaz (2015)

In the conductive materials, the current density (J) is directly proportional to electrical field magnitude (E):

$$E = \rho J = \rho \frac{I}{2\pi r^2} = -\frac{dV}{dr} \quad (\text{A III-1})$$

As shown in Figure III-1b, the measured voltage coming from two current-probes at point P is given by:

$$V = \int_0^V dV = -\frac{I\rho}{2\pi} \int_{r_1}^{r_2} \frac{dr}{r^2} = \frac{I\rho}{2\pi r_1} \quad (\text{A III-2})$$

Hence, the measured voltage at tip 2 and 3 (see Figure III-1a) is defined:

$$\begin{aligned} V_2 &= \frac{I\rho}{2\pi} \left(\frac{1}{s_{12}} - \frac{1}{s_{23} + s_{34}} \right), \\ V_3 &= \frac{I\rho}{2\pi} \left(\frac{1}{s_{12} + s_{23}} - \frac{1}{s_{34}} \right), \end{aligned} \quad (\text{A III-3})$$

where s_{12} , s_{23} , and s_{34} are distance between adjacent probes. Hence, the resulted voltage for equally placed probes can be found ($s = s_{12} = s_{23} = s_{34}$):

$$V = V_2 - V_3 = \frac{I\rho}{2\pi} \left(\frac{1}{s_{12}} - \frac{1}{s_{23} + s_{34}} - \frac{1}{s_{12} + s_{23}} + \frac{1}{s_{34}} \right) = \frac{I\rho}{2\pi s} \quad (\text{A III-4})$$

The conductivity measurement is highly affected by sample geometry, which is not semi-infinite layer in lateral and vertical direction. Hence, the resistivity is given by:

$$\rho = 2\pi s F \frac{V}{I}, \quad (\text{A III-5})$$

where F is a geometrical correction factor for samples thickness; lateral dimensions or placement of the probes relative to sample edges. This factor is defined by a combination of hyperbolic functions:

$$F = \frac{t/s}{2 \ln \left[\frac{\sinh(t/s)}{\sinh(t/2s)} \right]} \quad (\text{A III-6})$$

In the case of Chapter 5, sample thickness was $\sim 400 \text{ nm}$ and the spacing between probes was $\sim 100 \mu\text{m}$, hence, we deal with the case of $t \ll s$, which brings the correction factor of:

$$F = \frac{t/s}{2 \ln(2)} \quad (\text{A III-7})$$

Consequently, the resulted conductivity in the equation 5.2 is coming from the inverse equation of A III-5:

$$\sigma = \frac{1}{\rho} = \frac{1}{2\pi s F} \frac{I}{V} = \frac{2 \ln(2)}{2\pi s t / s} \frac{1}{R} = \frac{\ln(2)}{\pi t R}, \quad (\text{A III-8})$$

where $R = \frac{V}{I}$ is measured sheet resistance.

APPENDIX IV

MATLAB CODE FOR VISUAL ANALYSIS

Algorithm-A IV-1 Algorithm to extract the geometry of printed samples from the visible microscope images

```
1 % Open a designed image
2 JC=im2double(imread('design.tif')); d1=sqrt(0.7172/2); d2=d1; J1=JC;
3 % Open the optical microscope image with the define resolution in  $\mu\text{m}$ 
4 I=im2double(imread('file.tif'));
5 pix=93; xs=0.240; res=xs/pix;
6 s=4096; L=s/2+1;
7 % Make the image black & white
8 IG = (wiener2(1-I, [3030]));
9 [m, n]=size(IG);
10 I2=zeros(m,n);
11 for ii=1:m
12     for jj=1:n
13         if IG(ii,jj)>0.5
14             I2(ii,jj)=1;
15         else
16             I2(ii,jj)=0;
17         end
18     end
19 end
20 % Remove the noise by filtering in Fourier domain
21 aX=(fftshift(fft2(I2)));
22 % Low pass filter
23 [r,c]=size(I2); orgr=r/2; orgc=c/2;
24 mf= zeros(r,c); D0=100;
25 for i=1:r
26     for j=1:c
27         if sqrt((i-orgr).2+(j-orgc).2)<=D0
28             mf(i,j)=1;
29         end
30     end
31 end
```

```

32 % High pass filter
33 mfh= zeros(r,c); D0=3100;
34 for i=1:r
35     for j=1:c
36         if sqrt((i-orgr).2+(j-orgc).2)>=D0
37             mfh(i,j)=1;
38         end
39     end
40 end
41 % Filtered image
42 I4=aX.*(mfh+mf);
43 I8=abs(iff2(iff2shift(I4))); % Look for the first central point to make all figures uniform
44 m=430;
45 n=430;
46 v=[];
47 for i=1:m
48     for j=1:n
49         if II(i,j)==0
50             y1=i; x1=j; v=[x1, y1];
51         end
52         if isempty(v) ==1
53             break
54         end
55     end
56 end
57 vv=0;
58 for j=x1:x1+40
59     if II(y1,j) ==0
60         vv=j-1;
61         break
62     end
63 end
64 x1=ceil((vv-x1)/2+x1);
65 xx=[x1-50,x1+50];
66 VII=[];
67 for j=1:4096
68     VI=sum(II(j,xx(1):xx(2)));
69     VII=[VII; VI];
70 end

```

```

71 fff=diff(movmean(VII, 10));
72 ff=[];
73 for i=1:size(fff)-1
74     if VII(i)==101
75         ff=[ff;i];
76     elseif fff(i+1)<fff(i) && fff(i+1)<=0 && fff(i)>=0
77         ff=[ff; i];
78     end
79 end
80 diagonalY=[];
81 centersX=[];
82 for i=1:size(ff)-1
83     f=ff(i+1)-ff(i);
84     if f<100
85         f=[];
86     end
87     diagonalY=[diagonalY;f];
88     centersX=[centersX; ff(i)+ceil(f/2)];
89 end
90 v=[];
91 for j=1:m
92     for i=1:n
93         if II(i,j)==0
94             y2=i; x2=j;v=[x2, y2];
95         end
96         if isempty(v) =1
97             break
98         end
99     end
100 end
101 for j=y2:y2+20
102     if II(j,x2) =0
103         vv=j-1;
104         break
105     end
106 end
107 y2=ceil((vv-y2)/2+y2);
108 yy=[y2-50,y2+50];
109 VIIIX=[];

```

```

110 for j=1:4096
111     VI=sum(II(yy(1):yy(2),j));
112     VIIX=[VIIX; VI];
113 end
114 fff=diff(movmean(VIIX, 10));
115 ff=[];
116 for i=1:size(fff)-1
117     if VIIX(i)==101
118         ff=[ff;i];
119     elseif (fff(i+1))<(fff(i)) && fff(i+1)<=0 && fff(i)>=0
120         ff=[ff; i];
121     end
122 end
123 diagonalX=[];
124 centersY=[];
125 for i=1:size(ff)-1
126     f=ff(i+1)-ff(i);
127     if f<100
128         f=[];
129     end
130     diagonalX=[diagonalX;f];
131     centersY=[centersY; ff(i)+ceil(f/2)];
132 end
133 xc=centersY(1);
134 yc=centersX(1);
135 % Adding extraspace to overlap testing image and real
136 [m, n]=size(II);
137 if (yc-d1/res)<0
138     Ic=zeros(ceil(abs(yc-d1/res)), n);
139     for i=1:2*ceil(abs(yc-d1/res))
140         for j=1:n
141             Ic(i,j)=1;
142         end
143     end
144     k=0; II = [II(1:k,:); Ic; II(k+1:end,:)];
145 end
146 [m, n]=size(II);
147 if (xc-d1/res)<0
148     Ic=zeros(m, ceil(2*abs(xc-d1/res)));
149     for i=1:m
150         for j=1:ceil(2*abs(xc-d1/res))
151             Ic(i,j)=1;
152         end
153     end

```



```

154     k=0; II = [II(:,1:k) Ic II(:,k+1:end)];
155 end
156 I2 = ((imcrop(II,[ceil(abs(xc-d1/res)) ceil(abs(yc-d1/res)) s-1 s-1]]));
157 K2=I2;
158 figure; imshow(K2);
159 [m,n]=size(K2);
160 br=0;
161 for ii=1:m
162     for jj=1:n
163         if K2(ii,jj)==1
164             br=br+1;
165         end
166     end
167 end
168 % New central coordinates of the first rhombus
169 xcn=ceil(d1/res);
170 ycn=ceil(d1/res);
171 % Look for first row diagonals & coordinates of y centers
172 yy=[ycn-50; ycn+50];
173 VIIX=[];
174 for j=1:4096
175     VI=sum(K2(yy(1):yy(2),j));
176     VIIX=[VIIX; VI];
177 end
178 fff=movmean(diff(movmean(VIIX, 15)),15);
179 ff=[];
180 for i=1:size(fff)-1
181     if VIIX(i)==101
182         ff=[ff;i];
183     elseif (fff(i+1))<(fff(i)) && (fff(i+1))<0 && (fff(i))>=0
184         if abs(fff(i+1))<abs(fff(i))
185             ff=[ff; i+1];
186         else
187             ff=[ff; i];
188         end
189     end
190 end
191 diagonalX=[];
192 centersY=[];
193 for i=1:size(ff)-1
194     f=ff(i+1)-ff(i);
195     if f<100
196         f=[];
197     end

```

```

198 diagonalX=[diagonalX;f];
199 centersY=[centersY; ff(i)+ceil(f/2)];
200 end
201 % Look for first colomn diagonals & coordinates of X centers
202 xx=[xcn-50; xcn+50];
203 VII=[];
204 for j=1:4096
205     VI=sum(K2(j,xx(1):xx(2)));
206     VII=[VII; VI];
207 end
208 fff=movmean(diff((VII)),15);
209 ff=[];
210 for i=1:size(fff)-1
211     if VII(i)==101
212         ff=[ff;i];
213     elseif (fff(i+1))<(fff(i)) && (fff(i+1))<0 && (fff(i))>=0
214         if abs(fff(i+1))<abs(fff(i))
215             ff=[ff; i+1];
216         else
217             ff=[ff; i];
218         end
219     end
220 end
221 diagonalY=[];
222 centersX=[];
223 for i=1:size(ff)-1
224     f=ff(i+1)-ff(i);
225     if f<100 || f==1
226         f=[];
227     end
228     diagonalY=[diagonalY;f];
229     centersX=[centersX; ff(i)+ceil(f/2)];
230 end
231 % Going through the entire matrix for Y
232 overlapx=[];
233 overlapxf=[];
234 alldiagonalY=[];
235 ccY=[];
236 VIYY=[];
237 for ii=1:size(centersX)
238     xx=[centersX(ii)-50; centersX(ii)+50];
239     VII=[];

```

```

240         for j=1:4096
241             VI=sum(K2(j,xx(1):xx(2)));
242             VII=[VII; VI];
243         end
244     end
245     VIIV=[VIIV, sum(VII)];
246     fff=movmean(diff((VII)),15);
247     ff=[];
248     for i=1:size(fff)-1
249         if VII(i)==101
250             ff=[ff;i];
251             elseif (fff(i+1))<(fff(i)) && (fff(i+1))<0 && (fff(i))>=0
252                 if abs(fff(i+1))<abs(fff(i))
253                     ff=[ff; i+1];
254                 else
255                     ff=[ff; i];
256                 end
257             end
258     end
259     cY=[];
260     diagonalY=[];
261     for i=1:size(ff)-1
262         f=ff(i+1)-ff(i);
263         if f<100 || f==1
264             f=[];
265         else
266             overlapxf=[overlapxf;ff(i+1), ff(i)];
267         end
268         diagonalY=[diagonalY;f];
269         cY=[cY; ff(i)+ceil(f/2)];
270     end
271     for jj=1:size(overlapxf)-1
272         ov=overlapxf(jj+1,2)-overlapxf(jj,1);
273         if ov<10
274             kk=overlapxf(jj,1);
275             ss=K2(kk,xx(1)-50:xx(2)+50);
276             r=find(ss==0);
277             if size(r,2)<2
278                 ov=overlapxf(jj+1,2)-overlapxf(jj,1);
279             else
280                 ov=r(1)-r(end);
281             end
282         end

```

```

283 overlapx=[overlapx; ov];
284 end
285 overlapxf=[];
286 [m,n]=size(diagonalY);
287 if m =10 | any(diagonalY<220)
288     alldiagonalY=alldiagonalY;
289     else
290     alldiagonalY=[alldiagonalY, diagonalY];
291     ccY=[ccY, cY];
292 end
293 % Going through the entire matrix for X
294 overlapY=[];
295 overlapYf=[];
296 alldiagonalX=[];
297 overcheckY=[];
298 ccX=[];VIIX=[];
299 for ii=1:size(centersY)
300     yy=[centersY(ii)-50; centersY(ii)+50];
301     VII=[];
302     for j=1:4096
303         VI=sum(K2(yy(1):yy(2),j));
304         VII=[VII; VI];
305     end
306     VIIX=[VIIX, sum(VII)];
307     fff=movmean(diff((VII)),15);
308     ff=[];
309     for i=1:size(fff)-1
310         if VII(i)==101
311             ff=[ff;i];
312         elseif (fff(i+1))<(fff(i)) && (fff(i+1))<0 && (fff(i))>=0
313             if abs(fff(i+1))<abs(fff(i))
314                 ff=[ff; i+1];
315             else
316                 ff=[ff; i];
317             end
318         end
319     end
320 diagonalX=[];
321 cX=[];
322 for i=1:size(ff)-1
323     f=ff(i+1)-ff(i);
324     if f<100
325         f=[];
326     else

```

```

327         overlapf=[overlapf;ff(i+1), ff(i)];
328     end
329     diagonalX=[diagonalX;f];
330     cX=[cX; ff(i)+ceil(f/2)];
331 end
332 for jj=1:size(overlapf)-1
333     ov=overlapf(jj+1,2)-overlapf(jj,1);
334     if ov<10
335         kk=overlapf(jj+1,2);
336         ss=K2(yy(1)-50:yy(2)+50,kk);
337         r=find(ss==0);
338         if size(r,1)<2
339             ov=overlapf(jj+1,2)-overlapf(jj,1);
340         else
341             ov=r(1)-r(end);
342         end
343     end
344     overlap=[overlap; ov];
345 end
346 overchecky=[overchecky;overlapf];
347 overlapf=[];
348 [m,n]=size(diagonalX);
349 if m =10 | any(diagonalX<220)
350     alldiagonalX=alldiagonalX;
351 else
352     alldiagonalX=[alldiagonalX, diagonalX];
353     ccX=[ccX, cX];
354 end
355 end
356 minimumX=min(alldiagonalX(:));
357 maximumX=max(alldiagonalX(:));
358 edgesX=maximumX-minimumX;
359 minimumY=min(alldiagonalY(:));
360 maximumY=max(alldiagonalY(:));
361 edgesY=maximumY-minimumY;
362 latty=[];
363 [m,n]=size(ccY);
364 for j=1:n
365     for i=1:m-1
366         lat=ccY(i+1,j)-ccY(i,j);
367         latty=[latty; lat*res];
368     end
369 end

```

```

370 latticey=mean(latty);
371 ery=std(latty);
372 lattx=[];
373 [m,n]=size(ccX);
374 for j=1:n
375     for i=1:m-1
376         lat=ccX(i+1,j)-ccX(i,j);
377         lattx=[lattx; lat*res];
378     end
379 end
380 laticex=mean(lattx);
381 erx=std(lattx);
382 % Size of lattice in Y of the entire matrix
383 llatty=[];
384 for pp=1:size(centersX)-1
385     llatty=[llatty; centersX(pp+1)-centersX(pp)];
386 end
387 llatticey=mean(llatty*res);
388 eery=std(llatty*res);
389 % Size of lattice in X of the entire matrix
390 llattx=[];
391 for pp=1:size(centersY)-1
392     llattx=[llattx; centersY(pp+1)-centersY(pp)];
393 end
394 llaticex=mean(llattx*res);
395 eerx=std(llattx*res);
396 % Calculate # of gaps / laps
397 noverlapxp=sum((overlapx>0));
398 noverlapxn=sum((overlapx<=0));
399 noverlapyp=sum((overlapy>0));
400 noverlapyn=sum((overlapy<=0));

```

REFERENCES

- Abbel, R., van Lammeren, T., Hendriks, R., Ploegmakers, J., Rubingh, E. J., Meinders, E. R. & Groen, W. A. (2012). Photonic flash sintering of silver nanoparticle inks: a fast and convenient method for the preparation of highly conductive structures on foil. *MRS Communications*, 2(4), 145.
- Abdelwahab, N. S., El-Zeiny, B. A. & Tohamy, S. I. (2012). Two spectrophotometric methods for simultaneous determination of some antihyperlipidemic drugs. *Journal of pharmaceutical analysis*, 2(4), 279–284.
- Abu-Khalaf, J., Sarairoh, R., Eisa, S., Al-Halhouli, A. et al. (2018). Experimental characterization of inkjet-printed stretchable circuits for wearable sensor applications. *Sensors*, 18(10), 3476.
- Afsah-Hejri, L., Hajeb, P., Ara, P. & Ehsani, R. J. (2019). A comprehensive review on food applications of terahertz spectroscopy and imaging. *Comprehensive Reviews in Food Science and Food Safety*, 18(5), 1563–1621.
- Ahmadvand, A., Gerislioglu, B., Ramezani, Z., Kaushik, A., Manickam, P. & Ghoreishi, S. A. (2020). Femtomolar-level detection of SARS-CoV-2 spike proteins using toroidal plasmonic metasensors. *Preprint*, 1-21.
- Al Dhaybi, A., Degert, J., Brasselet, E., Abraham, E. & Freysz, E. (2019). Terahertz vortex beam generation by infrared vector beam rectification. *JOSA B*, 36(1), 12–18.
- Altay, B. N., Bolduc, M. & Cloutier, S. G. (2020). Sustainable Advanced Manufacturing of Printed Electronics: An Environmental Consideration. In *Green Energy and Environment*. IntechOpen.
- Amirkhan, F., Sakata, R., Takiguchi, K., Arikawa, T., Ozaki, T., Tanaka, K. & Blanchard, F. (2019). Characterization of thin-film optical properties by THz near-field imaging method. *JOSA B*, 36(9), 2593–2601.
- Andersen, T. R., Dam, H. F., Hösel, M., Helgesen, M., Carlé, J. E., Larsen-Olsen, T. T., Gevorgyan, S. A., Andreasen, J. W., Adams, J., Li, N. et al. (2014). Scalable, ambient atmosphere roll-to-roll manufacture of encapsulated large area, flexible organic tandem solar cell modules. *Energy & Environmental Science*, 7(9), 2925–2933.
- Azad, A. K., O'Hara, J. F., Singh, R., Chen, H.-T. & Taylor, A. J. (2012). A review of terahertz plasmonics in subwavelength holes on conducting films. *IEEE Journal of Selected Topics in Quantum Electronics*, 19(1), 8400416–8400416.

- Bao, Z., Feng, Y., Dodabalapur, A., Raju, V. & Lovinger, A. J. (1997). High-performance plastic transistors fabricated by printing techniques. *Chemistry of Materials*, 9(6), 1299–1301.
- Barr, M. C., Rowe, J. A., Lunt, R. R., Xu, J., Wang, A., Boyce, C. M., Im, S. G., Bulović, V. & Gleason, K. K. (2011). Direct monolithic integration of organic photovoltaic circuits on unmodified paper. *Advanced Materials*, 23(31), 3500–3505.
- Beedasy, V. & Smith, P. J. (2020). Printed Electronics as Prepared by Inkjet Printing. *Materials*, 13(3), 704.
- Berrier, A., Schaafsma, M. C., Nonglaton, G., Bergquist, J. & Rivas, J. G. (2012). Selective detection of bacterial layers with terahertz plasmonic antennas. *Biomedical optics express*, 3(11), 2937–2949.
- Bethe, H. A. (1944). Theory of diffraction by small holes. *Physical review*, 66(7–8), 163.
- Bitzer, A., Ortner, A., Merbold, H., Feurer, T. & Walther, M. (2011). Terahertz near-field microscopy of complementary planar metamaterials: Babinet's principle. *Optics express*, 19(3), 2537–2545.
- Blanchard, F., Doi, A., Tanaka, T., Hirori, H., Tanaka, H., Kadoya, Y. & Tanaka, K. (2011). Real-time terahertz near-field microscope. *Optics express*, 19(9), 8277–8284.
- Blanchard, F., Ooi, K., Tanaka, T., Doi, A. & Tanaka, K. (2012). Terahertz spectroscopy of the reactive and radiative near-field zones of split ring resonator. *Optics express*, 20(17), 19395–19403.
- Blanchard, F. & Tanaka, K. (2016). Improving time and space resolution in electro-optic sampling for near-field terahertz imaging. *Optics letters*, 41(20), 4645–4648.
- Blanchard, F., Doi, A., Tanaka, T. & Tanaka, K. (2013). Real-time, subwavelength terahertz imaging. *Annual Review of Materials Research*, 43, 237–259.
- Blanchard, F., Chai, X., Tanaka, T., Arikawa, T., Ozaki, T., Morandotti, R. & Tanaka, K. (2018). Terahertz microscopy assisted by semiconductor nonlinearities. *Optics letters*, 43(20), 4997–5000.
- Bolduc, M., Trudeau, C., Beaupré, P., Cloutier, S. & Galarneau, P. (2018). Thermal dynamics effects using pulse-shaping laser sintering of printed silver inks. *Scientific reports*, 8(1), 1–9.

- Bravo-Abad, J., Martín-Moreno, L., García-Vidal, F., Hendry, E. & Rivas, J. G. (2007). Transmission of light through periodic arrays of square holes: From a metallic wire mesh to an array of tiny holes. *Physical Review B*, 76(24), 241102.
- Burford, N. M. & El-Shenawee, M. O. (2017). Review of terahertz photoconductive antenna technology. *Optical Engineering*, 56(1), 010901.
- Cai, W. & Shalaev, V. M. (2010). *Optical metamaterials*. Springer.
- Castrejón-García, R., Castrejón-Pita, J., Martin, G. & Hutchings, I. (2011). The shadowgraph imaging technique and its modern application to fluid jets and drops. *Revista mexicana de física*, 57(3), 266–275.
- Celentano, A. & Di Lecce, V. (199). FFT-based technique for image-signature generation. *Storage and Retrieval for Image and Video Databases V*, 3022, 457–466.
- Chan, C.-h. & Pang, G. K. (2000). Fabric defect detection by Fourier analysis. *IEEE transactions on Industry Applications*, 36(5), 1267–1276.
- Chanana, A., Paulsen, A., Guruswamy, S. & Nahata, A. (2016). Hiding multi-level multi-color images in terahertz metasurfaces. *Optica*, 3(12), 1466–1470.
- Chen, H.-T., O'Hara, J. F., Azad, A. K. & Taylor, A. J. (2011). Manipulation of terahertz radiation using metamaterials. *Laser & Photonics Reviews*, 5(4), 513–533.
- Chen, H.-T., Taylor, A. J. & Yu, N. (2016). A review of metasurfaces: physics and applications. *Reports on progress in physics*, 79(7), 076401.
- Chen, T., Li, S. & Sun, H. (2012a). Metamaterials application in sensing. *Sensors*, 12(3), 2742–2765.
- Chen, W., Nikiforov, M. P. & Darling, S. B. (2012b). Morphology characterization in organic and hybrid solar cells. *Energy & Environmental Science*, 5(8), 8045–8074.
- Chen, W., Nikiforov, M. P. & Darling, S. B. (2012c). Morphology characterization in organic and hybrid solar cells. *Energy & Environmental Science*, 5(8), 8045–8074.
- Chen, X. & Pickwell-MacPherson, E. (2019). A sensitive and versatile thickness determination method based on non-inflection terahertz property fitting. *Sensors*, 19(19), 4118.

- Cheng, D., He, X., Huang, X., Zhang, B., Liu, G., Shu, G., Fang, C., Wang, J. & Luo, Y. (2018). Terahertz biosensing metamaterial absorber for virus detection based on spoof surface plasmon polaritons. *International Journal of RF and Microwave Computer-Aided Engineering*, 28(7), e21448.
- Cho, Y. T., Jeong, Y., Kim, Y. J., Kwon, S., Lee, S.-H., Kim, K. Y., Kang, D. & Lee, T.-M. (2017). Printing speed and quality enhancement by controlling the surface energy of cliché in reverse offset printing. *Applied Sciences*, 7(12), 1302.
- Cosentino, A. (2016). Terahertz and cultural heritage science: examination of art and archaeology. *Technologies*, 4(1), 6.
- Cui, Z. (2019). Printing practice for the fabrication of flexible and stretchable electronics. *Science China Technological Sciences*, 62(2), 224–232.
- De Abajo, F. G. (2007). Colloquium: Light scattering by particle and hole arrays. *Reviews of Modern Physics*, 79(4), 1267.
- De Abajo, F. G., Gómez-Medina, R. & Sáenz, J. (2005). Full transmission through perfect-conductor subwavelength hole arrays. *Physical review E*, 72(1), 016608.
- Degiron, A., Lezec, H., Yamamoto, N. & Ebbesen, T. (2004). Optical transmission properties of a single subwavelength aperture in a real metal. *Optics Communications*, 239(1–3), 61–66.
- Derby, B. (2010). Inkjet printing of functional and structural materials: fluid property requirements, feature stability, and resolution. *Annual Review of Materials Research*, 40, 395–414.
- Dexheimer, S. L. (2017). *Terahertz spectroscopy: principles and applications*. CRC press.
- Diaz, E., Ramon, E. & Carrabina, J. (2013). Inkjet patterning of multiline intersections for wirings in printed electronics. *Langmuir*, 29(40), 12608–12614.
- Doi, A., Blanchard, F., Hirori, H. & Tanaka, K. (2010). Near-field THz imaging of free induction decay from a tyrosine crystal. *Optics Express*, 18(17), 18419–18424.
- Doi, A., Blanchard, F., Tanaka, T. & Tanaka, K. (2011). Improving spatial resolution of real-time terahertz near-field microscope. *Journal of Infrared, Millimeter, and Terahertz Waves*, 32(8–9), 1043.
- Dolai, S. & Tabib-Azar, M. (2020). Terahertz Detection of Zika Viruses. 2020020232.

- Du, X., Hardt, D. & Anthony, B. (2019). Real-Time Imaging of Invisible Micron-Scale Monolayer Patterns on a Moving Web Using Condensation Figures. *IEEE Transactions on Industrial Electronics*, 67(5), 4077–4087.
- Ebisawa, F., Kurokawa, T. & Nara, S. (1983). Electrical properties of polyacetylene/polysiloxane interface. *Journal of applied physics*, 54(6), 3255–3259.
- Edmunds, J. D., Hibbins, A. P., Sambles, J. R. & Youngs, I. (2010). Resonantly inverted microwave transmissivity threshold of metal grids. *New Journal of Physics*, 12(6), 063007.
- El Haddad, J., Canioni, L. & Bousquet, B. (2014). Good practices in LIBS analysis: Review and advices. *Spectrochimica Acta Part B: Atomic Spectroscopy*, 101, 171–182.
- Ermak, O., Zenou, M., Toker, G. B., Ankri, J., Shacham-Diamand, Y. & Kotler, Z. (2016). Rapid laser sintering of metal nano-particles inks. *Nanotechnology*, 27(38), 385201.
- Espinosa, N., Lenzmann, F. O., Ryley, S., Angmo, D., Hösel, M., Søndergaard, R. R., Huss, D., Dafinger, S., Gritsch, S., Kroon, J. M. et al. (2013). OPV for mobile applications: an evaluation of roll-to-roll processed indium and silver free polymer solar cells through analysis of life cycle, cost and layer quality using inline optical and functional inspection tools. *Journal of Materials Chemistry A*, 1(24), 7037–7049.
- Eun, K., Chon, M.-W., Yoo, T.-H., Song, Y.-W. & Choa, S.-H. (2015). Electromechanical properties of printed copper ink film using a white flash light annealing process for flexible electronics. *Microelectronics Reliability*, 55(5), 838–845.
- Fajardo, J., Garduño, S. I. & Estrada, M. (2020). Analysis of Inkjet Printing Conditions for ZnO Nanoparticles Patterns Towards the Fabrication of Fully Printed Thin Film Devices. *2020 IEEE Latin America Electron Devices Conference (LAEDC)*, pp. 1–4.
- Fan, S., Li, T., Zhou, J., Liu, X., Liu, X., Qi, H. & Mu, Z. (2017). Terahertz non-destructive imaging of cracks and cracking in structures of cement-based materials. *AIP Advances*, 7(11), 115202.
- Fattinger, C. & Grischkowsky, D. (1989). Terahertz beams. *Applied Physics Letters*, 54(6), 490–492.
- Feng, X., Su, R., Happonen, T., Liu, J. & Leach, R. (2018). Fast and cost-effective in-process defect inspection for printed electronics based on coherent optical processing. *Optics express*, 26(11), 13927–13937.

- Fukuda, K. & Someya, T. (2017). Recent progress in the development of printed thin-film transistors and circuits with high-resolution printing technology. *Advanced materials*, 29(25), 1602736.
- Garnier, F., Peng, X., Horowitz, G. & Fichou, D. (1991). Organic-based field-effect transistors: Critical analysis of the semiconducting characteristics of organic materials. *Molecular Engineering*, 1(2), 131–139.
- Gbur, G. (2007). Singular optics. *The Optics Encyclopedia*, 1–23.
- Ge, S., Chen, P., Shen, Z., Sun, W., Wang, X., Hu, W., Zhang, Y. & Lu, Y. (2017). Terahertz vortex beam generator based on a photopatterned large birefringence liquid crystal. *Optics Express*, 25(11), 12349–12356.
- Genet, C. & Ebbesen, T. W. (2007). Light in tiny holes. *Nature*, 445, 39–46.
- Genevet, P., Yu, N., Aieta, F., Lin, J., Kats, M. A., Blanchard, R., Scully, M. O., Gaburro, Z. & Capasso, F. (2012). Ultra-thin plasmonic optical vortex plate based on phase discontinuities. *Applied Physics Letters*, 100(1), 013101.
- Gowen, A., O’Sullivan, C. & O’Donnell, C. (2012). Terahertz time domain spectroscopy and imaging: Emerging techniques for food process monitoring and quality control. *Trends in Food Science & Technology*, 25(1), 40–46.
- Greer, J. R. & Street, R. A. (2007). Thermal cure effects on electrical performance of nanoparticle silver inks. *Acta Materialia*, 55(18), 6345–6349.
- Guerboukha, H., Nallappan, K. & Skorobogatiy, M. (2018). Toward real-time terahertz imaging. *Advances in Optics and Photonics*, 10(4), 843–938.
- Guiramand, L., Zhuldybina, M., Arikawa, T., Tanaka, K. & Blanchard, F. (2020). Near-field THz imaging of a printed metallic checkerboard pattern. *Nonlinear Photonics*, pp. NpTu4D–16.
- Güney, D. Ö., Koschny, T. & Soukoulis, C. M. (2010). Intra-connected three-dimensionally isotropic bulk negative index photonic metamaterial. *Optics express*, 18(12), 12348–12353.
- Gupta, B., Pandey, S., Guruswamy, S. & Nahata, A. (2014). Terahertz plasmonic structures based on spatially varying conductivities. *Advanced Optical Materials*, 2(6), 565–571.
- Halonen, E., Viiru, T., Ostman, K., Cabezas, A. L. & Mantysalo, M. (2012). Oven sintering process optimization for inkjet-printed Ag nanoparticle ink. *IEEE Transactions on Components, Packaging and Manufacturing Technology*, 3(2), 350–356.

- Happonen, T., Kokko, T., Juntunen, E. & Rönkä, K. (2019). Quality assurance for rotary screen printed wiring backplanes with automated roll-to-roll electrical test equipment. *Flexible and Printed Electronics*, 4(2), 025002.
- He, J., Wang, X., Hu, D., Ye, J., Feng, S., Kan, Q. & Zhang, Y. (2013). Generation and evolution of the terahertz vortex beam. *Optics express*, 21(17), 20230–20239.
- He, X.-Y., Fu, X.-N. & Luo, Y.-W. (2009). Analysis of the extraordinary transmission properties of arrays of subwavelength holes on a metal film in the terahertz region. *Journal of Modern Optics*, 56(15), 1698–1703.
- Hebling, J., Almasi, G., Kozma, I. Z. & Kuhl, J. (2002). Velocity matching by pulse front tilting for large-area THz-pulse generation. *Optics Express*, 10(21), 1161–1166.
- Hebling, J., Yeh, K.-L., Hoffmann, M. C., Bartal, B. & Nelson, K. A. (2008a). Generation of high-power terahertz pulses by tilted-pulse-front excitation and their application possibilities. *JOSA B*, 25(7), B6–B19.
- Hebling, J., Yeh, K.-L., Hoffmann, M. C., Bartal, B. & Nelson, K. A. (2008b). Generation of high-power terahertz pulses by tilted-pulse-front excitation and their application possibilities. *JOSA B*, 25(7), B6–B19.
- Hedstrom, S., Henriksson, P., Wang, E., Andersson, M. R. & Persson, P. (2015). Temperature-Dependent Optical Properties of Flexible Donor–Acceptor Polymers. *The Journal of Physical Chemistry C*, 119(12), 6453–6463.
- Hoath, S. D. (2016). *Fundamentals of inkjet printing: the science of inkjet and droplets*. John Wiley & Sons.
- Hokari, R., Kurihara, K., Takada, N. & Hiroshima, H. (2018). Printed optical metamaterials composed of embedded silver nanoparticles for flexible applications. *Optics express*, 26(8), 10326–10338.
- Hrehorova, E., Rebros, M., Pekarovicova, A., Bazuin, B., Ranganathan, A., Garner, S., Merz, G., Tosch, J. & Boudreau, R. (2011). Gravure printing of conductive inks on glass substrates for applications in printed electronics. *Journal of Display Technology*, 7(6), 318–324.
- Hsu, S.-M. & Lo, C.-Y. (2019). Advanced qualification method for patterns with irregular edges in printed electronics. *Flexible and Printed Electronics*, 4(1), 015001.
- Hu, D., Wang, X., Feng, S., Ye, J., Sun, W., Kan, Q., Klar, P. J. & Zhang, Y. (2013). Ultrathin terahertz planar elements. *Advanced Optical Materials*, 1(2), 186–191.

- Huang, S.-W., Granados, E., Huang, W. R., Hong, K.-H., Zapata, L. E. & Kärtner, F. X. (2013). High conversion efficiency, high energy terahertz pulses by optical rectification in cryogenically cooled lithium niobate. *Optics letters*, 38(5), 796–798.
- Hudd, A. (2011). Inkjet printing technologies. *The chemistry of inkjet inks*, 3-18.
- Huemer, F., Jamalieh, M., Bammer, F. & Hönig, D. (2016). Inline imaging-ellipsometer for printed electronics. *tm-Technisches Messen*, 83(10), 549–556.
- İbili, H., Karaosmanoğlu, B. & Ergül, Ö. (2018). Demonstration of negative refractive index with low-cost inkjet-printed microwave metamaterials. *Microwave and Optical Technology Letters*, 60(1), 187–191.
- Ivanov, M., Thiele, I., Bergé, L., Skupin, S., Buožius, D. & Vaičaitis, V. (2019). Intensity modulated terahertz vortex wave generation in air plasma by two-color femtosecond laser pulses. *Optics letters*, 44(15), 3889–3892.
- Jahn, D., Eckstein, R., Schneider, L. M., Born, N., Hernandez-Sosa, G., Balzer, J. C., Al-Naib, I., Lemmer, U. & Koch, M. (2018). Digital Aerosol Jet Printing for the Fabrication of Terahertz Metamaterials. *Advanced Materials Technologies*, 3(2), 1700236.
- Janesch, J. (2013). Two-wire vs. four-wire resistance measurements: Which configuration makes sense for your application. *no. May*, 2–4.
- Jang, Y.-R., Joo, S.-J., Chu, J.-H., Uhm, H.-J., Park, J.-W., Ryu, C.-H., Yu, M.-H. & Kim, H.-S. (2020). A Review on Intense Pulsed Light Sintering Technologies for Conductive Electrodes in Printed Electronics. *International Journal of Precision Engineering and Manufacturing-Green Technology*, 1–37.
- Jansen, C., Wietzke, S., Peters, O., Scheller, M., Vieweg, N., Salhi, M., Krumbholz, N., Jördens, C., Hochrein, T. & Koch, M. (2010). Terahertz imaging: applications and perspectives. *Applied optics*, 49(19), E48–E57.
- Jenkins, G., Wang, Y., Xie, Y. L., Wu, Q., Huang, W., Wang, L. & Yang, X. (2015). Printed electronics integrated with paper-based microfluidics: new methodologies for next-generation health care. *Microfluidics and Nanofluidics*, 19(2), 251–261.
- Jepsen, P. U., Cooke, D. G. & Koch, M. (2011). Terahertz spectroscopy and imaging—Modern techniques and applications. *Laser & Photonics Reviews*, 5(1), 124–166.

- Kaltenecker, K., Fischer, B., Bollgruen, P., Korvink, J. & Walther, M. (2012). THz pulse propagation along inkjet-printed metal stripes: Towards a 3D wire-medium for subwavelength imaging. *2012 37th International Conference on Infrared, Millimeter, and Terahertz Waves*, pp. 1–2.
- Kampfrath, T., Tanaka, K. & Nelson, K. A. (2013). Resonant and nonresonant control over matter and light by intense terahertz transients. *Nature Photonics*, 7(9), 680–690.
- Kamyshny, A. & Magdassi, S. (2014). Conductive nanomaterials for printed electronics. *Small*, 10(17), 3515–3535.
- Kamyshny, A., Steinke, J. & Magdassi, S. (2011). Metal-based inkjet inks for printed electronics. *The Open Applied Physics Journal*, 4(1), 19–36.
- Kang, J. S., Kim, H. S., Ryu, J., Hahn, H. T., Jang, S. & Joung, J. W. (2010). Inkjet printed electronics using copper nanoparticle ink. *Journal of Materials Science: Materials in Electronics*, 21(11), 1213–1220.
- Kasap, S. O. (2006). *Principles of electronic materials and devices*. McGraw-Hill.
- Keikhaie, M., Akbari, J., Movahhedi, M. R. & Alemohammad, H. (2014). Sintering Characterizations of Ag-nano Film on Silicon Substrate. *Advanced Materials Research*, 829, 342–346.
- Kempa, K. (2010). Percolation effects in the checkerboard Babinet series of metamaterial structures. *physica status solidi (RRL)–Rapid Research Letters*, 4(8–9), 218–220.
- Keskinen, M. (2012). End-of-life options for printed electronics. In *Waste Electrical and Electronic Equipment (WEEE) Handbook* (pp. 352–364). Elsevier.
- Khan, S., Lorenzelli, L. & Dahiya, R. S. (2014). Technologies for printing sensors and electronics over large flexible substrates: a review. *IEEE Sensors Journal*, 15(6), 3164–3185.
- Khan, Y., Thielens, A., Muin, S., Ting, J., Baumbauer, C. & Arias, A. C. (2020). A new frontier of printed electronics: flexible hybrid electronics. *Advanced Materials*, 32(15), 1905279.
- Kim, H., Melinger, J. S., Khachatryan, A., Charipar, N. A., Auyeung, R. C. & Piqué, A. (2010). Fabrication of terahertz metamaterials by laser printing. *Optics letters*, 35(23), 4039–4041.
- Kim, K.-Y. (2009). Generation of coherent terahertz radiation in ultrafast laser-gas interactions. *Physics of Plasmas*, 16(5), 056706.

- Kim, S. & Sung, H. J. (2015). Effect of printing parameters on gravure patterning with conductive silver ink. *Journal of Micromechanics and Microengineering*, 25(4), 045004.
- Kimbrough, B. & Novak, E. (2015). In-line roll-to-roll metrology for flexible electronics. *Applied Advanced Optical Metrology Solutions*, 9576, 957603.
- Kipphan, H. (2001). *Handbook of print media: technologies and production methods*. Springer Science & Business Media.
- Knyazev, B., Choporova, Y. Y., Mitkov, M., Pavelyev, V. & Volodkin, B. (2015). Generation of terahertz surface plasmon polaritons using nondiffractive Bessel beams with orbital angular momentum. *Physical review letters*, 115(16), 163901.
- Ko, S. H., Pan, H., Grigoropoulos, C. P., Luscombe, C. K., Fréchet, J. M. & Poulidakos, D. (2007). All-inkjet-printed flexible electronics fabrication on a polymer substrate by low-temperature high-resolution selective laser sintering of metal nanoparticles. *Nanotechnology*, 18(34), 345202.
- Kreuzer, M., Whitworth, G. L., Francone, A., Gomis-Bresco, J., Kehagias, N. & Sotomayor-Torres, C. M. (2018). In-line metrology for roll-to-roll UV assisted nanoimprint lithography using diffractometry. *Apl Materials*, 6(5), 058502.
- Lee, D., Sung, H.-K. & Lim, S. (2016). Flexible subterahertz metamaterial absorber fabrication using inkjet printing technology. *Applied Physics B*, 122(7), 206.
- Lee, S.-H., Gee, S.-Y., Kang, C. & Kee, C.-S. (2010). Terahertz wave transmission properties of metallic periodic structures printed on a photo-paper. *Journal of the Optical Society of Korea*, 14(3), 282–285.
- Lee, Y., Choi, J.-r., Lee, K. J., Stott, N. E. & Kim, D. (2008). Large-scale synthesis of copper nanoparticles by chemically controlled reduction for applications of inkjet-printed electronics. *Nanotechnology*, 19(41), 415604.
- Lee, Y.-S. (2009). *Principles of terahertz science and technology*. Springer Science & Business Media.
- Lewis, A. P., Hunt, C., Thomas, O. & Wickham, M. (2017). High-speed non-contact sheet resistivity monitoring of printed electronics using inductive sensors. *Flexible and Printed Electronics*, 2(4), 044001.
- Lin, Q., Zheng, S., Song, Q., Zeng, X., Cai, Y., Li, Y., Chen, Z., Zha, L., Pan, X. & Xu, S. (2019). Generation of terahertz vortex pulses without any need of manipulation in the terahertz region. *Optics letters*, 44(4), 887–890.

- Liu, Y., Pharr, M. & Salvatore, G. A. (2017). Lab-on-skin: a review of flexible and stretchable electronics for wearable health monitoring. *ACS nano*, 11(10), 9614–9635.
- Logothetidis, S., Georgiou, D., Laskarakis, A., Koidis, C. & Kalfagiannis, N. (2013). In-line spectroscopic ellipsometry for the monitoring of the optical properties and quality of roll-to-roll printed nanolayers for organic photovoltaics. *Solar energy materials and solar cells*, 112, 144–156.
- Madou, M. J. (2018). *Fundamentals of microfabrication: the science of miniaturization*. CRC press.
- Madsen, M. H. & Hansen, P.-E. (2016). Scatterometry—fast and robust measurements of nano-textured surfaces. *Surface Topography: Metrology and Properties*, 4(2), 023003.
- Matsuhisa, N., Kaltenbrunner, M., Yokota, T., Jinno, H., Kuribara, K., Sekitani, T. & Someya, T. (2015). Printable elastic conductors with a high conductivity for electronic textile applications. *Nature communications*, 6, 7461.
- Merilampi, S., Björninen, T., Haukka, V., Ruuskanen, P., Ukkonen, L. & Sydänheimo, L. (2010). Analysis of electrically conductive silver ink on stretchable substrates under tensile load. *Microelectronics Reliability*, 50(12), 2001–2011.
- Minasyan, A., Trovato, C., Degert, J., Freysz, E., Brasselet, E. & Abraham, E. (2017). Geometric phase shaping of terahertz vortex beams. *Optics letters*, 42(1), 41–44.
- Mirka, B., Fong, D., Rice, N. A., Melville, O. A., Adronov, A. & Lessard, B. H. (2019). Polyfluorene-Sorted Semiconducting Single-Walled Carbon Nanotubes for Applications in Thin-Film Transistors. *Chemistry of Materials*, 31(8), 2863–2872.
- Mitra, D., Mitra, K. Y., Dzhagan, V., Pillai, N., Zahn, D. R. & Baumann, R. R. (2018a). Work function and conductivity of inkjet-printed silver layers: Effect of inks and post-treatments. *Journal of Electronic Materials*, 47(3), 2135–2142.
- Mitra, K. Y., Kapadia, S., Hartwig, M., Sowade, E., Xu, Z., Baumann, R. R. & Zichner, R. (2018b). Process Development of Large Area R2R Printing and Sintering of Conductive Patterns by Inkjet and Infra-Red Technologies Tailored for Printed Electronics. *NIP & Digital Fabrication Conference*, (1), 21-32.
- Mittleman, D., Gupta, M., Neelamani, R., Baraniuk, R., Rudd, J. & Koch, M. (1999). Recent advances in terahertz imaging. *Applied Physics B*, 68(6), 1085–1094.

- Miyamaru, F., Hayashi, S., Otani, C., Kawase, K., Ogawa, Y., Yoshida, H. & Kato, E. (2006). Terahertz surface-wave resonant sensor with a metal hole array. *Optics letters*, 31(8), 1118–1120.
- Miyamaru, F., Hattori, K., Shiraga, K., Kawashima, S., Suga, S., Nishida, T., Takeda, M. & Ogawa, Y. (2014). Highly sensitive terahertz sensing of glycerol-water mixtures with metamaterials. *Journal of Infrared, Millimeter, and Terahertz Waves*, 35(2), 198–207.
- Miyamoto, K., Kang, B. J., Kim, W. T., Sasaki, Y., Niinomi, H., Suizu, K., Rotermund, F. & Omatsu, T. (2016). Highly intense monocycle terahertz vortex generation by utilizing a Tsurupica spiral phase plate. *Scientific reports*, 6(1), 1–7.
- Murate, K. & Kawase, K. (2018). Perspective: Terahertz wave parametric generator and its applications. *Journal of Applied Physics*, 124(16), 160901.
- Murate, K., Roshtkhari, M. J., Ropagnol, X. & Blanchard, F. (2018). Adaptive spatiotemporal optical pulse front tilt using a digital micromirror device and its terahertz application. *Optics letters*, 43(9), 2090–2093.
- Naftaly, M., Vieweg, N. & Deninger, A. (2019). Industrial applications of terahertz sensing: State of play. *Sensors*, 19(19), 4203.
- Nasr, M., Richard, J. T., Skirlo, S. A., Heimbeck, M. S., Joannopoulos, J. D., Soljacic, M., Everitt, H. O. & Domash, L. (2017). Narrowband metamaterial absorber for terahertz secure labeling. *Journal of Infrared, Millimeter, and Terahertz Waves*, 38(9), 1120–1129.
- Neu, J. & Schmuttenmaer, C. A. (2018). Tutorial: An introduction to terahertz time domain spectroscopy (THz-TDS). *Journal of Applied Physics*, 124(23), 231101.
- Nguyen, H. A. D., Lee, J., Kim, C. H., Shin, K.-H. & Lee, D. (2013). An approach for controlling printed line-width in high resolution roll-to-roll gravure printing. *Journal of micromechanics and microengineering*, 23(9), 095010.
- Nishimura, T. & Ansell, M. (2002). Fast Fourier transform and filtered image analyses of fiber orientation in OSB. *Wood Science and Technology*, 36(4), 287–307.
- Oakley, C. & Chahal, P. (2018). Aerosol Jet Printed Quasi-Optical Terahertz Components. *IEEE Transactions on Terahertz Science and Technology*, 8(6), 765-772.
- Ofori-Okai, B. K., Sivarajah, P., Huang, W. R. & Nelson, K. A. (2016). THz generation using a reflective stair-step echelon. *Optics express*, 24(5), 5057–5068.

- Orrill, M. & LeBlanc, S. (2017). Printed thermoelectric materials and devices: Fabrication techniques, advantages, and challenges. *Journal of Applied Polymer Science*, 134(3), 44256.
- Owen, T. (1996). *Fundamentals of UV-visible spectroscopy: a primer*. Hewlett-Packard.
- Padilla, W., Aronsson, M., Highstrete, C., Lee, M., Taylor, A. & Averitt, R. (2007). Electrically resonant terahertz metamaterials: Theoretical and experimental investigations. *Physical Review B*, 75(4), 041102.
- Pan, Z., Wang, Y., Huang, H., Ling, Z., Dai, Y. & Ke, S. (2015). Recent development on preparation of ceramic inks in ink-jet printing. *Ceramics International*, 41(10), 12515-12528.
- Panin, A., Shugurov, A. & Oskomov, K. (2005). Mechanical properties of thin Ag films on a silicon substrate studied using the nanoindentation technique. *Physics of the Solid State*, 47(11), 2055–2059.
- Park, S., Hong, J., Choi, S., Kim, H., Park, W., Han, S., Park, J., Lee, S., Kim, D. & Ahn, Y. (2014). Detection of microorganisms using terahertz metamaterials. *Scientific reports*, 4, 4988.
- Park, S., Cha, S., Shin, G. & Ahn, Y. (2017). Sensing viruses using terahertz nano-gap metamaterials. *Biomedical optics express*, 8(8), 3551–3558.
- Pastorelli, F., Accanto, N., Jørgensen, M., van Hulst, N. F. & Krebs, F. C. (2017). In situ electrical and thermal monitoring of printed electronics by two-photon mapping. *Scientific reports*, 7(1), 1–6.
- Paulsen, A. & Nahata, A. (2015). K-space design of terahertz plasmonic filters. *Optica*, 2(3), 214–220.
- Pendry, J. B., Holden, A. J., Robbins, D. J. & Stewart, W. (1999). Magnetism from conductors and enhanced nonlinear phenomena. *IEEE transactions on microwave theory and techniques*, 47(11), 2075–2084.
- Perelaer, J. & Schubert, U. S. (2013). Novel approaches for low temperature sintering of inkjet-printed inorganic nanoparticles for roll-to-roll (R2R) applications. *Journal of Materials Research*, 28(4), 564.

- Perelaer, J., Smith, P. J., Mager, D., Soltman, D., Volkman, S. K., Subramanian, V., Korvink, J. G. & Schubert, U. S. (2010). Printed electronics: the challenges involved in printing devices, interconnects, and contacts based on inorganic materials. *Journal of Materials Chemistry*, 20(39), 8446–8453.
- Perelaer, J., Jani, R., Grouchko, M., Kamysny, A., Magdassi, S. & Schubert, U. S. (2012). Plasma and microwave flash sintering of a tailored silver nanoparticle ink, yielding 60% bulk conductivity on cost-effective polymer foils. *Advanced Materials*, 24(29), 3993–3998.
- Pipes, A. (2005). *Production for graphic designers*. Laurence King Publishing.
- Puglisi, G. & Battiato, S. (2009). Periodic pattern detection for real-time application. *International Workshop on Fuzzy Logic and Applications*, pp. 271–278.
- Qin, J., Ying, Y. & Xie, L. (2013). The detection of agricultural products and food using terahertz spectroscopy: a review. *Applied Spectroscopy Reviews*, 48(6), 439–457.
- Rahman, M. S., Shahzadeh, M., Rahman, M., Pisana, S. & Grau, G. (2020). High-speed contactless sintering characterization for printed electronics by frequency-domain thermorefectance. *Flexible and Printed Electronics*, 5(3), 035006.
- Redo-Sanchez, A., Laman, N., Schulkin, B. & Tongue, T. (2013). Review of terahertz technology readiness assessment and applications. *Journal of Infrared, Millimeter, and Terahertz Waves*, 34(9), 500–518.
- Redo-Sanchez, A., Heshmat, B., Aghasi, A., Naqvi, S., Zhang, M., Romberg, J. & Raskar, R. (2016). Terahertz time-gated spectral imaging for content extraction through layered structures. *Nature communications*, 7(1), 1–7.
- Ropagnol, X., Kovács, Z., Gilicze, B., Zhuldybina, M., Blanchard, F., Garcia-Rosas, C., Szatmári, S., Földes, I. & Ozaki, T. (2019). Intense sub-terahertz radiation from wide-bandgap semiconductor based large-aperture photoconductive antennas pumped by UV lasers. *New Journal of Physics*, 21(11), 113042.
- Rösch, R., Krebs, F. C., Tanenbaum, D. M. & Hoppe, H. (2012). Quality control of roll-to-roll processed polymer solar modules by complementary imaging methods. *Solar Energy Materials and Solar Cells*, 97, 176–180.
- Rossander, L. H., Zawacka, N. K., Dam, H. F., Krebs, F. C. & Andreasen, J. W. (2014a). In situ monitoring of structure formation in the active layer of polymer solar cells during roll-to-roll coating. *AIP Advances*, 4(8), 087105.

- Rossander, L. H., Zawacka, N. K., Dam, H. F., Krebs, F. C. & Andreasen, J. W. (2014b). In situ monitoring of structure formation in the active layer of polymer solar cells during roll-to-roll coating. *AIP Advances*, 4(8), 087105.
- Saini, R., Saini, S. & Sharma, S. (2010). Nanotechnology: the future medicine. *Journal of cutaneous and aesthetic surgery*, 3(1), 32.
- Selivanova, M., Coady, M. J., Pignanelli, J., Ocheje, M. U., Schlingman, K., Malik, A., Prado, M. & Rondeau-Gagné, S. (2020). Crack propagation and electronic properties of semiconducting polymer and siloxane-urea copolymer blends. *Flexible and Printed Electronics*, 5(3), 035001–035001.
- Seong, J., Kim, S., Park, J., Lee, D. & Shin, K.-H. (2015). Online noncontact thickness measurement of printed conductive silver patterns in roll-to-roll gravure printing. *International Journal of Precision Engineering and Manufacturing*, 16(11), 2265–2270.
- Shirakawa, H., Louis, E. J., MacDiarmid, A. G., Chiang, C. K. & Heeger, A. J. (1977). Synthesis of electrically conducting organic polymers: halogen derivatives of polyacetylene, (CH) x . *Journal of the Chemical Society, Chemical Communications*, (16), 578–580.
- Singh, M., Haverinen, H. M., Dhagat, P. & Jabbour, G. E. (2010a). Inkjet printing—process and its applications. *Advanced materials*, 22(6), 673–685.
- Singh, M., Haverinen, H. M., Dhagat, P. & Jabbour, G. E. (2010b). Inkjet printing—process and its applications. *Advanced materials*, 22(6), 673–685.
- Singh, R., Azad, A. K., O'Hara, J. F., Taylor, A. J. & Zhang, W. (2008). Effect of metal permittivity on resonant properties of terahertz metamaterials <https://doi.org/10.1364/OL.33.13.1506>. *Optics letters*, 33(13), 1506–1508.
- Skirlo, S. A., Richard, J. T., Nasr, M., Heimbeck, M. S., Joannopoulos, J. D., Soljacic, M., Everitt, H. O. & Domash, L. (2016). Millimeter Wave Absorber for Secure Identification. *Preprint*, 1-5.
- Smith, D. R., Padilla, W. J., Vier, D., Nemat-Nasser, S. C. & Schultz, S. (2000). Composite medium with simultaneously negative permeability and permittivity. *Physical review letters*, 84(18), 4184.
- Sneck, A., Mäkelä, T. & Alastalo, A. (2018). Reverse-offset for roll-to-roll high-resolution printing. *Flexible and Printed Electronics*, 3(1), 014001.
- Solymar, L. & Shamonina, E. (2009). *Waves in metamaterials*. Oxford University Press.

- Soukoulis, C. M. & Wegener, M. (2011). Past achievements and future challenges in the development of three-dimensional photonic metamaterials. *Nature photonics*, 5(9), 523–530.
- Sowade, E., Polomoshnov, M. & Baumann, R. R. (2016). The design challenge in printing devices and circuits: Influence of the orientation of print patterns in inkjet-printed electronics. *Organic Electronics*, 37, 428–438.
- Stantchev, R. I., Sun, B., Horneett, S. M., Hobson, P. A., Gibson, G. M., Padgett, M. J. & Hendry, E. (2016). Noninvasive, near-field terahertz imaging of hidden objects using a single-pixel detector. *Science advances*, 2(6), e1600190.
- Stevens, G., Edmunds, J., Hibbins, A. P. & Sambles, J. R. (2011). Microwave transmission of a hexagonal array of triangular metal patches. *Progress In Electromagnetics Research*, 20, 219–229.
- Sushko, O., Pigeon, M., Donnan, R. S., Kreouzis, T., Parini, C. G. & Dubrovka, R. (2017). Comparative study of sub-THz FSS filters fabricated by inkjet printing, microprecision material printing, and photolithography. *IEEE Transactions on Terahertz Science and Technology*, 7(2), 184–190.
- Takano, K., Miyamaru, F., Akiyama, K., Miyazaki, H., Takeda, M. W., Abe, Y., Tokuda, Y., Ito, H. & Hangyo, M. (2014). Crossover from capacitive to inductive electromagnetic responses in near self-complementary metallic checkerboard patterns. *Optics express*, 22(20), 24787–24795.
- Taleb, F., Al-Naib, I. & Koch, M. (2020). Free-Standing Complementary Asymmetric Metasurface for Terahertz Sensing Applications. *Sensors*, 20(8), 2265.
- Tan, H. W., An, J., Chua, C. K. & Tran, T. (2019). Metallic nanoparticle inks for 3D printing of electronics. *Advanced Electronic Materials*, 5(5), 1800831.
- Tang, C. W. (1986). Two-layer organic photovoltaic cell. *Applied physics letters*, 48(2), 183–185.
- Tao, H., Bingham, C., Pilon, D., Fan, K., Strikwerda, A., Shrekenhamer, D., Padilla, W., Zhang, X. & Averitt, R. (2010a). A dual band terahertz metamaterial absorber. *Journal of physics D: Applied physics*, 43(22), 225102.
- Tao, H., Padilla, W. J., Zhang, X. & Averitt, R. D. (2010b). Recent progress in electromagnetic metamaterial devices for terahertz applications. *IEEE Journal of Selected Topics in Quantum Electronics*, 17(1), 92–101.

- Tao, Y. H., Fitzgerald, A. J. & Wallace, V. P. (2020). Non-contact, non-destructive testing in various industrial sectors with terahertz technology. *Sensors*, 20(3), 712.
- Tenggara, A. P., Park, S., Yudistira, H. T., Ahn, Y. & Byun, D. (2017). Fabrication of terahertz metamaterials using electrohydrodynamic jet printing for sensitive detection of yeast. *Journal of Micromechanics and Microengineering*, 27(3), 035009.
- Tone, R. & Ganz, S. (2016). Characterization Techniques for Printed Electronics Robert. In Nisato, G., Lupo, D. & Ganz, S. (Eds.), *Organic and Printed Electronics: Fundamentals and Applications* (pp. 117-146). Location: CRC Press.
- TOPTICA. (2016). TeraFlash-pro. Consulted at <https://www.toptica.com/products/terahertz-systems/time-domain/teraflash-pro/>.
- Tousignant, M. N., Rice, N. A., Peltekoff, A., Sundaresan, C., Miao, C., Hamad, W. Y. & Lessard, B. H. (2020). Improving Thin-Film Properties of Poly (vinyl alcohol) by the Addition of Low-Weight Percentages of Cellulose Nanocrystals. *Langmuir*, 36(13), 3550–3557.
- Tremain, B., Durrant, C., Carter, I., Hibbins, A. P. & Sambles, J. R. (2015). The effect of rotational disorder on the microwave transmission of checkerboard metal square arrays. *Scientific reports*, 5(1), 1–9.
- Trudeau, C., Bolduc, M., Beaupré, P., Topart, P., Alain, C. & Cloutier, S. (2017). Inkjet-printed flexible active multilayered structures. *MRS Advances*, 2(18), 1015-1020.
- Tsai, H., Asadpour, R., Blancon, J.-C., Stoumpos, C. C., Durand, O., Strzalka, J. W., Chen, B., Verduzco, R., Ajayan, P. M., Tretiak, S. et al. (2018). Light-induced lattice expansion leads to high-efficiency perovskite solar cells. *Science*, 360(6384), 67–70.
- Urbas, R., Manojlovič, S., Šumiga, B. & Elesini, U. S. (2017). Influence of microcapsules on the properties of raised prints. *Cellul Chem Technol*, 51, 319–331.
- Vartiainen, J., Sadovnikov, A., Kamarainen, J.-K., Lensu, L. & Kälviäinen, H. (2008). Detection of irregularities in regular patterns. *Machine Vision and Applications*, 19(4), 249–259.
- Veselago, V. G. (1968). The electrodynamics of substances with simultaneously negative values of ϵ and μ . *Soviet Physics Uspekhi*, 10, 509.
- Walther, M., Ortner, A., Meier, H., Löffelmann, U., Smith, P. J. & Korvink, J. G. (2009). Terahertz metamaterials fabricated by inkjet printing. *Applied Physics Letters*, 95(25), 251107.

- Walther, M., Fischer, B. M., Ortner, A., Bitzer, A., Thoman, A. & Helm, H. (2010). Chemical sensing and imaging with pulsed terahertz radiation. *Analytical and bioanalytical chemistry*, 397(3), 1009–1017.
- Wang, X., Shi, J., Sun, W., Feng, S., Han, P., Ye, J. & Zhang, Y. (2016). Longitudinal field characterization of converging terahertz vortices with linear and circular polarizations. *Optics express*, 24(7), 7178–7190.
- Wang, X. & Liu, J. (2016). Recent advancements in liquid metal flexible printed electronics: Properties, technologies, and applications. *Micromachines*, 7(12), 206.
- Wen, Y., Ma, W., Bailey, J., Matmon, G., Aeppli, G. & Yu, X. (2014). Absorption modulation of terahertz metamaterial by varying the conductivity of ground plane. *Applied Physics Letters*, 105(14), 141111.
- Wikipedia. (2007). Optical vortex. Consulted at https://en.wikipedia.org/wiki/Optical_vortex.
- Withayachumnankul, W. & Abbott, D. (2009). Metamaterials in the terahertz regime. *IEEE Photonics Journal*, 1(2), 99–118.
- Withayachumnankul, W. & Naftaly, M. (2014). Fundamentals of measurement in terahertz time-domain spectroscopy. *Journal of Infrared, Millimeter, and Terahertz Waves*, 35(8), 610–637.
- www.instructables.com. How to Use a Multimeter Basics. Consulted at <https://www.instructables.com/How-to-Use-a-Multimeter-Basics/>.
- www.ossila.com. The Four-Point Probe System in contact with a sample. Consulted at <https://www.ossila.com/pages/four-point-probe-measurement-guide>.
- Xie, L., Gao, W., Shu, J., Ying, Y. & Kono, J. (2015). Extraordinary sensitivity enhancement by metasurfaces in terahertz detection of antibiotics. *Scientific reports*, 5(1), 1–4.
- Xu, W., Xie, L., Zhu, J., Wang, W., Ye, Z., Ma, Y., Tsai, C.-Y., Chen, S. & Ying, Y. (2017). Terahertz sensing of chlorpyrifos-methyl using metamaterials. *Food chemistry*, 218, 330–334.
- Yang, J., Li, X., Xu, J., Cao, Y., Zhang, Y., Wang, L. & Jiang, S. (2018). Development of an optical defect inspection algorithm based on an active contour model for large steel roller surfaces. *Applied optics*, 57(10), 2490–2498.

- Yang, X., Yang, K., Luo, Y. & Fu, W. (2016). Terahertz spectroscopy for bacterial detection: opportunities and challenges. *Applied microbiology and biotechnology*, 100(12), 5289–5299.
- Yilmaz, S. (2015). The geometric resistivity correction factor for several geometrical samples. *Journal of Semiconductors*, 36(8), 082001.
- Yu, L., Hao, L., Meiqiong, T., Jiaoqi, H., Wei, L., Jinying, D., Xueping, C., Weiling, F. & Yang, Z. (2019). The medical application of terahertz technology in non-invasive detection of cells and tissues: opportunities and challenges. *RSC advances*, 9(17), 9354–9363.
- Yu, N., Genevet, P., Kats, M. A., Aieta, F., Tetienne, J.-P., Capasso, F. & Gaburro, Z. (2011). Light propagation with phase discontinuities: generalized laws of reflection and refraction. *Science*, 334(6054), 333–337.
- Yudistira, H. T., Tenggara, A. P., Nguyen, V. D., Kim, T. T., Prasetyo, F. D., Choi, C.-g., Choi, M. & Byun, D. (2013). Fabrication of terahertz metamaterial with high refractive index using high-resolution electrohydrodynamic jet printing. *Appl. Phys. Lett*, 103(21), 211106.
- Yue, F., Wen, D., Zhang, C., Gerardot, B. D., Wang, W., Zhang, S. & Chen, X. (2017). Multichannel polarization-controllable superpositions of orbital angular momentum states. *Advanced Materials*, 29(15), 1603838.
- Zapka, W. (2017). *Handbook of industrial inkjet printing: a full system approach*. John Wiley & Sons.
- Zeitler, A. & Shen, Y.-C. (2012). Industrial Applications of Terahertz Imaging. In Peiponen, K.-E., Zeitler, A. & Kuwata-Gonokami, M. (Eds.), *Terahertz spectroscopy and imaging* (vol. 171, pp. 451–489). Springer.
- Zeng, Y., Edwards, M., Stevens, R., Bowen, J. W., Donnan, R. S. & Yang, B. (2017). Terahertz characterisation of UV offset lithographically printed electronic-ink. *Organic Electronics*, 48, 382–388.
- Zhao, J., Yiwen, E., Williams, K., Zhang, X.-C. & Boyd, R. W. (2019). Spatial sampling of terahertz fields with sub-wavelength accuracy via probe-beam encoding. *Light: Science & Applications*, 8(1), 1–8.
- Zhong, S. (2019). Progress in terahertz nondestructive testing: A review. *Frontiers of Mechanical Engineering*, 1–9.

- Zhou, X., Xu, H., Cheng, J., Zhao, N. & Chen, S.-C. (2015). Flexure-based roll-to-roll platform: A practical solution for realizing large-area microcontact printing. *Scientific reports*, 5, 10402.
- Zhuldybina, M., Ropagnol, X., Trudeau, C., Bolduc, M., Zednik, R. J. & Blanchard, F. (2019a). Caractérisation de l'électronique imprimable au moyen des ondes térahertz. *Substance ÉTS*.
- Zhuldybina, M., Ropagnol, X., Trudeau, C., Bolduc, M., Zednik, R. J. & Blanchard, F. (2019b). Contactless in situ electrical characterization method of printed electronic devices with terahertz spectroscopy. *Sensors*, 19(3), 444.
- Zhuldybina, M., Ropagnol, X., Bois, C., Zednik, R. J. & Blanchard, F. (2020). Printing accuracy tracking with 2D optical microscopy and super-resolution metamaterial-assisted 1D terahertz spectroscopy. *npj Flexible Electronics*, 4(1), 1–7.